A Search for Evidence of New Particle Production in pp Collisions at sqrt(s) = 8 TeV in the Lepton, Jets, and Photons Final State

Brian Patrick Francis

Charlottesville, VA

B.S., The University of Massachusetts Amherst, 2009

A Dissertation presented to the Graduate Faculty

of the University of Virginia in Candidacy for the Degree of

Doctor of Philosophy

Department of Physics

University of Virginia

August, 2015

Abstract

This dissertation presents a search for evidence of new particle production in the one- and two-photon, lepton, and b-jet final state in proton-proton collisions at center-of-mass energy 8 TeV. The search is performed in the full 2012 dataset, a total integrated luminosity of 19.7 fb^{-1}, collected by the Compact Muon Solenoid experiment at the Large Hadron Collider. A substantial imbalance in the transverse momentum of observed particles (missing transverse energy) in this final state would result from the theory of Supersymmetry, the fundamental symmetry of spin which may provide a solution to the hierarchy problem of particle physics. The presence of third-generation quark decays and photons in the final state are motivated by gauge-mediated models of Supersymmetry, and in particular by models which solve the hierarchy problem most naturally. The expected background distribution of missing transverse energy in these events, dominated by $t\bar{t}+\gamma$ and $t\bar{t}+\gamma\gamma$ production, is simulated in Monte Carlo and compared to the observed distribution in data. No significant excess of large missing transverse energy is observed. Upper limits on the cross sections of scalar top pair production are set at the 95% confidence level between 5 and 15 fb. The results of this search are among the first within gauge-mediated models of Supersymmetry with a light scalar top and places extraordinarily tight constraints on such models by excluding scalar top masses below 650–750 GeV/c^2.

Contents

List of Figures

List of Tables

Acknowledgements

Above all, this dissertation is made possible by the dedicated efforts of the thousands of outstanding individuals contributing to the design, construction, commissioning, and operation of the Large Hadron Collider and the Compact Muon Solenoid. The results presented here are built upon a lifetime of passionate work by many, and the excellent performance of the accelerator and experiment is a monumental achievement. I am proud and profoundly grateful to have participated in this great endeavor.

I would like to thank the SUSY Photons (née RA3) analysis group whose indispensable motivation enabled and refined my investigations. The leadership of David Mason, Yuri Gershtein, and Yurii Maravin helped realize and present the analysis to the wider CMS community, and provided a frank kick in the pants I so often needed. Working alongside and discussing with Rachel Yohay, David Morse, and Yutaro Iiyama formed the backbone of my nascent analysis abilities during the hectic early months of 8 TeV results, and without their input and knowledge I would not be the scientist I am today.

I would also like to thank my compatriots at UVA. Joseph Goodell, Thomas Anderson, and especially John Wood provided me with an invaluable sounding board and fielded many questions, exhibiting tremendous patience the many times I asked them to talk ideas through; I believe a great portion of my education was in these hashings-out. Evan Wolfe and Fan Xia accepted what tutelage I managed to offer them, and helped me immensely to realize I should know what I am talking about before I say something. Michael Balasz was the guru of HEP I got started with at the very beginning, learning to code and building the VPT rig which would later became the bane of John Wood's summers. Mike Arenton's skill and experience during my time at the Fermilab test beam facilities was immeasurably important and taught me a great deal about particle experiments. The encyclopedic knowledge of Al Tobias regarding the 4 T superconducting magnet in our laboratory was irreplaceable and it was a pleasure and honor to work alongside him in times of great chaos and strife. Thanks as well go to Professors Chris Neu and Bob Hirosky, both excellent physicists and teachers who are the very picture of the scientist I strive to one day become.

Immense gratitude goes to my advisor Professor Brad Cox, who has patiently focused my efforts over the last six years. Under his leadership the UVA CMS group has accomplished an incredible program of physics. Under his guidance I have travelled the world and have analyzed the highest reaches of experimental particle physics at the world's largest machine in history. I thank him endlessly for his education and the opportunities he has provided me.

To my friends in Charlottesville, across the United States, and abroad at CERN, I sincerely thank you for providing the 'life' in graduate student life these past years. With you I have shared unforgettable evenings, incredible concerts, and many fond memories. Thank you all in each your own way for providing me an outlet for my in(s)anities, and it is no small desire for me to continue in science to work or meet with you all again.

Finally I would like to thank my parents, who instilled in me from an early age a deep respect for learning and intellectual curiosity that has propelled my education and early career. Without the opportunities and encouragement they have provided me, I would not be here today.

Chapter 1

Introduction

The 2012 discovery of a boson of mass 125 GeV/c^2 [28, 29] and the substantial evidence of its consistency with the Higgs boson [30] are striking victories for the Standard Model (SM). Successfully describing electroweak symmetry breaking, the SM continues as the most well-tested and robust description of modern particle physics available today. However in passing this important test, the shortcomings of this model become all the more intriguing. The SM offers no explanation for the existence of dark matter or the masses of neutrinos, and cannot describe the observed disparity between matter and anti-matter in our Universe. The SM suffers what is known as the 'hierarchy problem', with its fundamental parameters varying over many orders of magnitude—in particular the mass of the Higgs boson is very light compared to corrections it should receive at the gravitational scale. A Higgs boson of mass 125 GeV/c^2 must either be the result of extraordinary numerical coincidences with a required precision on the order of one part in 10^{26}, or naturally protected from Planck-scale corrections by contributions from undiscovered new physics.

The models proposed to address these problems are generally referred to as Beyond the Standard Model (BSM) physics, as many of them attempt to extend the existing SM into higher energies while keeping the lower-energy behaviour in agreement with existing observations. Nearly all BSM theories predict the existence of heavy, undiscovered particles that are producible in particle collisions of sufficiently high energies. The oftentimes distinctive decays of these heavy new particles can be observed as significant deviations from SM predictions of the production rates or kinematics of such events.

One such BSM theory that provides an elegant solution to many outstanding issues in the SM, along with providing a candidate particle that could describe dark matter, is Supersymmetry (SUSY). SUSY extends the SM with the addition of a fundamental symmetry of spacetime, that of spin—for each known particle, there is a partner that shares all of its characteristics except differing by a spin of $\frac{1}{2}$. This symmetry must be a broken symmetry however, as for example there has been no observation of a spin-0 particle with the mass and charge of the electron. Many attempts to describe the manner in which this symmetry is broken have been made, but of interest is Gauge Mediated Supersymmetry Breaking (GMSB). GMSB introduces 'messenger' fields that are coupled indirectly to the Minimal Supersymmetric Standard Model (MSSM) through the ordinary SM gauge interactions, leading gravitational interactions to be far less important to the breaking than in other SUSY models. This manner of communication of the breaking is well-motivated because flavor-violating dynamics are suppressed, avoiding problematic flavor-changing neutral currents (FCNC) some models of SUSY introduce. Since in this model particle masses are driven by radiative corrections from messenger loop interactions which couple at SM gauge strength, superpartners of particles with small coupling strengths are the lightest. Because of this, the superpartners of the electroweak gauge bosons ('neutralinos', $\tilde{\chi}$) tend to be the next-to-lightest supersymmetric particle (NLSP) and the superpartner of the graviton ('gravitino', $\tilde{G}$) is the lightest supersymmetric particle (LSP). Neutralino decays to gauge bosons and gravitinos would result in well-measured particles such as photons and a significant momentum imbalance from energetic gravitinos escaping undetected by instrumentation, referred to as missing transverse energy ($E_{\mathrm{T}}^{\mathrm{miss}}$ or $\not{E}_{\mathrm{T}}$).

While many searches for GMSB have been performed in collider experiments already, few as yet have focused on naturalness—the concept that all free parameters in a viable physical model should be of the same order, or that parameters need not be 'fine-tuned' to specific values in order to successfully describe observations. To address the hierarchy problem, natural GMSB would be realized in a SUSY particle ('sparticle') mass hierarchy where the scalar top partner (and to a lesser degree the scalar bottom, called the stop and sbottom squarks) is much lighter than other sparticles. Since the coupling of the Higgs field to the top quark is significantly larger than to others, the Higgs mass correction from top loops is the most severe; a stop loop contributes to the Higgs mass with the opposite sign as a top loop, so a stop mass closer to the top mass (i.e., lighter) would provide a more natural cancellation than if it was far heavier than the top mass. The assumption of third-generation squarks decaying to neutralinos and third-generation quarks stands in great contrast to previous GMSB searches which assumed only first- and second-generation squarks were light enough to be observably produced—the presence of top or bottom quarks in a collider event is highly distinguishable from simple jets. Requiring third-generation quarks in the final state dramatically reduces SM backgrounds while providing discovery reach into GMSB phase-space most favorable to explain the hierarchy problem and the small mass of the Higgs boson.

Presented by this dissertation is a search for evidence of the production of pairs of stop squarks

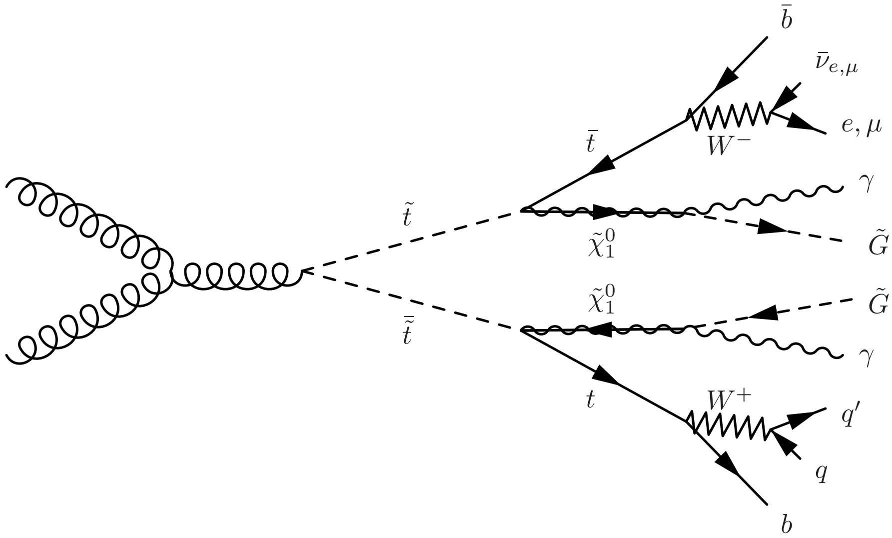

Figure 1.1: Strong pair production of stop squarks decaying to bino-like neutralinos and top quarks. The bino-like neutralino decays primarily to a photon and a gravitino. Shown above is the semi-leptonic decay of the $t\bar{t}$ system.

with a 'bino-like' NLSP neutralino. The choice of parameters for the signal model leads to mass eigenstates mixing the spin 1/2 partners of the gauge bosons, the gauginos, forming neutral 'neutralinos' and charged 'charginos'. With the lightest among them being a mostly bino-like mixture, the production of pairs of light stop squarks decaying to bino-like NLSPs would decay further to an event signature of a top quark, anti-top quark, two photons, and $\not\!\!E_{\mathrm{T}}$. The search is performed in the semi-leptonic decay mode of the top quark pair, resulting in a final state of one or more photons, one lepton (electron or muon), two bottom quark jets, and several additional jets. The results are interpreted by comparing the SM prediction of the distribution of $\not\!\!E_{\mathrm{T}}$ in these events against that of the observed data. This search is among the first experimental results within light third-generation GMSB models.

This search is performed in data collected from proton collisions at the Large Hadron Collider (LHC) with the Compact Muon Solenoid (CMS) experiment at the European Organization for Nuclear Research (CERN) in Geneva, Switzerland. The CMS detector is capable of efficiently identifying and measuring the kinematic properties of photons, leptons, jets, b-jets, and $\not\!\!E_{\mathrm{T}}$. The detector is so-named due to its high-granularity calorimetry and tracking systems being contained entirely within its 3.8 T axial superconducting solenoid, providing excellent resolution of charged particle trajectories and momenta by measuring their curvature through the magnetic field, and due to its high-resolution muon detector interspersed with the iron return yoke for the magnetic field. The hermetic design of the detector allows for the reconstruction of all interacting final state particles produced in the detector, giving good $\not\!\!E_{\mathrm{T}}$ resolution which is paramount to this search.

Chapter 2

The Standard Model of Particle Physics

Described by Steven Weinberg at the 30th anniversary of the discovery of neutral currents and the 20th anniversary of the discovery of the W and Z bosons [31], the Standard Model emerged from three particularly good ideas in the 1950s and 1960s:

- The quark model proposed independently in 1964 by Gell-Mann [32] and Zweig [33],
- The concept of local gauge symmetries, pioneered for $SU(2)$ by Yang and Mills [34] in 1954, and
- The concept of spontaneously broken symmetries, explored by Goldstone, Salam, and Weinberg in 1961 [35] and 1962 [36].

These ideas provided the necessary foundation for a number of developments that together form the SM. Glashow, Salam, and Ward postulated that the electromagnetic and weak forces were two facets of a unified electroweak force, mediated by vector gauge bosons [37, 38]. Glashow, Iliopoulos, and Maiani suggested the existence of a fourth quark to avoid flavor-changing neutral currents in kaon oscillations [39]. Kobayashi and Maskawa expanded on this to include a third generation of quarks to provide a mechanism for CP-violation in kaon decays [40, 41]. The near-simultaneous 1964 works of Englert and Brout [42], Higgs [43], and Guralnik, Hagen, and Kibble [44] showed that the electroweak gauge bosons could acquire a mass as the result of a spontaneously broken symmetry—a mechanism later named for Higgs. Lastly, the independent works of Weinberg and Salam in 1967 demonstrated that such a mechanism could be responsible for the breaking of the electroweak symmetry [45, 46].

The Standard Model stands as a tremendously successful predictor of physical quantities like particle production and decay rates, interaction cross sections, and the relationship between electroweak gauge bosons and their couplings. The many precision electroweak and QCD measurements of the Stanford Linear Collider (SLC) at SLAC and the Large Electron Positron collider (LEP) at CERN rigorously support the Standard Model to unprecedented accuracies [47]. Figure 2.1 shows a small selection of these measurements, where the data agrees very well with SM predictions.

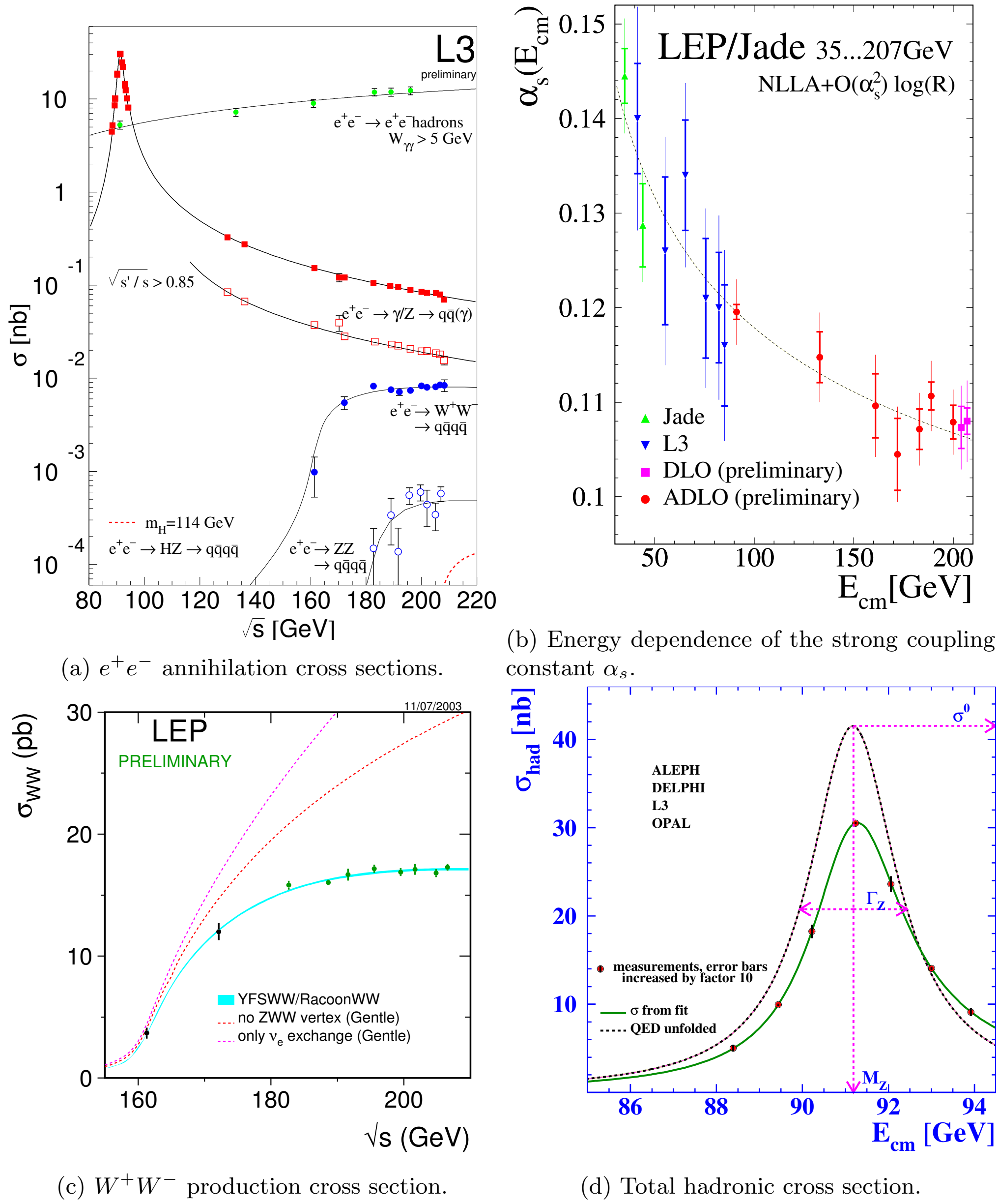

(a) e^+e^- annihilation cross sections.

(b) Energy dependence of the strong coupling constant α_s.

(c) W^+W^- production cross section.

(d) Total hadronic cross section.

Figure 2.1: Selected measurement results from LEP versus center of mass energy. The agreement with the SM predictions, as well as the precision are strong supporters of the SM at low energies. Reprinted from reference [1].

This chapter presents a brief introduction and overview of the mathematical foundations of the Standard Model in Section 2.1. The breaking of the electroweak symmetry is described in Section 2.2 and its implication of the hierarchy problem is explained in Section 2.3. Finally Section 2.4 relates several other shortcomings of the SM and the need for an additional theory, Supersymmetry.

2.1 The Standard Model

The Standard Model is the quantum field theory of the known fields: the fermion field ψ, the gluon field G_a, the electroweak boson fields W_1, W_2, W_3 and B, and the Higgs field ϕ. The dynamics of these fields are invariant under the internal symmetries of the gauge group

$$SU(3)_C \otimes SU(2)_L \otimes U(1)_Y \tag{2.1}$$

where $SU(3)_C$ is the gauge symmetry of color charge acting on G, $SU(2)_L$ is the gauge symmetry of weak isospin acting on W and ϕ, and $U(1)_Y$ is the gauge symmetry of weak hyper-charge acting on B and ϕ. The fermion field contents are assigned *representations* of the gauge group under which they transform by the actions of the bosonic fields. Fermion fields are separated into three generations, each sharing quantum numbers but differing in mass. The full content of the fermion field is shown in Table 2.1 and the boson field contents are shown in Table 2.2. The W and B fields are mixed by the breaking of the electroweak symmetry producing the observable bosons related by [48]

$$\begin{aligned} A_\mu &= \sin\theta_W W_\mu^3 + \cos\theta_W B_\mu \\ Z_\mu &= \cos\theta_W W_\mu^3 - \sin\theta_W B_\mu \\ W_\mu^\pm &= \frac{1}{\sqrt{2}}(W_\mu^1 \mp i W_\mu^2) \end{aligned} \tag{2.2}$$

with

$$\tan\theta_W = \frac{g'}{g_w} \tag{2.3}$$

where θ_W is known as the Weinberg Angle or the weak mixing parameter, g' and g_w are the coupling constants for weak hypercharge and isospin respectively, and A_μ is the electromagnetic (photon) field.

The strong interaction, or the theory of Quantum Chromodynamics (QCD), is described by the $SU(3)$ gauge symmetry of color charge. QCD is an asymptotically free interaction and couples weakly at short distances, resulting in confinement of the color charge and requiring that no observable state carries color charge. The QCD interaction Lagrangian can be written [48] as

$$\mathcal{L}_{QCD} = -\frac{1}{2} \text{ tr } G_{\mu\nu}G^{\mu\nu} + \sum_{k}^{n_f} \bar{q}_k(i\not{D} - m_k)q_k \tag{2.4}$$

where

$$\begin{aligned} G_{\mu\nu} &= \partial_\mu G_\nu - \partial_\nu G_\mu - ig[G_\mu, G_\nu] \\ \mathrm{D}_\mu q_k &= (\partial_\mu - igG_\mu)q_k \\ G_\mu &= \sum_{a=1}^{8} G^a_\mu \lambda^a/2 \end{aligned}$$

where $\not{D} \equiv \gamma^\mu \mathrm{D}_\mu$, the m_k's are the quark masses, and the λ^a's are the Gell-Mann matrices satisfying the $SU(3)$ commutation relations

$$\left[\frac{\lambda_a}{2}, \frac{\lambda_b}{2}\right] = if^{abc}\frac{\lambda^c}{2} \tag{2.5}$$

and normalized as

$$\text{tr}(\lambda^a\lambda^b) = 2\delta^{ab} \tag{2.6}$$

Type	Notation	Representation under $SU(3)_C \otimes SU(2)_L \otimes U(1)_Y$
Left-handed quark doublet	$Q_L : \begin{pmatrix} u \\ d \end{pmatrix}_L, \begin{pmatrix} c \\ s \end{pmatrix}_L, \begin{pmatrix} t \\ b \end{pmatrix}_L$	$(\mathbf{3}, \mathbf{2}, \frac{1}{3})$
Right-handed up-type quark singlet	$U_R : u_R, c_R, t_R$	$(\bar{\mathbf{3}}, \mathbf{1}, \frac{4}{3})$
Right-handed down-type quark singlet	$D_R : d_R, s_R, b_R$	$(\bar{\mathbf{3}}, \mathbf{1}, -\frac{2}{3})$
Left-handed lepton doublet	$L_L : \begin{pmatrix} \bar{\nu}_e \\ e^- \end{pmatrix}_L, \begin{pmatrix} \bar{\nu}_\mu \\ \mu^- \end{pmatrix}_L, \begin{pmatrix} \bar{\nu}_\tau \\ \tau^- \end{pmatrix}_L$	$(\mathbf{1}, \mathbf{2}, \text{-}1)$
Right-handed charge lepton singlet	$L_R : e^-_R, \mu^-_R, \tau^-_R$	$(\bar{\mathbf{1}}, \mathbf{1}, \text{-}2)$

Table 2.1: Fermion field content of the SM. A representation of **1** means a field is not transform under a symmetry (ie not charged) and is in a 1-dimensional representation of that gauge group. A bar over the representation signifies an adjoint representation. The right-handed fermion singlets do not transform under $SU(2)_L$ as they are not charged in weak isospin, and do not interact with the weak force. Similarly the leptons do not transform under $SU(3)_C$ as they are colorless, and do not interact with the strong force. Right-handed neutrinos are not observed in Nature.

The weak interaction can be separated into two distinct currents, flavor-changing charged

Type	Associated Charge	Representation under $SU(3)_C \otimes SU(2)_L \otimes U(1)_Y$
B	Weak hypercharge	($\mathbf{1}$, $\mathbf{1}$, 0)
W	Weak isospin	($\mathbf{1}$, $\mathbf{3}$, 0)
G	Color	($\mathbf{8}$, $\mathbf{1}$, 0)
H		($\mathbf{1}$, $\mathbf{1}$, 1)

Table 2.2: Boson field content. The W and B fields mix with the breaking of the electroweak symmetry to form the observable $W^{\pm}$, Z^0, and γ bosons.

currents and neutral currents. The neutral weak interaction has the form [48]

$$\mathcal{L}_{NC} = e \sum_f q_f \bar{f} \gamma_\mu f A^\mu + \frac{g}{\cos\theta_W} J^0_\mu Z^\mu \tag{2.7}$$

with

$$\begin{aligned} e &= g \sin\theta_W \\ J^0_\mu &= \sum_f [g^f_L \bar{f} \gamma_\mu \frac{(1-\gamma_5)}{2} f + g^f_R \bar{f} \gamma_\mu \frac{(1+\gamma_5)}{2} f] \\ g^f_{L,R} &= I_3(f_{L,R}) - q_f \sin^2\theta_W \end{aligned}$$

where I_3 is the weak isospin and $\frac{(1\mp\gamma_5)}{2}$ projects the left-handed (minus) and right-handed (plus) components of the spinor fields. The neutral current contains the electromagnetic coupling of fermions to the photon field A^μ and the coupling of like-handed fermions to the Z boson field.

The charged weak interaction has the form [48]

$$\mathcal{L}_{CC} = \frac{g}{\sqrt{2}} W^+_\mu \left[\bar{\nu}_i \gamma^\mu \frac{1-\gamma_5}{2} e_i + \bar{u}_i \gamma^\mu \frac{1-\gamma_5}{2} M^{CKM}_{ij} d_j \right] + \text{h.c.} \tag{2.8}$$

coupling the charged W boson to quarks and like-generation leptons, mixing quark generations by the unitary matrix M^{CKM} known as the Cabibbo-Kobayashi-Maskawa (CKM) matrix. The CKM matrix acts as a rotation between the mass eigenstate basis of down-type quarks (d, s, b) and the weak eigenstate basis. The charged weak interaction is also maximally parity violating—only the left-handed fermion doublets are coupled.

The complete Standard Model Lagrangian, including contributions from the Higgs field described in Section 2.2, is of the form [49]

$$
\begin{aligned}
\mathcal{L}_{SM} = & -\frac{1}{4}B_{\mu\nu}B^{\mu\nu} - \frac{1}{8}\ \mathrm{tr}\ \boldsymbol{W}_{\mu\nu}\boldsymbol{W}^{\mu\nu} - \frac{1}{2}\ \mathrm{tr}\ \boldsymbol{G}_{\mu\nu}\boldsymbol{G}^{\mu\nu} && (2.9a)\\
& + (\bar{\nu}_L, \bar{e}_L)\tilde{\sigma}^\mu i D_\mu \begin{pmatrix} \nu_L \\ e_L \end{pmatrix} + \bar{e}_R \sigma^\mu i D_\mu e_R + \bar{\nu}_R \sigma^\mu i D_\mu \nu_R + \mathrm{h.c.} && (2.9b)\\
& - \frac{\sqrt{2}}{\nu}\left[(\bar{\nu}_L, \bar{e}_L)\phi M^e e_R + \bar{e}_R \bar{M}^e \bar{\phi} \begin{pmatrix} \nu_L \\ e_L \end{pmatrix} \right] && (2.9c)\\
& - \frac{\sqrt{2}}{\nu}\left[(-\bar{e}_L, \bar{\nu}_L)\phi^* M^\nu \nu_R + \bar{\nu}_R \bar{M}^\nu \phi^T \begin{pmatrix} -e_L \\ \nu_L \end{pmatrix} \right] && (2.9d)\\
& + (\bar{u}_L, \bar{d}_L)\tilde{\sigma}^\mu i D_\mu \begin{pmatrix} u_L \\ d_L \end{pmatrix} + \bar{u}_R \sigma^\mu i D_\mu u_R + \bar{d}_R \sigma^\mu i D_\mu d_R + \mathrm{h.c.} && (2.9e)\\
& - \frac{\sqrt{2}}{\nu}\left[(\bar{u}_L, \bar{d}_L)\phi M^d d_R + \bar{d}_R \bar{M}^d \bar{\phi} \begin{pmatrix} u_L \\ d_L \end{pmatrix} \right] && (2.9f)\\
& - \frac{\sqrt{2}}{\nu}\left[(-\bar{d}_L, \bar{u}_L)\phi^* M^u u_R + \bar{u}_R \bar{M}^u \phi^T \begin{pmatrix} -d_L \\ u_L \end{pmatrix} \right] && (2.9g)\\
& + \overline{(D_\mu \phi)} D^\mu \phi - \frac{m_h^2}{2\nu^2}\left[\bar{\phi}\phi - \frac{\nu^2}{2} \right]^2 && (2.9h)
\end{aligned}
$$

with

$$
\begin{aligned}
D_\mu \begin{pmatrix} \nu_L \\ e_L \end{pmatrix} &= \left[\partial_\mu - \frac{ig_1}{2}B_\mu + \frac{ig_2}{2}\boldsymbol{W}_\mu \right] \begin{pmatrix} \nu_L \\ e_L \end{pmatrix}\\
D_\mu \begin{pmatrix} u_L \\ d_L \end{pmatrix} &= \left[\partial_\mu + \frac{ig_1}{6}B_\mu + \frac{ig_2}{2}\boldsymbol{W}_\mu + ig\boldsymbol{G}_\mu \right] \begin{pmatrix} u_L \\ d_L \end{pmatrix}\\
D_\mu \nu_R &= \partial_\mu \nu_R\\
D_\mu e_R &= \left[\partial_\mu - ig_1 B_\mu \right] e_R\\
D_\mu u_R &= \left[\partial_\mu + \frac{i2g_1}{3}B_\mu + ig\boldsymbol{G}_\mu \right] u_R\\
D_\mu d_R &= \left[\partial_\mu - \frac{ig_1}{3}B_\mu + ig\boldsymbol{G}_\mu \right] d_R\\
D_\mu \phi &= \left[\partial_\mu + \frac{ig_1}{2}B_\mu + \frac{ig_2}{2}\boldsymbol{W}_\mu \right] \phi
\end{aligned}
$$

2.2 Electroweak Symmetry Breaking

To maintain local gauge invariance, The Standard Model Lagrangian (Eqn. 2.9) contains no explicit mass terms. The left- and right-handed chiral fermions belong to different representations of $SU(2)_L$ and have different $U(1)_Y$ charges, and so transform as

$$\begin{aligned} \psi_L \to \psi'_L &= e^{iY_L\theta(x)} e^{\frac{1}{2}i\sigma^i\beta^i(x)}\psi_L \\ \psi_R \to \psi'_R &= e^{iY_R\theta(x)}\psi_R \end{aligned} \tag{2.10}$$

Thus a fermion mass term

$$-m\bar{\psi}\psi = -m(\bar{\psi}_L\psi_R + \bar{\psi}_R\psi_L) \tag{2.11}$$

cannot be gauge invariant. In a non-Abelian gauge theory the gauge bosons must similarly be massless. For a simple Lie group G, under which ψ has a representation of the set of matrices T^a with

$$\left[T^a, T^b\right] = i\epsilon^{abc}T^c \tag{2.12}$$

where ϵ^{abc} is the totally antisymmetric structure constants of G, any Lagrangian must be invariant under the transformation [48]

$$\psi(x) \to \psi'(x) = U(\mathbf{T}\cdot\boldsymbol{\theta}(x))\psi(x) \equiv U(\theta_x)(x) \tag{2.13}$$

$$\mathbf{T}\cdot\boldsymbol{A}_\mu(x) \to \mathbf{T}\cdot\boldsymbol{A}'_\mu(x) = U(\theta_x)\mathbf{T}\cdot\boldsymbol{A}_\mu U^{-1}(\theta_x) - \frac{i}{g}\left[\partial_\mu U(\theta_x)\right]U^{-1}(\theta_x) \tag{2.14}$$

and infinitesimally

$$\psi(x) \to \psi'(x) = \psi(x) - iT^a\theta^a(x)\psi(x) \tag{2.15}$$

$$A^a_\mu(x) \to A'^a_\mu(x) = A^a_\mu(x) + \epsilon^{abc}\theta^b(x)A^c_\mu(x) - \frac{1}{g}\partial_\mu\theta^a(x) \tag{2.16}$$

then a mass term

$$-m^2 A^a_\mu A^{a,\mu} \tag{2.17}$$

cannot be gauge invariant as well. The observation that the W and Z bosons have non-zero masses while the photon is massless presents the requirement that the electroweak $SU(2)_L \otimes U(1)_Y$ symmetry is a broken symmetry. That is, the Lagrangian is invariant under the gauge symmetry yet obtains a vacuum expectation value (VEV) such that the dynamics of the theory are not invariant—the symmetry is spontaneously broken

$$SU(2)_L \otimes U(1)_Y \xrightarrow{\langle\Phi\rangle_0} U(1)_{em} \tag{2.18}$$

by the acquisition of a vacuum state which is not a singlet of the symmetry group. This is accomplished by introducing a complex scalar doublet [48, 50]

$$\Phi = \begin{pmatrix} \phi^+ \\ \phi_0 \end{pmatrix}, \qquad Y(\Phi) = 1 \tag{2.19}$$

The Lagrangian for this additional scalar would be

$$\Delta\mathcal{L} = (\mathrm{D}_\mu\Phi)^\dagger(\mathrm{D}^\mu\Phi) - V(\Phi) \tag{2.20}$$

with

$$\mathrm{D}_\mu = \left(\partial_\mu - \frac{i}{2}gA^a_\mu\sigma^a - \frac{i}{2}g'B_\mu\right)\phi \tag{2.21}$$

$$V(\Phi) = \mu^2\Phi^\dagger\Phi + \lambda(\Phi^\dagger\Phi)^2 \tag{2.22}$$

where A^a_μ and B_μ are the $SU(2)$ and $U(1)$ gauge boson fields with coupling constants g and g', respectively. For values of $\mu^2 < 0$, $V(\Phi)$ has a minimum at the vacuum expectation value of

$$\langle\Phi\rangle_0 \equiv \langle 0|\Phi|0\rangle = \begin{pmatrix} 0 \\ \frac{\nu}{\sqrt{2}} \end{pmatrix}, \qquad \nu = \sqrt{\frac{-\mu^2}{\lambda}} \tag{2.23}$$

Evaluating 2.20 at this vacuum expectation value (VEV), the gauge boson mass terms appear as

$$\Delta\mathcal{L} = \big(0, \nu\big)\left(gA^a_\mu\sigma^a + \frac{1}{4}g'B_\mu\right)\left(gA^{b\mu}\sigma^b + \frac{1}{4}g'B^\mu\right)\begin{pmatrix} 0 \\ \nu \end{pmatrix} \tag{2.24}$$

$$= \frac{1}{2}\frac{\nu^2}{4}\left[g^2(A^1_\mu)^2 + g^2(A^2_\mu)^2 + (-gA^3_\mu + g'B_\mu)^2\right] \tag{2.25}$$

$$\equiv M^2_W W^+_\mu W^{-\mu} + \frac{1}{2}M^2_Z Z_\mu Z^\mu \tag{2.26}$$

The form of 2.26 follows from 2.25 with the identification of the observed gauge bosons

$$W^{\pm}_{\mu} = \frac{1}{\sqrt{2}}\left(A^1_{\mu} \mp iA^2_{\mu}\right) \tag{2.27}$$

$$M_W^2 = \frac{g^2\nu^2}{4} \tag{2.28}$$

and

$$\frac{1}{2}M_Z^2 Z_{\mu}Z^{\mu} = \frac{\nu^2}{8}\left(gA^3_{\mu} - g'B_{\mu}\right)^2 \tag{2.29}$$

$$= \frac{\nu^2}{8}\left(A^3_{\mu}, B_{\mu}\right)\begin{pmatrix} g^2 & -gg' \\ -gg' & g'^2 \end{pmatrix}\begin{pmatrix} A^{3\mu} \\ B^{\mu} \end{pmatrix} \tag{2.30}$$

$$= \frac{1}{2}\left(Z_{\mu}, A_{\mu}\right)\begin{pmatrix} M_Z^2 & 0 \\ 0 & 0 \end{pmatrix}\begin{pmatrix} Z^{\mu} \\ A^{\mu} \end{pmatrix} \tag{2.31}$$

The mass matrix in 2.30 above is diagonalized in 2.31 by the orthogonal transformation

$$A_{\mu} = \sin\theta_W W^3_{\mu} + \cos\theta_W B_{\mu}$$

$$Z_{\mu} = \cos\theta_W W^3_{\mu} - \sin\theta_W B_{\mu}$$

with

$$\tan\theta_W = \frac{g'}{g_w}$$

$$M_Z^2 = \frac{\nu^2}{4}\left(g^2 + g'^2\right) \tag{2.32}$$

$$M_W = M_Z\cos\theta_W \tag{2.33}$$

which is the precise form and origin of 2.2. The net result of the acquisition of a non-zero VEV for the field Φ is the spontaneous breaking of the electroweak symmetry, the generation of masses for the W and Z bosons while keeping the photon massless, and the introduction of a massive scalar 'Higgs' boson. Fermion masses can be introduced as Yukawa couplings to the Higgs field, resulting in the Standard Model Lagrangian of Equation 2.9.

The Glashow-Weinberg-Salam (GWS) model of the electroweak interaction was a tremendous success in predicting the relationship between the coupling constants g and g', the Higgs field VEV ν, and the masses of the W and Z bosons. These bosons were discovered in 1983 at the Super Proton-Antiproton Synchrotron (Sp$\bar{\text{p}}$S) [51, 52], and for their contribution Glashow, Weinberg, and Salam shared the Nobel Prize in 1979.

2.3 The Hierarchy Problem

While the Higgs mechanism describes the acquisition of mass by fermions and W/Z bosons, the mass of the Higgs boson itself is a free parameter in the Standard Model. The vacuum expectation value of the Higgs potential is known to be $\nu \sim 246\,\mathrm{GeV}$ due to measurements of the coupling constants and gauge boson masses. For values of the self-coupling constant λ small enough to allow for perturbation theory [53], the Higgs mass should not be too different from ν and one would expect

$$\mu^2 \sim -(100\,\mathrm{GeV})^2 \tag{2.34}$$

However the (mass)^2 of a scalar field receives radiative corrections that to one-loop order are proportional to Λ_{UV}^2, the square of the ultraviolet cutoff energy above which the SM is invalid [54]:

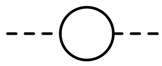

$$m_h^2 \approx m_{h_0}^2 - \frac{\lambda_f^2}{8\pi^2} N_C^f \int^{\Lambda_{UV}} \frac{d^4p}{p} \tag{2.35}$$

$$\approx m_{h_0}^2 + \frac{\lambda_f^2}{8\pi^2} N_C^f \Lambda_{UV}^2 \tag{2.36}$$

Ideally, without the introduction of new physics at some scale Λ, the Standard Model should be valid up to the Planck scale $\Lambda_{UV} = M_{\mathrm{Planck}} \sim 10^{19}\,\mathrm{GeV}/c^2$. If this were true however, a Higgs mass of the order of a few hundred GeV (or for the newly-discovered 125 GeV/c^2 candidate) would require an enormous and extremely precise counterterm at all orders of perturbation theory to avoid extending to M_{P}. Without new physics to offer such a counterterm, only an extraordinarily precise cancellation of physical constants would cancel these large corrections:

m^2 $\qquad$ $+g^2\Lambda_{UV}^2$ $\qquad$ $-y_f^2\Lambda_{UV}^2$

Such a confluence of coupling constants and particle masses is referred to as 'fine-tune' because the degree to which they must cancel to achieve a 125 GeV/c^2 Higgs boson is of the order of 1 part in 10^{30} – a condition described as being highly 'un-natural'.

The hierarchy problem is the discrepancy of many orders of magnitude between the effective scale of electroweak symmetry breaking and its renormalized parameters, namely the Higgs boson mass. More generally, it is the question of why the electroweak force is 10^{32} times stronger than gravity, a question for which the Standard Model offers no answer.

2.4 Problems of the Standard Model and the Need for Supersymmetry

The Standard Model is ultimately an effective low-energy theory embedded within more fundamental physics, as the broken electroweak symmetry shows plainly as an example that has been explained. However even accepting fine-tuning as a deeply unsatisfying explanation for the hierarchy problem, the SM suffers from a number of other problems that favor the existence of additional symmetries at higher energies. Supersymmetry (SUSY) is a Beyond the Standard Model (BSM) theory that introduces the larger symmetry of particle spin, proposing that the SM Lagrangian is the result of such a symmetry being spontaneously broken.

By introducing scalar partners to all fermions in the SM with the same quantum numbers and couplings ($\lambda_S = |\lambda_F|^2$), the quadratic divergences in the Higgs mass corrections exactly cancel as such partners would contribute with an opposite sign. In this way SUSY offers an elegant solution to the hierarchy problem [2]:

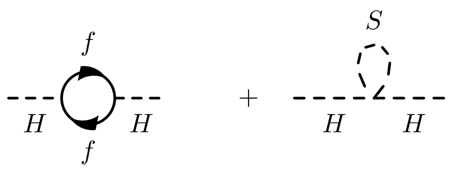

$$\frac{-|\lambda|_f^2}{8\pi^2}\Lambda_{UV}^2 + \ldots \qquad \frac{+\lambda_S}{16\pi^2}\Lambda_{UV}^2 + \ldots \qquad \Delta m_H \propto \lambda_f^2\big(m_S^2 - m_f^2\big)\ln\big(\Lambda_{UV}^2/m_S^2\big)$$

Without considering the mass of the Higgs boson, the breaking of the electroweak symmetry depends on the entirely arbitrary choice of $\mu^2 < 0$, without which there is no Higgs boson at all and the W and Z bosons remain massless. SUSY presents an explanation for this in the renormalization group equations for the Higgs mass, as μ^2 begins positive at the SUSY breaking scale and runs negative in the infrared, in fact triggering electroweak symmetry breaking [2].

As a low-energy theory contained within some larger BSM theory, the gauge couplings of the Standard Model are expected to unify at the 'Grand Unification' scale at very high energy scales ($\sim 10^{16}$ GeV). The running of SM gauge couplings do not unify at any energy scale, however the additional particles introduced by SUSY modifies the running to unify exactly at such an energy scale. Figure 2.2 shows the running of the inverse gauge couplings, and Figure 2.3 shows the running of SUSY mass parameters; both figures are reprinted from [2].

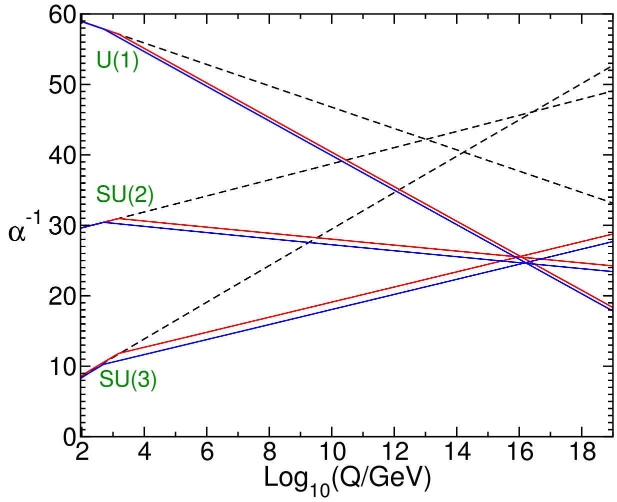

Figure 2.2: Two-loop renormalization group evolution of the gauge couplings. The dashed lines represent the running in the SM, and the red and blue lines represent a range of free parameter choices in a particular SUSY model. The SM couplings do not unify at any energy scale, and many SUSY models offer a very close unification. Reprinted from Figure 6.8 of reference [2].

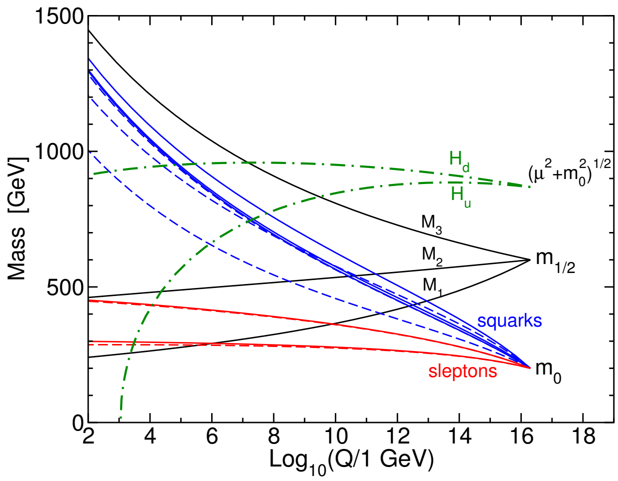

Figure 2.3: Renormalization group evolution supersymmetric masses in one particular model of SUSY. The running of $\mu^2 + m_{H_u}^2$ is negative below $\sim$1 TeV, triggering the breaking of the electroweak symmetry. Reprinted from Figure 8.4 of reference [2].

A final mystery for which the SM offers no insight into is the overwhelming presence of dark matter (DM) in the observable Universe, an invisible form of matter affecting the behavior and formation of cosmological structures and composes about 80% of the total matter in the Universe [55, 56]. The evidence for dark matter is compelling, one of the most powerful of which is the rotation curves for many different galaxies, an example of which is shown in Figure 2.4. The luminous (visible) matter is observed to make only a small contribution to the rotation curves.

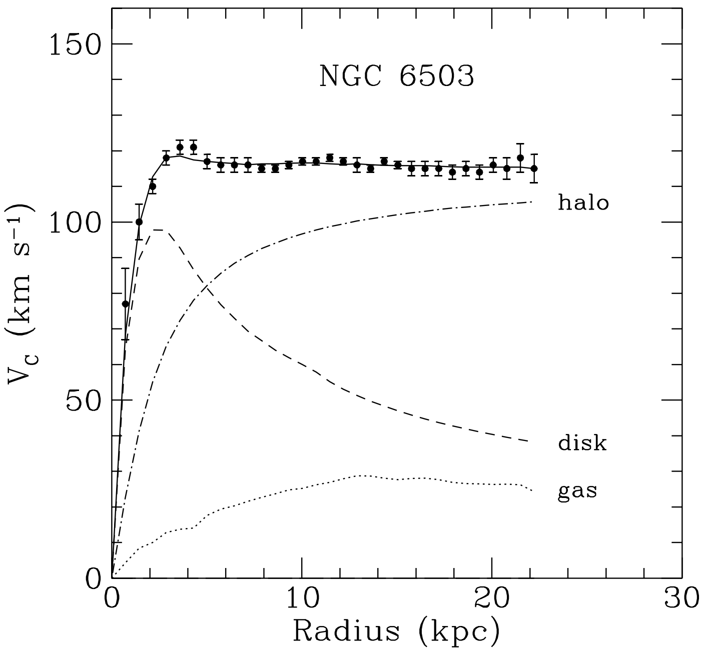

Figure 2.4: The circular velocities of stars and gas versus their distances from the galactic center, or rotation curve, for the galaxy NGC 6503. The different dashed lines represent the individual contributions from interstellar gas, the luminous disk (stars), and dark matter (halo). Reprinted from Figure 1 of reference [3].

The extended particle content of many SUSY models includes a stable, weakly-interacting, massive particle (WIMP) that provides a much sought-for dark matter candidate, which the SM simply does not provide.

The range of free parameters available to the many different models of SUSY is vast, allowing for a wide variation of its proposed solutions for these problems. The results of Run I of the LHC have placed strong constraints on this phase-space, but much remains experimentally viable while still providing a natural Higgs sector and a dark matter candidate consistent with cosmological observations. The following chapter formally introduces the mathematical foundations of SUSY and its phenomenology, with a focus on its consequences on these problems in the SM and the recent discovery of a 125 GeV/c^2 Higgs boson candidate [28, 29]. The particular model of Gauge

Mediated Supersymmetry Breaking (GMSB) will be introduced, and a model in which the scalar top quark partner is comparatively light will be motivated.

Chapter 3

The Supersymmetric Extension to the Standard Model

The following chapter is heavily adapted from references [2], [57], and other sources, using notations therein. A complete survey of Supersymmetry (SUSY) and the many different models of its breaking are well outside the scope of this dissertation, and as such only relevant phenomenological concerns will be discussed.

3.1 Mathematical Foundations

3.1.1 Supermultiplet Representation

The geometric interpretation of Supersymmetry is a spacetime manifold with four additional fermionic degrees of freedom over the typical bosonic coordinates, called *superspace*:

$$x^\mu,\ \theta^\alpha,\ \theta^\dagger_{\dot\alpha}.$$

where θ^α and $\theta^\dagger_{\dot\alpha}$ are Grassman-valued spinors representing these fermionic coordinates. That is, they are constant, complex, anti-commuting, two-component spinors with dimension $[\text{mass}]^{-1/2}$. Functions of superspaces to themselves are known as *superfields*, and the individual field components of superfields are know as *supermultiplets*.

Expanding a superfield in a power series of the anti-commuting variables, since there are two independent components of each fermionic coordinate, terminates with at most two θ terms and two $\theta^\dagger$ terms (up to $\theta\theta\theta^\dagger\theta^\dagger$ terms). Thus the most general form of any superfield is:

$$S(x,\theta,\theta^\dagger) = a + \theta\xi + \theta^\dagger\chi^\dagger + \theta\theta b + \theta^\dagger\theta^\dagger c + \theta\bar\sigma^\mu\theta^\dagger v_\mu + \theta^\dagger\theta^\dagger\theta\eta + \theta\theta\theta^\dagger\zeta^\dagger + \theta\theta\theta^\dagger\theta^\dagger d. \tag{3.1}$$

The components of the general superfield are 8 bosonic fields a, b, c, d and v_μ and 4 two-component fermionic fields $\xi, \chi^\dagger, \eta, \zeta^\dagger$. Shown over the next several sections, imposing different constraints on the general superfield reveals the actual supermultiplets of SUSY, the *chiral* and *vector gauge* supermultiplets, where any other superfield is a linear combination of the two types.

3.1.2 Supersymmetry Transformations

Translations in superspace are defined by the set of linear differential operators acting on superfields:

$$\hat{Q}_\alpha = i\frac{\partial}{\partial\theta^\alpha} - (\sigma^\mu\theta^\dagger)_\alpha\partial_\mu, \qquad \hat{Q}^\alpha = -i\frac{\partial}{\partial\theta_\alpha} + (\theta^\dagger\bar{\sigma}^\mu)^\alpha\partial_\mu, \tag{3.2}$$

$$\hat{Q}^{\dagger\dot{\alpha}} = i\frac{\partial}{\partial\theta^\dagger_{\dot{\alpha}}} - (\bar{\sigma}^\mu\theta)^{\dot{\alpha}}\partial_\mu, \qquad \hat{Q}^\dagger_{\dot{\alpha}} = -i\frac{\partial}{\partial\theta^{\dagger\dot{\alpha}}} + (\theta\sigma^\mu)_{\dot{\alpha}}\partial_\mu. \tag{3.3}$$

An infinitesimal translation by $\epsilon, \epsilon^\dagger$ for a superfield S is then:

$$\sqrt{2}\,\delta_\epsilon S = -i(\epsilon\hat{Q} + \epsilon^\dagger\hat{Q}^\dagger)S = \Big(\epsilon^\alpha\frac{\partial}{\partial\theta^\alpha} + \epsilon^\dagger_{\dot{\alpha}}\frac{\partial}{\partial\theta^\dagger_{\dot{\alpha}}} + i\big[\epsilon\sigma^\mu\theta^\dagger + \epsilon^\dagger\bar{\sigma}^\mu\theta\big]\partial_\mu\Big)S \tag{3.4}$$

$$= S(x^\mu + i\epsilon\sigma^\mu\theta^\dagger + i\epsilon^\dagger\bar{\sigma}^\mu\theta,\, \theta+\epsilon,\, \theta^\dagger+\epsilon^\dagger) - S(x^\mu,\, \theta,\, \theta^\dagger) \tag{3.5}$$

revealing these operators to be indeed translations in superspace. These generators satisfy the SUSY algebra of anti-commutation and commutation relations:

$$\Big\{\hat{Q}_\alpha,\, \hat{Q}^\dagger_{\dot{\beta}}\Big\} = 2i\sigma^\mu_{\alpha\dot{\beta}}\partial_\mu = -2\sigma^\mu_{\alpha\dot{\beta}}\hat{P}_\mu, \tag{3.6}$$

$$\Big\{\hat{Q}_\alpha,\, \hat{Q}_\beta\Big\} = 0, \qquad \Big\{\hat{Q}^\dagger_{\dot{\alpha}},\, \hat{Q}^\dagger_{\dot{\beta}}\Big\} = 0 \tag{3.7}$$

$$\Big[\hat{P}_\mu,\, \hat{Q}_\alpha\Big] = \Big[\hat{P}_\mu,\, \hat{Q}^\dagger_{\dot{\alpha}}\Big] = 0 \tag{3.8}$$

where $\hat{P}_\mu = -i\partial_\mu$ is the four-momentum generator of spacetime translations. Applied to each of the component fields of the general superfield S (Eq. 3.1), these generators are of precisely the form desired by SUSY:

$$Q|\text{Boson}\rangle = |\text{Fermion}\rangle, \qquad Q|\text{Fermion}\rangle = |\text{Boson}\rangle.$$

This of course is the fundamental feature of Supersymmetry, that for each particle in the Standard Model there should be a partner differing only by a spin of 1/2, where all other quantum numbers are invariant under these transformations.

3.1.3 Chiral Supermultiplets

Defining the *chiral* covariant derivatives as:

$$D_\alpha = \frac{\partial}{\partial\theta^\alpha} - i(\sigma^\mu\theta^\dagger)_\alpha\partial_\mu, \qquad D^\alpha = -\frac{\partial}{\partial\theta_\alpha} + i(\theta^\dagger\bar{\sigma}^\mu)^\alpha\partial_\mu \tag{3.9}$$

$$D^{\dagger\dot{\alpha}} = \frac{\partial}{\partial\theta^\dagger_{\dot{\alpha}}} - i(\bar{\sigma}^\mu\theta)^{\dot{\alpha}}\partial_\mu, \qquad D^\dagger_{\dot{\alpha}} = -\frac{\partial}{\partial\theta^{\dagger\dot{\alpha}}} + i(\theta\sigma^\mu)_{\dot{\alpha}}\partial_\mu \tag{3.10}$$

a *chiral* (left-chiral) supermultiplet is any superfield satisfying the condition that:

$$D^\dagger_{\dot{\alpha}}\Psi = 0. \tag{3.11}$$

An *anti-chiral* (right-chiral) supermultiplet is its complex conjugate satisfying:

$$D_\alpha\Psi^* = 0. \tag{3.12}$$

The general solution for a chiral supermultiplet, after a careful change of variables and a factor of $\sqrt{2}$ for convenience, is:

$$\Psi = \phi(y) + \sqrt{2}\theta\psi(y) + \theta\theta F(y) \tag{3.13}$$

$$\Psi^* = \phi^*(y) + \sqrt{2}\theta^\dagger(y^*) + \theta^\dagger\theta^\dagger F^*(y^*) \tag{3.14}$$

with

$$y^\mu \equiv x^\mu + i\theta^\dagger\bar{\sigma}^\mu\theta. \tag{3.15}$$

So the chiral superfield degrees of freedom consist of a complex scalar ϕ, a two-component fermion ψ, and an auxiliary field F. Applying the superspace translation operators Eqs. 3.3-3.5, the chiral fields transform between one another as:

$$\delta_\epsilon\phi = \epsilon\psi, \tag{3.16}$$

$$\delta_\epsilon\psi_\alpha = -i(\sigma^\mu\epsilon^\dagger)_\alpha\partial_\mu\phi + \epsilon_\alpha F, \tag{3.17}$$

$$\delta_\epsilon F = -i\epsilon^\dagger\bar{\sigma}^\mu\partial_\mu\psi. \tag{3.18}$$

As will be seen in future sections, a simple way to construct a chiral superfield is in a *superpotential* $W(\Psi_i)$ that is a holomorphic function of other chiral superfields Ψ_i; that is, a function of only chiral superfields and not of any antichiral fields.

3.1.4 Vector Supermultiplets

A real vector superfield V is any superfield satisfying the condition $V = V^*$. Constraining the general superfield S of Eq. 3.1 in this way, along with several conventional definitions, yields the component expansion of a vector supermultiplet:

$$\begin{aligned} V(x,\theta,\theta^\dagger) \;&=\; a+\theta\xi+\theta^\dagger\xi^\dagger+\theta\theta b+\theta^\dagger\theta^\dagger b^*+\theta\sigma^\mu\theta^\dagger A_\mu+\theta^\dagger\theta^\dagger\theta(\lambda-\frac{i}{2}\sigma^\mu\partial_\mu\xi^\dagger) \\ &\quad +\theta\theta\theta^\dagger(\lambda^\dagger-\frac{i}{2}\bar\sigma^\mu\partial_\mu\xi)+\theta\theta\theta^\dagger\theta^\dagger(\frac{1}{2}D+\frac{1}{4}\partial_\mu\partial^\mu a). \end{aligned} \tag{3.19}$$

Infinitesimal translations in superspace transform the vector supermultiplet fields as:

$$\sqrt{2}\,\delta_\epsilon a \;=\; \epsilon\xi+\epsilon^\dagger\xi^\dagger \tag{3.20}$$

$$\sqrt{2}\,\delta_\epsilon\xi_\alpha \;=\; 2\epsilon_\alpha b-(\sigma^\mu\epsilon^\dagger)_\alpha(A_\mu+i\partial_\mu a), \tag{3.21}$$

$$\sqrt{2}\,\delta_\epsilon b \;=\; \epsilon^\dagger\lambda^\dagger-i\epsilon^\dagger\bar\sigma^\mu\partial_\mu\xi, \tag{3.22}$$

$$\sqrt{2}\,\delta_\epsilon A^\mu \;=\; i\epsilon\partial^\mu\xi-i\epsilon^\dagger\partial^\mu\xi^\dagger+\epsilon\sigma^\mu\lambda^\dagger-\epsilon^\dagger\bar\sigma^\mu\lambda, \tag{3.23}$$

$$\sqrt{2}\,\delta_\epsilon\lambda_\alpha \;=\; \epsilon_\alpha D+\frac{i}{2}(\sigma^\mu\bar\sigma^\nu\epsilon)_\alpha(\partial_\mu A_\nu-\partial_\nu A_\mu), \tag{3.24}$$

$$\sqrt{2}\,\delta_\epsilon D \;=\; -i\epsilon\sigma^\mu\partial_\mu\lambda^\dagger-i\epsilon^\dagger\bar\sigma^\mu\partial_\mu\lambda \tag{3.25}$$

The degrees of freedom for a vector superfield are the gauge boson A^μ, gaugino λ, and gauge auxiliary fields D. The remaining components are additional auxiliary fields that can be 'supergauged' away by an appropriate choice of coordinates, and such a field is said to be in the Wess-Zumino gauge:

$$V_{\text{WZ gauge}} = \theta^\dagger\bar\sigma^\mu\theta A_\mu+\theta^\dagger\theta^\dagger\theta\lambda+\theta\theta\theta^\dagger\lambda^\dagger+\frac{1}{2}\theta\theta\theta^\dagger\theta^\dagger D. \tag{3.26}$$

3.1.5 Lagrangians in Superspace

The Lagrangian density $\mathcal{L}(x)$ for any superfield S is obtained by integrating over the fermionic coordinates. For the chiral and vector superfields of Equations 3.15 and 3.19, this is written as:

$$[V]_D \equiv \int d^2\theta d^2\theta^\dagger\, V(x,\theta,\theta^\dagger) \;=\; V(x,\theta,\theta^\dagger)\Big|_{\theta\theta\theta^\dagger\theta^\dagger} = \frac{1}{2}D+\frac{1}{4}\partial_\mu\partial^\mu a \tag{3.27}$$

$$[\Phi]_F \equiv \Phi\Big|_{\theta\theta} = \int d^2\theta\,\Phi\Big|_{\theta^\dagger=0} = \int d^2\theta d^2\theta^\dagger\,\delta^{(2)}(\theta^\dagger)\,\Phi \;=\; F \tag{3.28}$$

named the D- and F-term contributions respectively. The $\partial_\mu \partial^\mu a$ vanishes when integrating over spacetime, and to ensure the action is real, F-terms can be taken as $[\Phi]_F +$ c.c. combinations.

The Unbroken Chiral Lagrangian

For chiral supermultiplets, the unbroken SUSY Lagrangian is:

$$\mathcal{L}_{\text{chiral}}(x) = [\Phi^{*i}\Phi_i]_D + ([W(\Phi_i)]_F + \text{ c.c.}) \tag{3.29}$$

$$= -\partial^\mu \phi^{*i}\partial_\mu \phi_i - i\psi^{\dagger i}\bar{\sigma}^\mu \partial_\mu \psi_i - \frac{1}{2}\left(\frac{\delta^2 W}{\delta\phi^i \delta\phi^j}\psi_i\psi_j + \frac{\delta^2 W^*}{\delta\phi_i \delta\phi_j}\psi^{\dagger i}\psi^{\dagger j}\right) - \frac{\delta W}{\delta\phi^i}\frac{\delta W^*}{\delta\phi_i} \tag{3.30}$$

for any superpotential W holomorphic in chiral supermultiplets. For the superpotential of the Minimal Supersymmetric Standard Model (MSSM) of

$$W = \frac{1}{2}M^{ij}\Phi_i\Phi_j + \frac{1}{6}y^{ijk}\Phi_i\Phi_j\Phi_k \tag{3.31}$$

with y^{ijk} the Yukawa couplings between scalar and spinor fields and M^{ij} the fermion mass matrix, this expands to

$$\begin{aligned}\mathcal{L}_{\text{chiral}} = &-\partial^\mu \phi^{*i}\partial_\mu \phi_i - V_{\text{chiral}}(\phi,\phi^*) + i\psi^{\dagger i}\bar{\sigma}^\mu \partial_\mu \psi_i - \frac{1}{2}M^{ij}\psi_i\psi_j - \frac{1}{2}M^*_{ij}\psi^{\dagger i}\psi^{\dagger j} \\ &- \frac{1}{2}y^{ijk}\phi_i\psi_j\psi_k - \frac{1}{2}y^*_{ijk}\phi^{*i}\psi^{\dagger j}\psi^{\dagger k}\end{aligned} \tag{3.32}$$

with the scalar potential defined as

$$V_{\text{chiral}}(\phi,\phi^*) \equiv \frac{\delta W}{\delta\phi^i}\frac{\delta W^*}{\delta\phi_i} \tag{3.33}$$

$$\begin{aligned}=&M^*_{ik}M^{kj}\phi^{*i}\phi_j + \frac{1}{2}M^{in}y^*_{jkn}\phi_i\phi^{*j}\phi^{*k} \\ &+ \frac{1}{2}M^*_{in}y^{jkn}\phi^{*i}\phi_j\phi_k + \frac{1}{4}y^{ijn}y^*_{kln}\phi_i\phi_j\phi^{*k}\phi^{*l}\end{aligned} \tag{3.34}$$

The Unbroken Gauge Lagrangian

For a gauge symmetry with generators T_i^{aj}, the chiral superfields Φ_i transform as:

$$\Phi_i \to \left(e^{2ig_a\Omega^a T^a}\right)_i^{\ j}\Phi_j, \qquad \Phi^{*i} \to \Phi^{*j}\left(e^{-2ig_a\Omega^a T^a}\right)_j^{\ i} \tag{3.35}$$

where g_a are the gauge couplings and Ω^a are the transformation parameters which are chiral superfields themselves. For each generator, there is a vector superfield V^a that is free to be gauged into the Wess-Zumino gauge of Eq. 3.26. A field-strength chiral superfield can be defined:

$$\mathcal{W}_\alpha = -\frac{1}{4} D^\dagger D^\dagger \left(e^{-2g_a T^a V^a} D_\alpha e^{2g_a T^a V^a} \right). \tag{3.36}$$

In the Wess-Zumino gauge, this is:

$$(\mathcal{W}^a_\alpha)_{\text{WZ gauge}} = \lambda^a_\alpha + \theta_\alpha D^a - \frac{i}{2}(\sigma^\mu \bar{\sigma}^\nu \theta)_\alpha F^a_{\mu\nu} + i\theta\theta(\sigma^\mu \nabla_\mu \lambda^{\dagger a})_\alpha \tag{3.37}$$

with

$$F^a_{\mu\nu} = \partial_\mu A^a_\nu - \partial_\nu A^a_\mu + g f^{abc} A^b_\mu A^c_\nu \tag{3.38}$$

$$\nabla_\mu \lambda^a = \partial_\mu \lambda^a + g f^{abc} A^b_\mu \lambda^c \tag{3.39}$$

as the field strength and gauge covariant derivative.

Collecting all of this, the general renormalizable Lagrangian for an unbroken gauge supermultiplet is:

$$\mathcal{L} = \left(\frac{1}{4} - i\frac{g_a^2 \Theta_a}{32\pi^2} \right) [\mathcal{W}^{a\alpha} \mathcal{W}^a_\alpha]_F + \text{c.c.} + \left[\Phi^{*i} (e^{2g_a T^a V^a})_i{}^j \Phi_j \right]_D + ([W(\Phi_i)]_F + \text{c.c.}) \tag{3.40}$$

with Θ_a introduced as a CP-violating parameter.

3.1.6 The Unbroken Supersymmetry Lagrangian

The full, final unbroken SUSY Lagrangian, for chiral supermultiplets interacting with a single gauge supermultiplet, expanded completely is:

$$
\begin{aligned}
\mathcal{L} = &- \partial^\mu \phi^{*i} \partial_\mu \phi_i - i\psi^{\dagger i} \bar{\sigma}^\mu \partial_\mu \psi_i && \text{(3.41a)}\\
&- \frac{1}{4}\left(\partial_\mu A^a_\nu - \partial_\nu A^a_\mu\right)\left(\partial^\mu A^{\nu a} - \partial^\nu A^{\mu a}\right) - i\lambda^{\dagger a} \bar{\sigma}^\mu \partial_\mu \lambda^a && \text{(3.41b)}\\
&- M^*_{ik} M^{kj} \phi^{*i} \phi_j - \frac{1}{2} M^{ij} \psi_i \psi_j - \frac{1}{2} M^*_{ij} \psi^{\dagger i} \psi^{\dagger j} && \text{(3.41c)}\\
&+ ig \partial^\mu \phi^{*i} A^a_\mu \left(T^a \phi\right)_i - ig \partial_\mu \phi_i A^{\mu a} \left(\phi^* T^a\right)^i - g\psi^{\dagger i} \bar{\sigma}^\mu A^a_\mu \left(T^a \psi\right)_i && \text{(3.41d)}\\
&- ig \lambda^{\dagger a} \bar{\sigma}^\mu f^{abc} A^b_\mu \lambda^c && \text{(3.41e)}\\
&- \frac{1}{4} g f^{abc} \Big[\left(\partial_\mu A^a_\nu - \partial_\nu A^a_\mu\right) A^{\mu b} A^{\nu c} + A^b_\mu A^c_\nu \left(\partial^\mu A^{\nu a} - \partial^\nu A^{\mu a}\right)\Big] && \text{(3.41f)}\\
&- \frac{1}{2} M^*_{in} y^{jkn} \phi^{*i} \phi_j \phi_k - \frac{1}{2} M^{in} y^*_{jkn} \phi_i \phi^{*j} \phi^{*k} && \text{(3.41g)}\\
&- \frac{1}{2} y^{ijk} \phi_i \psi_j \psi_k - \frac{1}{2} y^*_{ijk} \phi^{*i} \psi^{\dagger j} \psi^{\dagger k} && \text{(3.41h)}\\
&- \sqrt{2} g \left(\phi^{*i} T^a \psi_i\right) \lambda^a - \sqrt{2} g \lambda^{\dagger a} \left(\psi^{\dagger i} T^a \phi_i\right) && \text{(3.41i)}\\
&- g^2 A^{\mu a} \left(\phi^* T^a\right)^i A^a_\mu \left(T^a \phi\right)_i - \frac{1}{4} g^2 f^{abc} A^b_\mu A^c_\nu f^{abc} A^{\mu b} A^{\nu c} && \text{(3.41j)}\\
&- \frac{1}{4} y^{ijn} y^*_{kln} \phi_i \phi_j \phi^{*k} \phi^{*l} - \frac{1}{2} g^2 \left(\phi^{i*} T^a \phi_i\right)^2 . && \text{(3.41k)}
\end{aligned}
$$

Piecewise, the terms in the SUSY Lagrangian are:

Lines a–b: kinetic terms for the fields $\phi, \psi, A_\mu, \lambda$.

Line c: (s)fermion mass terms for ϕ and ψ:

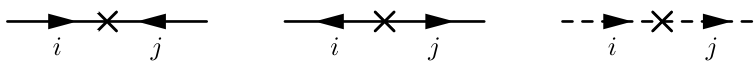

Lines d-e: cubic couplings of ϕ, ψ, and λ to A_μ:

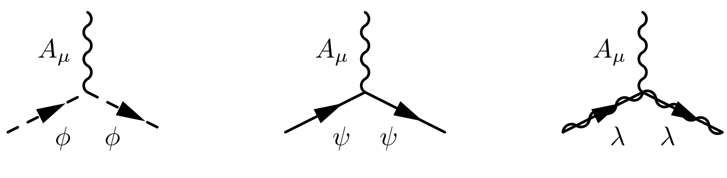

Line f: triple gauge boson coupling:

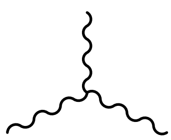

Line g: triple sfermion couplings:

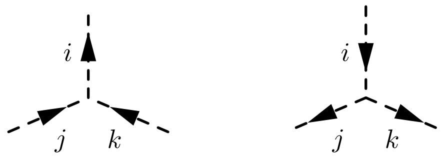

Line h: cubic coupling of ψ to ϕ:

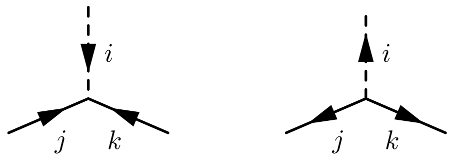

Line i: $\phi\psi\lambda$ coupling:

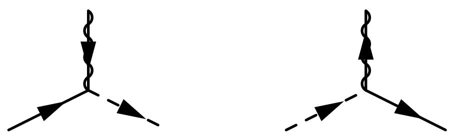

Line j: $AA\phi\phi$ and quadrupole gauge boson couplings:

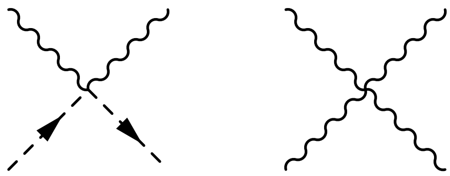

Line k: ϕ^4 vertices:

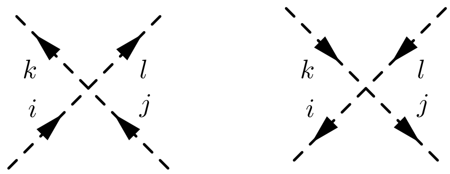

3.2 The Minimal Supersymmetric Standard Model

The Minimal Supersymmetric Standard Model (MSSM) is the minimal extension of the SM adding only the necessary new particles to complete the symmetry. The superpotential for the MSSM is:

$$W_{\text{MSSM}} = \bar{u}\mathbf{y_u}\mathbf{Q}\mathbf{H_u} - \bar{\mathbf{d}}\mathbf{y_d}\mathbf{Q}\mathbf{H_d} - \bar{\mathbf{e}}\mathbf{y_e}\mathbf{L}\mathbf{H_d} + \mu\mathbf{H_u}\mathbf{H_d}. \tag{3.42}$$

Each of the fields introduced here, listed in Table 3.1, are chiral superfields. Q contains the left-handed up- and down-type quarks and scalar quarks (squarks) , and L contains the left-handed leptons and scalar leptons (sleptons). $\bar{u}$, $\bar{d}$, and $\bar{e}$ contain the right-handed (s)quarks and (s)leptons. The MSSM contans two complex Higgs doublets, $H_u = \left(H_u^+, H_u^0\right)$ and $H_d = \left(H_d^0, H_d^-\right)$, each of which having corresponding spin 1/2 higgsino doublets. The 'μ term' μ is a supersymmetric version of the Standard Model Higgs mass.

The family indices of Eqn. 3.42 have been suppressed for clarity, but the Yukawa coupling parameters $\mathbf{y_u}$, $\mathbf{y_d}$, and $\mathbf{y_e}$ are 3×3 matrices in family space. Since the third generation quarks and tau leptons are much heavier than other generations, the Yukawa couplings are often approximated with only these contributions as non-negligible, $\mathbf{y_{u,d,e}} \approx \left(\begin{smallmatrix} 0 & 0 & 0 \\ 0 & 0 & 0 \\ 0 & 0 & y_{t,b,\tau} \end{smallmatrix}\right)$, reducing the superpotential to:

$$\begin{aligned} W_{\text{MSSM}} \approx\ & y_t(\bar{t}tH_u^0 - \bar{t}bH_u^+) - y_b(\bar{b}tH_d^- - \bar{b}bH_d^0) - y_\tau(\bar{\tau}\nu_\tau H_d^- - \bar{\tau}\tau H_d^0) \\ & + \mu(H_u^+H_d^- - H_u^0H_d^0). \end{aligned} \tag{3.43}$$

Names		Spin 0 Component	Spin 1/2 Component	Representation under $SU(3)_C \otimes SU(2)_L \otimes U(1)_Y$
(s)quarks	Q	$(\tilde{u}_L \ \ \tilde{d}_L)$	$(u_L \ \ d_L)$	$(\mathbf{3}, \mathbf{2}, \frac{1}{6})$
(×3 families)	$\bar{u}$	$\tilde{u}_R^*$	$u_R^\dagger$	$(\bar{\mathbf{3}}, \mathbf{1}, -\frac{2}{3})$
	$\bar{d}$	$\tilde{d}_R^*$	$u_R^\dagger$	$(\bar{\mathbf{3}}, \mathbf{1}, \frac{1}{3})$
(s)leptons	L	$(\tilde{\nu} \ \ \tilde{e}_L)$	$(\nu \ \ e_L)$	$(\mathbf{1}, \mathbf{2}, -\frac{1}{2})$
(×3 families)	$\bar{e}$	$\tilde{e}_R^*$	$e_R^\dagger$	$(\mathbf{1}, \mathbf{1}, \mathbf{1})$
Higgs, higgsinos	H_u	$(H_u^+ \ \ H_u^0)$	$(\tilde{H}_u^+ \ \ \tilde{H}_u^0)$	$(\mathbf{1}, \mathbf{2}, +\frac{1}{2})$
	H_d	$(H_d^0 \ \ H_d^0)$	$(\tilde{H}_d^0 \ \ \tilde{H}_d^-)$	$(\mathbf{1}, \mathbf{2}, -\frac{1}{2})$

Table 3.1: Chiral supermultiplets of the MSSM. As in the SM the right-handed fermions and their scalar partners are not charged in weak isospin, denoted by their **1**-dimensional representation. Leptons and higgs(inos) are colorless (**1**) and the bar over $\bar{\mathbf{3}}$ denotes belong to the adjoint representation of **3**. Adapted from Table 1.1 of reference [2].

Names	Spin 1/2 Component	Spin 1 Component	Representation under $SU(3)_C \otimes SU(2)_L \otimes U(1)_Y$
Gluino, gluons	$\tilde{g}$	g	$(\mathbf{8}, \mathbf{1}, \mathbf{0})$
Winos, W bosons	$\tilde{W}^\pm \ \ \tilde{W}^0$	$W^\pm \ \ W^0$	$(\mathbf{1}, \mathbf{3}, \mathbf{0})$
Binos, B boson	$\tilde{B}^0$	B^0	$(\mathbf{1}, \mathbf{1}, \mathbf{0})$

Table 3.2: Gauge supermultiplets of the MSSM. Adapted from Table 1.2 of reference [2].

3.2.1 R-parity

The MSSM is defined to be invariant under R-parity, a multiplicative quantum number defined for each particle as:

$$P_R = (-1)^{3(\mathrm{B}-\mathrm{L})+2s} \tag{3.44}$$

having a value of $+1$ for the Standard Model particles and -1 for 'supersymmetric' particles. Phenomenologically this conservation is of vital importance, because if the lightest sparticle with $P_R = -1$ (the LSP) is absolutely stable, all sparticle decays must eventually proceed to this LSP, and any sparticle production in a collider experiment must occur in even numbers (pair production).

Without requiring R-parity conservation, the superpotential of Eq. 3.42 more generally can contain terms violating the total baryon (B) or lepton (L) numbers which R-parity forbids [1]:

$$W_{\Delta \mathrm{L}=1} = \frac{1}{2}\lambda^{ijk} L_i L_j \bar{e}_k + \lambda'^{ijk} L_i Q_j \bar{d}_k + \mu'^{i} L_i H_u \tag{3.45}$$

$$W_{\Delta \mathrm{B}=1} = \frac{1}{2}\lambda''^{ijk} \bar{u}_i \bar{d}_j \bar{d}_k. \tag{3.46}$$

Without any form of suppression for the λ' or λ'' couplings, such terms would disastrously allow for unobserved processes such a proton decay $p^+ \to e^+\pi^0$ with minuscule decay lifetimes shown in Figure 3.1.

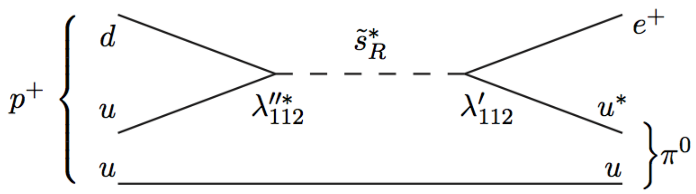

Figure 3.1: An example of the strange-squark mediated proton decay process $p^+ \to e^+\pi^0$ with unsuppressed λ' and λ'' couplings. Reprinted from Figure 6.5 of reference [2].

3.2.2 Soft SUSY Breaking

If SUSY exists as a symmetry, it must necessarily exist as an exact symmetry of the Lagrangian that is spontaneously broken in some way. In unbroken SUSY, the quadratic divergences in scalar masses vanish identically to all loop orders due to the degeneracy of scalar and fermion masses (see Section 2.4). If that were the case, a massless spin 1/2 photon or a scalar electron

[1] The chiral supermultiplets carry baryon number B = +1/3 for Q_i, B = -1/3 for $\bar{u}_i$, $\bar{d}_i$, and B = 0 for all others. The lepton number L = +1 for L_i, L = -1 for $\bar{e}_i$, and L = 0 for all else. A simple counting of these numbers in equations 3.45 and 3.46 reveal how $P_R = (-1)^{3(B-L)+2s}$ is violated.

with mass of the electron would have been easily discovered long ago in experiment.

In order to maintain this solution to the hierarchy problem while breaking SUSY, additional breaking terms are simply added to the unbroken Lagrangian of Eqn. 3.41 as $\mathcal{L} = \mathcal{L}_{\text{SUSY}} + \mathcal{L}_{\text{soft}}$. These terms must be 'soft', or of positive mass dimension, to avoid re-introducing quadratic divergences in scalar masses. For the MSSM, these terms are:

$$\begin{aligned}\mathcal{L}_{\text{soft}}^{\text{MSSM}} &= -\frac{1}{2}\left(M_3\tilde{g}\tilde{g} + M_2\tilde{W}\tilde{W} + M_1\tilde{B}\tilde{B} + \text{c.c.}\right) \\ &\quad -\left(\tilde{\bar{u}}\mathbf{a}_u\tilde{Q}H_u - \tilde{\bar{d}}\mathbf{a}_d\tilde{Q}H_d - \tilde{\bar{e}}\mathbf{a}_e\tilde{L}H_d + \text{c.c.}\right) \\ &\quad -\tilde{Q}^\dagger\mathbf{m}_Q^2\tilde{Q} - \tilde{L}^\dagger\mathbf{m}_L^2\tilde{L} - \tilde{\bar{u}}\mathbf{m}_{\bar{u}}^2\tilde{\bar{u}}^\dagger - \tilde{\bar{d}}\mathbf{m}_{\bar{d}}^2\tilde{\bar{d}}^\dagger - \tilde{\bar{e}}\mathbf{m}_{\bar{e}}^2\tilde{\bar{e}}^\dagger \\ &\quad -m_{H_u}^2H_u^*H_u - m_{H_d}^2H_d^*H_d - (bH_uH_d + \text{c.c.})\,. \end{aligned} \tag{3.47}$$

This soft breaking Lagrangian adds several new parameters. M_1, M_2, and M_3 are the bino ($\tilde{B}$), wino ($\tilde{L}$), and gluino ($\tilde{g}$) mass terms respectively. The 3×3 complex family-space matrices $\mathbf{a}_u$, $\mathbf{a}_d$, and $\mathbf{a}_e$ are analogous to the Yukawa couplings in the superpotential. The 3×3 family-space matrices $\mathbf{m}_Q^2$, $\mathbf{m}_{\bar{u}}^2$, $\mathbf{m}_{\bar{d}}^2$, $\mathbf{m}_L^2$, and $\mathbf{m}_{\bar{e}}^2$ are squark and slepton mass terms. Lastly $m_{H_u}^2$, $m_{H_d}^2$, and b are squared-mass terms for SUSY breaking contributions to the Higgs potential.

The soft breaking terms are added explicitly in the MSSM as they are simply the only terms of positive mass dimension that are not invariant under the SUSY transformations. In no way is the source of this breaking addressed. Many attempts at describing the larger SUSY-invariant theory the breaking occurs in have been made, but the search outlined in this dissertation is far more sensitive to *gauge-mediated* models than any other model. For brevity, the next section will detail only this type of breaking.

3.3 Gauge Mediated Supersymmetry Breaking

Gauge Mediated Supersymmetry Breaking (GMSB) models [58, 59, 60, 61, 62, 63] are those that introduce the soft breaking terms using the ordinary $SU(3)\times SU(2)\times U(1)$ gauge interactions rather than gravity, as many other models do. In the minimal approach to GMSB, a set of chiral supermultiplets called *messengers* are introduced, transforming under $SU(3)\times SU(2)\times U(1)$ as [2]:

$$q \sim (\mathbf{3}, \mathbf{1}, -\frac{\mathbf{1}}{\mathbf{3}}), \qquad \bar{\mathbf{q}} \sim (\bar{\mathbf{3}}, \mathbf{1}, \frac{\mathbf{1}}{\mathbf{3}}), \qquad \ell \sim (\mathbf{1}, \mathbf{2}, \frac{\mathbf{1}}{\mathbf{2}}), \qquad \bar{\ell} \sim (\mathbf{1}, \mathbf{2}, -\frac{\mathbf{1}}{\mathbf{2}}). \tag{3.48}$$

The scalar messenger squarks and sleptons q, $\bar{q}$, ℓ, and $\bar{\ell}$, as well as their fermionic messenger quark and lepton partners ψ_q, $\psi_{\bar{q}}$, ψ_ℓ, and $\psi_{\bar{\ell}}$ each receive very large masses by coupling to a

[2] Recall that $\mathbf{1}$ indicates no transformation under that gauge symmetry, and thus no charge. A bar ($\bar{\mathbf{3}}$) indicates the adjoint representation.

gauge singlet chiral supermultiplet S. This coupling is by an R-parity conserving superpotential:

$$W_{\text{messenger}} = y_2 S\ell\bar{\ell} + y_3 Sq\bar{q} \tag{3.49}$$

where y_2 and y_3 are coupling strength parameters.

The precise breaking mechanism of GMSB is delegated to a 'hidden breaking sector', a regime of physics that communicates with the MSSM only via flavor-blind interactions. In GMSB this communication is the ordinary gauge interactions. Simply introducing some hidden breaking terms as W_{breaking}, the scalar potential of the scalar messengers acquires a vacuum expectation value (VEV) at its minimum:

$$\begin{aligned} \langle S \rangle &\neq 0, & (3.50)\\ \langle \delta W_{\text{breaking}}/\delta S \rangle &= -\langle F_S^* \rangle \neq 0, & (3.51)\\ \langle \delta W_{\text{messenger}}/\delta S \rangle &= 0. & (3.52) \end{aligned}$$

At this VEV, the messengers obtain squared-mass matrices with eigenvalues:

$$\begin{aligned} \ell, \bar{\ell}: \quad & m^2_{\text{fermions}} = |y_2 \langle S \rangle|^2 , \quad & m^2_{\text{scalars}} |y_2 \langle S \rangle|^2 \pm |y_2 \langle F_S \rangle| , & \quad (3.53)\\ q, \bar{q}: \quad & m^2_{\text{fermions}} = |y_3 \langle S \rangle|^2 , \quad & m^2_{\text{scalars}} = |y_3 \langle S \rangle|^2 \pm |y_3 \langle F_S \rangle| . & \quad (3.54) \end{aligned}$$

The principle feature of this type of SUSY breaking is that this splitting of messenger masses by non-zero $\langle F_S \rangle$ is communicated to the MSSM through radiative corrections. The gaugino fields receive gauge coupling strength mass contributions through one-loop interactions with the messenger fields, and the scalar fields receive masses through two-loop diagrams:

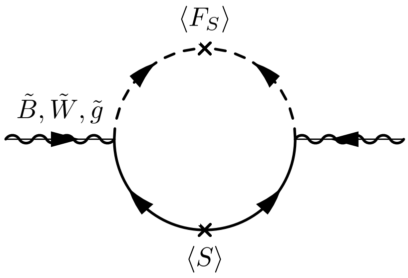

$$M_i = \frac{\alpha_i}{4\pi} \frac{\langle F_S \rangle}{\langle S \rangle} = \frac{\alpha_i}{4\pi} \Lambda \tag{3.55}$$

The scalar squared mass terms from two-loop interactions shown in Figure 3.2 are:

$$m^2_{\phi_i} = 2 \left[\frac{\langle F_S \rangle}{\langle S \rangle} \right]^2 \left[\left(\frac{\alpha_1}{4\pi} \right)^2 C_1(i) + \left(\frac{\alpha_2}{4\pi} \right)^2 C_2(i) + \left(\frac{\alpha_3}{4\pi} \right)^2 C_3(i) \right], \tag{3.56}$$

where the $C_a(i)$ are quadratic Casimir invariants. In a similar way, the (scalar)^3 couplings $\mathbf{a}_u$, $\mathbf{a}_d$, and $\mathbf{a}_e$ (the supersymmetrized Yukawa couplings) are suppressed compared to the gaugino

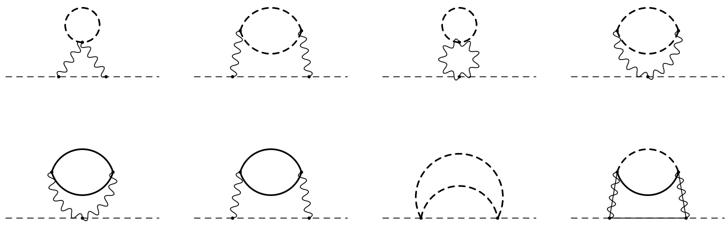

Figure 3.2: Squared mass contributions to scalars in GMSB at two-loop order, the leading contribution. Messenger scalars are shown as heavy dashed lines, and messenger fermions are shown as solid lines. SM gauge bosons are shown as wavy lines, and gauginos are shown as solid lines with wavy lines over them. Reprinted from Figure 7.5 of reference [2].

masses and to a good approximation at the messenger scale:

$$\mathbf{a}_u = \mathbf{a}_d = \mathbf{a}_e = 0. \tag{3.57}$$

This is a very strict realization of *universality* conditions [3] that many other models simply assume:

$$\mathbf{m^2_Q} \sim m^2_Q \mathbf{1}, \quad \mathbf{m^2_{\bar{u}}} \sim m^2_{\bar{u}} \mathbf{1}, \quad \mathbf{m^2_{\bar{d}}} \sim m^2_{\bar{d}} \mathbf{1}, \quad \mathbf{m^2_L} \sim m^2_L \mathbf{1}, \quad \mathbf{m^2_{\bar{e}}} \sim m^2_{\bar{e}} \mathbf{1} \tag{3.58}$$

where $\mathbf{1}$ is the unit 3×3 matrix. This condition, achieved by GMSB quite naturally, prevents significant mixing and CP- or flavor-violating processes that are not experimentally observed. Without universality, processes like $\mu \to e\gamma$ (see Figure 3.3) arise from non-diagonal $\mathbf{a_e}$ elements in the soft SUSY breaking term $\tilde{\bar{e}}\mathbf{a_e}\mathbf{\tilde{L}H_d}$ of Eqn. 3.47.

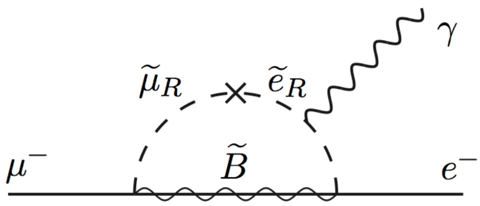

Figure 3.3: Contribution to the $\mu \to e\gamma$ process introduced by flavor-violating soft breaking terms in off-diagonal elements of $\mathbf{m^2_{\bar{e}}}$. In GMSB the slepton masses are generated at two-loop order at gauge coupling strength and are heavily suppressed. Reprinted from Figure 6.6(a) of reference [2].

[3] *Universal* meaning precisely the universality of interactions between the 3 quark flavors; with no off-diagonal mixings and all diagonal elements the same, universality is the mathematical expression of flavor-blindness.

3.4 Light Stops and the Higgs Sector

Of critical importance to naturalness and solving the hierarchy problem of the Standard Model is the masses of particles with the largest couplings to the Higgs boson. Seen in Section 2.4:

$$\Delta m_H \propto \lambda_f^2\left(m_S^2 - m_f^2\right) \ln\left(\Lambda_{UV}^2/m_S^2\right) \tag{3.59}$$

the Higgs mass is sensitive to the heaviest particles it couples to, and those particles also having large Yukawa couplings exacerbates the hierarchy problem SUSY is intended to solve.

After the electroweak symmetry is broken, the scalar potential V of the Higgs scalar fields in the MSSM [4] satisfy the minimum $\partial V/\partial H_u^0 = \partial V/\partial H_d^0 = 0$ with the conditions:

$$m_{H_u}^2 + |\mu|^2 - b\cot\beta - (m_Z^2/2)\cos(2\beta) = 0, \tag{3.60}$$

$$m_{H_d}^2 + |\mu|^2 - b\tan\beta + (m_Z^2/2)\cos(2\beta) = 0 \tag{3.61}$$

with

$$\tan\beta \equiv \frac{v_u}{v_d} = \frac{\langle H_u^0\rangle}{\langle H_d^0\rangle} \tag{3.62}$$

$$v_u^2 + v_d^2 = v^2 = \frac{2m_Z^2}{g^2 + g'^2} \approx (246\,\mathrm{GeV})^2. \tag{3.63}$$

These are necessary conditions for electroweak symmetry breaking and the acquisition of the VEV $v \sim 246\,\mathrm{GeV}$, however there must be fine-tuning here as Eqn. 3.60 contains H_u, H_d, and their mass term μ. These terms appear in the soft breaking superpotential (Eqn. 3.43) and are of the breaking scale. This is referred to as the 'little hierarchy problem'.

To avoid this, the renormalization group (RG) equations for the squared-mass terms of the Higgs and third generation squarks are considered. Due to the large Yukawa couplings of the third generation, their contributions are the most significant. To one-loop order, only three different combinations of terms appear, so for simplicity we can introduce:

$$X_t = 2\,|y_t|^2\left(m_{H_u}^2 + m_{Q_3}^2 + m_{\bar{u}_3}^2\right) + 2\,|a_t|^2 \tag{3.64}$$

$$X_b = 2\,|y_b|^2\left(m_{H_d}^2 + m_{Q_3}^2 + m_{\bar{d}_3}^2\right) + 2\,|a_b|^2 \tag{3.65}$$

$$X_\tau = 2\,|y_\tau|^2\left(m_{H_d}^2 + m_{L_3}^2 + m_{\bar{e}_3}^2\right) + 2\,|a_\tau|^2 \tag{3.66}$$

[4]Consider the neutral components of $H_u = \left(H_u^+, H_u^0\right)$ and $H_d = \left(H_d^0, H_d^-\right)$ in the last line of Eqn. 3.47.

In terms of X_t, X_b, and X_τ the one-loop RG running (evolution with scale) Higgs masses are:

$$16\pi^2 \frac{d}{dt} m_{H_u}^2 = 3X_t - 6g_2^2|M_2|^2 - \frac{6}{5}g_1^2|M_1|^2 + \frac{3}{5}g_1^2 S \tag{3.67}$$

$$16\pi^2 \frac{d}{dt} m_{H_d}^2 = 3X_b + X_\tau - 6g_2^2|M_2|^2 - \frac{6}{5}g_1^2|M_1|^2 - \frac{3}{5}g_1^2 S \tag{3.68}$$

where $S \equiv \mathrm{Tr}\left[Y_j m_{\phi_j}^2\right]$. This RG running has several important consequences. The X_t, X_b, and X_τ are positive in GMSB. The X_t term only appears for H_u and not for H_d, and due to y_t being much larger than any of the other Yukawa couplings this is much bigger than the other terms. Thus $m_{H_u}^2$ tends to run negative towards the lower electroweak scale, destabilizing the point $H_u = H_d$ and triggering electroweak symmetry breaking. The large top Yukawa coupling, in the MSSM, is principally responsible in this way for *radiative* electroweak symmetry breaking and naturally pushes the higgs mass to small values $m_{H_u}^2 < m_{H_d}^2$ at the electroweak scale.

The third-generation squark squared-masses have RG equations:

$$16\pi^2 \frac{d}{dt} m_{Q_3}^2 = X_t + X_b - \frac{32}{3}g_3^2|M_3|^2 - 6g_2^2|M_2|^2 - \frac{2}{15}g_1^2|M_1|^2 + \frac{1}{5}g_1^2 S \tag{3.69}$$

$$16\pi^2 \frac{d}{dt} m_{\bar{u}_3}^2 = 2\,X_b - \frac{32}{3}g_3^2|M_3|^2 - \frac{32}{15}g_1^2|M_1|^2 - \frac{4}{5}g_1^2 S \tag{3.70}$$

$$16\pi^2 \frac{d}{dt} m_{\bar{d}_3}^2 = 2\,X_b - \frac{32}{3}g_3^2|M_3|^2 - \frac{8}{15}g_1^2|M_1|^2 + \frac{2}{5}g_1^2 S \tag{3.71}$$

in contrast to the first and second generation squarks:

$$16\pi^2 \frac{d}{dt} m_{\phi_i}^2 = \sum_{a=1,2,3} 8C_a(i)g_a^2|M_a|^2 + \frac{6}{5}Y_i g_1^2 S \tag{3.72}$$

Compared to first and second generation squarks, stop and sbottom masses run much lower at the electroweak scale due to the X_t and X_b terms. The $|M_3|^2$ terms also contribute large mass contributions to stops and sbottoms that the Higgs scalars do not receive, encouraging the MSSM to deliver a VEV to the Higgs and not the squarks or sleptons.

Looking specifically at the stop masses, the large Yukawa coupling is responsible for several non-negligible contributions compared to first and second generation squarks. In the gauge-eigenstate basis:

$$\mathcal{L}_{\text{stop masses}} = -\begin{pmatrix} \tilde{t}_L^* & \tilde{t}_R^* \end{pmatrix} \mathbf{m}_{\tilde{\mathbf{t}}}^{\mathbf{2}} \begin{pmatrix} \tilde{t}_L \\ \tilde{t}_R \end{pmatrix} \tag{3.73}$$

with

$$\mathbf{m^2_{\tilde{t}}} = \begin{pmatrix} m^2_{Q_3} + m^2_t + \left(\frac{1}{2} - \frac{2}{3}\sin^2\theta_W\right)\cos 2\beta\, m^2_Z & v\left(a^*_t \sin\beta - \mu y_t \sin\beta\right) \\ v\left(a_t \sin\beta - \mu^* y_t \cos\beta\right) & m^2_{\bar{u}_3} + m^2_t + \frac{2}{3}\sin^2\theta_W \cos 2\beta\, m^2_Z \end{pmatrix} \tag{3.74}$$

The stop mass matrix can further be diagonalized to give mass eigenstates:

$$\begin{pmatrix} \tilde{t}_1 \\ \tilde{t}_2 \end{pmatrix} = \begin{pmatrix} c_{\tilde{t}} & -s^*_{\tilde{t}} \\ s_{\tilde{t}} & c_{\tilde{t}} \end{pmatrix} \begin{pmatrix} \tilde{t}_L \\ \tilde{t}_R \end{pmatrix} \tag{3.75}$$

where $|c_{\tilde{t}}|^2 + |s_{\tilde{t}}|^2 = 1$. The convention is to take $m^2_{\tilde{t}_1} < m^2_{\tilde{t}_2}$ as the eigenvalues of Eqn. 3.74. The large positive X_t term in the running of stop masses pushes $m^2_{\bar{u}_3} < m^2_{Q_3}$ and even moreso to lower masses than the first and second generation squarks and sleptons. The stop masses are generally larger than the top mass due to m_t in $\mathbf{m^2_{\tilde{t}}}$ which prevents un-observed super-light stops in collider experiments. Lastly, many models introduce significant stop mixing in the off-diagonal elements of $\mathbf{m^2_{\tilde{t}}}$. The effect of this mixing is to further separate the mass eigenvalues $m^2_{\tilde{t}_1}, m^2_{\tilde{t}_2}$ and push $\tilde{t}_1$ even lower in mass.

The net result is that the stop squark, in many models including GMSB, is naturally the lightest squark. This is a very attractive scenario, as the principle motivation for SUSY is to solve the hierarchy problem. The supersymmetric Higgs mass receives a correction:

$$\Delta m^2_{H_u} \sim -\frac{3Y^2_t}{4\pi^2} m^2_{\tilde{t}} \log\frac{\Lambda}{m_{\tilde{t}}} \tag{3.76}$$

which is mitigated by a lighter stop. This has important phenomenological consequences, as is covered in the next section.

3.5 Collider Phenomenology of GMSB

The most important feature of GMSB as collider phenomenology is concerned is that the lightest supersymmetric particle (LSP) is the gravitino ($\tilde{G}$), the spin-3/2 superpartner to the spin-2 graviton, having odd R-parity ($P_R = -1$).

The gravitino is more or less a gauge field associated to *local* SUSY transformations, when gravity is considered and such transformations are no longer global. A so-called 'super-Higgs' mechanism gives the gravitino a mass from the spontaneous breaking of SUSY labeled $m_{3/2}$:

$$m_{3/2} \sim \frac{\langle F \rangle}{M_P} \tag{3.77}$$

where M_P is the Planck mass. In GMSB the breaking scale is quite low ($\langle F \rangle \sim 10^8$ GeV) compared to mSUGRA [64, 65, 66, 67, 68, 69, 70] with $\langle F \rangle \sim 10^{20}$ GeV for example. From this the gravitino in GMSB models is very light (eV – keV).

As an R-parity conserving theory, GMSB signatures in collider experiments must follow several rules:

- All sparticles must be produced in even numbers, typically pairs.
- All sparticle decays must proceed to the NLSP and then to the gravitino LSP.
- The gravitino LSP is absolutely stable, and interacting only weakly it escapes instrumentation un-detected. In 4π hermetic detectors, this contributes to large missing transverse energy ($\not{E}_{\mathrm{T}}$).

Furthermore in pp collisions at the LHC, strong production dominates over electroweak production and the typical production mechanism is pairs of squarks or gluinos. Assuming that the stop squark is much lighter than all other squarks and gluinos, pairs of stop squarks are produced leading to third-generation final states.

A final consideration is the choice of NLSP. In principle any sparticle can be the NLSP in a model, but most GMSB models use the stau slepton or neutralinos (mass eigenstate mixtures of the neutral gauginos). This dissertation concerns itself only with the neutralino NLSP case, and specifically the bino ($\tilde{B}$) case.

In the limit where the soft breaking terms are much larger than the electroweak breaking scale, the neutralino and chargino masses, in the gauge eigenstate basis of $\psi^0 = \left(\tilde{B}, \tilde{W}^0, \tilde{H}_d^0, \tilde{H}_u^0\right)$ and $\psi^\pm = \left(\tilde{W}^+, \tilde{H}_u^+, \tilde{W}^-, \tilde{H}_d^-\right)$, can be diagonalized to reveal mass eigenstates:

$$m_{\tilde{\chi}_1^0} = M_1 - \frac{m_Z^2 \sin^2\theta_W (M_1 + \mu \sin 2\beta)}{\mu^2 - M_1^2} + \dots \tag{3.78}$$

$$m_{\tilde{\chi}_2^0} = M_2 - \frac{m_W^2 (M_2 + \mu \sin 2\beta)}{\mu^2 - M_2^2} + \dots \tag{3.79}$$

$$m_{\tilde{\chi}_3^0} = |\mu| + \frac{m_Z^2 (\mathrm{sgn}(\mu) - \sin 2\beta)(\mu + M_1 \cos^2\theta_W + M_2 \sin^2\theta_W)}{2(\mu + M_1)(\mu + M_2)} + \dots \tag{3.80}$$

$$m_{\tilde{\chi}_4^0} = |\mu| + \frac{m_Z^2 (\mathrm{sgn})\mu) + \sin 2\beta)(\mu - M_1 \cos^2\theta_W - M_2 \sin^2\theta_W)}{2(\mu - M_1)(\mu - M_2)} + \dots \tag{3.81}$$

$$m^2_{\tilde{\chi}_1^\pm} = M_2 - \frac{m_W^2 (M_2 + \mu \sin 2\beta)}{\mu^2 - M_2^2} + \dots \tag{3.82}$$

$$m^2_{\tilde{\chi}_2^\pm} = |\mu| + \frac{m_W^2 \mathrm{sgn}(\mu)(\mu + M_2 \sin 2\beta)}{\mu^2 - M_2^2} + \dots \tag{3.83}$$

where again $\tan\beta = \langle H_u^0 \rangle / \langle H_d^0 \rangle$.

In this limit the neutralino gauge eigenstates are very 'bino-like' ($\tilde{\chi}_1^0 \approx \tilde{B}$), 'wino-like' ($\tilde{\chi}_2^0 \approx$

$\tilde{W}^0$), and a 'higgsino-like' mixture $\tilde{\chi}_3^0$, $\tilde{\chi}_4^0 \approx (\tilde{H}_u^0 \pm \tilde{H}_d^0)/\sqrt{2}$; the charginos are a wino-like $\tilde{\chi}_1^\pm$ and higgsino-like $\tilde{\chi}_2^\pm$.

The above mass eigenvalues are an approximation that is not held for all SUSY models, however applying GMSB boundary conditions to the MSSM gives such values naturally. Of note is the near-degeneracy of $\tilde{\chi}_1^\pm$ and $\tilde{\chi}_2^0$, described in some literature as a 'wino-like co-NLSP' if all other terms are heavier. Due to the GMSB masses being given by the relation:

$$M_i = \frac{\alpha_i}{4\pi}\Lambda \tag{3.84}$$

then the mass spectrum of GMSB very naturally results in $\tilde{\chi}_1^0$ being the lightest neutralino, and the very-light gravitino ($\tilde{G}$) being the LSP gives the bino-like NLSP.

In overall summary, the phenomenology of interest to this dissertation is:

Strong pair production of stop squarks: – strong production dominates in pp collisions, and assuming the stop squark is the lightest squark or gluino this production would be observable at the LHC.

Stop squarks decaying to top quarks and bino-like NLSPs: – in the simple limit where all other sparticles are very heavy, the only R-parity respecting decay allowed for stops is to the NLSP. As GMSB couples sparticles via the ordinary gauge interactions, this decay cannot violate charge nor flavor, and if the NLSP is the neutral bino this must be to a top quark.

Bino-like NLSPs decaying to photons and the gravitino LSP: – the bino is an admixture of the Z and γ superpartners, and so both decays are allowed. This decay is predominantly to photons, although decays to Z are allowed at heavier bino masses. The branching ratios of these decays are shown in Figure 3.4.

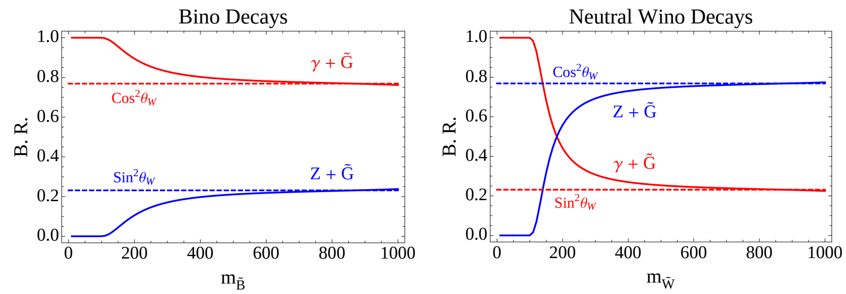

Figure 3.4: Bino and neutral wino NLSP branching ratios to $\gamma\tilde{G}$ and $Z\tilde{G}$. Reprinted from Figure 2 of reference [4].

The gravitino LSP escapes undetected: – the principle observable in this dissertation (and many other GMSB searches) is missing transverse energy ($\not{E}_{\mathrm{T}}$) from the weakly interacting gravitino not being seen by detector instrumentation.

These motivate the interest in $pp \to t\bar{t} + \gamma\gamma + \not{E}_{\mathrm{T}}$ shown in Figure 3.5 for which the analysis is optimized.

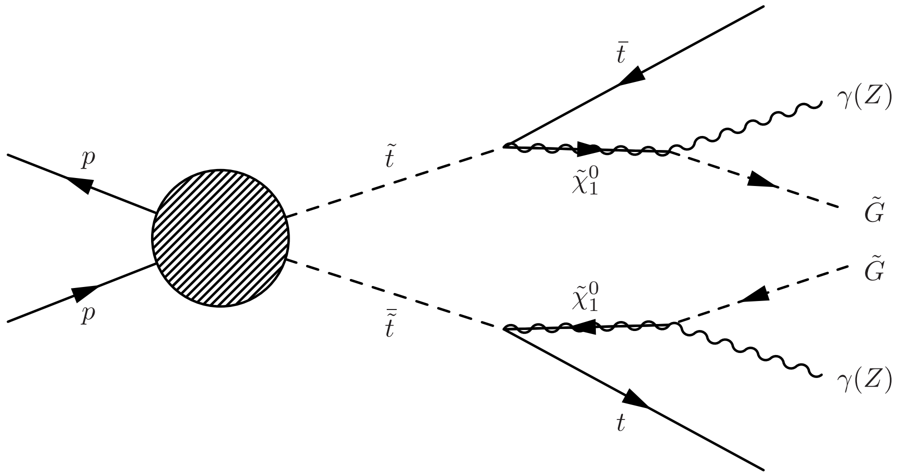

Figure 3.5: Production of stop pairs decaying to bino-like neutralinos.

3.6 Experimental Status of SUSY

Numerous searches for evidence of Supersymmetry have been performed, providing strict constraints on the viable parameters of any such model. To date no significant observation has been seen, although the discovery of a 125 GeV/c^2 scalar Higgs candidate makes very real the motivations for SUSY. The most stringent limits on a wide variety of SUSY breaking models have been set by LHC and Tevatron experiments, and recent Higgs results as well as cosmological (dark matter) measurements restrict SUSY further.

3.6.1 Direct Collider Searches

Early direct collider searches yielded important results beginning in the 1980s [71, 72, 73, 74, 75, 76, 77, 78, 79], establishing that any viable SUSY model must be a broken one.

Currently the strongest limits on SUSY are from the CMS [80] and ATLAS [81] Collaborations at the LHC. Both CMS and ATLAS present results evaluated against so-called 'Simplified Model Spectra' models which greatly simplify the available parameter space to focus on particular final states. Figure 3.6 shows the most recent limits set by CMS, and Figure 3.7 shows the current ATLAS results. In general, current limits exclude masses of $\sim$1–1.5 TeV for strongly-produced sparticles and $\sim$500 GeV for electroweak-ly produced gauginos.

Figure 3.8 shows the current limits set by ATLAS on the mSUGRA model ($\tan\beta = 30$) in the simplified sfermion–gaugino mass plane (m_0–$m_{1/2}$). These limits are extremely restrictive,

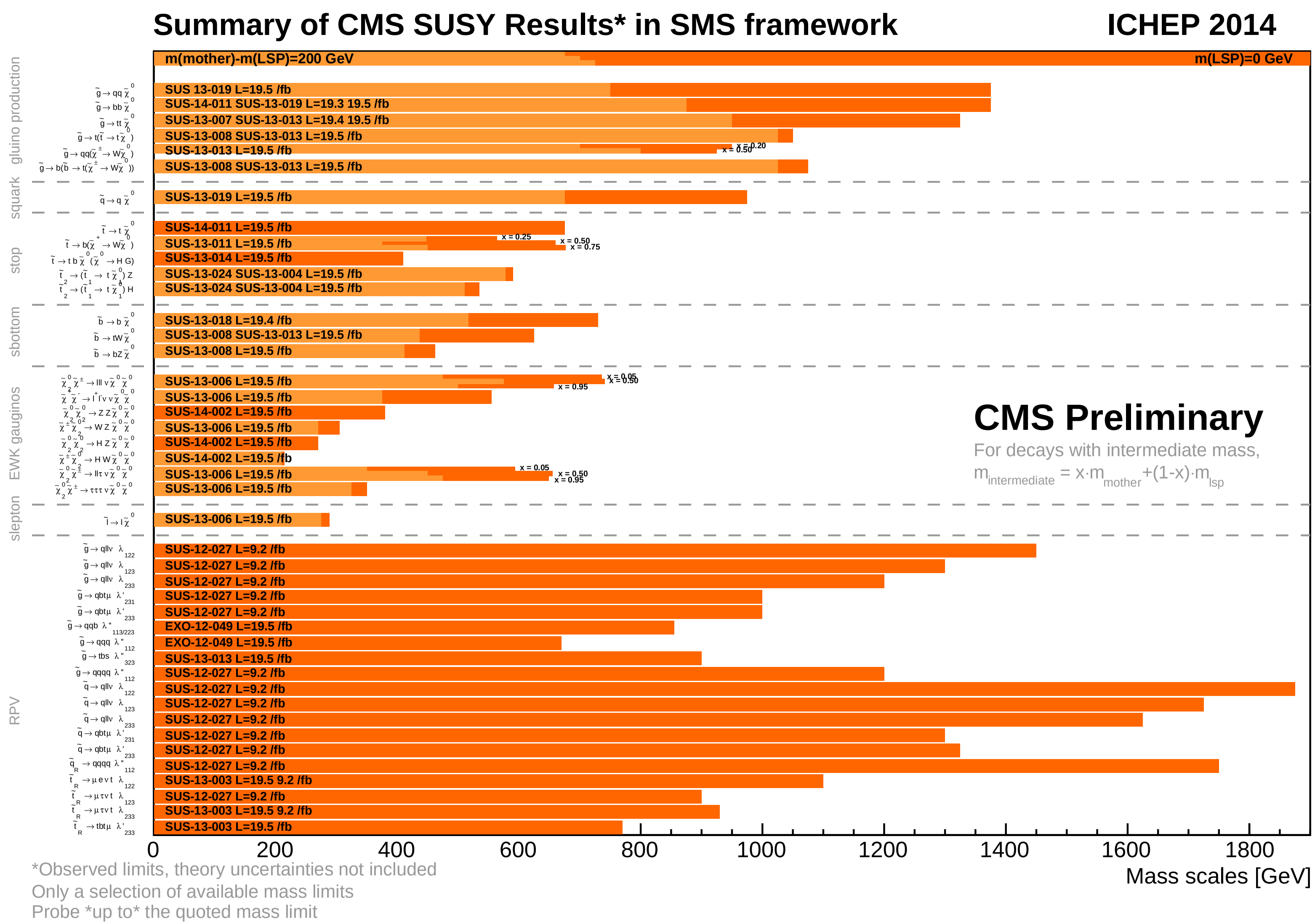

Figure 3.6: Summary of exclusion limits of CMS SUSY searches at $\sqrt{s} = 8\,\text{TeV}$ on the mass of mother particles in a Simplified Mass Spectra (SMS) framework. SMS models simplify event topologies by strongly producing pairs of heavy particles which decay 100% of the time to the final state of interest. The dark bands represent $m(\text{LSP}) = 0\,\text{GeV}$ and the light shades represent $m(\text{Mother}) - m(\text{LSP}) = 200\,\text{GeV}$. Reprinted from [5].

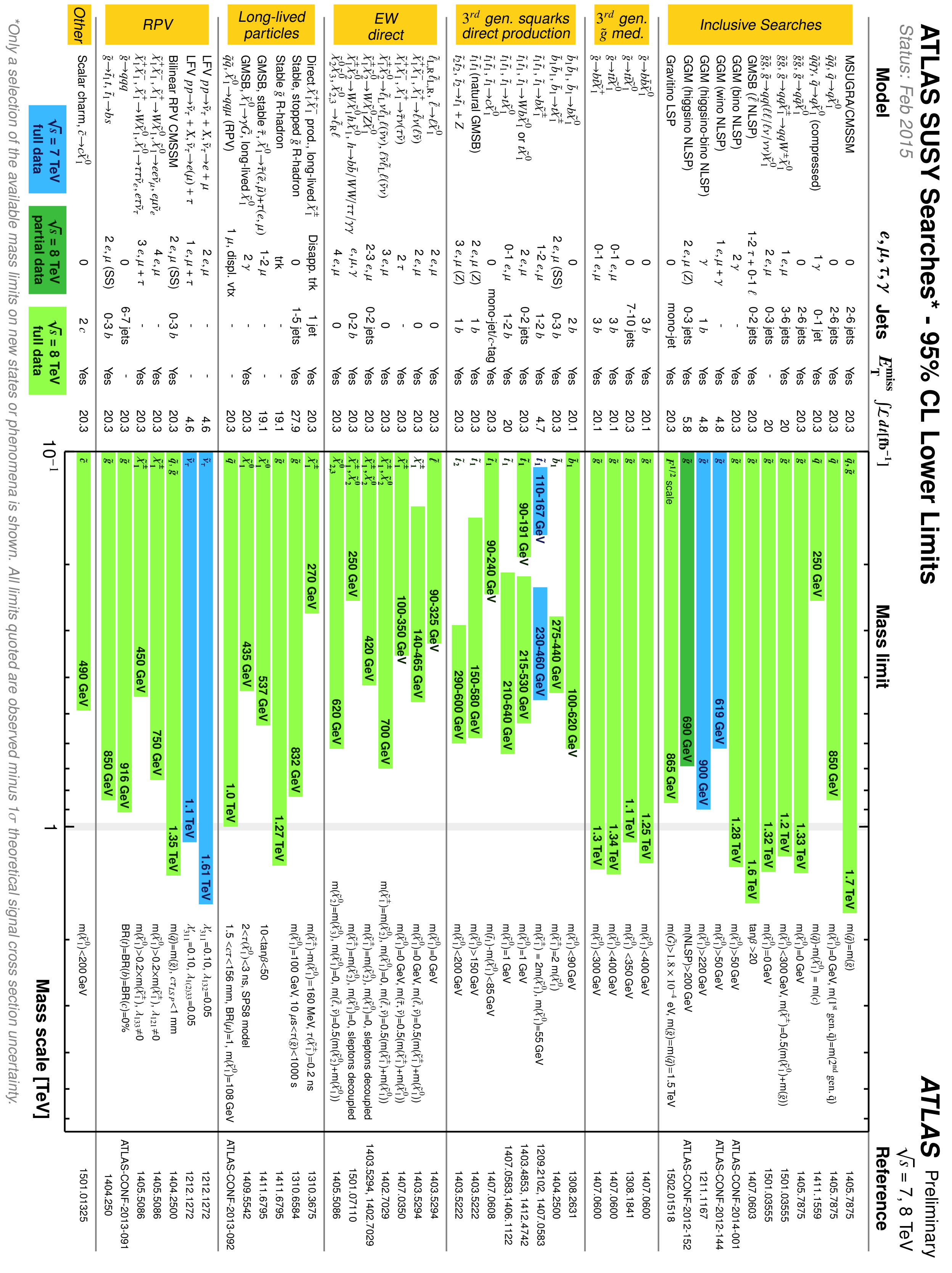

Figure 3.7: Summary of exclusion limits of ATLAS SUSY searches. Reprinted from [6].

pushing m_0 up to $\sim$6 TeV (and higher for some searches) and $m_{1/2}$ up to 500–800 GeV. Some phase space still exists that is favorable to solving the hierarchy problem, but natural solutions are becoming very rare as the LHC continues to provide more data.

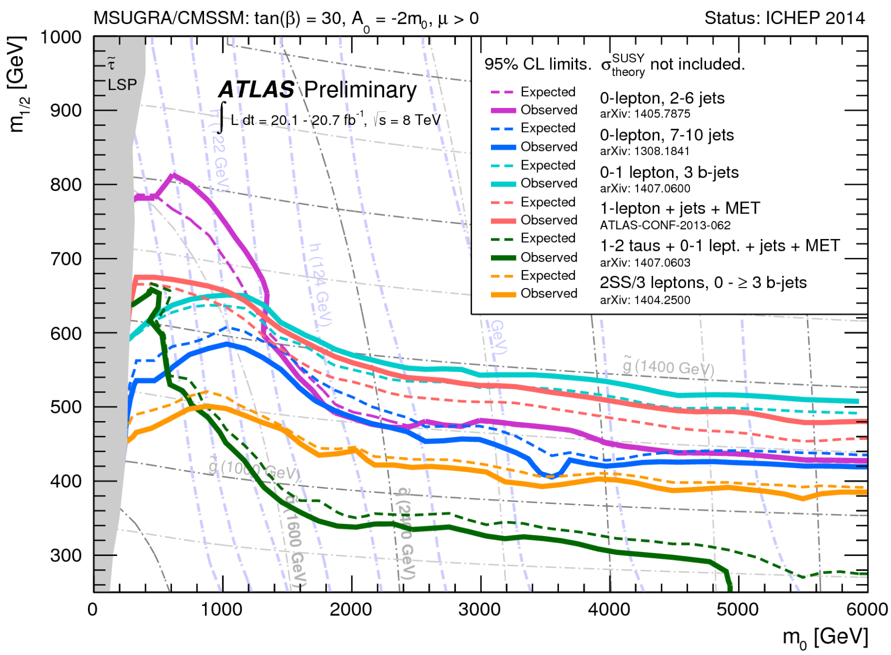

Figure 3.8: Exclusion limits in the simplified sfermion–gaugino (m_0–$m_{1/2}$) plane of mSUGRA/cMSSM models for $\sqrt{s} = 8$ TeV analyses at ATLAS. Masses compatible with a Higgs mass of 125 GeV are still allowed but increasingly restricted. Reprinted from [7].

Considering natural SUSY models, searches for direct stop pair production have excluded stop masses up to roughly 500–700 GeV, shown for CMS in Figure 3.9. It is important to consider that these results are not compatible with the results of the search presented in this dissertation, as the decay of stops to binos in a GMSB framework has significantly different final states and much smaller SM backgrounds.

Lastly, direct searches for GMSB in photon events have excluded gluino and squark masses up to $\sim$1 TeV in the light first/second generation scenario with a bino-like NLSP by CMS [9, 10]. Results at 7 and 8 TeV are shown in Figure 3.10. The results of this dissertation are not precluded by these, as they assumed third generation squarks were very heavy. While not natural models, these searches were optimized for earlier results by requiring only first/second generation jets rather than top quark decays.

Very few direct searches for natural GMSB have been published, and none for the bino-like NLSP scenario. Constraints on natural models with a Higgsino-like NLSP have resulted in stop mass lower bounds of 310 GeV/c^2 [82] and 500–600 GeV/c^2 [83] from ATLAS and 360–410 GeV/c^2 from CMS [84].

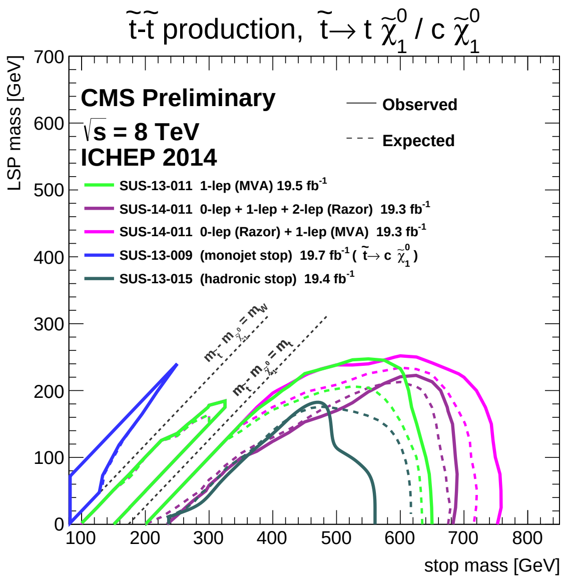

Figure 3.9: Summary of exclusion limits for direct stop searches by CMS at $\sqrt{s} = 8\,\text{TeV}$. Reprinted from [8].

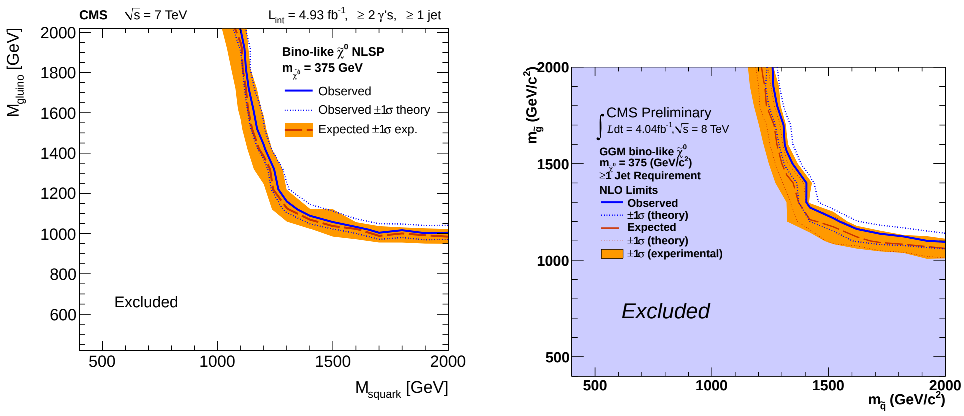

Figure 3.10: The currently best available limits on squark and gluino masses in the bino-like NLSP case for 7 TeV (left) and 8 TeV (right). Gluinos and first and second generation squarks are excluded up to ∼1 TeV, however stop squarks are not considered in these results. Reprinted from Figure 5 of reference [9] (left) and Figure 2 of reference [10] (right).

3.6.2 Higgs Boson Discovery

Assuming the newly-discovered Higgs candidate at 125 GeV/c^2 [28, 29, 30] is precisely the Standard Model Higgs boson and the h^0 of the MSSM has tremendous consequences on GMSB and Supersymmetry as a whole.

In the simplest ($N = 1$) models of GMSB, the higgs mass is maximally only $\sim$118 GeV while still requiring sparticle masses of less than roughly 2 TeV [85]. In the MSSM in general, larger higgs masses are achieved by large stop/top contributions by way of either large stop masses or introducing large stop mixing with large $A_t = a_t/y_t$ couplings [86]. Large stop masses are antithetical to the motivation for this dissertation and solving the hierarchy problem, and on the other hand GMSB naturally has vanishing A-terms at the breaking scale (Eqn. 3.57), so neither prospect is attractive. Plainly spoken, a higgs mass of 125 GeV is in a challenging range as it is low enough to require a solution to the hierarchy problem but slightly too large for minimal models of SUSY to produce.

The key implication in this is that the most minimal models are unsuitable, but many fairly straightforward extensions provide successful explanations. Recent proposals include introducing heavy superpartners (including stops) [87, 88]. More germane to the search of this dissertation for light stops, several recent papers suggest the existence of maximal stop mixing (large A-terms giving one light and one very heavy stop) by allowing for direct messenger-matter interactions and in some cases extending the hidden sector. For a thorough discussion of these scenarios, see references [89, 90, 86, 85, 91, 92].

In short, a 125 GeV is challengingly heavy for the most minimal models of SUSY, however the theory is profoundly robust and flexible.

3.6.3 Dark Matter Constraints

While GMSB is an attractive theory because it provides the gravitino as a dark matter candidate, astronomical observations place several constraints on the precise type of candidate this can be. From Section 3.5 and reference [2], the scale of SUSY breaking in GMSB models is much lower than in others, giving a gravitino mass in the eV–keV range. This typically classifies gravitino dark matter as *hot dark matter* (HDM) [93], a heavily disfavored scenario where the bulk of the Universe is highly relativistic lightweight particles that cannot account for cosmological structures. Higher SUSY breaking scales can push gravitinos towards *warm dark matter* (WDM) [94] in the keV range.

Many models however take careful consideration of the gravitino's goldstino component, the helicity-1/2 component absorbed in the 'super-Higgs' mechanism where the gravitino became massive. Several mixed dark matter (MDM) scenarios are proposed [95, 96] in which the behaviors of the helicity-3/2 component with only gravitational interactions and helicity-1/2 with non-gravitational interactions are combined. Recent lower bounds on warm or mixed warm+cold states limit $m_{\mathrm{WDM}} > 8keV$ and some $m_{\mathrm{WDM+CDM}} > 1.1$–$1.5$ keV [97, 98].

As relevant for collider phenomenology, the current WMAP relic density measurement of $\Omega_{\mathrm{DM}}h^2 = 0.118$ [99] (where h is Hubble's constant) places a (rather weak) bound on the lifetime of the NLSP neutralino [100]:

$$(c\tau)_{\tilde{\chi}_1^0 \to \gamma \tilde{G}_{3/2}} \sim 130 \left(\frac{100\,\mathrm{GeV}}{m_{\tilde{\chi}_1^0}} \right)^5 \left(\frac{\sqrt{\langle F \rangle}}{100\,\mathrm{TeV}} \right)^4 \mu\mathrm{m}. \tag{3.85}$$

For values of $\sqrt{F} \sim 3000\,\mathrm{TeV}$ and $m_{\tilde{\chi}_1^0} = 100\,\mathrm{GeV}$ this is $c\tau \sim 100$ m, which is detectable on collider distance scales. Smaller breaking scales for GMSB result in much smaller decay lifetimes, approaching the prompt case assumed in the analysis.

Chapter 4

The Large Hadron Collider

N.B.: Unless explicitly cited otherwise, the following is heavily adapted from the excellent summary of reference [12].

The Large Hadron Collider (LHC) is currently the highest energy and highest intensity particle accelerator and collider in the world. Composed of eight straight sections and eight arcs, the 26.7 km tunnel was initially constructed for the CERN Large Electron-Positron collider (LEP) between 1984 and 1989 and is located 45–170 meters beneath the French and Swiss border outside of Geneva, Switzerland, seen in Figure 4.1.

The two counter-rotating superconducting rings of the LHC were designed to deliver protons at an energy of 7 TeV per beam with a maximum instantaneous luminosity of $10^{34}\mathrm{cm}^{-2}\mathrm{s}^{-1}$ for a center-of-mass energy of 14 TeV. The LHC is also designed to collide lead ions ($^{208}\mathrm{Pb}^{82+}$) at beam energies up to 2.76 TeV/nucleon, giving a total lead-lead center-of-mass energy of up to 1.15 PeV at a peak luminosity of $10^{27}\mathrm{cm}^{-2}\mathrm{s}^{-1}$.

The LHC provides four interaction regions to several experiments shown in Figure 4.2. The Compact Muon Solenoid (CMS) and 'A Toroidal LHC Apparatus' (ATLAS) experiments are high-luminosity general-purpose detectors. The LHC-beauty (LHCb) and 'Total Cross Section, Elastic Scattering and Diffraction Dissociation' (TOTEM) experiments are designed for lower luminosity (peak $2 \times 10^{29}\mathrm{cm}^{-2}\mathrm{s}^{-1}$ with 156 bunches). 'A Large Ion Collider Experiment' (ALICE) is dedicated to lead ion collisions. Lastly the LHC-forward (LHCf) and 'Monopole and Exotics Detector At the LHC' (MoEDAL) experiments share interaction points with ATLAS and LHCb respectively.

At the time of this writing, the LHC has begun providing proton collisions for physics experiments at $\sqrt{s} = 13\,\mathrm{TeV}$ in Run II [101]. During Run I the LHC provided 6.1 fb^{-1} of high-quality pp data at $\sqrt{s} = 7\,\mathrm{TeV}$ and 23.3 fb^{-1} at $\sqrt{s} = 8\,\mathrm{TeV}$ [13], shown in Figure 4.3.

Figure 4.1: Aerial view of CERN and the LHC area. The Franco-Swiss border and the subterranean LHC tunnel with the positions of each of the experiments are marked. Photo credit Maximilien Brice for CERN PhotoLab 2008, reference [11].

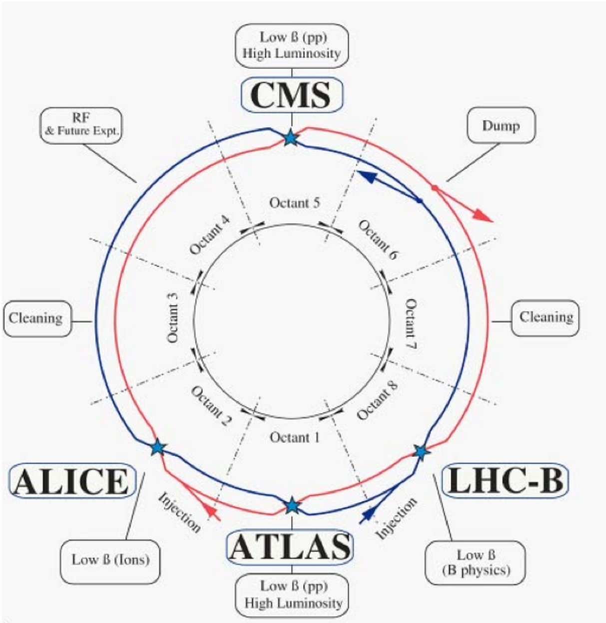

Figure 4.2: Schematic layout of the LHC. Reprinted from Figure 2.1 of reference [12].

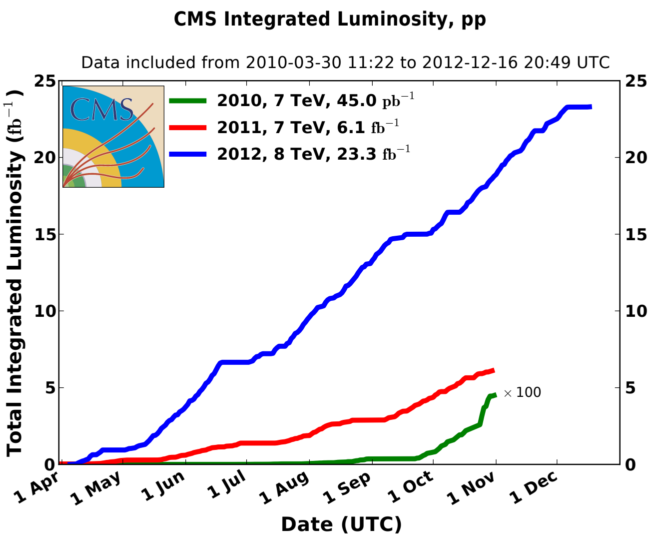

Figure 4.3: Cumulative luminosity versus day delivered to CMS during stable beams for *pp* collisions. Reprinted from reference [13].

The following sections provide an overview of the LHC machine. Section 4.1 details the overall design of the machine and limitations on performance, Section 4.2 describes the LHC injection scheme. A brief description of the superconducting magnets and cryogenic systems is given in Section 4.3, and finally the radiofrequency cavities are described in Section 4.4.

4.1 Performance Goals and Limitations

The principle goal of the LHC machine is to provide high energy proton-proton collisions at a high instantaneous luminosity. For a process of cross section σ_{event} the number of events generated per second in the interaction points (IP) is

$$N_{\text{event}} = L\sigma_{\text{event}} \tag{4.1}$$

where the machine luminosity L is given by

$$L = \frac{N_b^2 n_b f_{\text{rev}} \gamma_r}{4\pi\varepsilon_n\beta^*}F \tag{4.2}$$

where N_b is the number of particles per bunch, n_b is the number of bunches per beam, f_{rev} is the revolution frequency, γ_r is the relativistic gamma factor for the particles, ε_n the normalized beam emittance, β^* the beta function at the IP, and F is the geometric luminosity reduction factor due to the crossing angle at the IP.

Achieving high luminosities is in part a matter of the bunch intensities and number of bunches. A smaller emittance ε_n results in the beam being squeezed into a tighter phase space. A smaller value of β^*, the minimum ratio of the square of the transverse beam size to the emittance (the β function), is achieved by the focusing strength of triplet magnets near the IPs. The β function varies along the beamline as in accelerating sections it is kept large so that the proton momenta are more uniform.

The machine luminosity is limited in several ways. Nonlinear beam-beam interactions in the collision points scale the luminosity $\propto N_b$ rather than $\propto N_b^2$ after a certain saturated bunch intensity, measured by keeping the linear tune shift small:

$$\xi = \frac{N_b r_p}{4\pi\varepsilon_n} < 0.005 \tag{4.3}$$

where r_p is the classical radius of the proton. The physical aperture of the LHC beam screen and the maximum β function value of 180 m limit the emittance ε_n to 3.75 μm. These considerations limit the maximum bunch intensity to $N_b = 1.15 \times 10^{11}$.

Physical limitations on the focusing triplet magnets limit the minimum value for β^* to 0.55 with a maximum crossing angle of 285 μrad [102] at the IPS. The magnet safety systems and beam dump must be able to adequately handle the stored energy in the LHC rings at all times.

Collisions in 2012 at $\sqrt{s} = 8\,\text{TeV}$ were taken with $n_b = 1374$ of the 2808 proton bunches filled, for a bunch spacing of 50 ns, giving a peak luminosity of $7.7 \times 10^{33}\text{cm}^{-2}\text{s}^{-1}$. The average number of proton-proton collisions per bunch crossing was $\sim$40, a challenging environment of simultaneous interactions known as *pileup*. For a more complete summary and discussion of the performance of the LHC during Run I, see reference [103].

4.2 Beam Injection

The ramping of proton energies to the design 7 TeV is a multi-stage process, applied by a series of increasingly powerful accelerators, shown in Figure 4.4.

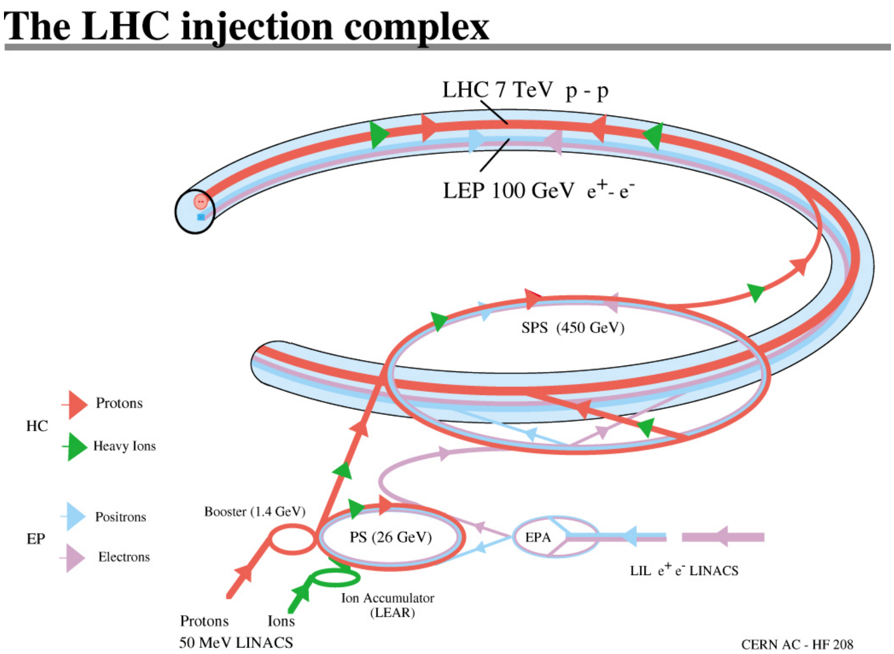

Figure 4.4: The LHC injection complex. Reprinted from reference [14].

Protons initially are ionized from hydrogen gas and accelerated to 50 MeV by the Linac2 linear accelerator [104, 105]. The Proton Synchrotron Booster (PSB) accelerates protons further to 1.4 GeV, injecting them next into the Proton Synchrotron (PS) which brings them up to 25 GeV. The Super Proton Synchrotron (SPS) accelerates these protons to an energy of 450 GeV, and finally injects them into the LHC where they are accelerated up to the chosen operation energy. In 2010 and 2011 the LHC operated at a beam energy of 3.5 TeV, in 2012 4 TeV, and Run II begins in 2015 at 6.5 TeV and soon to the design energy of 7 TeV per beam.

Proton bunches are injected into the LHC by the SPS in ‘trains’ of 72 bunches three or for at a time, with a bunch spacing of 25 ns. An 8-bunch gap (220 ns) is left after each train due to the rise time of the SPS kicker magnets. After each three- or four-train group, the LHC inject kicker gap of 38-39 bunches (0.94 μs) is left. The total bunch structure, shown in Figure 4.5, is 3564 total bunches, 2808 for protons and a 119 bunch (88.924 μs) *abort gap* at the end to allow for the LHC beam dump kicker rise time.

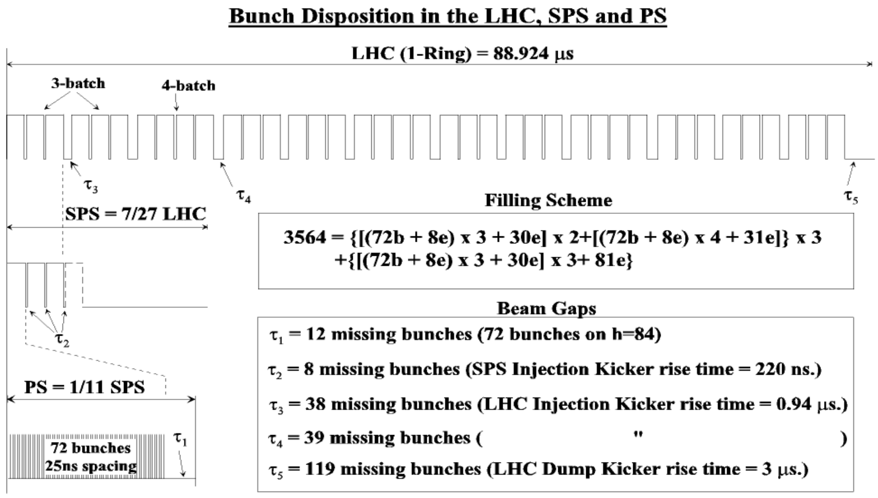

Figure 4.5: The LHC bunch injection structure. Reprinted from Figure 12.2 of reference [12].

4.3 Magnets and Cryogenic Systems

The LHC consists mainly of 1232 twin-bore superconducting dipole magnets that steer the proton beams into circular orbits. Each bore sits within an 8.33 T magnetic field provided by superconducting Niobium-Titanium (NbTi) coils kept at a temperature of 1.9 K by the surrounding iron yoke cold mass. Figure 4.6 shows a diagram of the dipole magnets. Each dipole+cryostat assembly is about 16.5 m long and 27.5 t in weight.

Several types of multipole magnets provide fine control over beam parameters and focusing to beam interaction points. There are 392 quadrupole magnets, shown in Figure 4.7, on the LHC ring to finely control the magnetic field and the emittance and β function. Low-β inner triplets perform the final squeezing of beams before each IP by providing a field gradient of 215 T/m. A large number of orbit and multipole corrector magnets are utilized in the arc sections of the ring, from dipole to sextuple to combinations of higher moments. A full 110 m long cell of magnets composing an LHC octant is shown in Figure 4.8.

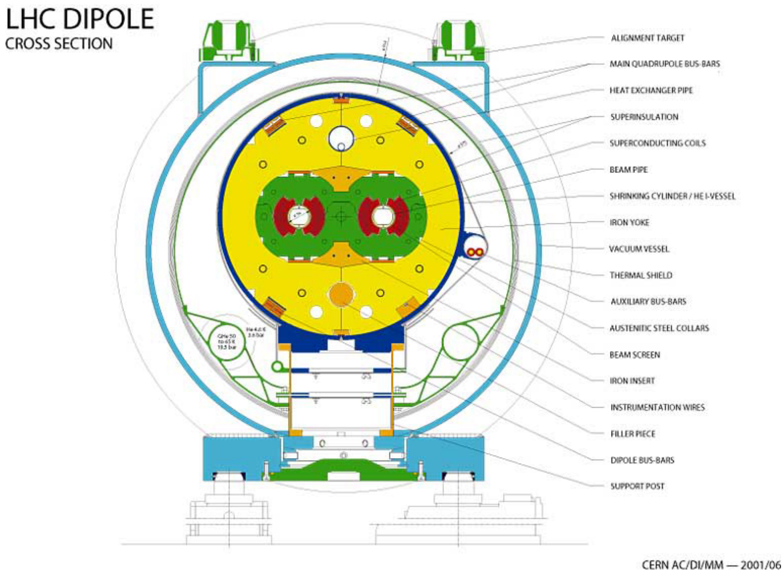

Figure 4.6: Cross section view of an LHC dipole magnet and cryostat. Reprinted from Figure 3.3 of reference [12].

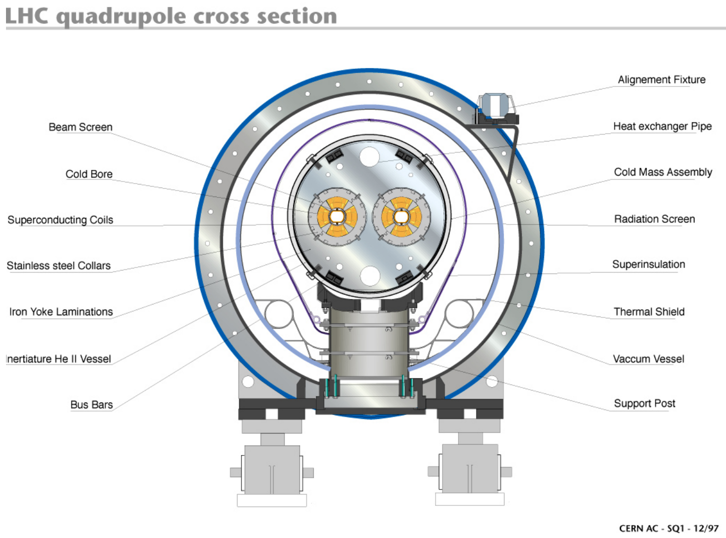

Figure 4.7: Cross section view of an LHC quadrupole magnet and cryostat. Reprinted from reference [15].

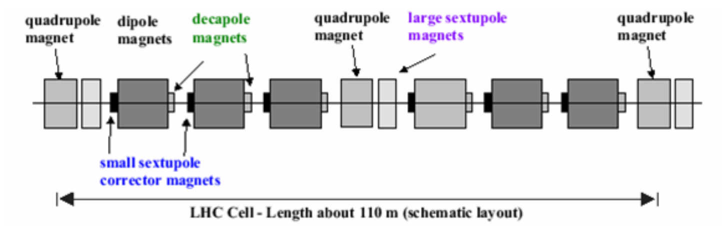

Figure 4.8: Typical structure of a 110 m long cell of magnets in an LHC octant. Reprinted from reference [16].

4.4 Radiofrequency Cavities

The LHC captures and accelerates proton bunches from 450 GeV to 3.5–7 TeV using 400 MHz superconducting radiofrequency cavities. Each beam requires an independent RF system of 8 cavities at design beam energy to provide the needed 8 MV (megavolts) of RF voltage at injection and 16 MV at full beam energy of 7 TeV. A total power of 275 kW is delivered to each beam at 7 TeV operation.

Each cavity is tuned such that its oscillating electric field is at its maximum as proton bunches arrive, passing through a potential difference of 2 MV in each of 8 RF cavities. Proton bunches are accelerated by these cavities each time they pass, and are ramped up to the equilibrium energy desired. Each passing of the beam through these cavities imparts ∼485 KeV to the protons, and orbiting over 11,000 revolutions per second this results in a roughly 20 minute ramp-up time from injection to full 7 TeV beam energy. A diagram of the RF cavities is shown in Figure 4.9.

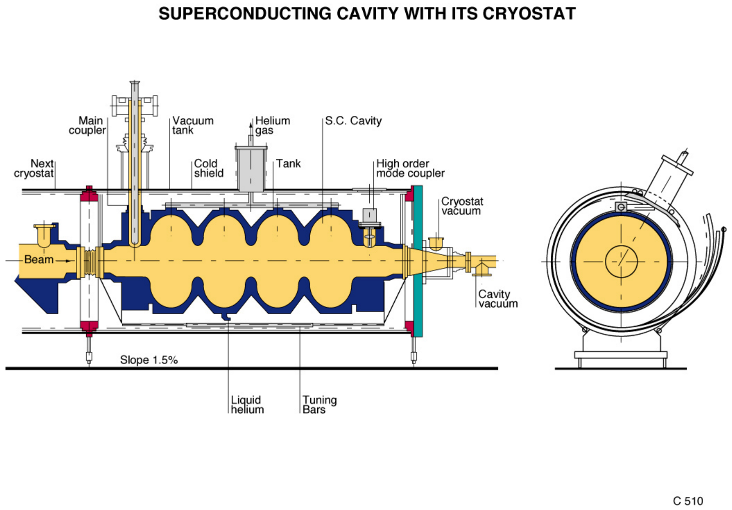

Figure 4.9: Diagram of the RF cavities used to accelerate protons to LHC collision energies. Each cavity delivers 2 MV to proton bunches. Reprinted from reference [17].

Chapter 5

The Compact Muon Solenoid

N.B.: Unless otherwise cited, all technical information is taken from reference [20].

The Compact Muon Solenoid (CMS) is a general-purpose detector experiment situated at the Point 5 (P5) interaction point of the LHC. It is capable of identifying and measuring charged and neutral hadrons, photons, electrons, muons, and tau leptons. Its hermetic 4π coverage of the interaction point allows it to measure weakly interacting particles by reconstructing a momentum imbalance in observed particles, the energy of which is called missing transverse energy ($\not{E}_{\mathrm{T}}$).

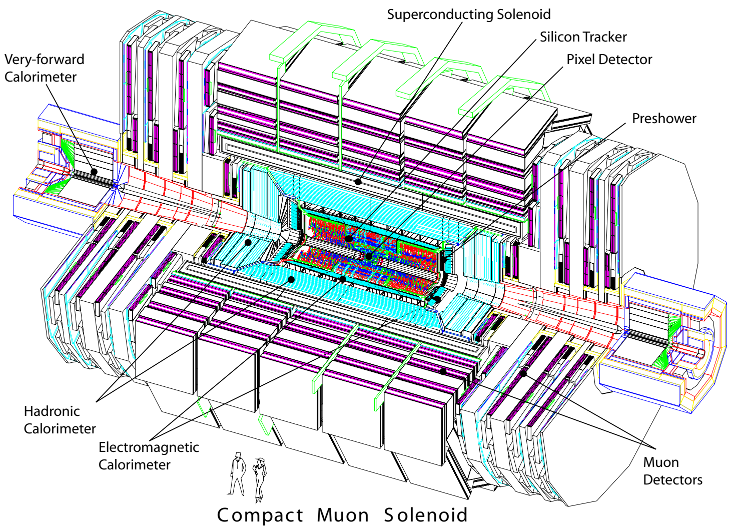

Figure 5.1: Cutaway perspective view of the CMS detector. Each sub-detector is labeled, and two people are shown at the bottom for size comparison. Reprinted from reference [18].

The detector is comprised of five sub-detector systems and is so-named 'Compact' due to its calorimetry residing entirely within its defining feature, a 3.8 T superconducting solenoid providing momentum and charge resolution from curved particle trajectories in its magnetic field. The name 'Muon' refers to the Muon detector system interspersed with the iron return yoke of the magnet, providing excellent muon momentum and timing resolutions. The CMS detector is a staggering 15 m diameter over a 28.7 m length, with a weight of over 14,000 tons. Figure 5.1 shows a perspective view of CMS with each sub-detector visible.

CMS uses a right-handed coordinate system with the nominal interaction point as the origin. The $\hat{x}$ direction points towards the center of the LHC ring, the $\hat{y}$ direction points directly upwards towards the surface at P5 in Cessy, France, and the $\hat{z}$ direction points counter-clockwise along the LHC ring. Polar coordinates are more typically used, with $\hat{r}$ pointing outwards from the IP, $\hat{\phi}$ the azimuthal angle being the angle with the positive $\hat{x}$ direction, and $\hat{\theta}$ the polar angle being the angle the positive $\hat{z}$ direction. The *pseudorapidity* η is a good approximation of the *rapidity* y for relativistic particles, and is a Lorentz invariant expression of the polar angle $\hat{\theta}$:

$$\eta = -\ln\left(\tan\frac{\theta}{2}\right) \tag{5.1}$$

$$y = \frac{1}{2}\ln\left(\frac{E + p_z c}{E - p_z c}\right) \tag{5.2}$$

The transverse energy $E_T = E\cos\phi$ and transverse momentum $p_T = p\cos\phi$ are typically referred to rather than the energy E or momentum p.

The constituent sub-detectors comprising the detector are arranged as concentric cylinders with 'endcaps' surrounding the interaction point. A cross-sectional view of CMS is shown in Figure 5.2 highlighting the individual sub-detectors.

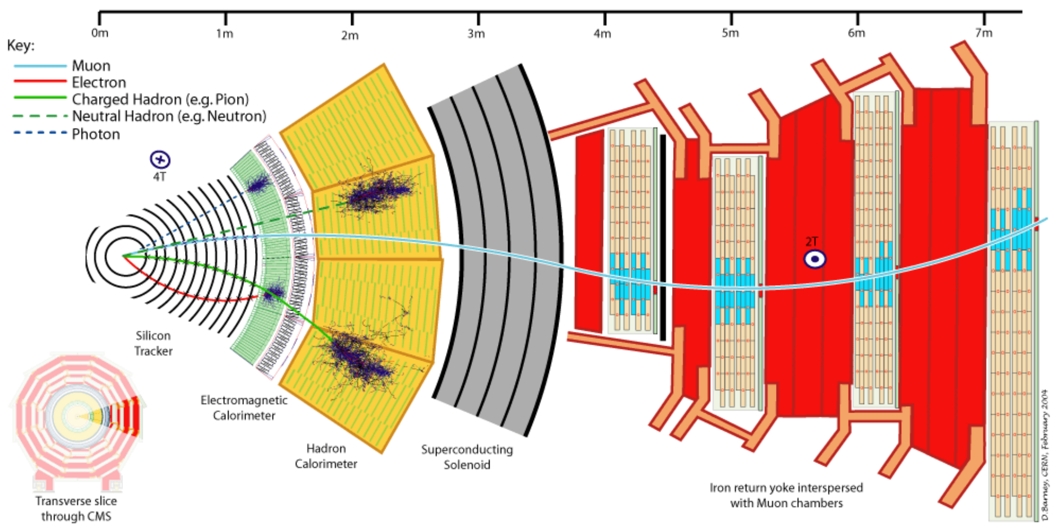

Figure 5.2: Transverse slice view of the CMS detector with each sub-detector shown and labeled. Particles of different types and their interactions with the various sub-detectors are shown as well. Reprinted from reference [19].

The inner-most detector is the Tracker with silicon pixel and strip detectors, providing high precision position and momentum measurements of charged particles. The Tracker allows for the reconstruction of charged particle tracks and interaction vertices near the interaction point.

Beyond the Tracker is the Electromagnetic Calorimeter (ECAL), a single-layer array of lead-tungstate ($PbWO_4$) crystals absorbing electromagnetic energy. The geometry of the crystals is designed to fully capture a single electromagnetic shower, providing excellent energy resolution for photons and electrons. The next layer outside of the ECAL is the Hadronic Calorimeter (HCAL), a sampling calorimeter using plastic scintillators and brass absorber layers. The HCAL provides instrumentation to the forward η regions up to $|\eta| < 5.2$ which gives good resolutions for missing transverse energy and energetic jets. The ECAL and HCAL compose the calorimetry of CMS.

The iron return yoke of the superconducting solenoid is interspersed within the Muon detector system, which consists of drift tubes (DTs), resistive plate capacitors (RPCs), and cathode strip chambers (CSCs). Combined with Tracker measurements, the Muon system is capable of reconstructing muons up to $p_{\mathrm{T}} \sim 1$ TeV. The return yoke also provides structural support for the Muon system.

The Following Section 5.1 briefly describes the individual sub-detectors, and Section 5.1.5 describes the trigger system. All technical information, unless otherwise cited, is taken from [20].

5.1 Sub-detectors

5.1.1 The Tracker

At the design luminosity of $10^{34}\mathrm{cm}^{-2}\mathrm{s}^{-1}$, the hit rate density a distance of 4 cm from the interaction point is an astounding 1 MHz/mm^2, necessitating a low occupancy, pixellated and radiation-hard design for the inner-most regions. For further distances of 20 cm $< r <$ 110 cm the hit rate density lowers to 3 – 60 kHz/mm^2, allowing for the use of silicon strip detectors. Tremendous radiation doses accumulate over time in the Tracker system, which causes increases leakage current in the electronics and can overheat the sensors. To combat this, the entire tracker is cooled to $-10°$ C. At this temperature, the silicon sensors have a signal-to-noise ratio of 10:1 and are expected to maintain that performance for 10 years.

The Tracker presents materials of 0.4–1.8 X_0 radiation lengths, giving high spatial resolutions but degrading the ECAL performance slightly, as approximately 50% of photons will convert into e^+e^- pairs in the large mass in front of ECAL.

The Silicon Pixel Detector

The pixel detector consists of 66 million 100×150 μm silicon pixels arranged in three barrel pixel (BPix) layers between $r = 4.4$ cm and $r = 10.2$ cm of the beam line and two forward pixel (FPix) layers, with pseudorapidity coverage up to $|\eta| < 2.5$. Due to the magnetic field of the solenoid, charge carriers in a single pixel experience a Lorentz drift in the ϕ direction and share particle hits with multiple neighboring pixels. This is used in the hit reconstruction software to achieve a 15–20 μm spatial resolution, which is comparable to the pixel pitch. Figure 5.3 shows the layout of each BPix and FPix module.

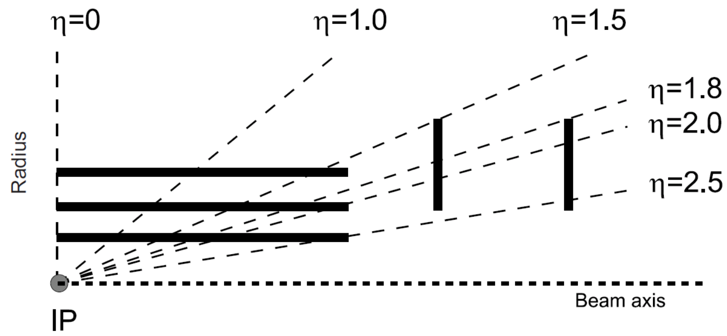

Figure 5.3: A view of one quarter of the pixel detector, with three barrel layers (FPix) and two endcap layers (BPix). Reprinted from Figure 3.6 of reference [20].

The Silicon Strip Detector

The silicon strip detector is made up of four components: the tracker inner barrel (TIB), tracker inner disks (TID), tracker outer barrel (TOB), and tracker endcaps (TEC) covering the radial region 61–108 cm from the interaction point. A total of 15,148 detector modules are distributed throughout, with a sensor thickness of 320 μm for the TIB, TID, and inner four layers of the TECs, and a thickness of 500 μm for the outer 3 TEC layers and TOB. A total of 24,244 sensors deliver an active area of 198 m^2 of active silicon detector. Figure 5.4 shows the layout of each component.

5.1.2 The Electromagnetic Calorimeter

The Electromagnetic Calorimeter (ECAL) is of critical importance to the analysis presented by this dissertation, as the high-precision measurement of photons and electrons is central to the rejection of Standard Model backgrounds. The ECAL is a single-layer crystal calorimeter in two sections, the barrel (EB) covering the region $|\eta| < 1.479$ and endcap (EE) covering $1.653 < |\eta| < 2.6$. A total of 75,848 lead-tungstate ($PbWO_4$) crystals make up the detector, with 61,200 in the barrel arranged in 20×85 grids in $\phi \times \eta$ supermodules (SM) and 7,324 crystals

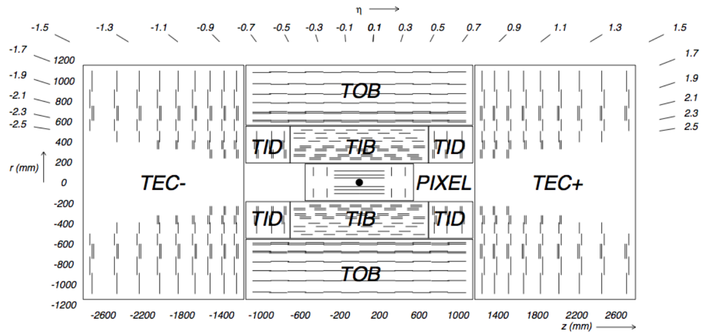

Figure 5.4: Cross-sectional view of the silicon strip detector, with the pixel detector shown. Reprinted from Figure 3.1 of reference [20].

in each endcap in 5×5 superclusters (SC). A two-layer preshower detector stands in front of the EE disks, each layer made of a lead absorber and a 1.9 mm pitch silicon strip detector as in the Tracker. The preshower is designed to provide additional spatial resolution for high energy neutral pions decaying to two closely-spaced photons that otherwise would be reconstructed as a single photon. Figure 5.5 shows the layout of the ECAL.

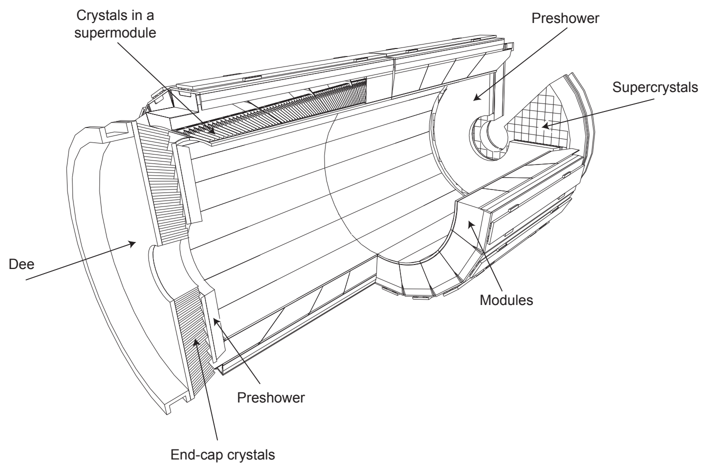

Figure 5.5: Layout of the Electromagnetic Calorimeter (ECAL). Reprinted from Figure 4.5 of reference [20].

Lead-tungstate was chosen as the crystal material for its excellent qualities and to achieve the desired energy resolution of 0.5%. $PbWO_4$ is a very dense material (8.28 g/cm^3) with a short radiation length ($X_0 = 0.89$ cm) and Molère radius (2.2 cm), so any photon or electron entering the front face of a crystal will electromagnetically shower within one and only one 23 cm long crystal (25.8 X_0). The crystals scintillate at 440 nm, the blue-green range of the visible spectrum, and ∼80% of the scintillation light is emitted within 25 ns. Figure 5.6 shows a simulated shower developing and contained with a crystal. The barrel crystals have a front face of 22×22 mm^2 1.29 m from the interaction point, and slightly taper over their length to a rear face of 26×26 mm^2. Endcap crystals are slightly larger with a front face of 28.62×28.62 mm^2 and a rear face of 30×30 mm^2.

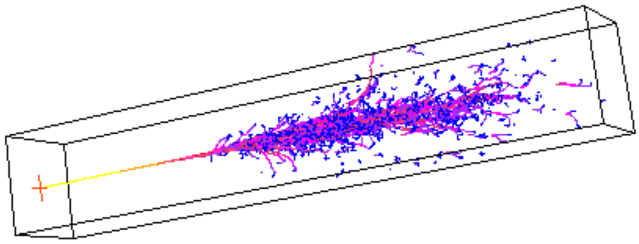

Figure 5.6: Simulated development of an electromagnetic shower initiated by an electron entering the center of an ECAL crystal. Reprinted from reference [21].

Scintillation light is collected at the rear of each crystal with a pair of avalanche photodiodes (APDs) in the EB or a single vacuum phototriode (VPTs) in the EE. Kept to a temperature of 18° C the electronics collect ∼4.5 photoelectrons per MeV of electromagnetic energy deposited in each crystal. Figure 5.7 shows the barrel and endcap sensors installed on a crystal.

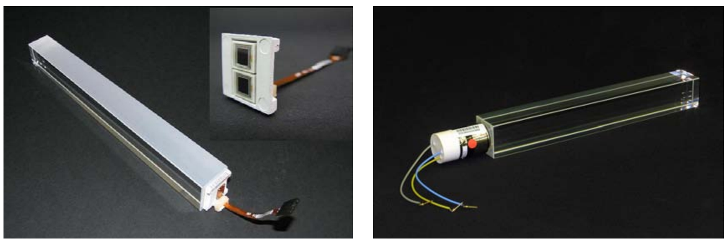

Figure 5.7: Left: EB crystal with attached APD. Right: EE crystal with attached VPT. Reprinted from Figure 4.2 of reference [20].

5.1.3 The Hadronic Calorimeter

The Hadronic Calorimeter (HCAL) consists of four parts: the barrel (HB), endcap (HE), outer calorimeter (HO), and forward calorimeter (HF). The HCAL is especially important in measuring hadronic jets and calculating missing transverse energy ($\not\!\!E_{\mathrm{T}}$) due to weakly interacting particles un-detected by instrumentation. The HB, HE, and HO provide coverage for $|\eta| < 3$ and the HF extends this to $|\eta| < 5.2$. A diagram of the different sections of the HCAL is shown in Figure 5.8.

The HB, HE, and HO systems are sampling calorimeters composed of alternating layers of brass absorber plates and plastic scintillator tiles. Hadrons passing through the absorber initiate hadronic showers which scintillate in the scintillator tiles, the light from which is read out by wavelength-shifting (WLS) fibers connected to a hybrid photodiode (HPD).

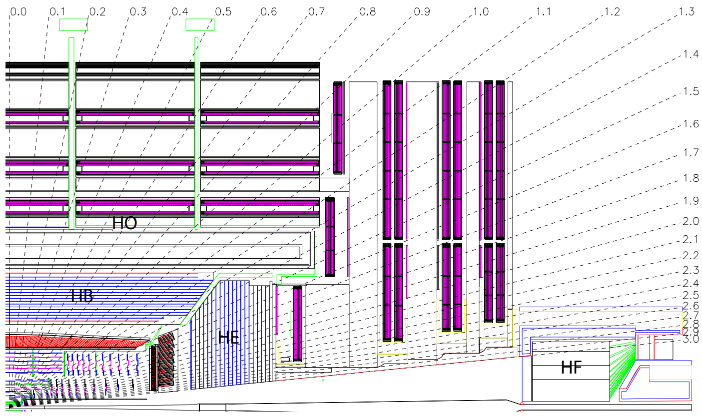

Figure 5.8: Longitudinal view of one quarter of the HCAL, with Muon chambers shown in purple. Reprinted from Figure 5.1 of reference [20].

The HF sits within the most extreme radiation environment near the beam line, and is designed differently as a 1.2 m thick by 1.7 m long steel absorber ring with radiation-hard quartz fibers installed within the steel parallel to the beam line. Hadronic showers initiated in the steel absorber emit Cerenkov light which is sampled by the quartz fibers. This light is transmitted via total internal reflection to a photomultiplier tube (PMT) and measured. As only relativistic particles emit Cerenkov radiation in the fibers, the HF is mostly sensitive to the electromagnetic component of hadronic showers.

5.1.4 Muon Chambers

The muon chambers sit the farthest from the interaction point of any sub-detector system, and are composed of three different technologies: drift tubes (DT) in the barrel section (MB), cathode strip chambers (CSCs) in the endcap section (ME), and resistive plate chambers (RPCs) in both sections providing an independent trigger with excellent timing resolution.

Each DT chamber consists of two $r \cdot \phi$ superlayers and one z SL (except for the outermost layer), containing four rows of drift tubes each. The drift cell is a hollow 13×42 mm tube with a 1.5 mm thick wall isolating it from neighboring cells. Each cell is filled with an 85% argon and 15% CO_2 gas mixture, and an anode wire running the length of the tube is held at 3600 V. The walls are held at either 1800 V or -1200 V. A muon passing through a drift tube ionizes gas atoms whose freed electrons are read out by the anode wire. The maximum drift time is 380 ns. Figure 5.9 shows a diagram of a drift tube with the electric field lines from ionizing muons.

Cathode strip chambers (CSCs) in the endcap provide additional spatial resolution for muons. These are multiwire proportional chambers comprised of 6 anode wire planes interleaved amongst 7 cathode panels. The volume of the chamber is filled with a 40% argon, 50% CO_2, and 10%

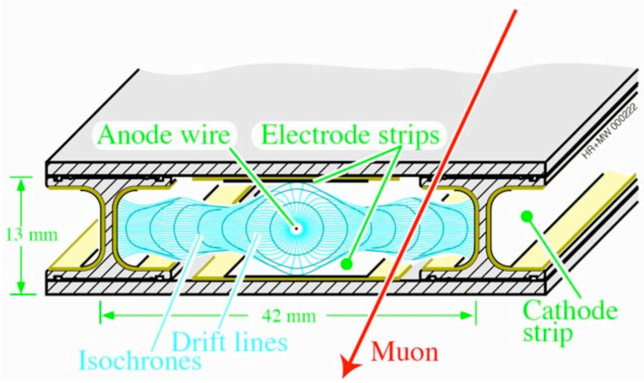

Figure 5.9: Electric field lines within a drift tube and the contours of equal drift time. Reprinted from Figure 7.5 of reference [20].

CF_4 gas mixture. The anode and cathodes are arranged perpendicular to one another, so a passing muon ionizing the gas provides a 2-dimensional measurement of the muon's position. Figure 5.10 shows a diagram of a CSC chamber.

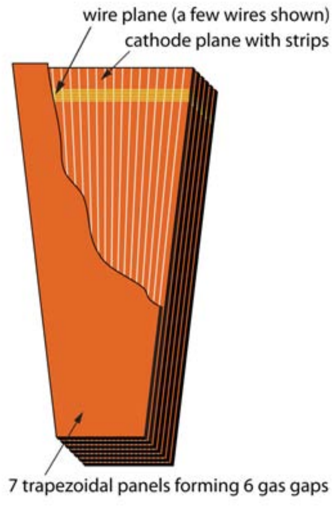

Figure 5.10: A CSC station with 7 layers and 6 interleaved gas chambers. Reprinted from Figure 7.49 of reference [20].

The resistive plate chambers (RPCs) supplement the timing resolution of DTs in the barrel and CSCs in the endcaps. They are made of two plates of highly resistive material with one held at positive voltage as the anode and the other at negative voltage as the cathode. The volume between the two plates is filled with a gas similar to the DTs. A passing muon ionizes this gas and freed electrons are accelerated towards the positive plate, creating an avalanche of secondary electrons. The drop in voltage observed on the anode provides a timing signal well within the 25 ns LHC bunch spacing, and is used in the triggering system. Figure 5.11 shows a diagram of an RPC.

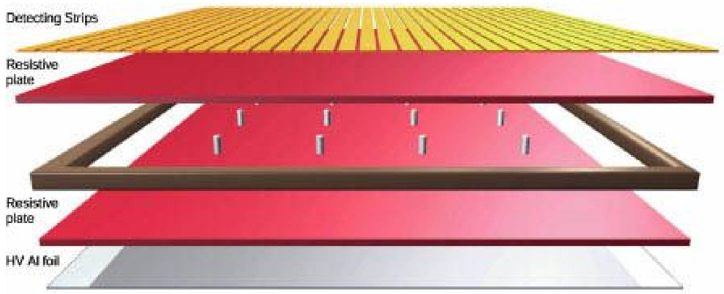

Figure 5.11: An exploded view of an RPC. Reprinted from reference [22].

5.1.5 Level-1 and High-Level Trigger

With a bunch spacing of 25 ns, the LHC delivers proton-proton collisions at a crossing frequency of 40 MHz. At the design luminosity, an expected 20 simultaneous collisions occur each beam crossing. Such a massive rate is impossible to store as data and processed for analysis, so a trigger system is used to reduce this rate and isolate only the physics processes of interest. This rate reduction is accomplished in two steps called the Level-1 (L1) Trigger and High-Level Trigger (HLT). The L1 trigger consists of custom-designed programmable electronics and hardware data buffers that perform basic physics calculations such as calorimeter energy deposits and muon hits to determine if an event should be kept for analysis. The design output rate limit from the L1 trigger is 100 kHz. The HLT is a software system implemented in a farm of $\sim$1000 computer processors and performs sophisticated reconstruction of tracks and energy deposits and can calculate complex algorithms to determine whether to keep an event. The HLT reduces the rate to a manageable 100 Hz.

Chapter 6

Object Reconstruction

The Particle Flow (PF) event reconstruction algorithm [106] combines the CMS sub-detectors to determine the energy, direction, and particle type of all stable particles in collision events, including electrons, muons, photons, charged hadrons, and neutral hadrons. The identified particles are used to reconstruct jets, calculate the missing transverse energy $\not{E}_{\mathrm{T}}$, tag b-jets, and calculate many physics quantities for analysis such as isolation energy sums of particles with respect to nearby particles.

Photons are reconstructed with excellent energy resolution by the essentially hermetic ECAL. The high granularity of the ECAL is a key feature to PF as it allows photons to be separated from charged particle energy deposits even in jets with a p_{T} of hundreds of GeV/c. By combining calorimeter information with the superior angular and position and energy resolution of the Tracker, PF is able to separate charged and neutral hadrons within high p_{T} jets, which would be otherwise impossible with the HCAL alone.

Electrons are reconstructed from a combination of tracks and energy deposits in the ECAL, including Bremsstrahlung photons radiated within the Tracker. Isolated muons are reconstructed, along with muons contained within jets, with a very high efficiency by combing muon chamber information with tracking.

6.1 Particle Flow Event Reconstruction

Most individual stable particles produced in pp collisions have low p_{T}, with constituent particles of 500 GeV/c jets being on the order of 10 GeV/c [106]. To identify interesting or exotic particles targeted by analyses, it is necessary for the reconstruction to identify as many of these low p_{T} particles as possible. The PF algorithm begins by reconstructing its fundamental 'elements', charged particle tracks and calorimeter energy clusters, and then topologically linking them in 'blocks'. Finally these blocks are interpreted as particles. The following section detail these steps.

6.1.1 Iterative Tracking

Approximately two-thirds of the energy of a jet is carried by charged hadrons, so the reconstruction of charged tracks is of key importance to the Particle Flow algorithm [106]. Tracking efficiency is desired to be as close to 100% as possible with as small a rate of fake tracks as possible. To achieve this, CMS uses an iterative tracking strategy known as the Combinatorial Track Finder (CTF) [107]. This strategy seeks to reduce the combinatorial complexity of associating hits to tracks by finding the easiest (highest p_{T}) tracks first and removing associated hits from future iterations. Each iteration proceeds as:

1. Tracks are seeded using initial track candidates using only a few (2 or 3) hits.
2. Seed trajectories are extrapolated along the expected flight paths of charged particles, associating additional hits to the track candidate.
3. A Kalman filter [108] is used to provide the best-fit values of the parameters of each seed trajectory.
4. Track candidates are ranked by their quality, and poor-quality tracks are rejected.

Six iterations are used, each with different starting seeds or kinematic requirements, and removing successfully found tracks for the future iterations to reduce complexity. The first iterations have very strict requirements to achieve a negligible fake rate. After the first and second iterations, the criteria are loosened to increase tracking efficiency. By the third iteration, more than 90% of tracks associated with charged hadrons are identified. The remaining iterations loosen the criteria on the track closest to the primary vertex. This allows for reconstruction of secondary charged particles from photon conversions and nuclear interactions in the tracker volume.

6.1.2 Calorimeter Clustering

The clustering algorithm in the calorimeters is designed to measure the energy and direction of stable neutral particles (such as photons and neutral hadrons), separate neutral particles from charged particle energy deposits, reconstruct and identify electrons and all associated Bremsstrahlung photons, and improve the energy resolution of charged hadrons for which the track quality is low (high p_{T} tracks) [106]. The algorithm is applied independently for the ECAL barrel, ECAL endcaps, HCAL barrel, and HCAL endcaps. No clustering algorithm is used in the HF, and each cell is used as a cluster in events.

The clustering algorithm proceeds as [106]:

1. 'Cluster seeds' are identified as local calorimeter cell maxima above a given threshold energy.

2. 'Topological clusters' are grown from seeds by aggregating cells adjacent to a cell already in the cluster, requiring a minimum threshold energy.

The energy thresholds represent 2σ deviations from the electronics noise, an amount ranging from 80–300 MeV in the ECAL (increasing towards the endcaps) and 800 MeV in the HCAL. Topological clusters give rise to 'Particle Flow clusters' as seeds in this same manner. A cell identified by two clusters has its energy shared amongst the clusters according to the distance from the cell to the center of each cluster. Cluster energies and positions are iteratively determined as new cells are added to the cluster.

6.1.3 Linking

Once clusters are formed in the calorimeters, they are associated with nearby tracks in the pixel and silicon tracker in a process known as 'linking' [106]. Single particles are formed out of 'blocks' of linked tracks and calorimeter clusters, without allowing for double-counted elements. Due to the high granularity of the calorimetry, a typical particle block will contain two to four elements.

The linking between tracks and clusters is performed by extrapolating the last-measured hit in the tracker to each calorimeter. Firstly to the ECAL preshower (PS), then to the ECAL to a depth of one interaction length, then finally to the HCAL to a depth of one interaction length. A track is linked to a cluster if its extrapolation falls within the cluster boundaries.

An HCAL cluster may be associated to many tracks, but each track may only be associated to one cluster whose center is the closest to the track. In the case of an electromagnetic fluctuation of a hadron shower, a single track can be associated to many clusters in the ECAL to avoid assigning those clusters to other tracks and double-counting the energy. For electrons, bremsstrahlung photon candidates are extrapolated to ECAL clusters as lines tangent to the electron track. ECAL clusters are linked to HCAL clusters if they fall within the boundary of an HCAL cluster, since the granularity of the ECAL is finer than the HCAL. Lastly, muon chambers are linked to the inner tracker via a χ^2 fit to muon trajectories traversing the entire detector.

6.2 Physics Object Reconstruction

Once tracks are formed and linked to calorimeter clusters, the Particle Flow algorithm can reconstruct physics objects. Muons are reconstructed first, followed by electrons and photons, and lastly charged and neutral hadrons. The hadrons are clustered together to build jets which can be tagged as hadronic τs or b-jets. After each object is reconstructed, its constituent PF blocks are removed from consideration so as not to double-count any energy contributions.

6.2.1 Muons

Muons are reconstructed first among Particle Flow particles. This begins by identifying 'global muons' as a muon having tracks in the pixel and strip trackers matched to tracks in the muon chambers. If the momentum measured in the muon chambers is consistent with the momentum measured by the tracker, it is labeled a 'Particle Flow muon'. A small amount of energy deposited by muons in the ECAL and HCAL must be removed along with the PF candidate blocks, which is measured to be 0.5 (3) GeV $\pm$100% in the ECAL (HCAL) in a study of cosmic rays.

Figures 6.1 and 6.2 showcase the excellent muon resolution and di-muon invariant mass reconstruction achieved by CMS.

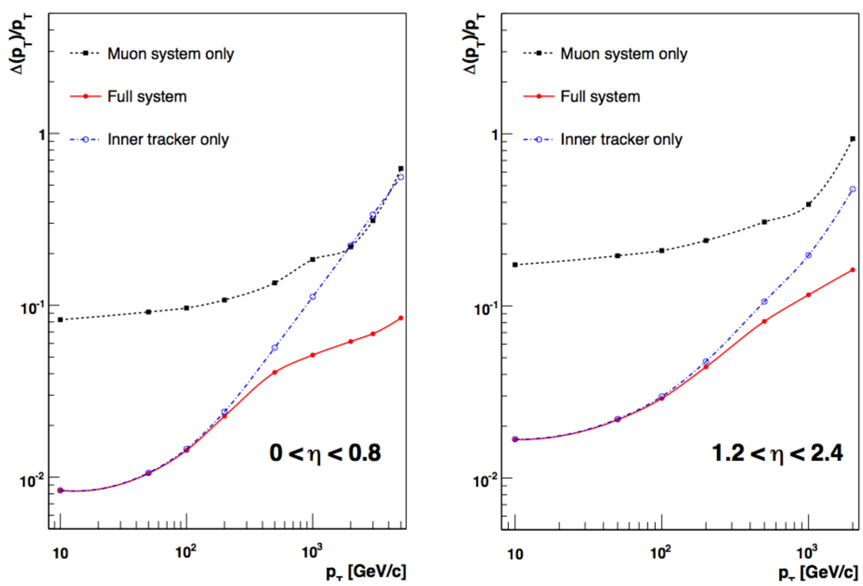

Figure 6.1: The muon p_{T} resolution as a function of the p_{T} using the muon system only, the inner tracking only, and both. Left: $|\eta| < 0.8$, right: $1.2 < |\eta| < 2.4$. Reprinted from Figure 1.2 of reference [20].

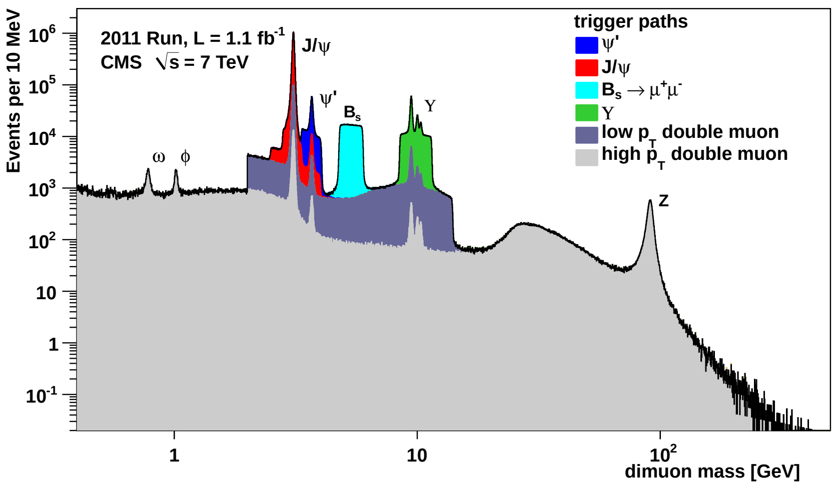

Figure 6.2: Invariant mass spectra of opposite-sign muon pairs for a superposition of various di-muon trigger paths. The data corresponds to an integrated luminosity of 1.1 fb^{-1} collected by early July 2011. Reprinted from reference [23].

6.2.2 Electrons

Electrons are reconstructed after muons [106]. Electron tracks tend to be shorter due to bremsstrahlung in the tracker volume, a highly non-linear process the Kalman filter of the track identification is not optimized for. Electron tracks are re-fitted with the Gaussian Sum Filter (GSF) [109] algorithm. The GSF algorithm accounts for the change in trajectory due to bremsstrahlung, extending the linking of ECAL clusters in the ϕ direction. PF blocks that have GSF tracks linked to ECAL clusters, including clusters from bremsstrahlung photons, and additionally linked to an HCAL cluster with much smaller energy than in the ECAL are identified as 'Particle Flow electron'. Figure 6.3 shows a selection of electron commissioning from 7 TeV data taken in 2010.

6.2.3 Charged Hadrons

Charged hadrons are identified after electrons [106]. Tighter criteria are applied for the remaining tracks, requiring the relative uncertainties of track momenta to be smaller than the energy uncertainty for charged hadrons in the calorimeters; only 0.2% of candidates are removed by this consideration, however these energies are still included in calorimeter clusters. A 'Particle Flow charged hadron' is identified when tracks are linked to both ECAL and HCAL clusters, and when the calorimeter energies and track momenta are compatible. A fit is performed on all of the tracks and HCAL clusters to determine the optimum momentum measurement. In the case where there is only one track, this fit reduces to a weighted average of the track and HCAL energies.

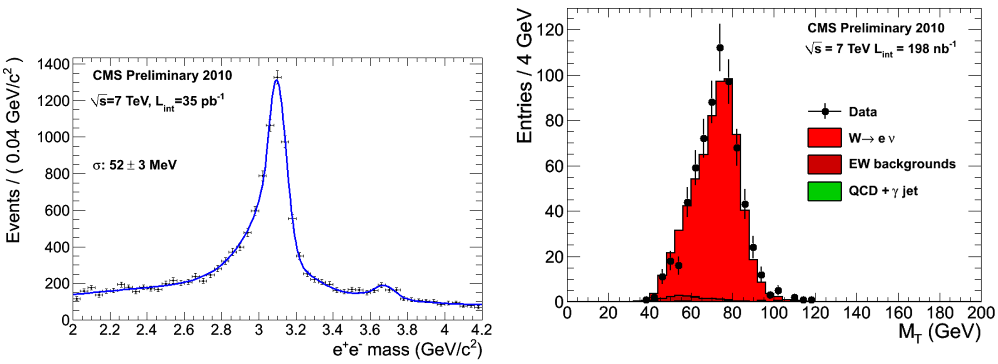

Figure 6.3: Selected electron reconstruction commission plots from 7 TeV data taken in 2010. Left: reconstructed $J\Psi$ mass from di-electron events; reprinted from reference [24]. Right: reconstructed transverse mass of W bosons in single electron events; reprinted from reference [25]. The asymmetric distributions here are described by the Crystal Ball function, a Gaussian core with a power law tail to low energies, accounting for energy losses due to final-state photon radiation.

6.2.4 Photons and Neutral Hadrons

The next step looks for ECAL and HCAL clusters that are not matched to any tracks, or where matched tracks have a much lower energy than the calorimeter cluster energies (lower than the calorimeter energy resolutions) [106]. In both cases, if the total energy excess in HCAL is greater than in ECAL, a 'Particle Flow photon' is reconstructed using the ECAL energy clusters and a 'Particle Flow neutral hadron' is reconstructed using the remaining HCAL energy. In the case where the ECAL energy is greater than the HCAL energy, both calorimeter clusters are used to reconstruct a PF photon. This is done because in jets nearly 25% of the energy is carried by photons while only neutral hadrons deposit only $\sim$3% in the ECAL.

6.2.5 Jets

Once photons and hadrons have been formed, jets can be reconstructed by clustering these objects together using the anti-k_T algorithm [26]. This algorithm is based on particles' momentum-weighted spatial separation from one another, defined as:

$$d_{ij} = \min\left(\frac{1}{p_{iT}^2}, \frac{1}{p_{jT}^2}\right)\frac{\Delta_{ij}^2}{R^2} \tag{6.1}$$

where $\Delta_{ij}^2 = (y_i - y_j)^2 + (\phi_i - \phi_j)^2$ is the distance in the rapidity-ϕ plane and R is the user-defined distance parameter in that y–ϕ plane. In the ideal case of a single isolated jet, the anti-k_T algorithm clusters particles within a circle of radius R.

The anti-k_T algorithm calculates d_{ij} for all PF candidates and combines the two candidates with the minimum d_{ij} into a single object. This is repeated until the minimum pair-wise $d_{ij} >$

$\frac{1}{p_{iT}^2}$ for all remaining combinations. This parameter is lower for pairs of low-p_{T} objects than for equally-separated high-p_{T} objects, and thus the algorithm clusters softer particles around harder particles before clustering around themselves. If no hard particles are present, the algorithm simply clusters soft particles within a circle of radius R.

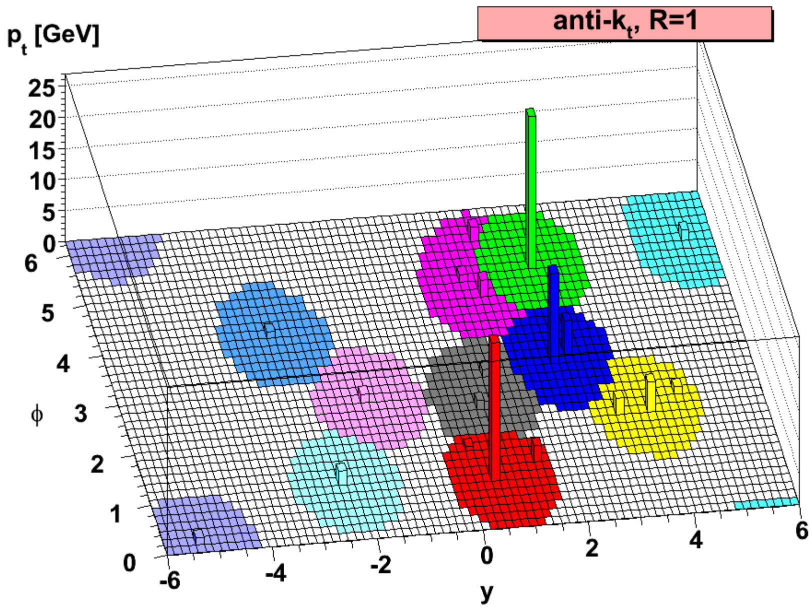

Figure 6.4: An example of the resulting jets from applying the anti-k_T algorithm with distance parameter $R = 1$. Reprinted from Figure 1 of reference [26].

This algorithm tends to cluster high-p_{T} objects into circular jets, however more irregularly shaped jets can be formed by soft clusters intersecting harder clusters. An example of this is shown in Figure 6.4 at $(\phi, y) = (5, 2)$.

b-Tagging

Jets originating from b-quarks are uniquely distinguishable from other quarks or gluon jets due to the relatively long lifetimes of B-hadrons. The observable flight distance within the inner tracker gives rise to secondary vertices. b-Jets tend to have higher p_{T} and can decay semi-leptonically, with soft non-prompt muons being a useful tool to identify to tag b-jets. Combining the kinematics of jets with the impact parameters of secondary vertices allows for the discrimination of b-jets against light-flavor jets, a process described in detail in Section 7.2.6. Figure 6.5 highlights the impact parameter d_0 of secondary vertices created by non-prompt decays.

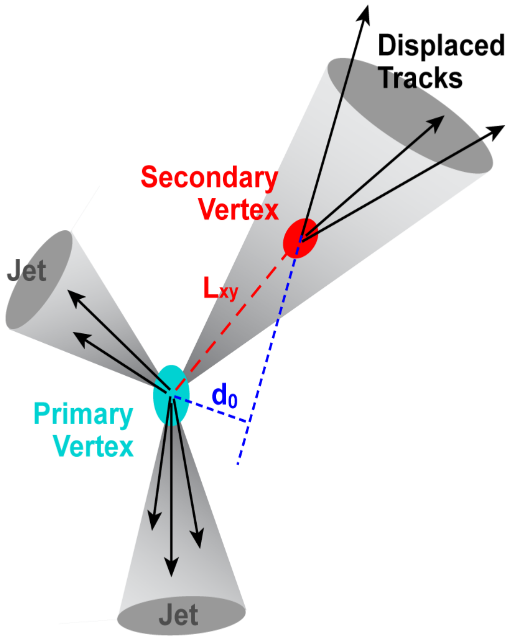

Figure 6.5: A b-meson travels a short distance L_{xy} before weakly decaying, creating a secondary vertex seen in the Tracker. The impact parameter d_0 is very important in discriminating b-jets from lighter flavor jets. Reprinted from reference [27].

6.2.6 Missing Transverse Energy

After all Particle Flow candidates are identified, CMS can utilize its hermetic design to measure any momentum imbalances from weakly-interacting particles such as neutrinos. The near-4π coverage ensures that nearly all visible particles would be reconstructed by the detector. Since the proton beams collide with zero transverse component, the conservation of momentum allows the reconstruction of any un-observed particles passing through the detector.

The missing transverse momentum ($\not{p}_{\mathrm{T}}$) and energy ($\not{E}_{\mathrm{T}}$) are defined as sums over all Particle Flow particles:

$$\not{p}_{\mathrm{T}} = -\sum_{\mathrm{PF}} \vec{p}_{T\,i} \tag{6.2}$$

$$\not{E}_{\mathrm{T}} = |\not{p}_{\mathrm{T}}| \tag{6.3}$$

The $\not{E}_{\mathrm{T}}$ reconstruction was commissioned and calibrated in 2010 with 7 TeV data using minimum-bias and QCD multi-jet events with no true $\not{E}_{\mathrm{T}}$ [110]. An extensive measurement of the $\not{E}_{\mathrm{T}}$ was performed in 8 TeV data [111], providing precise calibration for the analysis presented by this thesis in the following section.

Chapter 7

Data Analysis

The production and decay of stop squark pairs with a bino-like NLSP would be observable as an excess of $t\bar{t}+\gamma\gamma$ events with large $E_{\mathrm{T}}^{\mathrm{miss}}$ over expected Standard Model processes, the most significant of which being $t\bar{t}+jets$ and $t\bar{t}+\gamma(\gamma)$. The strategy of this search is to select events consistent with the decay of a $t\bar{t}$ pair and containing additional photons. Essentially 100% of top quarks decay to a W boson and a b-quark, of which the W boson decays further to either a charged lepton and a neutrino or a pair of quarks. The decays of a $t\bar{t}$ pair then span the range of combinations of two W boson decays:

- hadronic – each W decays to quarks ($t\bar{t} \to bbjjjj$),
- di-leptonic – each W decays leptonically ($t\bar{t} \to bb\ell\ell\nu\nu$),
- semi-leptonic – one W decays leptonically ($t\bar{t} \to bbjj\ell\nu$).

This analysis is performed in the semi-leptonic channel (e, μ) to avoid the large QCD multijet and $\gamma+jets$ backgrounds in the hadronic channel and the low branching ratio of the di-leptonic channel. The final state of interest for stop squark pair decays in this channel is $\ell bbjj\gamma\gamma+E_{\mathrm{T}}^{\mathrm{miss}}$, with ℓ being either an electron or a muon and the $E_{\mathrm{T}}^{\mathrm{miss}}$ comprised of a neutrino (and two gravitinos in the case of GMSB). To allow for losses of jets and photons due to fiducial detector acceptances, as well as reconstruction and btagging inefficiencies, events are only required to have at least three jets and one or more btags. Similarly, since only photons in the ECAL barrel fiducial region are considered, two signal categories are defined for events with one photon and with two or more photons. This categorization additionally provides information about the distribution of the photon multiplicity of the observed events, which is fundamentally different between background and the decay of heavy binos.

The results of this analysis are interpreted by comparing the distribution of $E_{\mathrm{T}}^{\mathrm{miss}}$ in data in the signal regions against the expected SM backgrounds as simulated in Monte Carlo (MC), and as such the principle concern is the modeling of the $E_{\mathrm{T}}^{\mathrm{miss}}$ in the simulated background events. The performance of this distribution is affected by two issues: (i) the relative normalization of different backgrounds having different shapes in $E_{\mathrm{T}}^{\mathrm{miss}}$, the adjustment of which would alter the shape of their sum, and (ii) the underlying $E_{\mathrm{T}}^{\mathrm{miss}}$ resolution in Monte Carlo compared to that in data.

Mismodeling of simulated backgrounds in MC can lead to an incorrect calculation of cross section normalizations, disturbing the summed shape of $E_{\mathrm{T}}^{\mathrm{miss}}$. In MadGraph the b-quark content of radiated jets is observed to be too low, resulting in an underestimation of backgrounds such as $W/Z + jets$ when requiring btagged jets. The misidentification rate of electrons as photons and the purity of selected photons are observed to be different in data than in MC as well. These mismodelings are corrected by deriving scale factors from signal-limited control regions using template fits in key kinematic distributions.

The purity of photons in the signal regions, or the amount of real prompt photons versus jets misidentified as photons (non-prompt), is closely examined for any effect on the overall $E_{\mathrm{T}}^{\mathrm{miss}}$ distribution shape. Without a precise simulation of $t\bar{t}+\gamma\gamma$ events, the analysis must avoid dependence on the absolute prediction of the rate of prompt photons or the misidentification rate of jets as photons; this is especially true when requiring two photons. Should the shape of $E_{\mathrm{T}}^{\mathrm{miss}}$ be significantly different between prompt and non-prompt photons, a more detailed measurement of their relative rates (purity) is required. To investigate this, the simulated photon purity is adjusted to the purity observed in data. The effect on the $E_{\mathrm{T}}^{\mathrm{miss}}$ shape of this adjustment is seen to be negligible, allowing the signal region requiring two photons to not depend on its true photon content. To further reduce dependence on the jet misidentification rate and the $t\bar{t}+\gamma\gamma$ production rate, the $t\bar{t}+jets$ and $t\bar{t}+\gamma(\gamma)$ backgrounds are allowed to float freely in the upper limit calculation, which causes the evaluation of the results to be purely a shape comparison. In the final limit determination, the maximum-likelihood value of these float values are in the range of 0–11% upwards of the central values, and do not correlate strongly with signal.

The underlying $E_{\mathrm{T}}^{\mathrm{miss}}$ resolution in MC is tested by comparing it to the observed data in control regions containing 'fake' photons, an object defined similarly to a photon except for the inversion of the cuts on its charged hadron isolation sum or its $\sigma_{i\eta i\eta}$. By leaving the H/E requirement unchanged and requiring fakes to fail the cuts (i.e. pass the *anti-cuts*) designed to distinguish photons from jets, the $t\bar{t}+jets$ background of these fake control regions is greatly enhanced while retaining the EM energy scale and resolution of photons expected in the signal regions. In this way the control regions offer a sample of data events similar to those in the control region but without considerable signal presence, and the performance of the MC simulation of $E_{\mathrm{T}}^{\mathrm{miss}}$ is taken as a comparison to this data.

The following sections detail the analysis procedure and results. Section 7.1 lists the samples of events used and describes the simulation of signal and background events. Section 7.2 enumerates the event selection criteria. Section 7.3 describes the derivation of scale factors for several background processes, as well as the control region observation of $E_{\mathrm{T}}^{\mathrm{miss}}$ performance. Finally Section 7.4 discusses systematic uncertainties, and the results are shown in Section 7.5.

7.1 Data and Simulated Samples

7.1.1 Data Samples

The data represented by this search corresponds to the full 2012 CMS dataset of ~19.7 fb^{-1} at $\sqrt{s} = 8\,\mathrm{TeV}$. The datasets used, listed in Table 7.1, were collected based on single electron and muon triggers and reconstructed with the latest detector conditions available ('22Jan2013'). The luminosities are calculated from the Forward HCAL (HF) calculation, having a 2.6% uncertainty.

Dataset	Run Range	Integrated Luminosity (fb^{-1})
Total SingleMu 22Jan2013-v1	**190456–208686**	**19.7**
Run2012A	190456–193621	0.89
Run2012B	193833–196531	4.41
Run2012C	198022–203742	7.15
Run2012D	203777–208686	7.29
Total SingleElectron 22Jan2013-v1	190456–208686	**19.7**
Run2012A	190456–193621	0.89
Run2012B	193833–196531	4.41
Run2012C	198022–203742	7.15
Run2012D	203777–208686	7.29

Table 7.1: List of datasets used in this analysis.

7.1.2 Background Samples

To estimate the expected $\not\!\!E_{\mathrm{T}}$ from Standard Model backgrounds, this analysis uses Monte Carlo simulation for all processes. Most samples are generated with the MadGraph [112] tree-level matrix element generator matched to pythia [113] for the parton shower. Single top quark events are generated with the NLO generator powheg [114] combined with pythia, modeling the decay of tau leptons with tauola [115]. The precise set of parameters used for the underlying event in these generators, referred to as a 'tune', is the Z2 tune [116].

In the case of $t\bar{t}+\gamma$, with possibly large angles of radiation and photon energies, a more robust simulation than typical MadGraph or is required. Simulation of $t\bar{t}+\gamma$ is generated at leading order with MadGraph in a direct $2 \to 7$ configuration, $pp \to bbjj\ell\nu\gamma$ (or any other WW final state). This allows for large radiation angles and energies while accounting for interference effects of photon radiation from W bosons and b quarks. Photons from QED showering are also in the inclusive $t\bar{t}+jets$ samples, albeit with far lower accuracy, so it is necessary to remove such events falling into the defined phase space of the $t\bar{t}+\gamma$ sample to prevent double-counting. The $t\bar{t}+\gamma$ phase space is defined by generator-level cuts on the parton level:

- $p_{\mathrm{T}}(\gamma_{gen}) > 13\,\mathrm{GeV}$
- $\Delta R(\gamma_{gen}, \text{other gen}) > 0.3$

A plot of this phase space for $t\bar{t}+jets$ and $t\bar{t}+\gamma$ samples is shown in Figure 7.1. The removal of overlapping $t\bar{t}+jets$ events rejects ~0.55% of $t\bar{t}+jets$ events passing the pre-selection, and rejects ~16% of $t\bar{t}+jets$ events passing the pre-selection and having at least one selected photon.

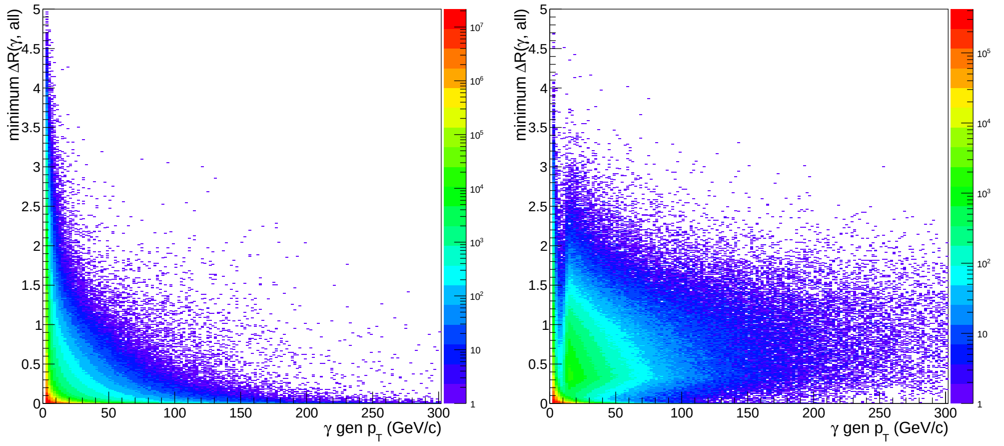

Figure 7.1: Generated photon phase space for $t\bar{t}+jets$ (left) and $t\bar{t}+\gamma$ (right) MC. To eliminate double counting of generated photons in the $t\bar{t}+jets$ sample falling in the defined $t\bar{t}+\gamma$ sample phase space, such overlapping events are rejected. The remaining photons in the $t\bar{t}+jets$ sample are low-p_{T} or close to other objects, largely composed of soft final state radiation.

The cross sections are calculated at at least Next-to-Leading Order (NLO) using the CTEQ6M PDF set using a number of different tools including MCFM 6.6, FEWZ 3.1, HATHOR v2.1 [117, 118], and TOP++ v2.0 [119]. Generated events are reconstructed using the same CMSSW environment as used for data events. Table 7.2 lists the MC samples used and their cross sections.

7.1.3 Signal Samples

To simulate signal events from the wide range of parameters available to GMSB models, it is necessary to simplify the available phase space in a scheme referred to as General Gauge Mediation (GGM). GGM forces the production of final state behaviors most useful to interpreting the results of analyses by defining mass spectra with a relatively high 'decoupling mass' to kinematically suppress the production of irrelevant particles [1]. For the interpretation of the

[1]In comparison, many CMS SUSY searches interpret search results against Simplified Model Spectra (SMS) schemes where the final state of interest is created by forcing decay branching ratios to 100% or 0% as desired. With appropriately high decoupling masses, GGM and SMS interpretations are equivalent. This analysis uses GGM for historical reasons of previous GMSB searches.

Sample	Dataset	σ (pb)
$t\bar{t} + jets$	MadGraph	
$\rightarrow$ jets	Hadronic	112.33
$\rightarrow \ell\nu$ + 4 jets	Semi-leptonic	107.66
$\rightarrow \ell\nu\ell\nu$ + 2 jets	Fully leptonic	25.81
$t\bar{t} + \gamma$	MadGraph ($2 \rightarrow 7$ LO)	2.87
$t\bar{t} + W$	MadGraph	0.232
$t\bar{t} + Z$	MadGraph	0.206
$W + jets \rightarrow \ell\nu$	MadGraph	
	W + 3 jets	626.3
	W + $\geq$ 4 jets	258.3
$Z/\gamma^* + jets \rightarrow \ell\ell$	MadGraph, $M_{\ell\ell} > 50\,\mathrm{GeV}/c^2$	
	Z/γ^* + 1 jet	672.1
	Z/γ^* + 2 jets	216.8
	Z/γ^* + 3 jets	66.6
	Z/γ^* + $\geq$ 4 jets	27.6
Single t	powheg, tauola	
	s-channel	3.79
	t-channel	56.4
	tW-channel	11.1
Single $\bar{t}$	powheg, tauola	
	s-channel	1.76
	t-channel	30.7
	tW-channel	11.1
WW	pythia	57.11
WZ	pythia	32.32
ZZ	pythia	8.26
$V\gamma$	MadGraph, tauola	
	$Z\gamma \rightarrow \ell\ell\gamma$	159.1
	$W\gamma \rightarrow \ell\nu\gamma$	553.9

Table 7.2: List of background MC datasets and cross sections used for normalization.

results of this analysis, M_3 is decoupled at 5 TeV, and M_2 and all sfermion masses excepting M_{tR} are decoupled at 4 TeV, making for the production of stop squarks decaying to very bino-like neutralino NLSPs which decay primarily to a gravitino and a photon. A range of stop squark and bino masses are generated from 150 GeV to nearly 1 TeV. To retain a bino-like NLSP and on-shell W bosons from the decay of stop squarks, the stop mass is restricted to $m_{\tilde{t}} > m_W + m_b + m_{\tilde{\chi}_1^0}$.

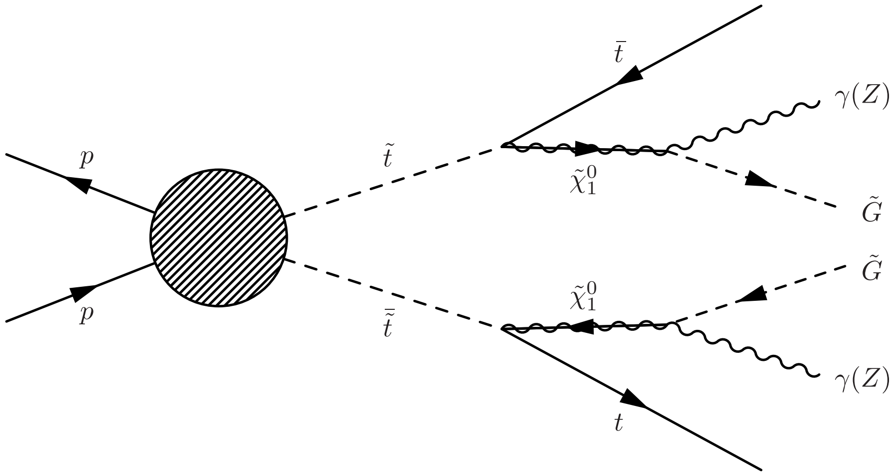

Figure 7.2: Production of stop pairs decaying to bino-like neutralinos. To simplify the simulation of such events to the final state of interest, irrelevant particles are suppressed by decoupling SUSY mass scales to very high values.

To facilitate the computing- and time-intensive simulation of a large number of stop and bino mass models, Fast Simulation (FastSim) [120] is employed rather than the typical GEANT4-based or 'Full Simulation' simulation. By using a simplified detector geometry, assuming calorimeter homogeneity, and parameterizing hadron and muon energy responses based on FullSim response, FastSim achieves a $\sim$100-fold improvement in event generation times while still agreeing with FullSim on the percent level or below.

GMSB simulation and reconstruction is performed using PYTHIA 6 and FastSim using a pileup scenario of the expected 2012 running conditions. Cross sections for pair-production of stops are calculated with NLL-fast [121] using NLO results from PROSPINO [122], with PDF and scale uncertainties following the PDF4LHC recommendations [123].

7.1.4 MC Pileup Reweighting

With the large instantaneous luminosities of the LHC, a single recorded event will contain several overlapping proton collisions, termed 'pileup' events. Pileup interactions generally produce a large number of low-energy particles, resulting in many charged tracks and calorimeter deposits not associated with the objects of interest to analyses. These tracks and energy deposits degrade the quality of reconstruction and selection by providing what amounts to physical noise in the

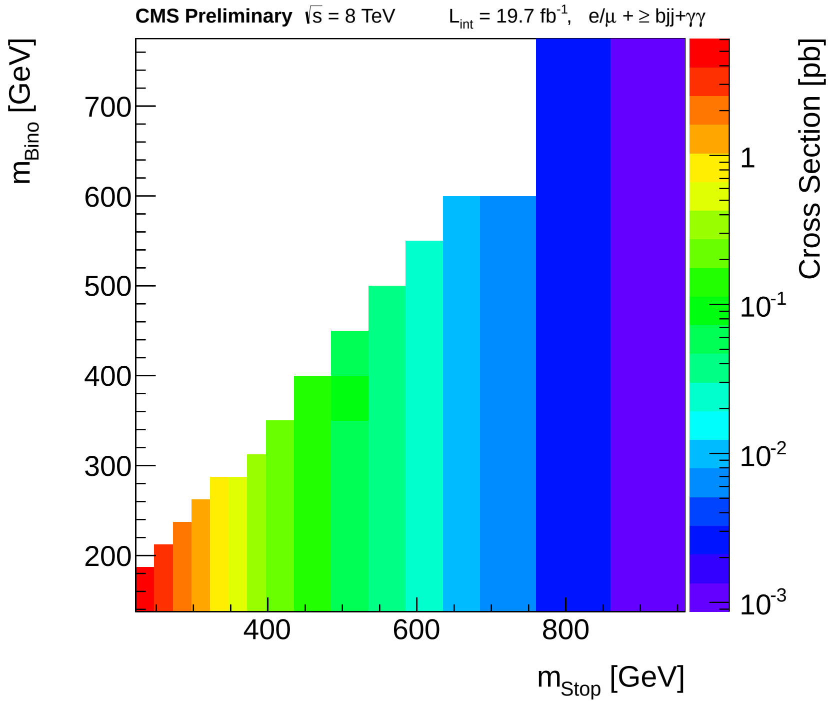

Figure 7.3: NLO cross sections for stop pair-production for the range of stop and bino masses simulated. The cross section is a function only of the stop mass.

detector, effecting for example particle isolation sums and jet energy resolution. When simulating Monte Carlo events like background and GMSB signal, it is important to simulate the pileup environment properly to describe its effect on reconstruction as in the data.

In data, the distribution of the number of pileup interactions depends on the instantaneous luminosity of each bunch pair, a measured quantity, and the total inelastic cross section ($\sigma_{inelastic}$) of the proton. A value of $\sigma_{inelastic} = 69.4mb$ is found to describe the data very well, estimated with a systematic uncertainty of $\pm5\%$. In MC simulation, the pileup distribution must be chosen a-priori. Some of the samples used in this analysis were generated well after 2012 data-taking had been completed, meaning that this choice could be the observed data distribution. However other samples were generated while the LHC luminosities were still increasing and the total data distribution was not yet known; the choice for these samples was taken as an average number of pileup events being conservatively large to allow for reweighting to a smaller average number. To match the pileup distribution in data, each MC sample used in this analysis is reweighted by the ratio of the distribution of the number of pileup interactions in data to that of the sample. Figure 7.4 shows the number of reconstructed vertices in data and in MC, both before and after this reweighting is applied. The reweighting procedure gives a greatly improved agreement between data and MC.

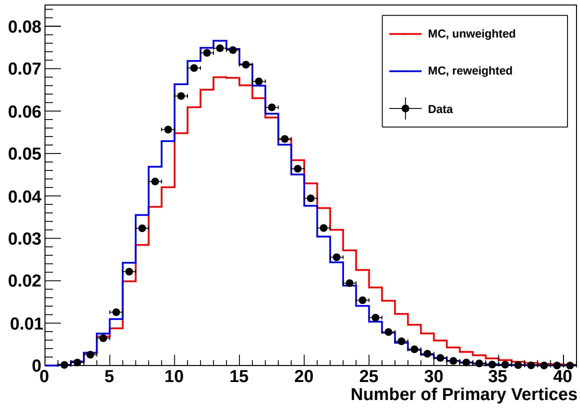

Figure 7.4: Comparison of the number of reconstructed vertices for data (black) and all background samples before (red) and after (blue) pileup reweighting. After reweighting for pileup, the MC describes the data well.

7.1.5 Top PT Reweighting

It has generally been observed in top quark measurements at CMS that the leptons and jets produced by top decays exhibit a softer p_{T} spectrum than predicted by Monte Carlo simulations. Investigations by CMS find this to be caused by the differential cross section in top quark p_{T} being softer than in existing $t\bar{t}$ MC, and find that the data compares more favorably to calculations done at approximate NNLO accuracy [124, 125].

The measured differential cross sections in H_{T}, the scalar sum of jet p_{T} in each event, allows for the determination of a correction procedure [126]. For the $t\bar{t}$ inclusive background samples, events are reweighted as a function of the parton truth values of generated top and anti-top p_{T}::

$$w = \sqrt{SF_{top} \cdot SF_{anti-top}} \tag{7.1}$$

where

$$SF(p_{\mathrm{T}}) \equiv e^{a+b\cdot p_{\mathrm{T}}} \tag{7.2}$$

where the values of a and b are given in Table 7.3.

$t\bar{t}$ decay channel	a	b
all combined	0.156	-0.00137
e/μ + jets	0.159	-0.00141
ee/eμ/$\mu\mu$	0.148	-0.00129

Table 7.3: Top p_{T} reweighting constants determined from the differential $t\bar{t}$ cross section in H_{T}.

A systematic uncertainty for this reweighting is provided by reweighting $t\bar{t}$ samples twice (i.e. by the weights squared) and by not reweighting at all.

7.2 Event Selection

This section defines the selection requirements of individual objects and events. Leptons are defined in two categories, tight and loose, and each event is required to have exactly one tight lepton (e, μ), rejecting additional loose leptons. As photons are not required by the High-Level Trigger (HLT), events are 'pre-selected' inclusive of the number of photons ($N_\gamma \geq 0$) and later separated by the number of photons.

7.2.1 Event Quality

For data and MC events, each event is required to pass several cuts designed to remove non-physical and non-collision events such as spurious instrumental noise or beam backgrounds. Firstly all events must have at least one primary vertex (PV) passing the following quality cuts:

- In the vertex fit, the number of degrees of freedom nDOF > 4
- $|z| < 24$ cm
- $|\rho| < 2$ cm
- Not identified as 'fake':
  - $\chi^2_{\text{vertex fit}} \neq 0$,
  - $\text{nDOF}_{\text{vertex fit}} \neq 0$,
  - The number of tracks associated to the vertex $\neq 0$.

As a search for $E_{\mathrm{T}}^{\text{miss}}$, it is of critical importance that events from known detector anomalies creating false $E_{\mathrm{T}}^{\text{miss}}$ [127] be rejected. Events must pass each of the following filters:

- CSC tight beam halo filter – secondary particles are produced in showers initiated by collisions of the beam with residual gas inside the LHC vacuum chamber or by interactions of the beam halo with limiting aperatures. Charged particles are also deflected by the magnetic field of the beam optics.
- HBHE noise filter with isolated noise rejection – instrumentation issues associated with HCAL electronics in the barrel and endcap regions can produce anomalous noise extending to TeV energies.

- HCAL laser filter – a small number of events contain the HCAL calibration laser erroneously firing during collision bunch-crossings.

- ECAL dead cell trigger primitive filter – roughly 1% of crystals in the ECAL are masked in the reconstruction due to being noisy. Some of these masked crystals are in regions with dead readout electronics, leading to the possibility that significant energy may be lost in these masked, dead cells.

- Tracking failure filter – track reconstruction may fail in some cases, giving events with large calorimeter deposits but very few tracks. This can be caused by having too-large a number of calorimeter clusters failing the tracking algorithm, or by collisions not in the interaction point but in a satellite RF bucket displaced by 75 cm (2.5 ns).

- Bad EE supercrystal filter – two particular 5x5 crystal regions in the ECAL EE give anomalously high energies from spurious high amplitude electronics pulses.

- ECAL laser correction filter – a small number of ECAL crystals receive unphysically large transparency corrections in the laser calibration.

- Tracking POG filters – some events are affected by a partly aborted track reconstruction and coherent noise in the Strip Tracker.

7.2.2 HLT

Events in data and MC are required to pass one of several High Level Triggers (HLT) listed in Table 7.4. Muon+jet events must pass the SingleMu trigger, and electron+jet events must pass the SingleEle trigger. To collect additional poorly isolated muon events to estimate the QCD background in muon+jet events, events are allowed to pass an OR of two SingleMu triggers, listed in Table 7.5.

Dataset	Trigger name
SingleEle	HLT_Ele27_WP80_v*
SingleMu	HLT_IsoMu24_eta2p1_v*

Table 7.4: List of triggers used to collect signal candidates.

Dataset	Trigger name
SingleMu (QCD)	HLT_IsoMu24_eta2p1_v* HLT_Mu24_eta2p1_v*

Table 7.5: List of triggers used to collect QCD candidates in muon+jet data.

For the electron trigger, the name HLT_Ele27_WP80 signifies the requirement of $p_{\mathrm{T}} > 27\,\mathrm{GeV}/c$ and that the candidate electron passes several loose cuts, designed as a 'working point'

(WP) of roughly 80% efficiency. WP80 applies loose cuts on tracker-based isolation energy sums, track impact parameters, the ratio of HCAL energy to ECAL energy (H/E), and track compatibility. Many of these quantities are used in the off-line electron selection, described below in Section 7.2.4.

For the muon trigger, the names HLT_IsoMu24_eta2p1 and HLT_Mu24_eta2p1 signify the requirement of $p_{\mathrm{T}} > 24\,\mathrm{GeV}/c$, and $|\eta| < 2.1$. The 'Iso' refers to the requirement of the Particle Flow-based isolation sum within a cone of radius $\Delta R = 0.5$ being less than 15% of the reconstructed muon p_{T}.

7.2.3 Muon Selection

Muons are selected from the collection of reconstructed Particle Flow muons in both tight and loose categorizations, defined in Table 7.6.

Cuts	Tight μ	Loose μ
p_T	> 30 GeV/c	> 10 GeV/c
PFRelIso (0.4)	< 0.12	< 0.2
$\lvert\eta\rvert$	< 2.1	< 2.5
ID	Global Muon	Global Muon or Tracker Muon
ID	PFMuon	PFMuon
N_{layers} (tracker)	> 5	
X^2/N_{DOF} of track fit	< 10	
N_{hits} (pixel)	> 0	
N_{hits} (muon chamber)	> 0	
$N_{segments}(\mu)$	> 1	
$\lvert d0(PV)\rvert$	< 0.2 cm	
$\lvert dZ(PV)\rvert$	< 0.5 cm	

Table 7.6: Tight and loose muon definitions.

The qualities required of candidate muons are:

- p_{T} – the transverse momentum of the reconstructed muon.
- PFRelIso (0.4) – the relative isolation, or the ratio of the total candidate-removed energy deposits within a cone of size $\Delta R = 0.4$ to the candidate muon energy.
- $|\eta|$ – the absolute value of the pseudorapidity of the reconstructed muon.
- ID – muons can be reconstructed by the Particle Flow algorithm (PFMuon), or with a χ^2 fit to tracks from the tracker only (Tracker Muon), or with a χ^2 fit to tracks from both the tracker and muon chambers (Global Muon).
- N_{layers} (tracker) – the number of layers in the tracker with hits used in the muon track reconstruction.

- χ^2/N_{DOF} of track fit – the reduced chi-squared of the track fit.
- N_{layers} (pixel) – the number of layers in the inner pixel detector with hits used in the muon track reconstruction.
- N_{hits} (muon chamber) – the number of hits in the muon chambers used in the muon track reconstruction.
- $N_{segments}(\mu)$ – the number of segments of the muon chambers used in the muon track reconstruction.
- $|d_0(PV)|$ – the transverse distance of the extrapolated muon track to the primary vertex, calculated from the beamspot.
- $|d_z(PV)|$ – the longitudinal distance of the extrapolated muon track to the primary vertex, calculated from the beamspot.

7.2.4 Electron Selection

Like muons, electrons are selected from the collection of reconstructed Particle Flow electrons in both tight and loose categorizations, defined in Table 7.7.

Cuts	Tight e	Loose e
p_T	> 30 GeV/c	> 10 GeV/c
PFRelIso (0.3)	< 0.1	< 0.2
$\|\eta\|$	< 2.5 not $(1.4442 < \|\eta\| < 1.566)$	< 2.5 not $(1.4442 < \|\eta\| < 1.566)$
ID	MVA ID("mvaTrigV0") > 0.5	MVA ID("mvaTrigV0") > 0.5
ID	passConversionVeto	passConversionVeto
Converted Photon Rejection	ExpectedInnerTrackHits ≤ 0	ExpectedInnerTrackHits ≤ 0
$\|d0(PV)\|$	< 0.02 cm	< 0.04 cm
$\|dZ(PV)\|$	< 1 cm	

Table 7.7: Tight and loose electron definitions.

The relative isolation for electrons is computed with a cone size $\Delta R = 0.3$, and are rejected if falling in the crack between the ECAL barrel and endcap $(1.4442 < |\eta| < 1.5666)$. Qualities required of electrons not already described for muons in Section 7.2.3 are:

- MVA ID – a multivariate analysis (MVA) technique provides a discriminant which separates real and fake electrons. The MVA is trained on tracking information, shower shapes in the ECAL, and energy matching information. The MVA is trained for both triggering and non-triggering electrons, where the triggering version used here ('mvaTrigV0') does not train on impact parameter information.

- Conversion veto – the electron must not be reconstructed from a photon which converts to an electron-positron pair within the tracker. A simple conversion reconstruction is performed using the angle between and the distance of closest approach between conversion candidate tracks.
- Converted Photon Rejection – similar to the conversion veto, electron candidates are required to have zero missing expected tracker hits.

7.2.5 Jet Selection

Jets are selected from those reconstructed from the set of Particle Flow particles using the anti-kt clustering algorithm [26] with a distance parameter of 0.5. The qualities required of jets, defined in Table 7.8, are:

- CEF/NHF/NEF/CHF – the charged electromagnetic, neutral hadronic, neutral electromagnetic, and charged hadronic energy fractions to the total energy of the jet candidate.
- NCH – the number of charged hadrons of the jet candidate.
- $N_{constituents}$ – the multiplicity of all Particle Flow particles in the jet candidate.

Cuts	Jet
p_T	> 30 GeV/c
$\lvert\eta\rvert$	< 2.4
CEF/NHF/NEF	< 0.99
CHF/NCH	> 0
$N_{constituents}$	> 1

Table 7.8: Jet definition.

The jet energies must be corrected for the non-linear response of the calorimeters to particles in order to reconstruct the energy of the initial parton. This is done in a factorized approach of Jet Energy Corrections (JEC), with the `L1FastL2L3` algorithm. First the L1Fast correction removes the energy from pileup events. This should remove any dependence on luminosity before any other corrections are applied. Next the L2 Relative correction makes the jet energy response uniform in eta by correcting an arbitrary-eta jet relative to a jet in the central ($|\eta| < 1.3$) region. Lastly, the L3 Absolute correction makes the jet energy response uniform in jet p_{T}. The L2 and L3 corrections are derived from both MC truth information and from dijet (L2) or $Z/\gamma+jet$ (L3) balance in data. A fourth step is required in data to correct for small (up to 10%) differences between MC and data. This 'Residual' JEC is applied for data events after the MC truth L2L3 step is applied. A more complete description of the determination of JEC factors is given at 7 TeV in [128], with information on the full 19.8 fb^{-1} 8 TeV dataset given in [129].

7.2.6 b-tag Selection

The Combined Secondary Vertex (CSV) [130] algorithm is used to identify jets from the production of bottom quarks. The weak decay of b-hadrons is characterized by a relatively long lifetime ($\sim$1.5ps or $c_\tau \approx 450\mu$m) giving an observable flight distance within the inner tracker and the reconstruction of secondary vertices. b-hadron decays are also marked by large charged particle multiplicities and mass, with the b-hadron carrying most of the jet energy. b- and c-hadrons also can decay semi-leptonically, leading towards some b-jets containing electrons or muons. The CSV algorithm combines information about the kinematics of jets and the characteristics of their secondary vertices, as well as track impact parameters to derive a discriminant on the likelihood that a jet is from the decay of a b-quark.

Definition

The following section is a brief summary of [130] describing how the CSV discriminant is calculated.

Tracks associated to a b-tag candidate must pass the following selection cuts:

- at least 8 total reconstructed hits in the pixel and silicon strip detectors,
- at least 2 reconstructed hits in the pixel detectors,
- $p_{\mathrm{T}} > 1\,\mathrm{GeV}/c$,
- $\chi^2/\mathrm{N}_{dof} < 10$ for the track fit,
- $|d_0(PV)| < 2$ mm – this requirement on the transverse impact parameter rejects charged particle tracks from sources with much larger displacement from the PV than b-quarks, as to first order the impact parameter is invariant under boosts of a b-hadron.

Charged particle tracks passing these selection cuts and within $\Delta R < 0.3$ of the jet axis are associated to the jet. From the vertices reconstructed from these tracks, a secondary vertex candidate is required to pass the following cuts:

- the transverse distance from the primary and secondary vertex, L_T, must be between 100 μm and 2.5 cm,
- $\frac{L_T}{\sigma_{L_T}} > 3$,
- the invariant mass of all charged particles associated to the vertex must be less than $6.5\ \mathrm{GeV}/c^2$,

- vertices with two oppositely charged tracks must not have an invariant mass within 50 MeV/c^2 of the nominal K^0_S mass.

Once charged tracks and secondary vertices are selected, the candidate jet is defined as one of three categories:

1. *RecoVertex* – at least one secondary vertex candidate passing all criteria is reconstructed. All tracks from all accepted vertices are used in the discriminant calculation.
2. *PseudoVertex* – without any secondary vertex candidates selected, a 'pseudo' vertex is created from at least two charged tracks not compatible with the primary vertex having a signed impact parameter significance of at least 2.
3. *NoVertex* – if neither of the above two categories are satisfied.

For all categories, the CSV discriminant uses the impact parameter significance of tracks passing the following:

- the distance of closest approach of the track to the jet axis must be less than 0.07 cm,
- oppositely charged pairs of tracks associated to the jet must not have an invariant mass within 30 GeV/c^2 of the nominal K^0_S mass.

For *RecoVertex* and *PseudoVertex* categories, the following additional variables are considered in the discriminant:

- the invariant mass of charged particles associated to the secondary vertex,
- the multiplicity of charged particles associated to the secondary vertex,
- the transverse distance between primary and secondary vertices, divided by its error (only for the *RecoVertex* category),
- the fraction of energy in charged particles associated to the secondary vertex to charged particles associated to the entire jet,
- the rapidities of charged tracks associated to the secondary vertex with respect to the jet axis,
- the track impact parameter of the first track exceeding a charm hadron threshold of 1.5 GeV/c^2. This charm discrimination is found by computing the invariant mass of the leading n tracks and increasing n until the invariant mass surpasses the threshold.

These input parameters are combined with a likelihood ratio technique to form a single discriminating variable. Since the inputs are very different for c-jets and light-flavor ($udsg$) jets, the likelihood function is defined separately for each as:

$$\mathcal{L}^{b,c,q} = f^{b,c,q}(\alpha) \times \prod_i f_\alpha^{b,c,q}(x_i) \tag{7.3}$$

where ($\alpha = 1, 2, 3$) is the vertex category, x_i are the input variables and $f^{b,c,q}$ are the probabilities for b-, c-, and light-flavor jets to fall into category α.

The combined discriminant is then defined as:

$$d = f_{BG}(c) \times \frac{\mathcal{L}^b}{\mathcal{L}^b + \mathcal{L}^c} + f_{BG}(q) \times \frac{\mathcal{L}^b}{\mathcal{L}^b + \mathcal{L}^q} \tag{7.4}$$

where $f_{BG}(c)$ and $f_{BG}(q)$ are the expected a priori probabilities for c- and q-content in non-b jets ($f_{BG}(c) + f_{BG}(q) = 1$).

This discriminant is calculated for all selected jets, defined previously in 7.2.5, and a jet is considered b-tagged if it is greater than 0.679. This is the recommended 'medium' or CSVM working point defined by the BTag Physics Object Group (POG) [131], chosen to have a light-flavor ($udsg$) mis-tagging rate of ∼1% and a tagging efficiency for b-jets of ∼70%.

MC Scale Factor Reweighting

As with all other physics objects, small differences between the b-tagging efficiencies and mis-tagging rates in MC and in data are observed and must be corrected by weighting MC events with a scale factor $SF = \epsilon_{data}/\epsilon_{MC}$. However for b-tagging, scale factors are measured on a per-jet basis, while the total efficiency and mis-tagging rate for the b-tag multiplicity requirement is what must be corrected. The b-tag requirement in this analysis is inclusive ($\mathrm{N}_{btag} \geq 1$), so the adjustment of per-jet efficiencies represents a more complicated combinatorial problem.

Several methods for deriving this event weight exist. One method ignores the actual b-tag status of each jet, allowing for each event to appear in each N_{tag} bin weighted by a probability determined by the per-jet scale factors and measured tagging efficiencies. Another method uses only the scale factors for each jet as a pseudo-probability, adjusting the tag status of each individual jet randomly according to the scale factors. These two methods approach each other over large numbers of events, however within each event many b-tag related variables become ill-defined due to this ignoring or randomization of tag statuses.

The method used in this analysis is to adjust the weight of only selected events, without needing to 'add back' un-selected events without any b-tags, and without changing the N_{tags} of selected events. In this way all b-tagging related variables remain well-defined. The goal of this method is to construct a weight w such that

$$\sum_{j}^{\text{pre-tag data}} P_j^{\text{data}}(nb_j, nc_j, nl_j) = \sum_{j}^{\text{pre-tag MC}} w_j P_j^{\text{MC}}(nb_j, nc_j, nl_j) \tag{7.5}$$

where $P^{\text{data/MC}}$ are the probabilities for selected an event in data or MC as a function of its true b, c, and light quark content, which can be written as

$$P = \sum_{tb}^{nb}\sum_{tc}^{nc}\sum_{tl}^{nl} C\epsilon_b^{tb}(1-\epsilon_b)^{nb-tb}\epsilon_c^{tc}(1-\epsilon_c)^{nc-tc}\epsilon_l^{tl}(1-\epsilon_l)^{nl-tl}S \tag{7.6}$$

with

$$C = \begin{pmatrix} tb \\ nb \end{pmatrix}\begin{pmatrix} tc \\ nc \end{pmatrix}\begin{pmatrix} tl \\ nl \end{pmatrix}$$

$$S = \theta(tb+tc+tl \geq t_{min}) = \begin{cases} 1 & \text{if } tb+tc+tl \geq t_{min} \\ 0 & \text{else} \end{cases}$$

where C is a product of binomial coefficients representing the combinations of tagged and un-tagged jets, and S is a selection function simply requiring at least t_{min} tags. The number of true bottom, charm, and light ($udsg$) quarks are labeled nb, nc, and nl respectively, and the number of these tagged by the b-tagger are labeled tb, tc, and tl. Given the scale factors SF_i, P^{data} can be written in terms of the MC efficiencies and scale factors, and from Equations 7.5 and 7.6 the b-tagging weight can be written as

$$w = \frac{\sum_{tb}^{nb}\sum_{tc}^{nc}\sum_{tl}^{nl} C \prod_{i}^{b,c,l}(\epsilon_{i,mc}SF_i)^{ti}(1-\epsilon_{i,mc}SF_i)^{ni-ti}S}{\sum_{tb}^{nb}\sum_{tc}^{nc}\sum_{tl}^{nl} C \prod_{i}^{b,c,l}\epsilon_{i,mc}^{ti}(1-\epsilon_{i,mc})^{ni-ti}S} \tag{7.7}$$

where ti is the number of tagged jets of flavor $i = (b, c, l)$. For each MC sample, the efficiencies are measured as a function of jet p_{T} and $|\eta|$ and all selected MC events are reweighted in this way.

7.2.7 Photon Selection

Photons are selected by applying a loose, cut-based approach defined to have an efficiency of $\sim$90% [132], described in Table 7.9. Only photons in the ECAL barrel ($|\eta| < 1.4442$) are considered. Photons are additionally required to be separated from other selected objects by at least $\Delta R > 0.7$ to suppress initial and final state radiation from high-p_{T} leptons or partons.

Cuts	Photon (γ)
E_T	> 20 GeV
$\lvert\eta\rvert$	< 1.4442
H / E	< 0.05
Neutral Hadron Isolation	$< 3.5 + 0.04 \cdot P_T(\gamma)$
Photon Isolation	$< 1.3 + 0.005 \cdot P_T(\gamma)$
Charged Hadron Isolation	< 2.6
$\sigma_{i\eta i\eta}$	$\sigma_{i\eta i\eta} < 0.012$
ID	passElectronVeto

Table 7.9: Photon definition.

The qualities required of candidate photons are:

- E_{T} – the transverse energy of the reconstructed photon.
- $|\eta|$ – the absolute value of the pseudorapidity of the reconstructed photon.
- H / E – the ratio of hadronic energy to electromagnetic energy. The numerator is the energy of the single HCAL tower located behind the seed crystal of the seed basic cluster of the photon supercluster. The denominator is the energy of the photon supercluster.
- Particle Flow isolation [133] – the isolation energy around the photon is computed in two steps:
  - Computation of Iso Deposits (direction and p_{T} of all PF particles) within a cone size of $\Delta R < 0.3$ for charged hadrons associated to the primary vertex, neutral hadrons, and photons separately.
  - Computation of the sum of the p_{T} of the above Iso Deposits passing an additional veto. Charged hadrons must be separated by $\Delta R > 0.02$ and other photons must be separated by $\Delta\eta > 0.015$ from the candidate supercluster position. PF photons sharing the same SC as the candidate photon are removed from this sum. An illustration of the isolation cones and veto areas is shown in Figure 7.5.
- $\sigma_{i\eta i\eta}$ – the shower shape variable, or the log-energy weighted pseudorapidity width defined as [134]:

$$\sigma_{i\eta i\eta} = \sqrt{\frac{\sum_i^{5\times5} w_i \cdot (0.0175 \cdot \Delta N_i^{\mathrm{seed}} + \eta^{\mathrm{seed\ crystal}} - \bar{\eta}_{5\times5})^2}{\sum_i^{5\times5} w_i}} \tag{7.8}$$

$$w_i = \max(0, 4.2 + \ln\frac{E_i}{E_{5\times5}}) \tag{7.9}$$

where the sum is over the 5×5 crystal matrix centered on the seed crystal. Here $0.0175 \cdot \Delta N_i^{\text{seed}}$ is the average crystal η times the number of crystals away from the seed, $\eta^{\text{seed crystal}}$ is the η of the seed, $\bar{\eta}_{5\times5}$ is the mean η of the 5×5 matrix, E_i is the energy of the i^{th} crystal, and $E_{5\times5}$ is the energy of the 5×5 matrix.

- Conversion-safe electron veto – the same procedure as in the electron selection (passConversionVeto) in Section 7.2.4 is applied, only requiring the opposite result.

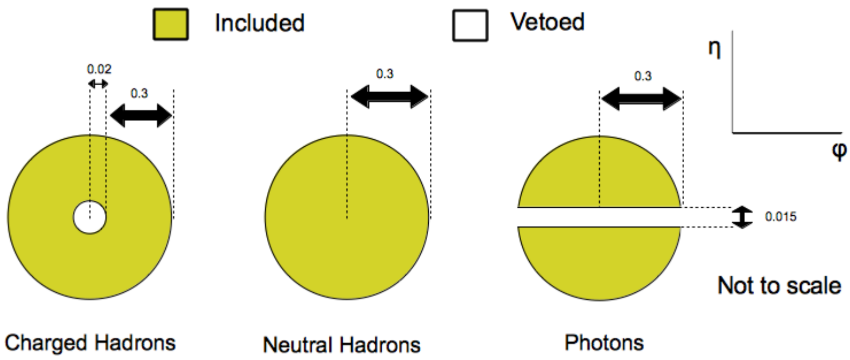

Figure 7.5: Particle Flow based isolation cones. PF photons sharing the same supercluster as the photon candidate are removed from the photon isolation sum.

The isolation energies for photons are corrected for pileup-dependence by subtracting the expected pileup energy deposits from the shower area. This is done by computing the average energy deposited in the detector per unit area (ρ) for $|\eta| < 2.5$ and knowing the detector effective areas for each type of Particle Flow particle, determined from γ+jet MC [132] and listed in Table 7.10, subtracting the Particle Flow isolation energy sums (PFIso) as

$$\text{PFIso}_{\text{corrected}} = max(0, \text{PFIso} - \rho \cdot A_{eff}). \quad (7.10)$$

	A_{eff} charged hadrons	A_{eff} neutral hadrons	A_{eff} photons
$\lvert\eta\rvert < 1.0$	0.012	0.030	0.148
$1.0 < \lvert\eta\rvert < 1.479$	0.010	0.057	0.130
$1.479 < \lvert\eta\rvert < 2.0$	0.014	0.039	0.112
$2.0 < \lvert\eta\rvert < 2.2$	0.012	0.015	0.216
$2.2 < \lvert\eta\rvert < 2.3$	0.016	0.024	0.262
$2.3 < \lvert\eta\rvert < 2.4$	0.020	0.039	0.260
$\lvert\eta\rvert > 2.4$	0.012	0.072	0.266

Table 7.10: Photon effective areas.

Fake Photons

Fake photons (‘*fakes*’) are defined in addition to candidate photons to provide control regions in which to compare the performance of $E_{\mathrm{T}}^{\mathrm{miss}}$ in MC to data. Fakes are defined similarly to candidate photons in Table 7.9 but are required to fail either the $\sigma_{i\eta i\eta}$ or the charged hadron isolation requirements:

	γ	*fake*
Requirement	$\sigma_{i\eta i\eta} < 0.012$ and chHadIso < 2.6	chHadIso < 20 and ($\sigma_{i\eta i\eta} \geq 0.012$ or chHadIso ≥ 2.6)

Table 7.11: Fake photons are defined as failing either the $\sigma_{i\eta i\eta}$ or charge hadron isolation requirement of the candidate photon selection. An upper window of 20 GeV is required for the isolation to retain similarity between the two objects.

An upper limit of 20 GeV is placed on the allowed fake charged hadron isolation sum to ensure that poorly isolated QCD multi-jet events with very dissimilar $E_{\mathrm{T}}^{\mathrm{miss}}$ resolution are not included in any fake comparison. The value of 20 GeV is chosen for historical reasons of the inclusive $\gamma\gamma$ $E_{\mathrm{T}}^{\mathrm{miss}}$ search [135].

7.2.8 Lepton and Photon Efficiencies

Differences between the efficiencies of the lepton selection and trigger requirement in data and in MC are observed and corrected by applying a scale factor $SF = \epsilon_{data}/\epsilon_{MC}$ to the event weight of simulated backgrounds and signal processes. The lepton selection criteria and single lepton triggers used in this analysis are common to many analyses from CMS, and as such the efficiencies in data are well-measured and not necessary to re-measure. What follows is a brief summary of these measurements in the manner outlined by [136]. The electron scale factors are derived in [137], and the muon scale factors are provided by the Muon POG [138].

The ID, isolation, and trigger efficiencies for leptons are measured using a ‘tag and probe’ technique exploiting the Z boson mass resonance in di-lepton events. Two oppositely charged, same-flavored (e^+e^-, $\mu^+\mu^-$) leptons with an invariant mass of $76 < m_{\ell\ell} < 106\,\mathrm{GeV}$, within 15 GeV of the Z mass. The ‘tag’ lepton is very tightly selected using the full object selection criteria, as well as having $p_{\mathrm{T}} > 30\,\mathrm{GeV}/c$ and in the case of ID/isolation measurements is required to fire the relevant trigger. The ‘probe’ lepton is very loosely selected to study its properties, as the charge and invariant mass requirement strongly constrain its identity as the other lepton of the Z decay. The efficiency in data of the ID, isolation, and trigger requirements are taken as a function of p_{T} and η from the efficiency of each requirement on the probe leptons. The scale factors used in this analysis are shown in Figure 7.6 as a function of p_{T} and η.

The photon scale factor is treated as two distinct pieces, the identification efficiency scale

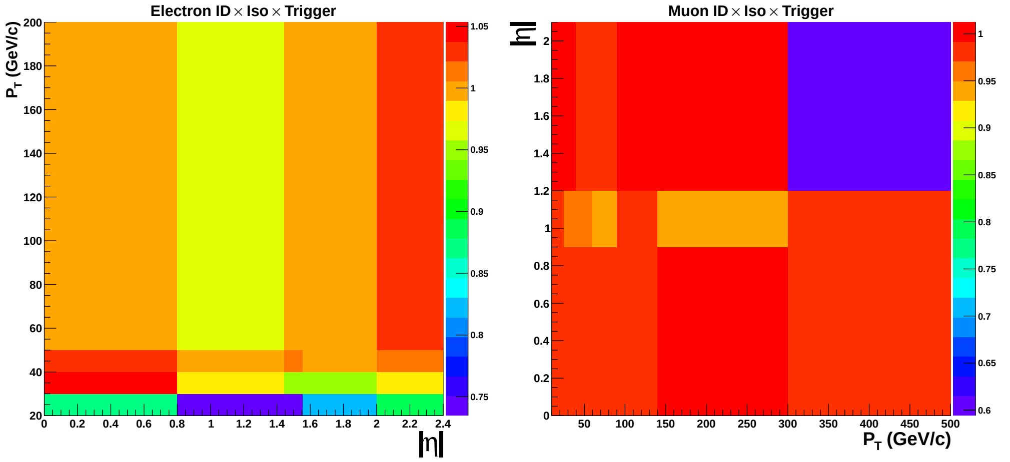

Figure 7.6: Electron (left) and muon (right) ID, isolation, and Trigger efficiency scale factors as a function of p_{T} and $|\eta|$.

factor and the conversion-safe electron veto efficiency scale factor [132]. Both scale factors are shown in Figure 7.7. For events with multiple photons, the event is weighted by the product of the two scale factors and the uncertainty is taken as the uncertainty of each scale factor added in quadrature. The identification efficiency is measured in data similarly to leptons, however using the fact that electrons are also reconstructed as photons failing the electron veto. The measurement is again a tag and probe using $Z \to ee$ events, where the tag is a tight electron firing the SingleElectron trigger with $p_{\mathrm{T}} > 30\,\mathrm{GeV}/c$. The probe is a photon candidate with $p_{\mathrm{T}} > 15\,\mathrm{GeV}/c$, and the tag-probe mass is required to be $60 < m_{TP} < 120\,\mathrm{GeV}/c^2$. The efficiency is extracted from a simultaneous fit of passing and failing probes to the m_{TP} distribution of simulated $Z \to ee$ events.

The conversion-safe electron veto efficiency in data is measured differently, using the highly clean sample of photons found in $Z \to \mu\mu\gamma$ events. Events are selected in data with $m_{\mu\mu} < 180$ and $70 < m_{\mu\mu\gamma} < 110\,\mathrm{GeV}/c^2$ with tightly selected muons having $p_{\mathrm{T}} > 20(10)$ and firing a di-muon trigger. A simple counting experiment is performed to extract the efficiency of the electron veto.

7.2.9 Pre-selection

The cut-based pre-selection of $t\bar{t}$ events used in this analysis requires that each event:

- Passes event cleaning and trigger requirements
- Has exactly one tight, isolated lepton (e, μ)
- Has no additional loose leptons

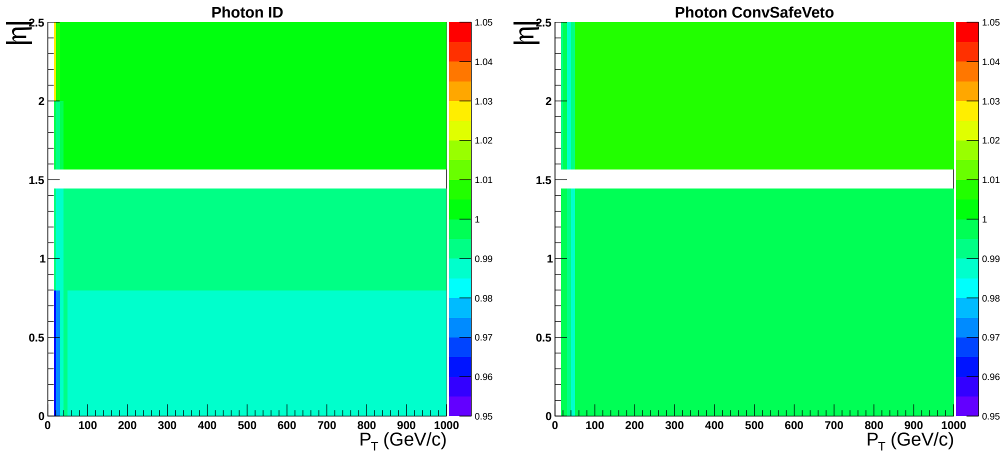

Figure 7.7: Photon ID (left) and conversion-safe electron veto (right) scale factors binned in p_{T} and $|\eta|$.

- Has at least 3 jets
- At least one selected jet is b-tagged by CSVM.

After this pre-selection is applied, events are separated into two signal regions and two control regions, depending on the number of selected photons (N_γ) and fakes (N_f) found in them:

Signal Region 1 (SR1): – $N_\gamma = 1$.

Signal Region 2 (SR2): – $N_\gamma \geq 2$.

Control Region 1 (CR1): – $N_\gamma = 0$, $N_f = 1$.

Control Region 2 (CR2): – $N_\gamma = 0$, $N_f \geq 2$.

The control regions veto the presence of selected photons to avoid overlap with signal regions. Due to selection efficiencies and the barrel-only fiducial acceptance of photons, as well as the $\sim$20% branching ratio of binos to Z bosons, the majority of signal events have only one selected photon as seen in Figure 7.8. The most sensitive region however is with two selected photons (for $m_{\tilde{t}} = 460$ GeV and $m_{\tilde{\chi}^0_1} = 175$ GeV, SR2 has $\frac{S}{\sqrt{B}} = 17.6$ compared to 2.2 in SR1).

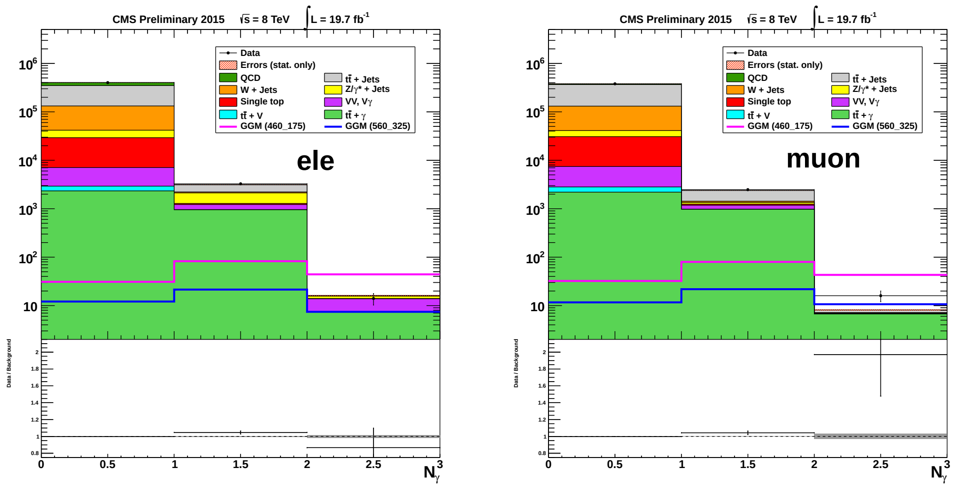

Figure 7.8: Comparison of the number of selected photons for the electron (left) and muon (right) channel. Errors shown here are statistical only. The signal model listed as (460_175) refers to $m_{\tilde{t}} = 460$ GeV, $m_{\tilde{\chi}_1^0} = 175$ GeV and similarly for (560_325).

Channel	Pre-selection	SR1	SR2
QCD	53129 ± 469	–	–
$t\bar{t}$ + jets	217189 ± 470	901 ± 4	0.47 ± 0.04
W + jets	90652 ± 501	100 ± 2	–
Z + jets	13355 ± 94	816 ± 10	1.80 ± 0.13
Single t	22281 ± 30	63 ± 2	–
Diboson	1736 ± 2	14.9 ± 0.1	0.11 ± 0.00
Vγ	2677 ± 17	239 ± 3	6.2 ± 0.1
$t\bar{t} + W$	338 ± 1	3.8 ± 0.1	0.03 ± 0.02
$t\bar{t} + Z$	265 ± 1	4.3 ± 0.1	0.09 ± 0.01
$t\bar{t} + \gamma$	3292 ± 4	953 ± 2	7.3 ± 0.2
Total Background	404914 ± 838	3095 ± 12	16.0 ± 0.3
GMSB (460_175)	158 ± 3	82 ± 2	44 ± 2
GMSB (560_325)	41 ± 1	21 ± 1	7.4 ± 0.3
Data	404337	3266	14

Table 7.12: Observed data and expected event yields in 19.7 fb^{-1} for signal and backgrounds in the electron channel. The errors represented in this table are statistical only. The dashes indicate negligibly small contributions.

Channel	Pre-selection	SR1	SR2
QCD	14291 ± 298	–	–
$t\bar{t}$ + jets	235482 ± 476	944 ± 4	0.95 ± 0.12
W + jets	90256 ± 515	83 ± 2	0.11 ± 0.01
Z + jets	10376 ± 61	100 ± 1	0.22 ± 0.00
Single t	23399 ± 30	67 ± 2	–
Diboson	1731 ± 2	7.8 ± 0.1	0.08 ± 0.00
Vγ	3092 ± 18	192 ± 3	–
$t\bar{t}+W$	355 ± 1	3.8 ± 0.1	0.04 ± 0.00
$t\bar{t}+Z$	262 ± 1	2.8 ± 0.1	–
$t\bar{t}+\gamma$	3182 ± 4	973 ± 2	6.7 ± 0.2
Total Background	382426 ± 765	2374 ± 6	8.1 ± 0.3
GMSB (460_175)	155 ± 3	80 ± 2	43 ± 2
GMSB (560_325)	44 ± 1	22 ± 1	10.7 ± 0.6
Data	381772	2475	16

Table 7.13: Observed data and expected event yields in 19.7 fb^{-1} for signal and backgrounds in the muon channel. The errors represented in this table are statistical only. The dashes indicate negligibly small contributions.

7.2.10 Data-driven QCD Selection

QCD multi-jet and γ+jet backgrounds are negligibly small in the signal regions, but not so in the control regions and in the preselection. To collect a sample of events from data with which to describe the $E_{\mathrm{T}}^{\mathrm{miss}}$ distribution of such events, alternate lepton definitions are employed that are orthogonal to the definitions in Sections 7.2.3 and 7.2.4. QCD muon candidates must be in a sideband of isolation and are allowed to fire an additional non-isolated, non-prescaled trigger (Table 7.5). QCD electron candidates must be in a sideband of both the isolation and MVA identification criteria. No overlap in QCD leptons and tight/loose leptons are allowed by these definitions, detailed in Tables 7.14 and 7.15. The pre-selection is applied as in Section 7.2.9, but requiring exactly one QCD lepton instead of one tight lepton. The loose lepton veto and all other requirements are left intact.

Cuts	eQCD
p_T	> 30 GeV/c
PFRelIso (0.3)	$0.25 \leq$ relIso < 1
$\lvert\eta\rvert$	< 2.5 not ($1.4442 < \lvert\eta\rvert < 1.566$)
ID	-1 < MVA ID("mvaTrigV0") < -0.1
ID	passConversionVeto
Converted Photon Rejection	ExpectedInnerTrackHits ≤ 0
$\lvert d0(PV)\rvert$	< 0.02 cm
$\lvert dZ(PV)\rvert$	< 1 cm

Table 7.14: QCD electron (eQCD) definition. This is the tight definition as in Table 7.7, with the isolation and MVA ID requirements inverted.

Cuts	μQCD
p_T	> 30 GeV/c
PFRelIso (0.4)	$0.25 \leq$ relIso < 1
$\lvert\eta\rvert$	< 2.1
ID	Global Muon
ID	PFMuon
N_{layers} (tracker)	> 5
X^2/N_{DOF} of track fit	< 10
N_{hits} (pixel)	> 0
N_{hits} (muon chamber)	> 0
$N_{segments}(\mu)$	> 1
$\lvert d0(PV)\rvert$	< 0.2 cm
$\lvert dZ(PV)\rvert$	< 0.5 cm

Table 7.15: QCD muon (μQCD) definition. This is the tight definition as in Table 7.6, with the isolation requirement inverted.

7.3 Estimation of Missing Transverse Energy

All backgrounds are taken from their simulation in MC. After applying the event selection to each MC sample, they are normalized to the total integrated luminosity of the data given their predicted cross sections. The samples are then reweighted to correct for differences between MC and data in pileup, b-tagging efficiencies, lepton efficiencies, and photon efficiencies.

Additional scale factors must be derived from comparisons between data and MC to correct for mismodeling dependent on the analysis selection. These are measured as template fits in key kinematic distributions discriminating the desired process from other backgrounds and isolating the scale factor required to match the data. The fits are performed in control regions well-separated from the signal regions to avoid contamination.

Lastly, the performance of the underlying $E_{\mathrm{T}}^{\mathrm{miss}}$ resolution in MC is compared to data in the fake photon control regions (CR1, CR2).

7.3.1 Template Fit Procedure

A binned maximum likelihood template fit procedure is used in several ways in this analysis. With an exact knowledge of the normalized shape of each process $d_{process}(x)$, a fit can be used to extract the number of expected events from each as:

$$n(x; n_{signal}, n_{background}) = n_{signal} \cdot d_{signal}(x) + n_{background} \cdot d_{background}(x) \tag{7.11}$$

where signal and background processes are chosen appropriately by the user [2]. In practice this is accomplished by fitting for a single variable, the fraction of signal events f_{sig} of the whole, using RooFit [139] and the Minuit numerical minimizer [140]:

$$d(x; f_{sig}) = f_{sig} \cdot d_{sig}(x) + (1 - f_{sig}) \cdot d_{bkg}(x) \tag{7.12}$$

The fit is optimized by maximizing the binned log-likelihood:

$$\log \mathcal{L}(x; f_{sig}) = \sum_{i\,\in\,\mathrm{bins}} \log \left[f_{sig} \cdot d_{sig}(x_i) + (1 - f_{bkg}) \cdot d_{bkg}(x_i) \right], \quad 0 \leq f_{sig} \leq 1 \tag{7.13}$$

From the resulting fit, one can construct scale factors for each process to correct the relative composition and overall normalization of their sum:

[2] 'Signal' here is not to be confused with the SUSY signal. In the context of the template fit procedure, 'signal' simply designates the process of interest in the fit.

$$SF_{sig} = f_{sig} \cdot \frac{N_{data}}{N_{sig}} \tag{7.14}$$

$$SF_{bkg} = (1 - f_{bkg}) \cdot \frac{N_{data}}{N_{bkg}} \tag{7.15}$$

$$\Rightarrow$$

$$SF_{sig} \cdot N_{sig} + SF_{bkg} \cdot N_{bkg} = N_{data}$$

where N_{data}, N_{sig}, and N_{bkg} are the initial yields for the observed data and each process. The errors on the scale factors are taken as the statistical uncertainty of the sample template and data combined in quadrature with the fit uncertainty reported by Minuit:

$$\sigma(SF_{sig}) = SF_{sig} \cdot \sqrt{(\frac{\sigma(f_{sig})}{f_{sig}})^2 + \frac{1}{N_{data}} + (\frac{\sigma(N_{sig})}{N_{sig}})^2} \tag{7.16}$$

For all systematic uncertainties on fitted scale factors, the quoted values are calculated by fluctuating the templates for each source of systematic uncertainty and adding the fluctuations in quadrature. The fit results are not considered to have their own independent source of systematic uncertainty.

7.3.2 QCD Background

The contribution of QCD multi-jet and γ+jet events to the signal region is extremely limited due to the requirement of two or more electromagnetic objects in the final state. This process is taken as negligible in the signal regions, but it is expected in the inclusive pre-selection where the W+jets cross section is constrained as well as the electron channel in CR1.

Events are selected from data as described in Section 7.2.10; no kinematic reweighting is applied. To account for non-QCD contamination of the data-driven sample [3], the QCD selection is also applied to all MC backgrounds and their luminosity-normalized yields are subtracted from the nominal QCD estimate, shown in Figure 7.9. After this subtraction, any histogram bin with a negative yield is taken as having zero QCD rate.

To constrain the overall rate and lepton fake rate for QCD events surviving this selection, the data-driven sample is normalized in a binned template fit in $E_{\mathrm{T}}^{\mathrm{miss}}$ after the MC subtraction is applied. The signal template taken from the data-driven sample and the background template is taken from all simulated non-QCD backgrounds. The resulting scale factor for the non-QCD backgrounds is not used because any cross section differences it may describe are better described

[3] While the isolation and MVA ID variables are steeply falling and efficient requirements, a small number of real leptons with poor isolation will fall into the data-driven QCD sample. This represents the possibility to overestimate the QCD background, so this effect is estimated by selecting QCD leptons from non-QCD MC and subtracted.

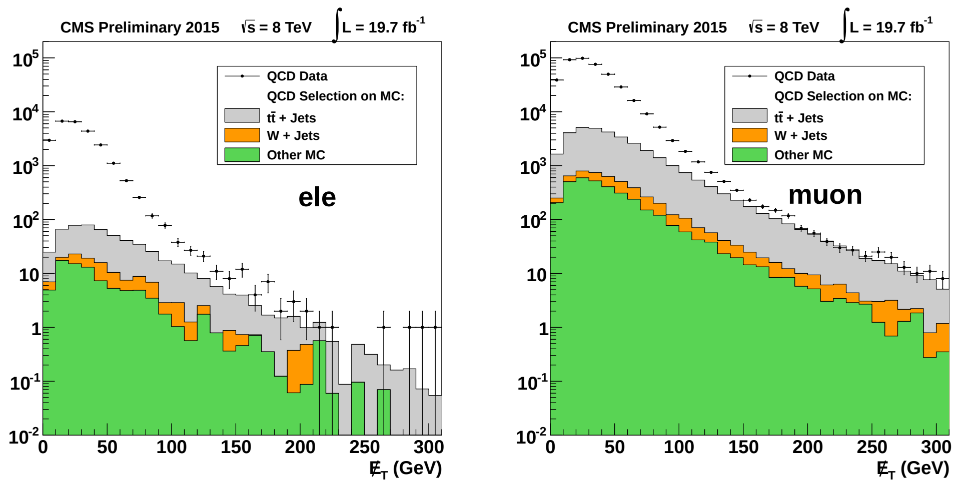

Figure 7.9: Subtraction of non-QCD contributions to the expected QCD shape in $E_{\mathrm{T}}^{\mathrm{miss}}$ for the electron (left) and muon (right) channels in the pre-selection ($\mathrm{N}_\gamma \geq 0$). For each event variable, the MC events passing the QCD selection are subtracted from the data-driven sample. The difference between data and MC in the above plots is taken as the shape of $E_{\mathrm{T}}^{\mathrm{miss}}$ for QCD.

by the W/Z+Jets scale factors derived later. An alternative to the template fit constraint is to simply normalize the QCD background to the data ($SF = \frac{N_{data}-N_{MC}}{N_{QCD}}$) in the low $E_{\mathrm{T}}^{\mathrm{miss}}$ region (≤ 20 GeV) which yields similar results. The results of both methods are summarized in Table 7.16, and the template fit results shown in Figure 7.10.

Channel	Template Fit		$E_{\mathrm{T}}^{\mathrm{miss}} < 20\,\mathrm{GeV}$
	SF_{QCD}	SF_{MC}	SF_{QCD}
e	2.15 ± 0.03	1.10 ± 0.003	2.04 ± 0.04
μ	0.04 ± 0.002	1.12 ± 0.003	0.03 ± 0.002

Table 7.16: QCD scales applied to the data-driven sample. The non-QCD SF_{MC} is not applied due to being more appropriately derived for only W/Z+Jets. An alternative to the template fit is to simply normalize the QCD background to the low $E_{\mathrm{T}}^{\mathrm{miss}}$ region in data.

7.3.3 W+Jets Cross Section

The cross section for W+Jets production is observed to be poorly simulated when requiring b-tagged jets, as well as from the usage of only $W+3$ and $W+4$ Jets samples. Without a full kinematic reconstruction of the top quarks in $t\bar{t}$ events, the most discriminating variable for W+Jets from the dominant $t\bar{t}$ background is the 'M3' variable. The M3 variable is defined as the invariant mass of the three-jet system in an event having the highest transverse momentum of all three-jet combinations. Hadronic decays of boosted top quarks will produce a three-jet system with large p_{T} and having a mass near the top quark mass, $\sim$175 GeV/c^2; other processes without a heavy decay to three jets show a much smoother invariant mass distribution. M3 additionally is largely insensitive to the jet energy scale uncertainty. By using a template fit in

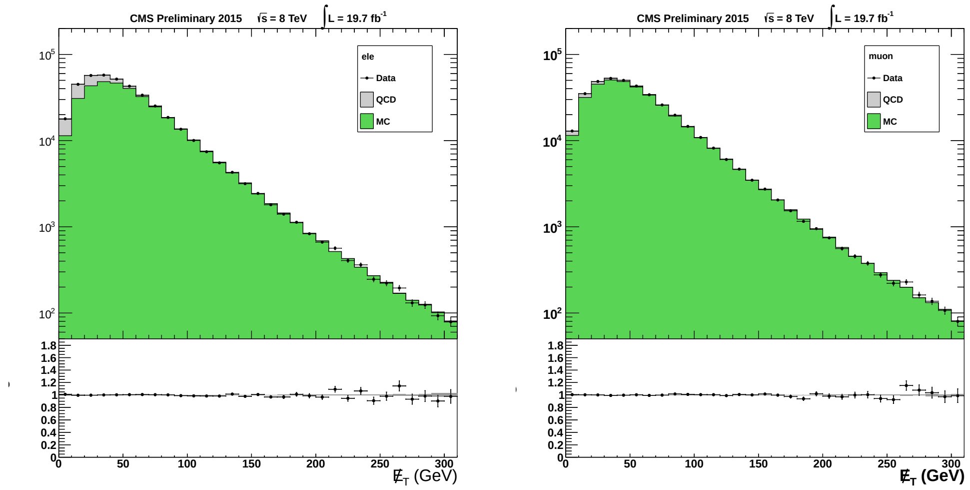

Figure 7.10: Template fit results of the QCD normalization in $E_{\mathrm{T}}^{\mathrm{miss}}$ for the electron (left) and muon (right) channels. Both SF_{QCD} and SF_{MC} (see Table 7.16) are applied for comparison. Errors shown are statistical only.

M3, the W+Jets cross section can be corrected for the selection used in this analysis.

This method is also very similar to the measurement of the $t\bar{t}$ cross section using the M3 method, as used in [141]. As a scale factor for W+Jets is derived, so too is a scale factor for $t\bar{t}$. This method additionally serves as a check of the simulation of $t\bar{t}$, and is applied to the $t\bar{t}$ background in the signal regions.

The template fit is performed in the M3 variable in the pre-selection, inclusive of photon multiplicity. The signal template is taken from $t\bar{t}$ +Jets MC, and the background template is taken from W+Jets MC. All other backgrounds are subtracted from the data before the fit procedure. The results of the fit are shown in Table 7.17 and Figure 7.11. Considering the $t\bar{t}$ sample is initially normalized by the NLO calculation of 245.8 pb, the scale factors are in good agreement with the current measurement by CMS [142] and with each other:

$$\sigma_{CMS} = 239 \pm 2 \text{ (stat.)} \pm 11 \text{ (syst.)} \ \pm 6 \text{ (lumi.) pb}$$
$$SF_e \cdot \sigma_{NLO} = 233 \pm 2 \text{ (fit+stat.)} \pm 6 \text{ (syst.) pb}$$
$$SF_\mu \cdot \sigma_{NLO} = 242 \pm 2 \text{ (fit+stat.)} \pm 9 \text{ (syst.) pb}$$

Channel	SF_W	$SF_{t\bar{t}}$
e	1.96 ± 0.03 (fit+stat.) ± 0.39 (syst.)	0.95 ± 0.01 (fit+stat.) ± 0.02 (syst.)
μ	1.87 ± 0.03 (fit+stat.) ± 0.44 (syst.)	0.99 ± 0.01 (fit+stat.) ± 0.04 (syst.)

Table 7.17: Scale factors (k-factors) for the normalization of W+Jets and $t\bar{t}$. The systematic errors included here are all systematics except for theoretical cross section uncertainties, combined in quadrature.

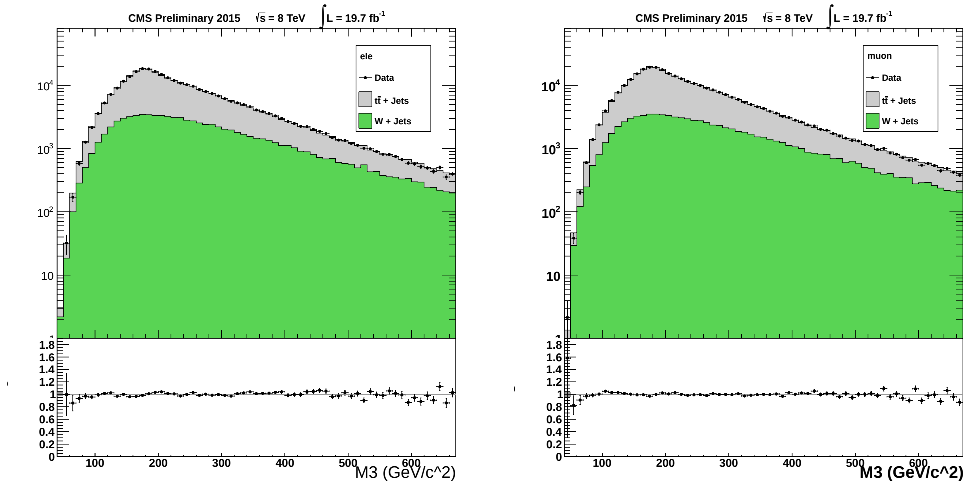

Figure 7.11: Template fit results for the W+Jets and $t\bar{t}$ normalization in M3 for the electron (left) and muon (right) channels. Errors shown are statistical only.

7.3.4 Electron Misidentification Rate

The electron channel shows a significant difference to the muon channel in the non-negligible rate of electrons misidentified as photons. The MC simulation of this rate is shown to be insufficient, and is correctable by deriving a scale factor from the plentiful $Z \to ee$ events in data. $Z \to ee$ events with an electron misidentified as a photon (and $Z\gamma$ to a smaller degree) can be observed as a peak in the invariant mass of reconstructed $e\gamma$ pairs in SR1 near 90 GeV/c^2. Other backgrounds in SR1 do not exhibit a peak in this distribution, so a template fit in $m_{e\gamma}$ is well suited for this purpose. This process relies on the assumption that the cross section for simulated Z and $Z\gamma$ (denoted $Z(\gamma)$ for brevity here on in) production is correct, and a second scale factor must be constructed to account for any differences to the data in the number of estimated Z bosons.

$Z(\gamma)$+Jets Normalization

The k-factor dependence on the selection criteria for $Z(\gamma)$ MC and the prediction of the number of Z boson events is important both for the prediction of the $E_{\mathrm{T}}^{\mathrm{miss}}$ shape in the signal regions and for the the measurement of the number of electrons from those Z bosons faking photons in the reconstruction. To measure this k-factor, a di-leptonic selection is constructed to directly observe $Z \to ee(\mu\mu)$. The pre-selection outline in Section 7.2.9 is modified to require two tight leptons of the same flavor. No charge identification is applied. The di-leptonic selection is:

- Passes event cleaning and trigger requirements
- Has exactly two tight, isolated leptons of the same flavor (ee, $\mu\mu$)
- Has no additional loose leptons

- Has at least 3 jets.

Both b-tagged (≥ 1) and non-b-tagged (≥ 0) samples are collected, as the electron to photon fake rate relaxes the tagging requirement. No photons are required. While triggering on the presence of one lepton, attention must be paid to the MC trigger efficiency scale factors as there are two sources for the triggers to fire. The trigger scale factor for this di-leptonic selection is:

$$SF_{trigger} = 1 - (1 - SF^{\ell\,1}_{trigger})(1 - SF^{\ell\,2}_{trigger}) \tag{7.17}$$

The isolation and identification scale factors are taken as the product of the scale factors for each individual lepton. QCD is a negligible contribution to this sample in and is not included.

The k-factor is constructed from a binned template fit in $m_{\ell\ell}$ with the Z+Jets and $Z\gamma$+Jets MC samples taken as the signal template, and all other MC backgrounds taken as the background template. The results of this fit are shown in Figure 7.12 and Table 7.18. Here also is an interesting opportunity to observe the performance of the $E_{\mathrm{T}}^{\mathrm{miss}}$ simulation in events that are dominated by processes with no true $E_{\mathrm{T}}^{\mathrm{miss}}$. Seen in Figure 7.13 is the $E_{\mathrm{T}}^{\mathrm{miss}}$ for the di-leptonic sample, restricted to within 10 GeV of the Z boson mass.

Channel	$SF_{Z(\gamma)}$
e	1.38 ± 0.02 ± 0.15
e (no b-tag)	1.24 ± 0.01 ± 0.13
μ	1.60 ± 0.02 ± 0.17
μ (no b-tag)	1.36 ± 0.01 ± 0.15

Table 7.18: Scale factors (k-factors) for the normalization of $Z(\gamma)$+Jets backgrounds. Errors are quoted as (fit $\oplus$ stat.) $\pm$ systematic.

Electron Misidentification Rate

The misidentification of electrons as photons is most visible in the peak near 90 GeV/c^2 in the invariant mass of $e\gamma$ pairs when requiring one photon in SR1. The simulation of this rate is seen in Figure 7.14 to be smaller than in data. In fact without looking at the the broader kinematic behavior of MC backgrounds, an analyzer may be misled into believing that QCD multi-jet and γ+jet events are a non-negligible component of the electron channel background when requiring one photon because the $E_{\mathrm{T}}^{\mathrm{miss}}$ shape of QCD events is very similar to that of $Z(\gamma)$ events. A normalization of QCD to data in the low-$E_{\mathrm{T}}^{\mathrm{miss}}$ ($\leq 20\,\mathrm{GeV}$) region would allow the QCD constraint to absorb the discrepancy where it is most pronounced. However this is not the case, as closer inspection of both the $m_{e\gamma}$ and $E_{\mathrm{T}}^{\mathrm{miss}}$ distributions in SR1, and comparing electron and muon channels, reveals that including QCD may approximate the $E_{\mathrm{T}}^{\mathrm{miss}}$ background shape but distort the $m_{e\gamma}$ distribution further. A kinematic reweighting of the data-driven QCD sample

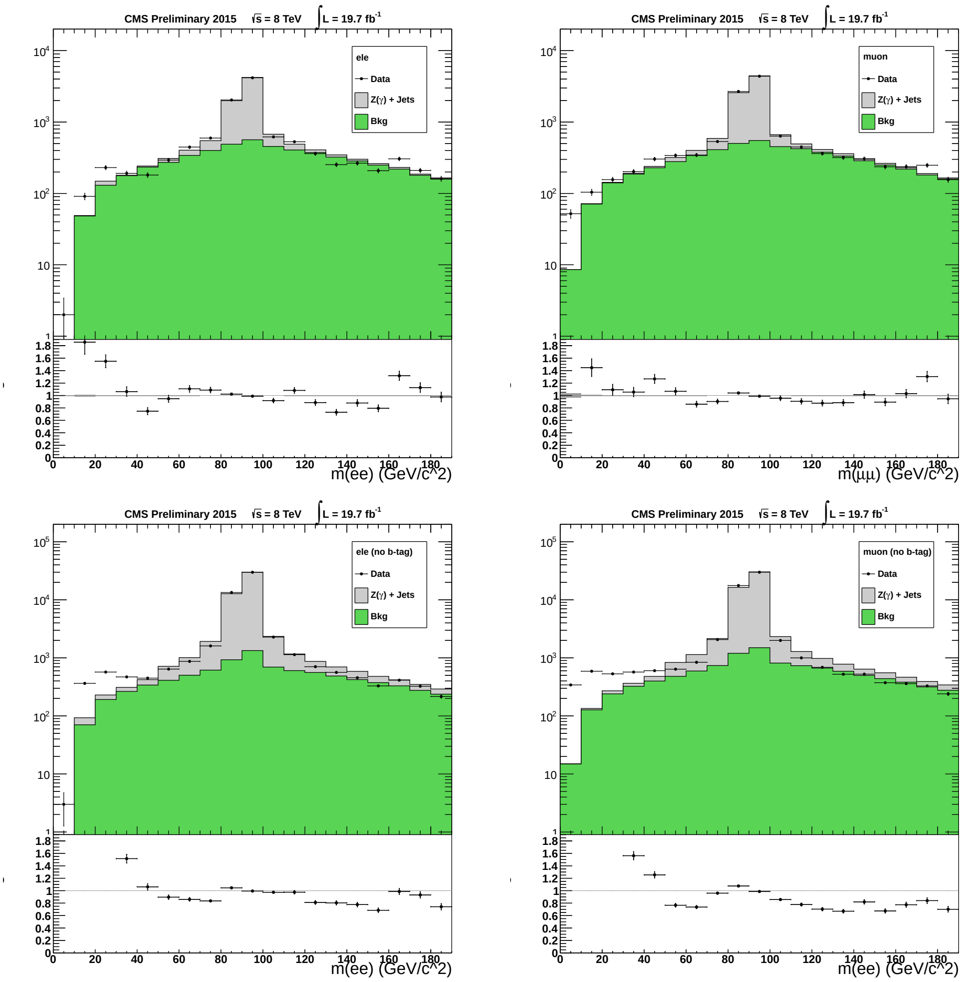

Figure 7.12: Template fit results for the electron (left) and muon (right) channels, both requiring (top) and not requiring (bottom) a b-tag. Errors shown are statistical only.

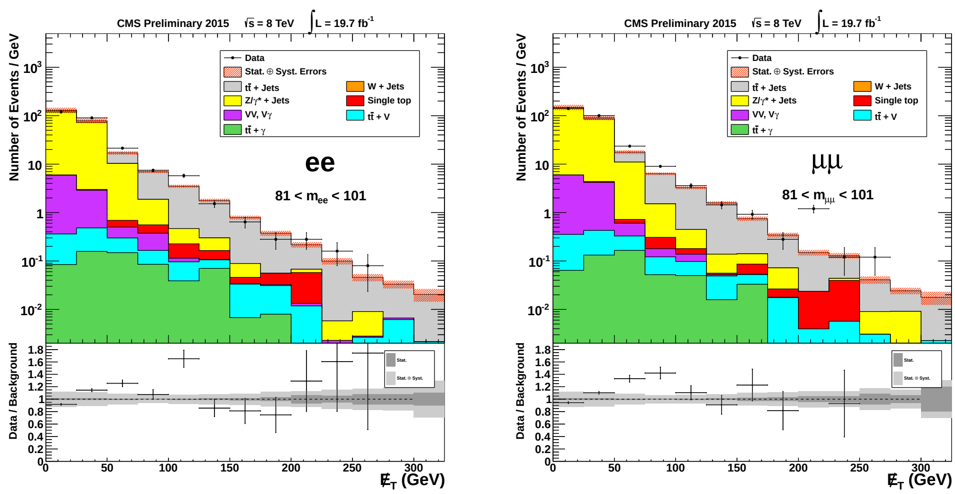

Figure 7.13: Comparison of the $E_{\mathrm{T}}^{\mathrm{miss}}$ for the di-leptonic selection, restricted to the invariant mass of the lepton pair being within 10 GeV/c^2 of the Z boson mass.

may allow QCD to explain this, but unnecessarily complicates the background estimation. In addition this would reintroduce the risk of signal contamination and the constriction of the $E_{\mathrm{T}}^{\mathrm{miss}}$ range usable in the upper limit evaluation by normalizing QCD to data at low $E_{\mathrm{T}}^{\mathrm{miss}}$.

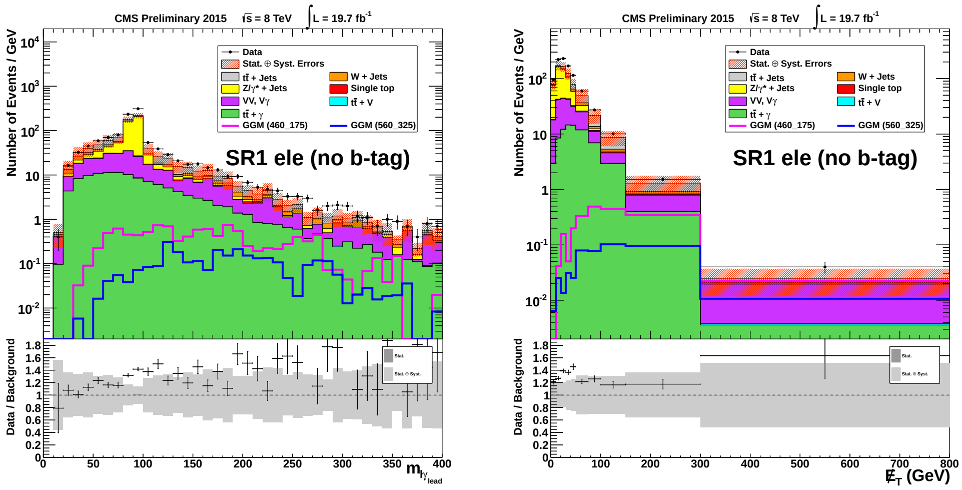

Figure 7.14: Comparison of the $m_{e\gamma}$ (left) and $E_{\mathrm{T}}^{\mathrm{miss}}$ (right) in data and MC for the electron channel, requiring one photon but relaxing the b-tagging requirement. It is clear from the $E_{\mathrm{T}}^{\mathrm{miss}}$ discrepancy that the simulation is deficient, and the $m_{e\gamma}$ discrepancy reveals this to be caused by the Z+Jets background. The above are adjusted for the $Z(\gamma)$ k-factor derived earlier.

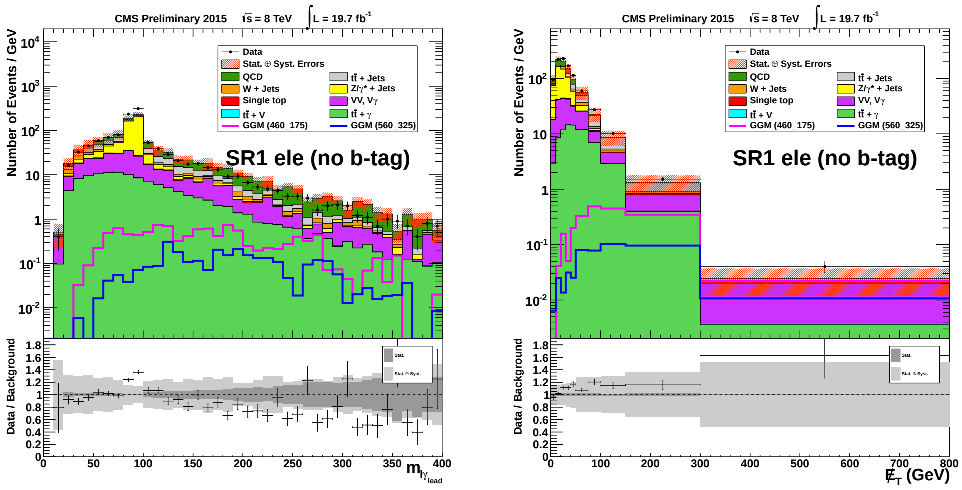

Figure 7.15: The same comparison as in Figure 7.14 but including data-driven QCD. The $E_{\mathrm{T}}^{\mathrm{miss}}$ shape of QCD and Z+Jets is similar, allowing the QCD normalization to cover any difference between MC and data fairly well, however the $m_{e\gamma}$ of QCD events overestimates the high-mass backgrounds and does not address the Z boson peak. The above are adjusted for the $Z(\gamma)$ k-factor derived earlier.

Considering all of this, a truth-matching procedure in MC backgrounds is applied to find events with an electron misidentified as a photon. For all reconstructed photons in all MC backgrounds, the generator-level truth is determined by finding the matching generator particle requiring:

- $\Delta R(\gamma_{reco},\ \gamma_{gen}) < 0.01$ in the case of matching to a photon, or
- $\Delta R(\gamma_{reco},\ e_{gen}) < 0.04$ in the case of matching to an electron
- $\Delta R(e(\gamma)_{gen},\ other_{gen}) > 0.2$ – considering all other generated final-state particles with $p_{\mathrm{T}} > 2\,\mathrm{GeV}$
- $|\Delta\eta(\gamma_{reco},\ e(\gamma)_{gen})| < 0.005$
- $|p_{\mathrm{T}}^{reco} - p_{\mathrm{T}}^{gen}| \,/\, p_{\mathrm{T}}^{gen} < 0.1$

Reconstructed photons are categorized by whether they are matched to a photon or an electron in this way, or if matched to neither the photon is considered as matched to a jet.

The electron misidentification rate scale factor is measured as a template fit of $m_{e\gamma}$ in SR1, with the signal template taken from Z+Jets and $Z/W+\gamma$ MC where the photon is matched to a generated electron. The background template is taken from all other MC backgrounds, as well as Z+Jets and $Z/W+\gamma$ MC where the photon is matched to a generated photon or jet. To increase the statistics available for each template, the b-tagging requirement is lifted. The k-factor for $Z(\gamma)$ MC described earlier is applied before the fit is performed. The results of this fit are shown in Figure 7.16 and give a scale factor of:

$$SF_{e\to\gamma} = 1.58 \pm 0.03 \pm 0.02 \tag{7.18}$$

This scale factor is applied to the Z+Jets and $Z/W+\gamma$ backgrounds for the electron channel both with and without b-tagging required, in addition to the $Z(\gamma)$+Jets k-factor derived from di-lepton events previously.

7.3.5 Photon Purity

The choice of a loose cut-based photon identification is due to the high efficiency (∼90%) of its selection, despite its low overall purity of real, prompt photons. The high $\not{E}_{\mathrm{T}}$ backgrounds in each of the signal regions is then a rather impure mixture of $t\bar{t}+\gamma(\gamma)$ and $t\bar{t}+jets$ with many selected 'photons' being misidentified jets. As a search optimized for discovery and mass exclusion reach, the precise composition of the signal region samples is of no concern – only the accurate estimation of the $\not{E}_{\mathrm{T}}$ distribution is necessary [4].

The pertinent question of photon purity is if there is any dependence of the $\not{E}_{\mathrm{T}}$ shape on the composition of these backgrounds. The highly electromagnetic jets contributing to the signal regions are known to have a poorer energy resolution than prompt photons, and create

[4]If a significant excess is observed, the photon purity would be sensitive to the characterization of the excess, and would be analyzed more closely.

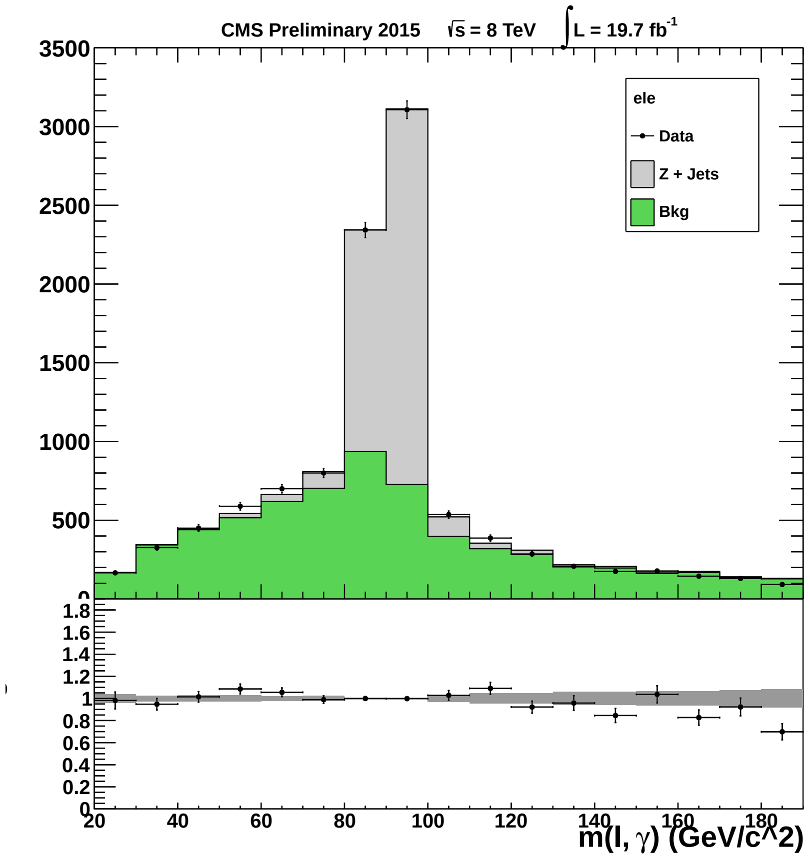

Figure 7.16: Template fit result for the electron to photon misidentification rate. Exactly one photon is required (SR1) and the b-tagging requirement is removed. Errors shown are statistical only.

instrumental $\not\!\!E_{\mathrm{T}}$ due to their mismeasurement. However compared to other photon $\not\!\!E_{\mathrm{T}}$ searches, the requirement of a $t\bar{t}$ final state is expected to far more strongly affect the resolution of the $\not\!\!E_{\mathrm{T}}$ calculation with its significant hadronic activity.

Of further importance to the photon purity is the lack of a dedicated $t\bar{t}+\gamma$ sample of simulated events. Two assertions are made supporting that such a sample is not necessary: (i) the cross section of SM $t\bar{t}+\gamma\gamma$ production is extremely small, such that any observed events would not have both photon momenta large enough where PYTHIA QED showering could not describe them properly, and (ii) the $\not\!\!E_{\mathrm{T}}$ distribution is observed to be very similar between events with prompt photons and misidentified jets. These facts do not constrain the jet misidentification rate, nor the $t\bar{t}+\gamma\gamma$ rate, so the analysis is solely focused on a shape-based comparison rather than an absolute background yield. The overall normalization of the $t\bar{t}+jets$ and $t\bar{t}+\gamma(\gamma)$ backgrounds are allowed to float freely in the upper limit calculation.

This section describes a measurement of the simulated photon purity and an adjustment to the purity of the observed data. The effect of this purity adjustment on the $\not\!\!E_{\mathrm{T}}$ distribution shape is scrutinized to test the aforementioned assumptions. The scale factors derived for this adjustment are not applied to the central value of the background estimates, as the nominal yields are allowed to float.

Purity Measurement

The photon purity is measurable as a template fit in variables discriminating between prompt photons and jets. The most discriminating variables are the charged hadron isolation (chHadIso) and $\sigma_{i\eta i\eta}$ of candidate photons; these same variables are inverted for the control region definition of 'fake' photons. Rather than inverting these requirements to enhance the non-prompt sample, the requirements are lifted to extend the fit range of a template fit in each.

The signal and background templates are formed for both chHadIso and $\sigma_{i\eta i\eta}$ in SR1 by removing the requirement on each variable (not both like in the fake photon definition) and matching the reconstructed photon to its generator-level MC truth as outlined in Section 7.3.4. The signal template is taken from $t\bar{t}+jets$ and $t\bar{t}+\gamma$ MC where the photon is matched to either an electron or a photon, and the background template is taken from $t\bar{t}+jets$ and $t\bar{t}+\gamma$ where the photon is not matched. All other backgrounds are subtracted from the observed data. The $\not\!\!E_{\mathrm{T}}$ is also required to be less than 50 GeV to limit signal presence. The results of each fit are shown in Figure 7.17, and listed in Tables 7.19 and 7.20.

The χ^2/N_{dof} is quite poor for the $\sigma_{i\eta i\eta}$ template fit; this is assumed by other analyses [143] to be caused by a mismodeling of shower evolution in GEANT4. This result is taken as an informative backup to the more successful charged hadron isolation result, and as neither result

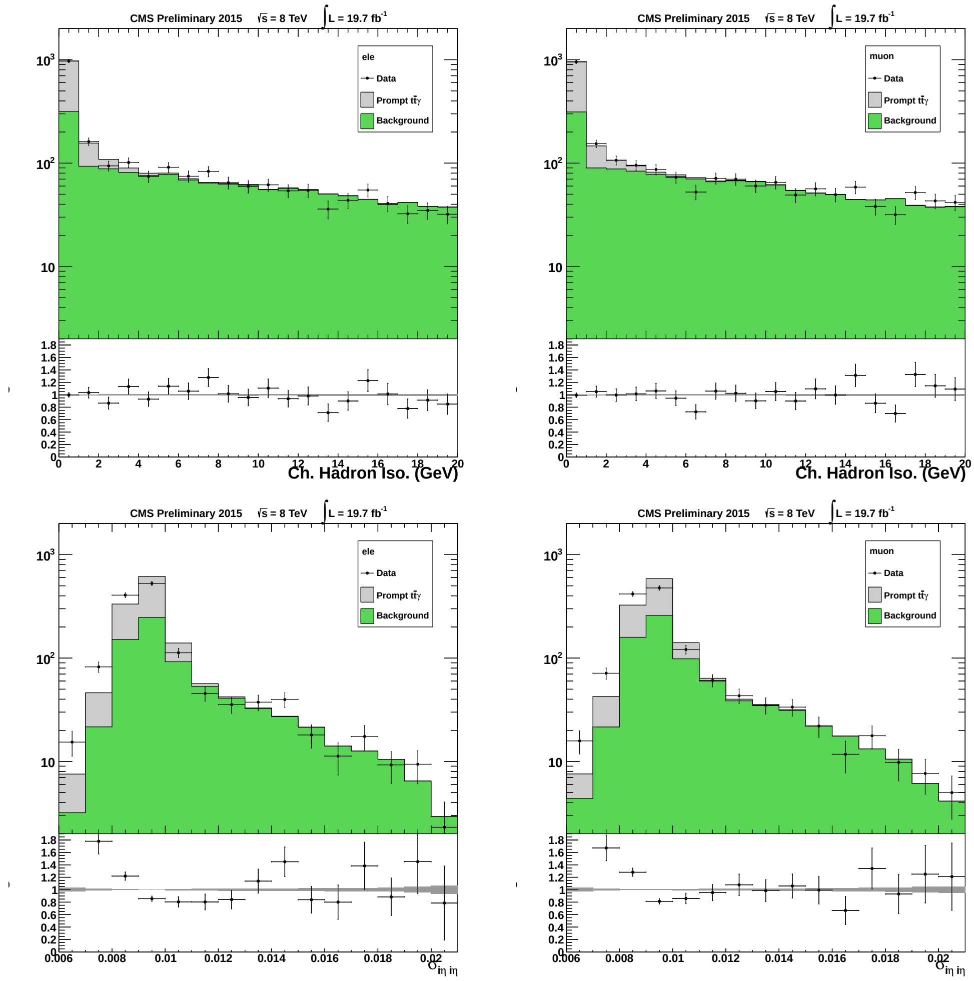

Figure 7.17: Template fit results for the electron (left) and muon (right) channels, in the photon variables charged hadron isolation (top) and $\sigma_{i\eta i\eta}$ (bottom). The low side of the $\sigma_{i\eta i\eta}$ peak is known to be in poor agreement with data due to a mismodeling of shower evolution in GEANT4.

is used in the central estimate of the backgrounds this is not seen as problematic.

Channel	γ Purity	
	MC	Fit
e		
chHadIso	$0.597 \pm 0.002 \pm 0.009$	$0.623 \pm 0.010 \pm 0.004$
$\sigma_{i\eta i\eta}$	$0.589 \pm 0.001 \pm 0.009$	$0.526 \pm 0.011 \pm 0.007$
μ		
chHadIso	$0.579 \pm 0.001 \pm 0.011$	$0.619 \pm 0.01 \pm 0.004$
$\sigma_{i\eta i\eta}$	$0.572 \pm 0.001 \pm 0.011$	$0.485 \pm 0.012 \pm 0.013$

Table 7.19: Photon purity from simulation and fit to data. The $\sigma_{i\eta i\eta}$ fit method suffers from a mismodeling of the shower evolution in GEANT4, but otherwise the MC agrees well with data.

Channel	SF		SF	
	Prompt	Non-prompt	$t\bar{t} + jets$	$t\bar{t} + \gamma$
e				
chHadIso	$1.18 \pm 0.06 \pm 0.04$	$1.06 \pm 0.03 \pm 0.06$	$1.17 \pm 0.01 \pm 0.04$	$1.09 \pm 0.01 \pm 0.05$
$\sigma_{i\eta i\eta}$	$1.01 \pm 0.08 \pm 0.04$	$1.30 \pm 0.09 \pm 0.08$	$1.04 \pm 0.01 \pm 0.04$	$1.23 \pm 0.01 \pm 0.06$
μ				
chHadIso	$1.16 \pm 0.06 \pm 0.04$	$0.98 \pm 0.03 \pm 0.06$	$1.14 \pm 0.01 \pm 0.04$	$1.02 \pm 0.01 \pm 0.05$
$\sigma_{i\eta i\eta}$	$0.91 \pm 0.08 \pm 0.03$	$1.3 \pm 0.08 \pm 0.1$	$0.96 \pm 0.01 \pm 0.03$	$1.21 \pm 0.01 \pm 0.08$

Table 7.20: Photon purity scale factors. As the templates are from prompt and non-prompt truth-matching to reconstructed photons, there is a small difference between scale factors on the matched templates and inclusive MC samples. The scale factors for $t\bar{t} + jets$ and $t\bar{t} + \gamma$ samples are listed as well, being a weighted average of the matched scale factors. Despite a known issue with the $\sigma_{i\eta i\eta}$ modeling, the scale factors agree with one another within uncertainties.

The effect of applying the scale factors in Table 7.20 on the $t\bar{t} + jets$ and $t\bar{t} + \gamma$ samples is shown in Figure 7.18. In SR2 with two photon purities to adjust, these scale factors are applied twice (ie their square). Besides affecting an overall scale adjustment, the variation of $\not\!\!E_{\mathrm{T}}$ shape is extremely limited — on the order of a few percent, well below statistical fluctuations. As mentioned earlier in this section, it is seen here that the $\not\!\!E_{\mathrm{T}}$ distribution is not appreciably different due to the true source of reconstructed photons. This is taken as a demonstration that a dedicated $t\bar{t} + \gamma\gamma$ sample is not necessary, as the shape of $\not\!\!E_{\mathrm{T}}$ is well modeled even with low energy radiated photons and misidentified jets. To eliminate dependence on the $t\bar{t} + \gamma\gamma$ cross section, the $t\bar{t} + jets$ and $t\bar{t} + \gamma$ normalizations are allowed to float freely in the final upper limit determination. For the background-only hypothesis, the post-fit values for these floating normalizations are found to be upwards fluctuations of 11–24% for SR1 and 45–52% for SR2; the correlation with signal-strength for the signal+background hypothesis is found to be negligible.

7.3.6 Control Region Comparison

The performance of the simulation in describing the $E_{\mathrm{T}}^{\mathrm{miss}}$ distribution of background processes is observed by comparing data to MC in the control regions. The control regions are defined by selecting 'fake' photons (described in Section 7.2.7) and separated by fake multiplicity in

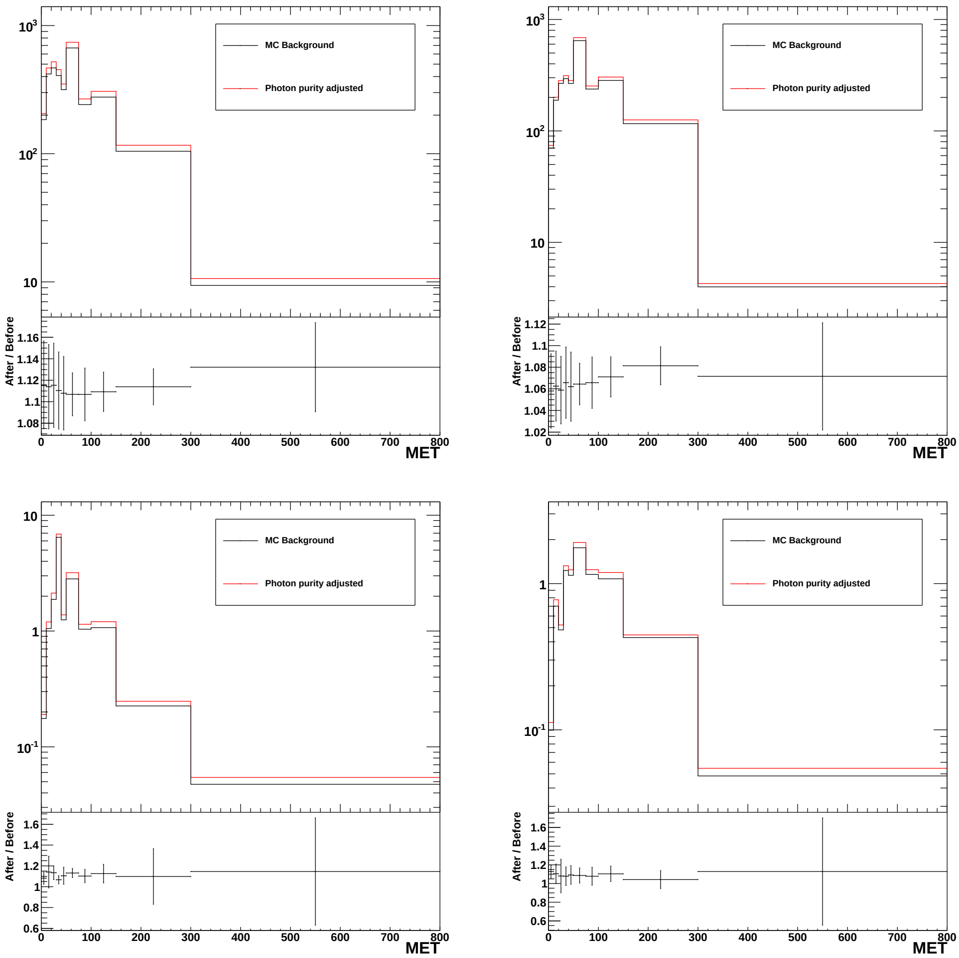

Figure 7.18: Comparison of the total background $\not{E}_{\mathrm{T}}$ shape before and after reweighting with the charged hadron isolation scale factors $t\bar{t} + jets$ and $t\bar{t} + \gamma$ samples. The electron (left) and muon (right) channels are shown both for SR1 (top) and SR2 (bottom). Besides an overall normalization adjustment, the effect on the shape of the distribution is extremely small and well below statistical variations.

the same way as the signal regions (see Section 7.2.9). By selecting events failing the nominal isolation or $\sigma_{i\eta i\eta}$ requirements yet passing the H/E requirement for photons, the control regions maintain the electromagnetic energy scale and resolutions of the signal region photons but with a greatly enhanced population of the photon-like jets contributing the most to poorly measured and simulated $E_{\mathrm{T}}^{\mathrm{miss}}$ events comprising the background estimate. Furthermore by only altering the photons in the control regions, the dominant effect on $E_{\mathrm{T}}^{\mathrm{miss}}$ resolution by the $t\bar{t}$ system can be compared against the smaller effect of the photons. By comparing data to MC in these samples, an estimate of any failings of the MC can be extracted as a bin-by-bin rate of any differences; this is taken as an additional systematic uncertainty on the background estimate in the signal regions.

The data and MC for the control regions are shown in Figure 7.19 with total event yields listed in Tables 7.21 and 7.22. The agreement is very good for one photon events in CR1 (within $\sim$10%), however the extremely small sample size in CR2 makes separating systematic and statistical fluctuations impossible in a bin-by-bin approach – thus the shape systematic uncertainty for SR2 is taken from the difference in CR1 as well. The precise implementation of this uncertainty is described in Section 7.4.

Channel	CR1	CR2
QCD	157 ± 38	–
$t\bar{t}$ + jets	2766 ± 9	12.0 ± 0.3
W + jets	279 ± 3	1.36 ± 0.02
Z + jets	132 ± 2	0.01 ± 0.00
Single t	141 ± 2	0.77 ± 0.02
Diboson	7.9 ± 0.1	–
Vγ	9.9 ± 0.3	–
$t\bar{t} + W$	8.1 ± 0.1	0.04 ± 0.00
$t\bar{t} + Z$	5.9 ± 0.1	0.08 ± 0.01
$t\bar{t} + \gamma$	95 ± 1	1.26 ± 0.07
Total Background	3444 ± 10	15.5 ± 0.3
Data	3794	12

Table 7.21: Observed data and expected event yields in 19.7 fb^{-1} for the control regions in the electron channel. The errors represented in this table are statistical only.

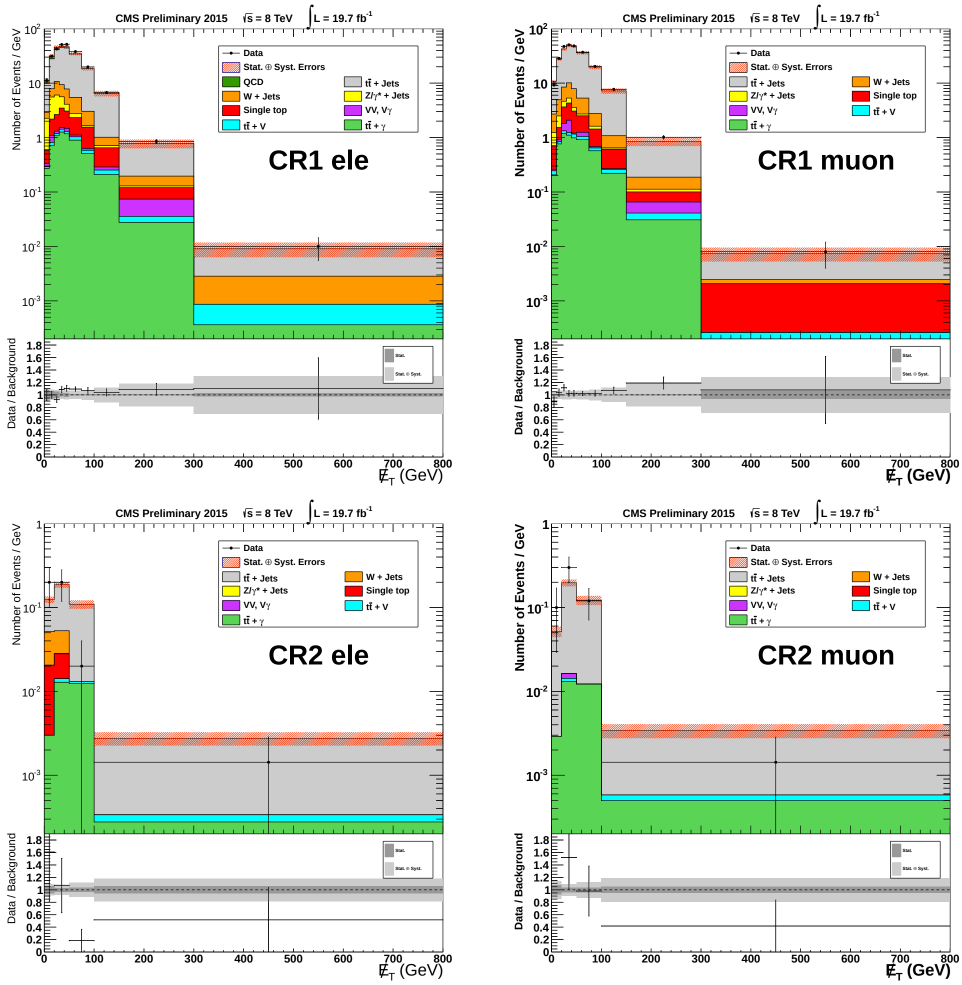

Figure 7.19: Comparison of data and MC in $E_{\mathrm{T}}^{\mathrm{miss}}$ for the control regions. Electron (left) and muon (right) channels are shown for both CR1 (top) with one fake photon and CR2 (bottom) with two or more fake photons. The small disagreement of less than ∼10% between data and MC in CR1 is taken as an additional shape-based systematic uncertainty in the signal regions. The comparatively poor agreement in CR2 is attributable to the very small number of events in data and is not taken as an additional uncertainty.

Channel	CR1	CR2
QCD	–	–
$t\bar{t}$ + jets	3034 ± 9	13.9 ± 0.3
W + jets	296 ± 3	–
Z + jets	53 ± 0	–
Single t	143 ± 2	–
Diboson	6.4 ± 0.1	0.06 ± 0.00
Vγ	18.7 ± 1.8	–
$t\bar{t} + W$	7.4 ± 0.1	0.06 ± 0.02
$t\bar{t} + Z$	6.7 ± 0.1	0.03 ± 0.00
$t\bar{t} + \gamma$	96 ± 1	1.41 ± 0.08
Total Background	3661 ± 10	15.5 ± 0.4
Data	3813	18

Table 7.22: Observed data and expected event yields in 19.7 fb^{-1} for the control regions in the muon channel. The errors represented in this table are statistical only.

7.4 Systematic Uncertainties

Considered in this analysis are several types of systematic uncertainties: those that affect only the overall rate of a background or signal process, those that affect only the overall shape of the $E_{\mathrm{T}}^{\mathrm{miss}}$ distribution of a background or signal process, or those that affect both. For systematic effects affecting both rate and shape, both contributions are treated simultaneously so that they are completely correlated. Unless otherwise noted, each effect is treated as 100% correlated between all background and signal processes. The following is a list and description of the systematic sources of uncertainty considered. The effect of each systematic on the relative event yield is detailed in Table 7.25, and for systematics that affect the shape of the $E_{\mathrm{T}}^{\mathrm{miss}}$ distribution in signal regions the magnitude of the effect is shown in Appendix B.

Luminosity: The uncertainty on the total integrated luminosity is 2.6%; this affects all backgrounds and signal rates.

Background cross sections: The cross section normalizations for expected background yields are calculated from the theoretical predictions with at least NLO accuracy. Uncertainties affecting these overall rates are listed in Table 7.23. Each process is given an uncertainty due to its Parton Distribution Function (PDF) and QCD scaling, and each of these depends on the production mechanism of each particular process. For factors contributing to these uncertainties that are common to multiple processes, they are treated as 100% correlated. For example Z+Jets is produced in quark-antiquark annihilation ($q\bar{q}$) and its PDF uncertainty is correlated with that of other $q\bar{q}$ initiated processes. The $V\gamma$ cross section uncertainty is taken conservatively as $\pm 50\%$.

Signal cross sections: As described in Section 7.1.3, the uncertainties on strong stop-pair production are calculated using NLL-fast and PROSPINO and the PDF4LHC recommendations. In a range of stop masses of 125–1000 GeV, the overall rate uncertainty in signal events ranges approximately from 16 to 28% [144].

Jet energy scale (JES): The JES systematic is evaluated by shifting the jet energy scale up and down by one standard deviation using the standard JetMET POG [145] procedure. All events in data and MC are re-analyzed with the shifted JES, and the $E_{\mathrm{T}}^{\mathrm{miss}}$ spectrum of signal region events is again collected.

b-tag scale factors: The systematic uncertainty on b-tagging events in MC is evaluated by independently scaling light and heavy flavor scale factors up and down by their uncertainties prescribed by the BTV POG [146].

Process	PDF			QCD Scale		
	gg	$q\bar{q}$	qg	$t\bar{t}$	V	VV
$t\bar{t}$ + jets	2.6%			$^{+2.5}_{-3.4}\%$		
W+jets		3.4%			$^{+0.65}_{-0.32}\%$	
Z+jets		3.3%			$^{+0.5}_{-0.31}\%$	
single t						
s-channel			3.4%	1.8%		
t-channel			2.0%	$^{+3.7}_{-0.53}\%$		
tW-channel			6.3%	2.6%		
single $\bar{t}$						
s-channel			4.5%	0.57%		
t-channel			$^{+2.9}_{-3.6}\%$	2.3%		
tW-channel			6.3%	2.7%		
Diboson						
WW			3.5%			4.0%
WZ			4.0%			4.0%
ZZ			3.6%			3.6%
W/Z + γ			50%			50%
$t\bar{t}$ +W		13%		29%		
$t\bar{t}$ +Z				$^{+9.2}_{-3.6}\%$		
$t\bar{t}$ +γ	$^{+2.6}_{-3.4}\%$			50%		

Table 7.23: Cross section uncertainties used for the background processes. Each column is an independent source of uncertainty, with all uncertainties within the same column taken as 100% correlated with one another.

Lepton ID and trigger scale factors: The systematic uncertainty arising from lepton scale factors are evaluated by varying the scale factors up and down by their uncertainties. These are expressed as two completely correlated sources added in quadrature: uncertainty in the lepton identification and isolation scale factors, and the lepton trigger scale factors. Electrons and muons are treated as separate nuisance parameters, each accounting for an approximate $\sim$1% uncertainty.

Photon ID scale factors: The systematic associated to the uncertainty in photon scale factors is evaluated by varying the scale factors up and down by their measured uncertainties. In Signal Region 2 (SR2) where two photons are required, the second photon's scale factor uncertainty is taken as completely uncorrelated to the first's, and the two are combined in quadrature. This effect accounts for an approximate 1.2% uncertainty in the final background yield.

Pileup reweighting: The uncertainty in reweighting MC events for pileup is evaluated by shifting the minimum bias cross section up and down by 5% of its nominal 69.4 mb value. The weights are recalculated with these shifted cross sections and applied to all events.

Top quark p_{T} reweighting: The systematic uncertainty from the reweighting of top quark p_{T}

in $t\bar{t}$ simulated events is evaluated as follows: in the downwards fluctuation, no reweighting is applied at all, and in the upwards fluctuation the reweighting is applied twice, i.e. the square of the weights is used. This scheme is chosen as appropriate because the difference between the nominal and uncorrected scales was the variation initially observed to warrant this correction, and the upwards fluctuation is chosen to be symmetric by reweighting twice.

Monte Carlo statistics: The effect of limited MC statistics in background and signal samples is evaluated in the manner described in [147, 148]. For each bin of $E_{\mathrm{T}}^{\mathrm{miss}}$ in each background and both channels, a nuisance parameter is included to allow that bin to float within its statistical uncertainty. This results in 42 additional nuisance parameters.

User-derived scale factors: The W+Jets, $Z(\gamma)$+Jets, and electron to photon fake rate adjustment derived in Sections 7.3.4 and 7.3.3 are not included as nuisance parameters, however are re-measured with the fluctuations of all other systematic uncertainties. The fit and statistical uncertainties in these scale factors are included in the statistical uncertainty of the background estimate.

QCD definition: The QCD multijet and γ + jet background is determined to be negligible for all signal regions due to the requirement of multiple electromagnetic objects and b-jets. However the data-driven QCD affects the measurement of the W+Jets scale factor used in the signal regions, and the choice of definition for the QCD lepton selection has a small effect on the final results from this. This systematic is evaluated by fluctuating the isolation requirement for QCD anti-isolated leptons up and down by 10% of the nominal definition (relIso ≥ 0.25). The data-driven QCD estimate is collected with these altered definitions and treated in the same way as the central value, and this effect is taken as the $\pm 1\sigma$ uncertainty for this definition. This effect is a small fluctuation in the W+Jets normalization, which is already very small in the signal regions, and ultimately the QCD definition systematic is negligibly small.

Additional $t\bar{t}$ and $t\bar{t}+\gamma$ rate uncertainty: This analysis is sensitive to Standard Model $t\bar{t}+\gamma\gamma$ production, a process which has not yet been measured closely. Due to the lack of directly simulated $t\bar{t}+\gamma\gamma$ events, the PYTHIA electromagnetic showering of second photons and MADGRAPH hadronization of jets faking photons must be relied on as the source for such events.

The $t\bar{t}+\gamma$ Monte Carlo has been shown to be in excellent agreement with the observed rate in data [149, 150]. The shape of the $E_{\mathrm{T}}^{\mathrm{miss}}$ resolution is also observed to be insensitive to fluctuations in the rate or kinematics of additional photon vertices in $t\bar{t}$ production and decay – see Section 7.3.5. Lastly, the SM production rate of $t\bar{t}+\gamma\gamma$ is extremely small, such that any events produced in the dataset used are highly unlikely to be with both photons having high-p_{T} or large radiation angles where the PYTHIA showering becomes inaccurate.

To parametrize the ignorance of the overall rates of $t\bar{t}+jets$, $t\bar{t}+\gamma$, and $t\bar{t}+\gamma\gamma$ production, these backgrounds are allowed to float freely in the upper limit determination. This is implemented with two ±100% log-uniform distributed nuisance parameter, each correlated between $t\bar{t}+jets$ and $t\bar{t}+\gamma$ in both electron and muon channels to. One of these is for SR1 only and the other for SR2 only, uncorrelated with one another to allow the global fit to float one-photon versus two-photon events and determine the appropriate rate of additional photons in SR2. The intercorrelations here are clarified in Table 7.24.

	$t\bar{t}+jets$				$t\bar{t}+\gamma$			
	SR1		SR2		SR1		SR2	
	e	μ	e	μ	e	μ	e	μ
float_ttg_ttjets_SR1	✓	✓			✓	✓		
float_ttg_ttjets_SR2			✓	✓			✓	✓

Table 7.24: Correlations of nuisance parameters for the floating of $t\bar{t}+jets$ and $t\bar{t}+\gamma$. Both backgrounds for both electrons and muons are allowed to float together within SR1 and independently within SR2. This allows their total contributions to float while keeping the lepton content the same, yet allowing the photon content to float as well.

Control Region $E_{\mathrm{T}}^{\mathrm{miss}}$ comparison: The difference between observed data and MC background estimates in the control regions is taken as an additional bin-by-bin shape systematic uncertainty. In translating the control regions to a description of the signal region, an additional piece is necessary. The procedure amounts to the fact that a conversion between the background estimates in each sample can be defined as:

$$\chi(\not{E}_{\mathrm{T}}) \equiv \frac{B_{SR}(\not{E}_{\mathrm{T}})}{B_{CR}(\not{E}_{\mathrm{T}})} \tag{7.19}$$

such that

$$B_{SR} = \chi \cdot B_{CR}$$

where B_{SR} and B_{CR} are the background estimates in the signal and control regions, binned in $\not{E}_{\mathrm{T}}$. In these terms the fractional uncertainty of the signal region background estimate is:

$$\frac{\sigma(B_{SR})}{B_{SR}} = \sqrt{\left(\frac{\sigma(B_{CR})}{B_{CR}}\right)^2 + \left(\frac{\sigma_\chi}{\chi}\right)^2} \tag{7.20}$$

When no systematic is considered for the control region background (i.e. $\sigma(B_{CR}) = 0$) the above expression reduces simply to the uncertainty of the signal region background. The additional systematic uncertainty of the difference between observed data and background in the control region modifies this as:

$$\frac{\sigma(B_{SR})}{B_{SR}} = \sqrt{\left(\frac{Obs_{CR} - B_{CR}}{B_{CR}}\right)^2 + \left(\frac{\sigma(B_{SR}/B_{CR})}{B_{SR}/B_{CR}}\right)^2} \tag{7.21}$$

For the systematic in SR2 where there is not enough statistics available in CR2 to provide a reasonable data-to-MC comparison, the data-to-MC difference in CR1 is simply used – this results in a third term due to the difference in background shapes in SR1 and SR2:

$$B_{SR2} \equiv \chi\, \xi\, B_{CR1} \tag{7.22}$$

$$= \left[\frac{B_{SR1}(\not{E}_{\mathrm{T}})}{B_{CR1}(\not{E}_{\mathrm{T}})}\right]\left[\frac{B_{SR2}(\not{E}_{\mathrm{T}})}{B_{SR1}(\not{E}_{\mathrm{T}})}\right] \cdot B_{CR1} \tag{7.23}$$

$$\Rightarrow$$

$$\frac{\sigma(B_{SR2})}{B_{SR2}} = \sqrt{\left(\frac{Obs_{CR1} - B_{CR1}}{B_{CR1}}\right)^2 + \left(\frac{\sigma(B_{SR1}/B_{CR1})}{B_{SR1}/B_{CR1}}\right)^2 + \left(\frac{\sigma(B_{SR2}/B_{SR1})}{B_{SR2}/B_{SR1}}\right)^2} \tag{7.24}$$

In summary the fractional, bin-by-bin difference between observed data and MC in CR1 is taken as a systematic uncertainty on the total background, as well as the error on the ratio of the background estimates in each sample being compared. The first two terms in 7.22 are taken as correlated between SR1 and SR2 and uncorrelated between electron and muon channels, while the third term is used only for SR2 and uncorrelated between channels and the first two terms.

Source	Shape	Rate	Notes
Luminosity		2.6%	Signal and all backgrounds
Lepton ID/Trigger	✓	0.1 – 1.1 %	”
Photon ID	✓	0.6 – 1.5 %	”
Pileup	✓	0.1 – 1.8 %	”
JES	✓	1.8 – 4.8 %	”
b-tagging	✓	0.6 – 2.6 %	”
Top Quark P_T	✓	$t\bar{t}$+jets only	
QCD Scale ($t\bar{t}$)		2.5 – 25 %	Scale uncertainty for NLO $t\bar{t}$ and single top backgrounds
QCD Scale (V)		0.3 – 0.7 %	Scale uncertainty for NNLO W and Z backgrounds
QCD Scale (VV)		1 – 20 %	Scale uncertainty for NLO diboson backgrounds
PDF (gg)		2.6 – 10 %	PDF uncertainty for gg-initiated backgrounds ($t\bar{t}$, $t\bar{t}+Z$, $t\bar{t}+\gamma$)
PDF ($q\bar{q}$)		3.3 – 3.4 %	PDF uncertainty for $q\bar{q}$-initiated backgrounds ($t\bar{t}+W$, W, Z)
PDF (qg)		3.6 %	PDF for qg-initiated backgrounds (single top)
Control Region Δ	✓	10 – 20 %	Observed data discrepancy in CR1
SR1/CR1 Ratio	✓	1 – 8 %	Shape difference between SR1 and CR1
SR2/SR1 Ratio	✓	10 – 50 %	Shape difference between SR2 and SR1 – only for SR2
$t\bar{t}$ Floating Normalization		100 %	Log-uniform distributed nuisance paramater floating $t\bar{t}$+jets and $t\bar{t}+\gamma$ backgrounds
SUSY Cross Sections		16 – 28 %	Signal only

Table 7.25: Summary of systematic uncertainties considered. Each source is treated as a single, independent nuisance parameter in the upper limit calculation. Where range are given for the overall effect on rate, the range covers both the electron/muon channels and up/down fluctuations. The SUSY cross section rate uncertainty ranges from stop masses of 125–1000 GeV/c^2.

7.5 Results

The observed data in SR1 and SR2 are summarized in Tables 7.26 and 7.27, and shown in Figures 7.20 – 7.23 below.

Considering the overall floating of $t\bar{t}+jets$ and $t\bar{t}+\gamma$ backgrounds described in Section 7.3.5, no clear excess or deficit can be found in the overall background yield and observed data counts. While the total event yields do differ from the predicted background levels, these figures are inclusive of $\not\!\!E_{\mathrm{T}}$ and could represent a fluctuation of either background or the presence of signal; the shape-based comparison of $\not\!\!E_{\mathrm{T}}$ is far more sensitive to such a hypothesis. No clear shape discrepancy is observable in all four signal regions as would be expected of the observation of GMSB SUSY.

Channel	SR1	SR2
$t\bar{t}$ + jets	901 ± 4	0.47 ± 0.04
W + jets	100 ± 2	–
Z + jets	816 ± 10	1.80 ± 0.13
Single t	63 ± 2	–
Diboson	14.9 ± 0.1	0.11 ± 0.00
Vγ	239 ± 3	6.2 ± 0.1
$t\bar{t}+W$	3.8 ± 0.1	0.03 ± 0.02
$t\bar{t}+Z$	4.3 ± 0.1	0.09 ± 0.01
$t\bar{t}+\gamma$	953 ± 2	7.3 ± 0.2
Total Background	3095 ± 12	16.0 ± 0.3
GMSB (460_175)	82 ± 2	44 ± 2
GMSB (560_325)	21 ± 1	7.4 ± 0.3
Data	3266	14

Table 7.26: Observed data and expected event yields in 19.7 fb^{-1} for signal and backgrounds in the electron channel. The errors represented in this table are statistical only.

Channel	SR1	SR2
$t\bar{t}$ + jets	944 ± 4	0.95 ± 0.12
W + jets	83 ± 2	0.11 ± 0.01
Z + jets	100 ± 1	0.22 ± 0.00
Single t	67 ± 2	–
Diboson	7.8 ± 0.1	0.08 ± 0.00
Vγ	192 ± 3	–
$t\bar{t}+W$	3.8 ± 0.1	0.04 ± 0.00
$t\bar{t}+Z$	2.8 ± 0.1	–
$t\bar{t}+\gamma$	973 ± 2	6.7 ± 0.2
Total Background	2374 ± 6	8.1 ± 0.3
GMSB (460_175)	80 ± 2	43 ± 2
GMSB (560_325)	22 ± 1	10.7 ± 0.6
Data	2475	16

Table 7.27: Observed data and expected event yields in 19.7 fb^{-1} for signal and backgrounds in the muon channel. The errors represented in this table are statistical only.

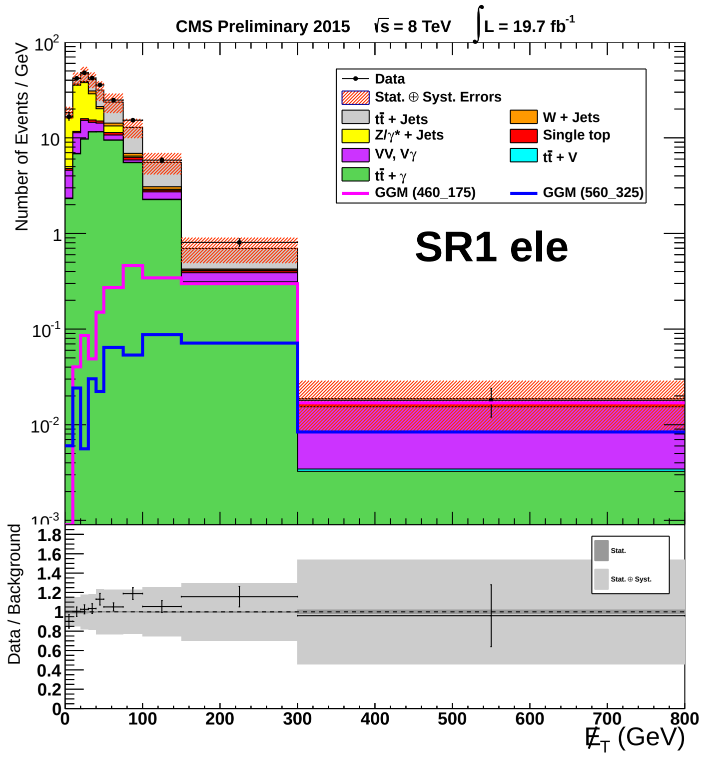

Figure 7.20: Comparison of the $\not\!\!E_T$ of observed data and predicted backgrounds in SR1 for the electron channel.

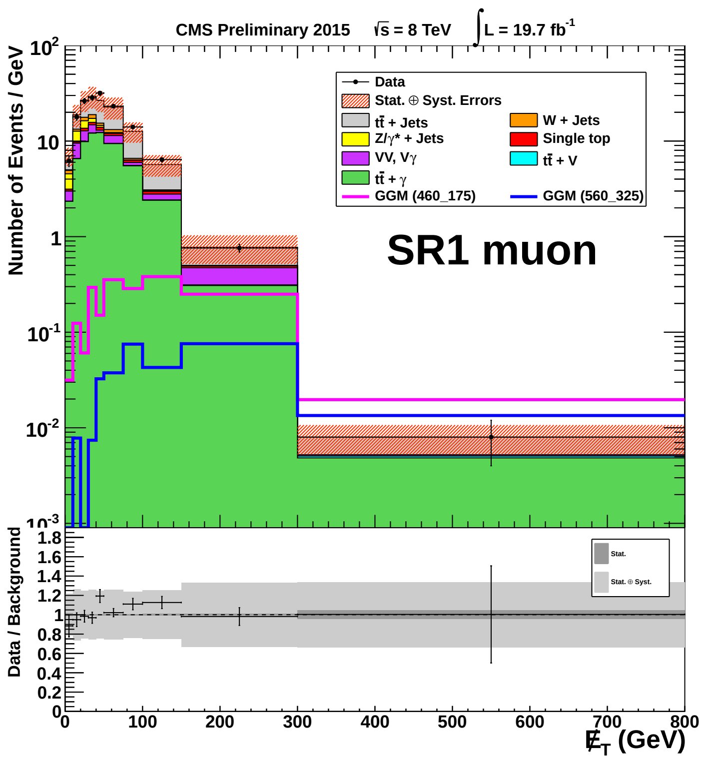

Figure 7.21: Comparison of the $\not\!\!E_T$ of observed data and predicted backgrounds in SR1 for the muon channel.

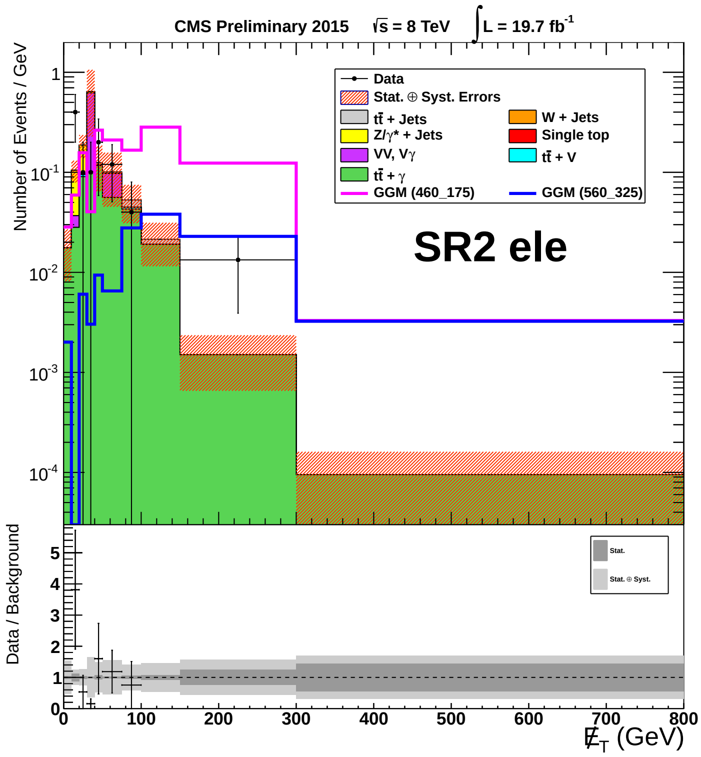

Figure 7.22: Comparison of the $\not\!\!E_T$ of observed data and predicted backgrounds in SR2 for the electron channel.

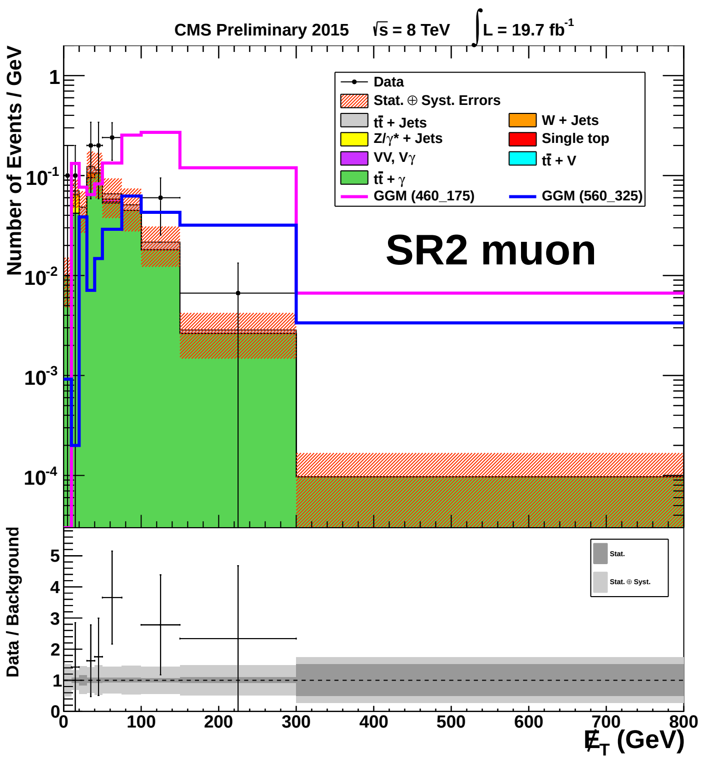

Figure 7.23: Comparison of the $\not\!\!E_T$ of observed data and predicted backgrounds in SR2 for the muon channel.

Chapter 8

Interpretation of Results

As no significant shape-based excess is observed across all four signal regions in Section 7.5, the results are interpreted by calculating upper limits on the production rate of GMSB SUSY models in a range of stop and bino masses. The generation of signal models is described in detail in Section 7.1.3, and the event selection criteria is applied to each generated event; the acceptance times efficiency is shown in Figure 8.1 and the NLO cross sections are shown in Figures 8.2.

The acceptance times efficiency exhibits several features affecting experimental reach. The compressed mass region ($m_{\text{stop}} - m_{\text{bino}} < m_{\text{top}}$) where the mass difference between stop and bino is not large enough to produce on-shell top quarks is severely limited by the requirement of 30 GeV b-jets and leptons. The selection efficiency also decreases as this mass difference becomes very large as the jets from boosted top quark decays tend to merge spatially and the jet multiplicity requirement limits sensitivity. High-p_{T} jets in boosted top decays suffer as well from reduced efficiency of the b-tagging algorithm, due to three effects [151]: the track impact parameter resolution being higher at low p_{T}, the decay lengths of heavy hadrons which scale with jet p_{T}, and the track selection criteria used in the tagging algorithm. Lastly as bino masses increase, there is increased phase space available for $\tilde{\chi}_1^0 \to Z\tilde{G}$ and $\tilde{\chi}_1^0 \to H\tilde{G}$ decays without photons, limiting the efficiency of requiring two photons.

While models in the compressed mass region ($m_{\text{stop}} - m_{\text{bino}} < m_{\text{top}}$) are generated, upper limits for these models are not considered due to concerns about the simulation of the decays of off-shell top quarks and the PYTHIA factorization of three-body stop decays ($\tilde{t} \to W^+ b\tilde{\chi}_1^0$) for such mass splittings. Flavor-violating stop decays and heavily mixed squark states are not considered, but the requirement of isolated leptons would strongly limit sensitivity to decays such as $\tilde{q} \to c\tilde{\chi}_1^0$ that could dominate in this region.

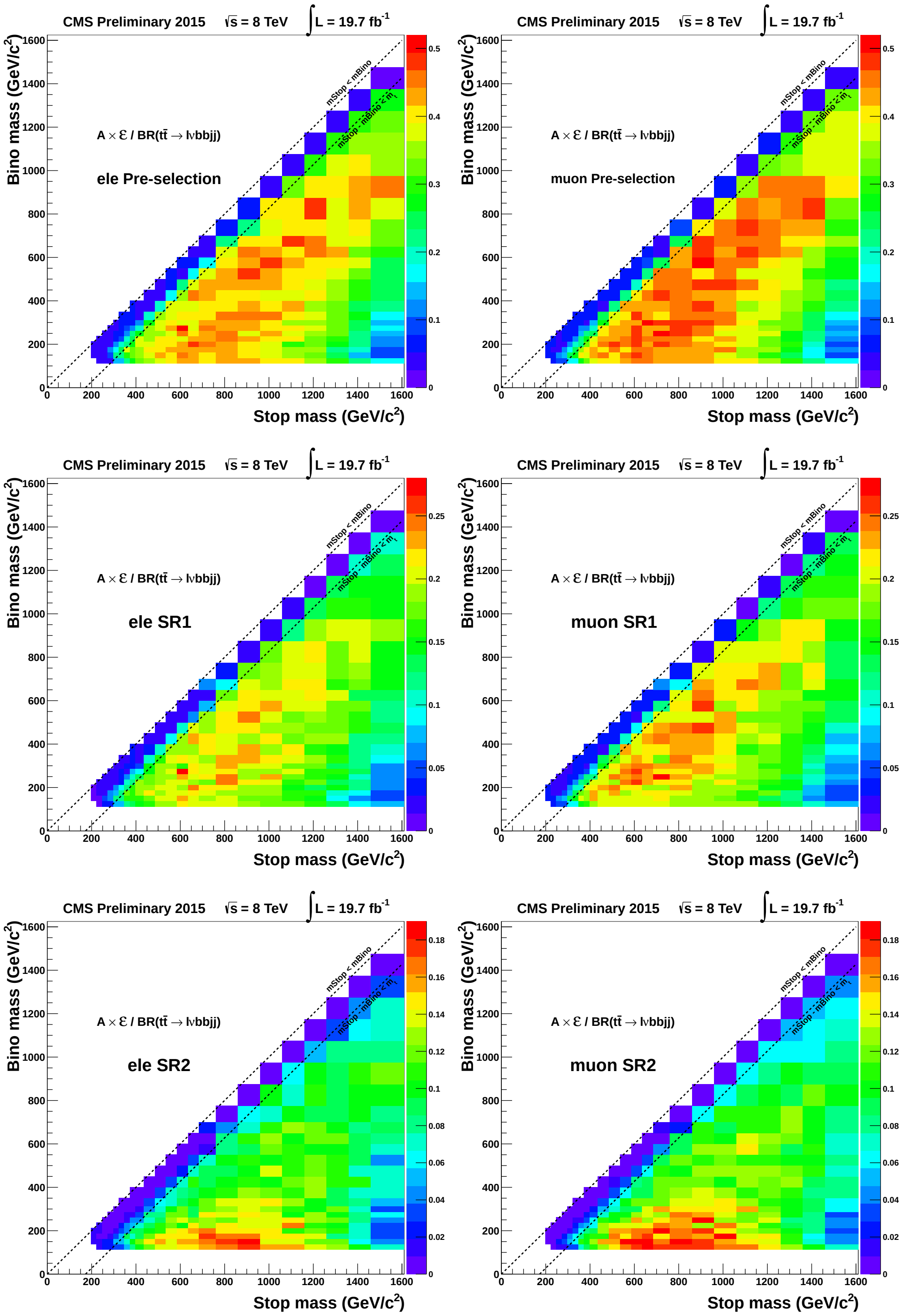

Figure 8.1: Acceptance times efficiency, relative to the branching ratio of $t\bar{t}$ decaying to a single lepton and inclusive of $\not{E}_{\mathrm{T}}$. Shown here is the electron (left) and muon (right) channels for the pre-selection (top), SR1 (middle), and SR2 (bottom). The pre-selection is shown for reference to compare the effect of requiring the first photon.

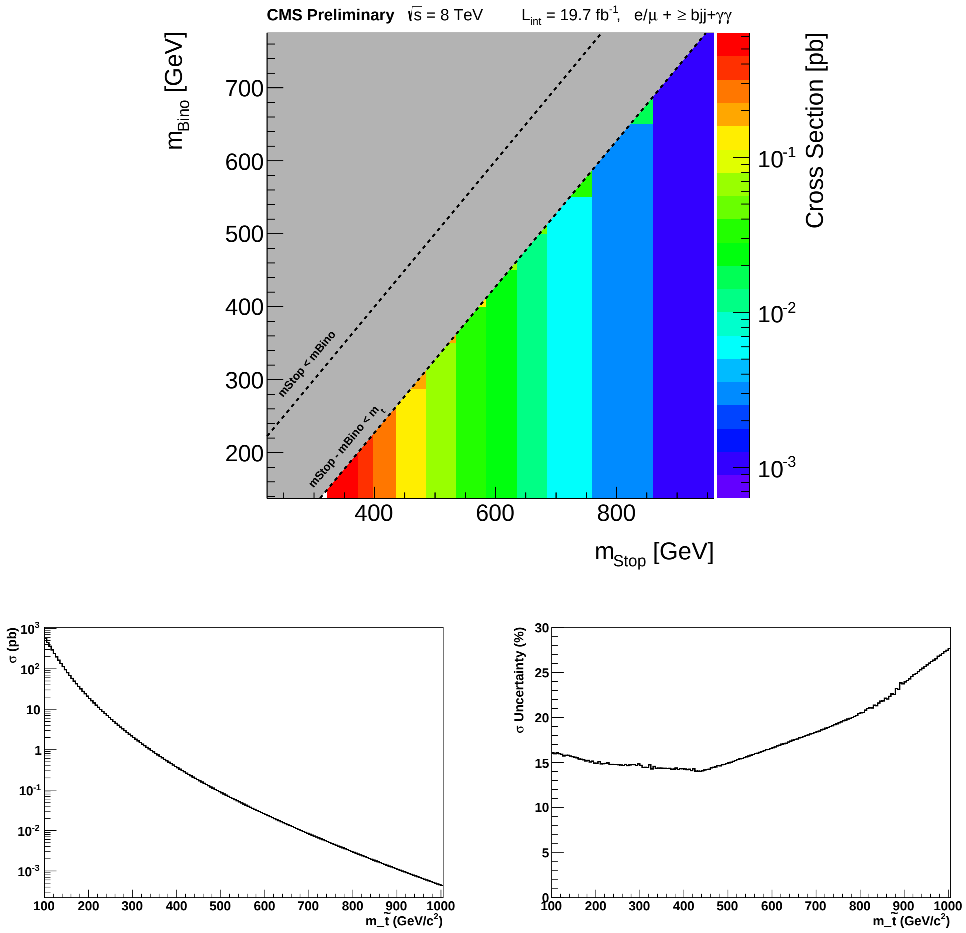

Figure 8.2: NLO cross sections for the GMSB SUSY models considered in the interpretation of the results (top). The production rate depends only on the stop mass, shown one-dimensionally (bottom left) with its relative uncertainty (bottom right) used as a systematic uncertainty.

8.1 Statistical Method

Upper limits are calculated using the 'modified frequentist' method, or CL$_s$ [152], using a profiled likelihood ratio as the test statistic [153]. What follows is a brief summary of the precise implementation detailed in the 2011 ATLAS + CMS Higgs limit combination procedure [154].

The likelihood of 'data', either the experimental observation or pseudo-data used to construct sampling distributions, given the signal strength modifier μ and the set of nuisance parameters θ is defined as:

$$\mathcal{L}(\text{data}\,|\,\mu,\theta) \equiv \text{Poisson}\big(\text{data}\,|\,\mu\cdot s(\theta)+b(\theta)\big)\cdot p(\tilde{\theta}\,|\,\theta) \tag{8.1}$$

$$= \prod_i \frac{(\mu s_i + b_i)^{n_i}}{n_i!} e^{-(\mu s_i + b_i)}\cdot p(\tilde{\theta}\,|\,\theta) \tag{8.2}$$

where s_i, b_i, and n_i are respectively the expected signal, background, and observed data in bin i. The product is over the 10 bins of $\not{E}_{\mathrm{T}}$ shown in Figures 7.20 – 7.23: [0, 10), [10, 20), [20, 30), [30, 40), [40, 50), [50, 75), [75, 100), [100, 150), [150, 300), and [300, ∞) GeV.

Systematic Uncertainties As Nuisance Parameters

The systematic error probability distribution function (*pdf*) $\rho(\theta\,|\,\tilde{\theta})$, where $\tilde{\theta}$ is the default value of the nuisance parameters, reflects the degree of confidence in what the true value of θ might be. This is re-interpreted as a 'posterior' arising from real or imaginary measurements $\tilde{\theta}$, as given by Bayes' theorem:

$$\rho(\theta\,|\,\tilde{\theta}) \sim p(\tilde{\theta}\,|\,\theta)\cdot\pi_\theta(\theta), \tag{8.3}$$

where $\pi_\theta(\theta)$ are expressions of the confidence in a hypothesis before these 'measurements' are made, called 'hyper-priors'. The re-interpretation of the systematic error *pdf* in terms of the *pdf* of an auxiliary 'measurement' , $p(\tilde{\theta}\,|\,\theta)$, allows the likelihood of the observed measurement to be constrained in a frequentist calculation; it also allows for the construction of sampling distributions of the test statistic in the frequentist prescription. For rate systematic uncertainties, this auxiliary *pdf* is taken as a log-normal distribution:

$$\rho(\theta) = \frac{1}{\sqrt{2\pi}\ln(\kappa)}\exp\left(-\frac{(\ln(\theta/\tilde{\theta}))^2}{2(\ln\kappa)^2}\right)\frac{1}{\theta} \tag{8.4}$$

where the κ parameter determines the width of this distribution and $\tilde{\theta}$ is the nominal value of the observable. The $t\bar{t}+jets$ and $t\bar{t}+\gamma$ backgrounds are additionally allowed to float in normalization by applying a log-uniform distributed *pdf.*

For shape systematic uncertainties, a 'vertical morphing' technique [155] is applied. The $\not{E}_{\mathrm{T}}$ is recalculated for the $\pm 1\sigma$ fluctuations of each shape-based systematic and supplied to this method; a single, Gaussian-distributed nuisance parameter is constructed to interpolate a Taylor expansion of the deviations from the nominal value. This interpolation is taken as quadratic for fluctuations within $\pm 1\sigma$, and linearly beyond that from the nominal value.

Limit-Setting Procedure

To compare the compatibility of the data with the background-only and signal+background (of some signal strength μ) hypotheses, the test statistic is defined as the profile likelihood ratio and constructed as:

$$\tilde{q}_\mu = -2\ln\frac{\mathcal{L}(\mathrm{data}\,|\,\mu,\hat{\theta}_\mu)}{\mathcal{L}(\mathrm{data}\,|\,\hat{\mu},\hat{\theta})}, \qquad 0 \leq \hat{\mu} \leq \mu \tag{8.5}$$

where $\hat{\theta}_\mu$ is the maximum likelihood estimation of θ given μ, and $\hat{\mu}$ and $\hat{\theta}$ correspond to the global maximum of the likelihood.

The constraint $0 \leq \hat{\mu}$ is the physical requirement that the signal rate be non-negative, and the upper constraint $\hat{\mu} \leq \mu$ is imposed to ensure a one-sided confidence interval – physically this ensures that upward fluctuations of the data such that $\hat{\mu} > \mu$ are not considered evidence the signal hypothesis of signal strength μ.

The best-fit, maximum likelihood values for the nuisance parameters describing the observed data are found for the *background-only* hypothesis ($\hat{\theta}_0^{obs}$) and for the *signal+background* hypothesis ($\hat{\theta}_\mu^{obs}$). These are used to generate *pseudo-data* datasets with which to construct *pdf*s $f(\tilde{q}_\mu\,|\,\mu,\hat{\theta}_\mu^{obs})$ and $f(\tilde{q}_\mu\,|\,0,\hat{\theta}_0^{obs})$ for each hypothesis.

With these *pdf*s the *p*-values for each hypothesis can be formed:

$$p_\mu = P\big(\tilde{q}_\mu \geq \tilde{q}_\mu^{obs}\,|\,\text{signal+background}\big) \tag{8.6}$$
$$= \int_{\tilde{q}_\mu^{obs}}^{\infty} f(\tilde{q}_\mu\,|\,\mu,\hat{\theta}_\mu^{obs})d\tilde{q}_\mu \tag{8.7}$$
$$1 - p_b = P\big(\tilde{q}_\mu \geq \tilde{q}_\mu^{obs}\,|\,\text{background-only}\big) \tag{8.8}$$
$$= \int_{\tilde{q}_0^{obs}}^{\infty} f(\tilde{q}_\mu\,|\,0,\hat{0}_0^{obs})d\tilde{q}_\mu \tag{8.9}$$

Then

$$\mathrm{CL}_s(\mu) \equiv \frac{p_\mu}{1-p_b} \tag{8.10}$$

From this definition the 95% Confidence Level upper limit on the signal strength μ is quoted by adjusting μ until $\mathrm{CL}_s = 0.05$. Any model for which $\mathrm{CL}_s \leq 0.05$ is excluded.

The $\pm 1\sigma$ and $\pm 2\sigma$ bands around the median expected upper limit are calculated by generating a large number of pseudo-data samples or 'toy' datasets and calculating CL_S and $\mu^{95\%\mathrm{CL}}$ for each. A cumulative probability distribution of the results then reveals the $\pm 1\sigma$ bands by the crossing-points of the 16 (84)% quantiles, and the $\pm 2\sigma$ bands by the 2.5 (97.5) % quantiles.

Technical Implementation

In the upper limit calculation, the backgrounds are separated into the categories: $t\bar{t}+jets$, single top (all channels combined), W+jets, Z+jets, $t\bar{t}$ $+W$, $t\bar{t}$ $+Z$, dibosons (WW, WZ, ZZ), $V\gamma$ ($W\gamma$, $Z\gamma$), and $t\bar{t}+\gamma$.

As described in Section 7.4, all systematic uncertainties are taken as uncorrelated nuisance parameters, completely uncorrelated with all other nuisances. All rate uncertainties are implemented as log-normal distributed nuisances, excepting the additional floating allowed for the $t\bar{t}+jets$ and $t\bar{t}+\gamma$ which is implemented as a log-uniform distribution. Shape systematics are implemented by the 'vertical morphing' technique.

8.2 Upper Limits and Mass Exclusion Contour

The 95% Confidence Level upper limits on the stop production cross section are shown in Figure 8.3 and the mass exclusion contour is shown in Figure 8.4. Stop masses of 650–750 GeV/c^2 are excluded depending on bino mass. The observed upper limits are slightly below the expected, indicating a small (non-significant) deficit in the observed data from the predicted background predictions.

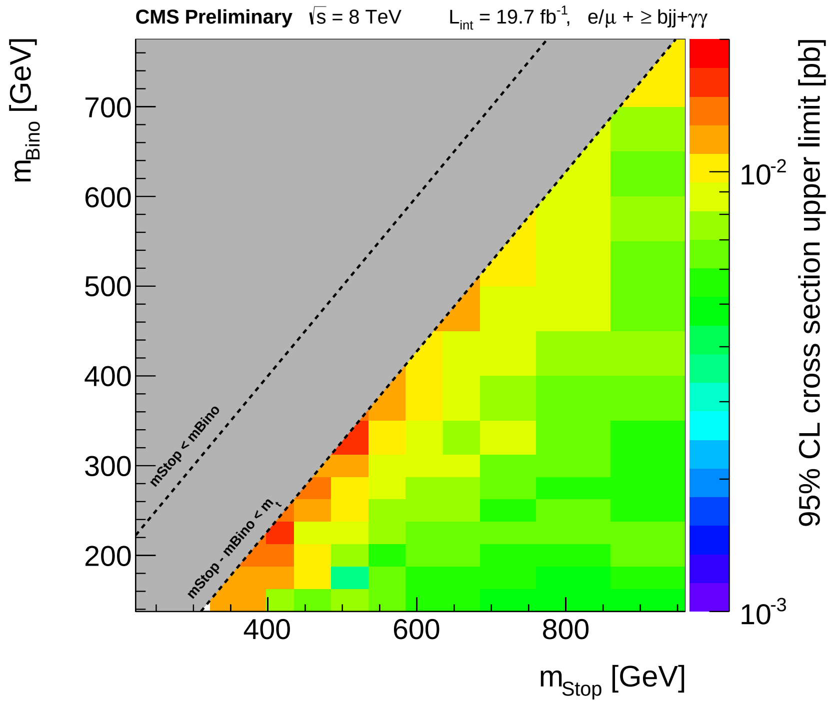

Figure 8.3: The observed 95% Confidence Level upper limits on the theoretical cross section for GMSB stop pair production as a function of stop and bino masses.

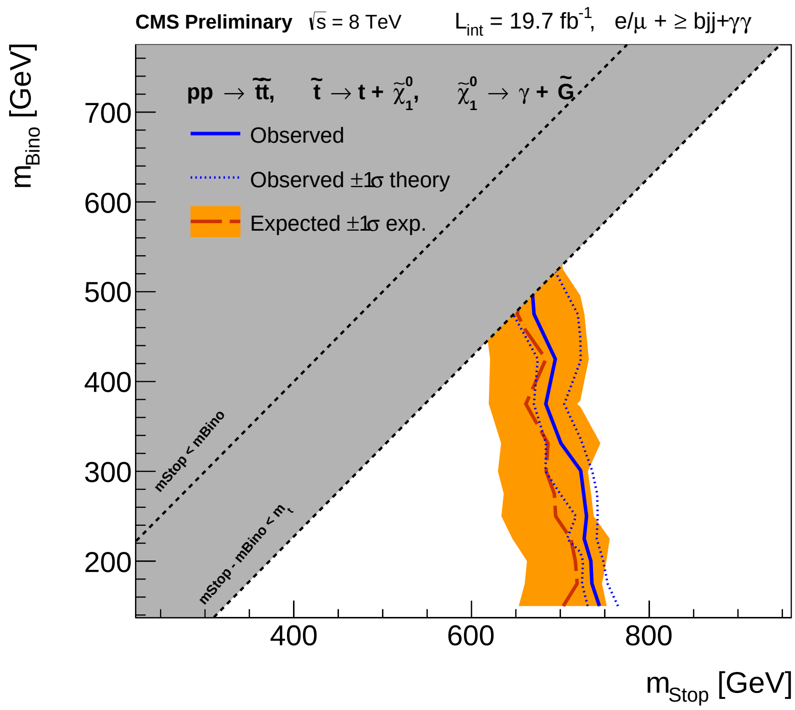

Figure 8.4: The observed and expected 95% Confidence Level exclusion contours for stop and bino masses. Stop masses up to 650–750 GeV/c^2 are excluded depending on the bino mass.

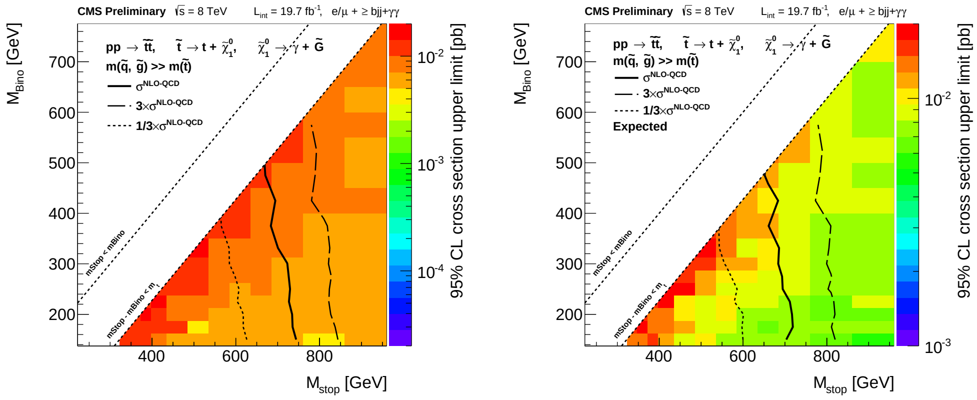

Figure 8.5: The observed (left) and expected (right) exclusion contours overlaid n the 95% C.L. upper limits on the cross sections, in the style of presentation more commonly used for Simplified Model Spectra (SMS) results. Here the $\pm 1\sigma$ bands are replaced with bands determined by simply scaling the theoretical cross section prediction up and down by a factor of 3.

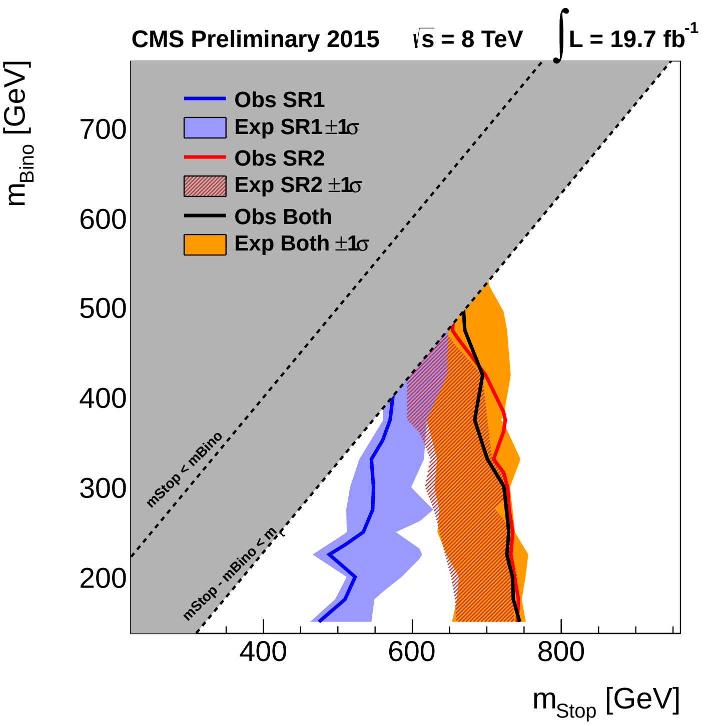

Figure 8.6: Comparison of the exclusion contours when considering only SR1 (blue on blue), only SR2 (red on hashed red), and both channels combined (black on orange). The signal sensitivity is dominated by SR2 due to greatly reduced backgrounds, and the inclusion of SR1 constrains the $\not{E}_T$ in the global fit (the profiling of nuisance parameters).

Chapter 9

Conclusions

The results of this search for evidence of new particle production in pp collisions at $\sqrt{s} = 8$ TeV in the lepton, jets, and photons final state have been presented. No significant deviation of the distribution of missing transverse energy ($\not\!\!E_{\mathrm{T}}$) from expected Standard Model processes is observed, and the results have been interpreted as upper limits on the production rate of light stop squarks in General Gauge Mediated (GGM) models of Gauge Mediated Supersymmetry Breaking (GMSB). Stop squark masses below 650–750 GeV/c^2 are excluded, depending on the mass of bino-like NLSPs.

While these results do not exclude supersymmetry, they place extraordinarily tight constraints on natural models of GMSB. Similar constraints for a Higgsino-like NLSP are stop mass lower bounds of 310 GeV/c^2 [82] and 500–600 GeV/c^2 [83] from ATLAS and 360–410 GeV/c^2 from CMS [84]. A stop mass lower bound of 330 GeV/c^2 can be determined from the observed $h \to \gamma\gamma$ branching ratio [156]. Within the scenario presented by this dissertation, stop masses of above 750 GeV/c^2 would infer a fine-tuning of greater than $\sim$10% [157].

SUSY is under great tension and many models promising naturalness are now constrained to be fine-tuned, but many models remain that can accommodate heavier sparticle spectra. As Run II is just beginning in 2015 at $\sqrt{s} = 13$ TeV, early benchmark searches will be performed just as in 7 and 8 TeV operation. Future photonic searches for SUSY will include the di-photon inclusive ($\gamma\gamma + X$) and could easily improve third generation squark sensitivity by requiring a b-jet ($\gamma\gamma + b + X$). Natural Higgsino searches will be very important in stop mass sensitivity.

A very interesting scenario similar to the search presented here is light stop production with a wino-like co-NLSP: $\tilde{t}\tilde{t} \to b\tilde{\chi}_1^+ + t\tilde{\chi}_1^0 \to b\bar{b}W^+W^- + \gamma + \not\!\!E_{\mathrm{T}}$. This final state is similar to $t\bar{t} + \gamma$ with only one photon, except a careful reconstruction of the top quarks will reveal one on-shell and one off-shell top quark candidate.

The future of SUSY searches at the LHC is bright and exciting, with many still expecting to observe it in the future. Run I of the LHC has bolstered both the predictions and problems of the Standard Model, and there must be more physics to discover.

Appendix A

Data to Monte Carlo Comparisons

This section compares observed data to Monte Carlo simulations for a number of different kinematical distributions. For brevity of the captions, each figure in this appendix compares a single channel (electron or muon) with CR1 on the top-left, CR2 on the top-right, SR1 on the bottom-left, and SR2 on the bottom-right. The regions are printed on each figure for clarity.

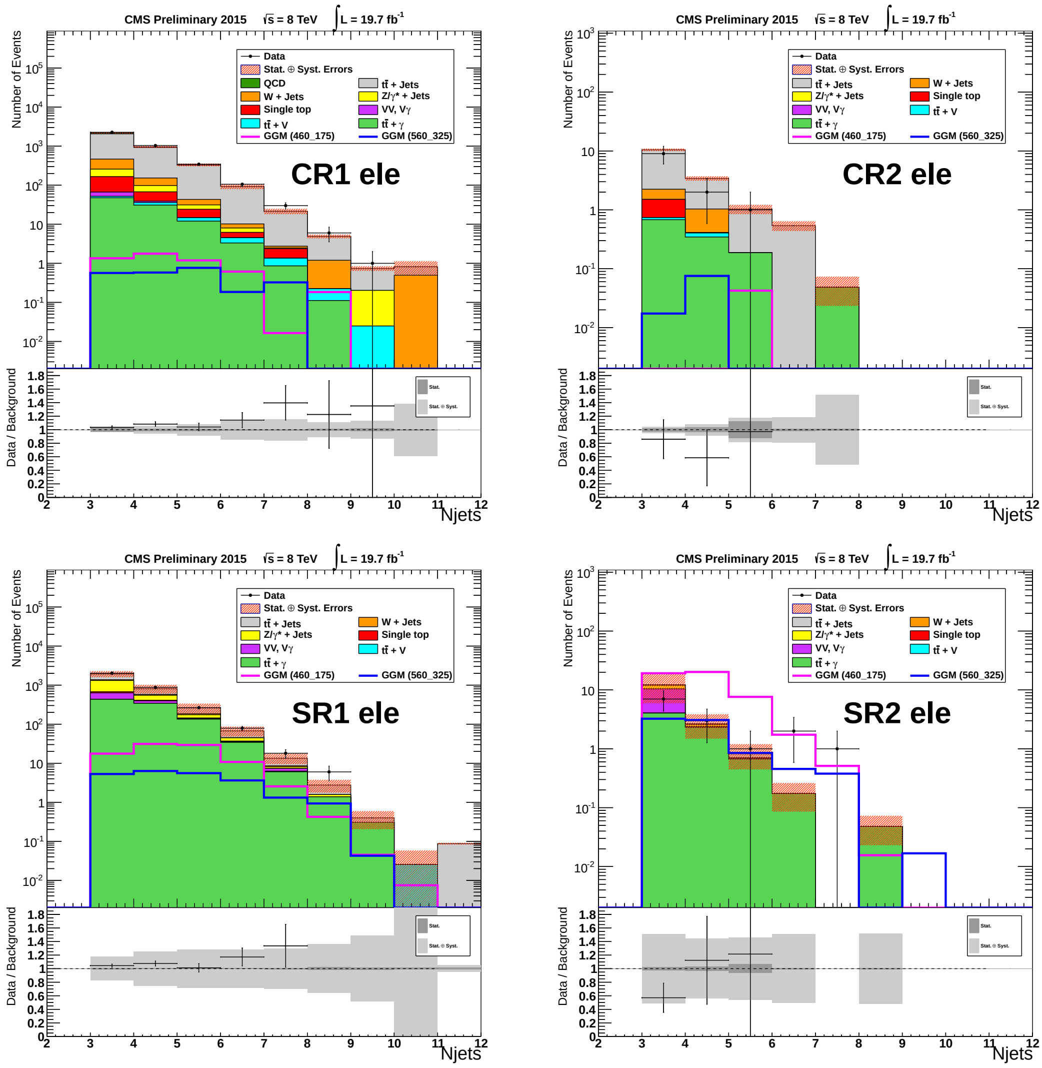

Figure A.1: Comparison of the jet multiplicity for the electron channel.

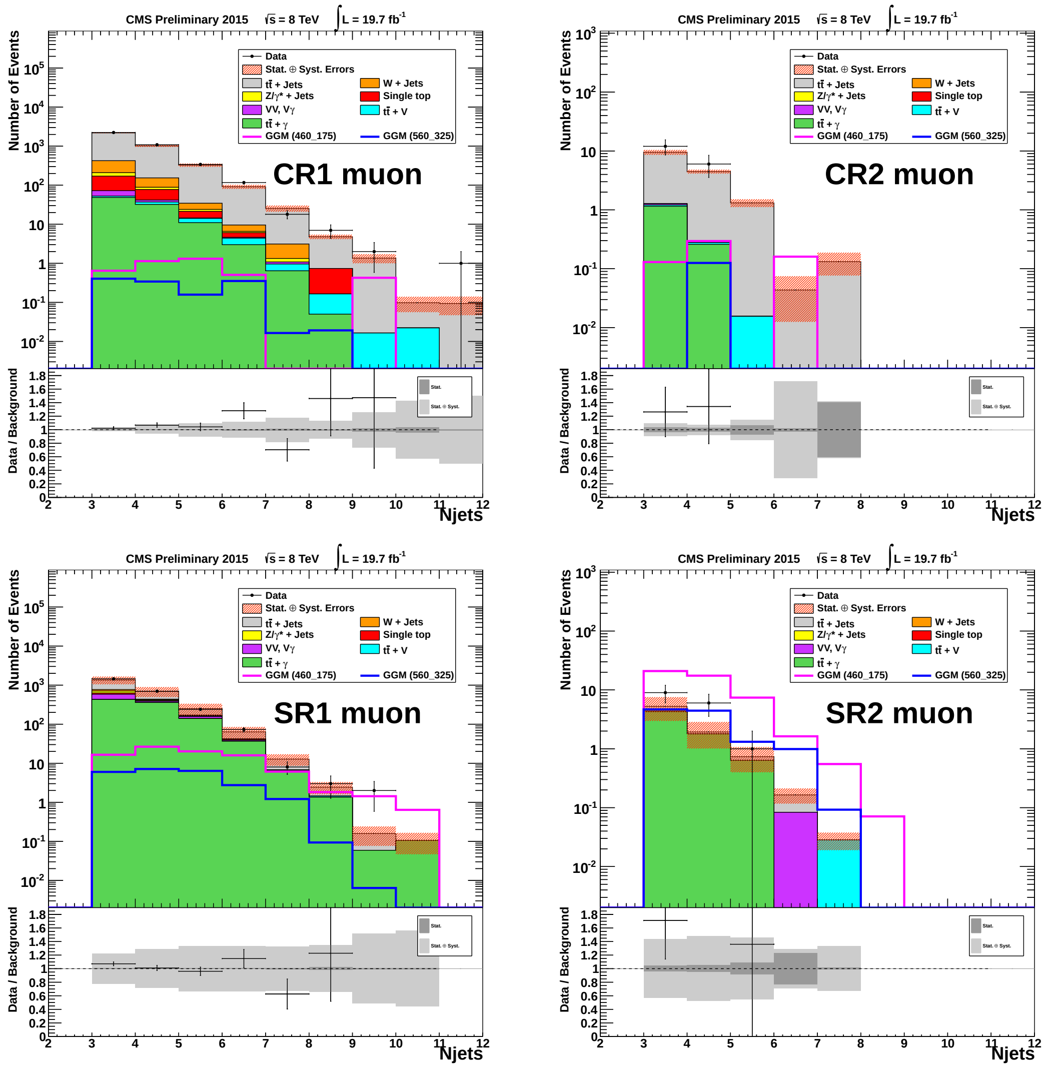

Figure A.2: Comparison of the jet multiplicity for the muon channel.

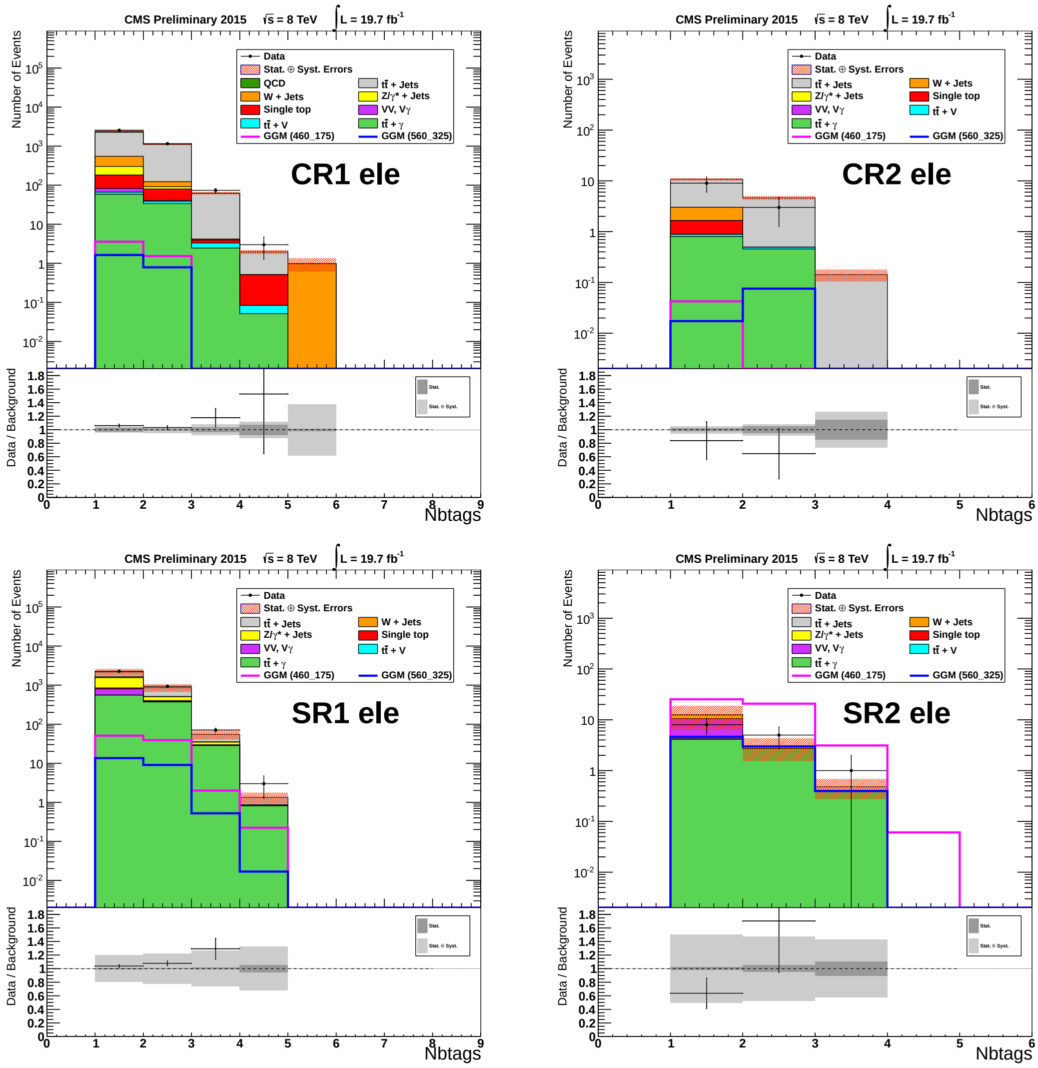

Figure A.3: Comparison of the b-tag multiplicity for the electron channel.

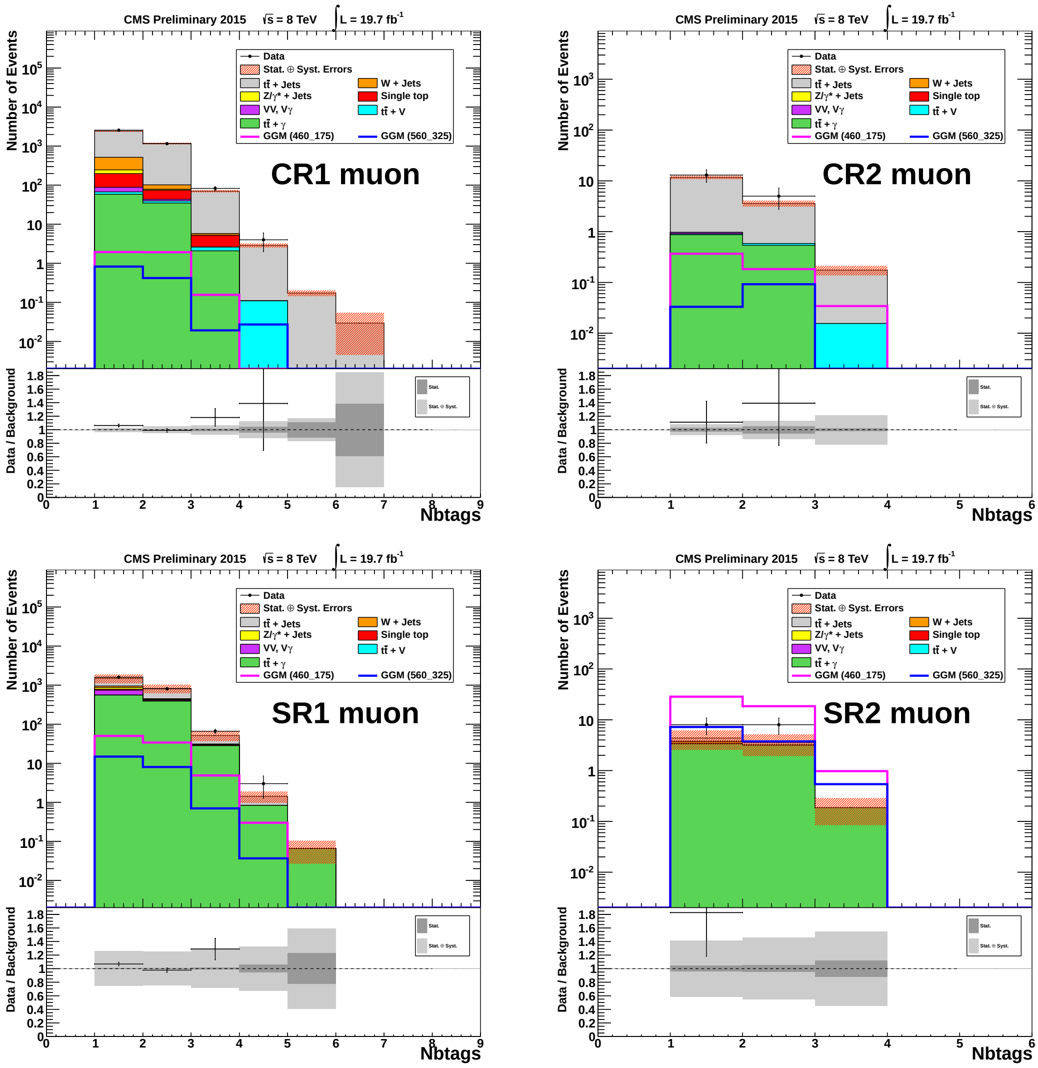

Figure A.4: Comparison of the b-tag multiplicity for the muon channel.

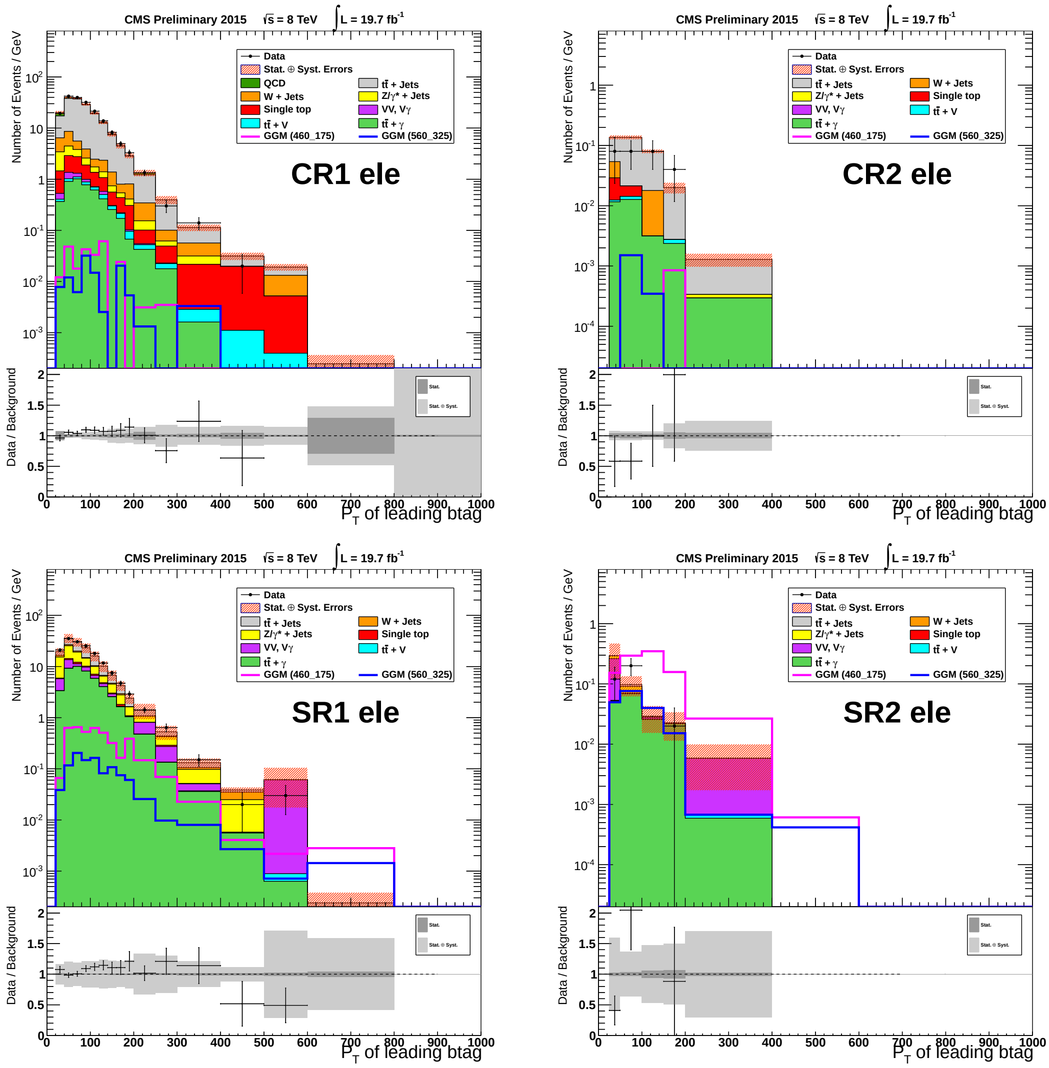

Figure A.5: Comparison of the lead b-jet p_{T} for the electron channel.

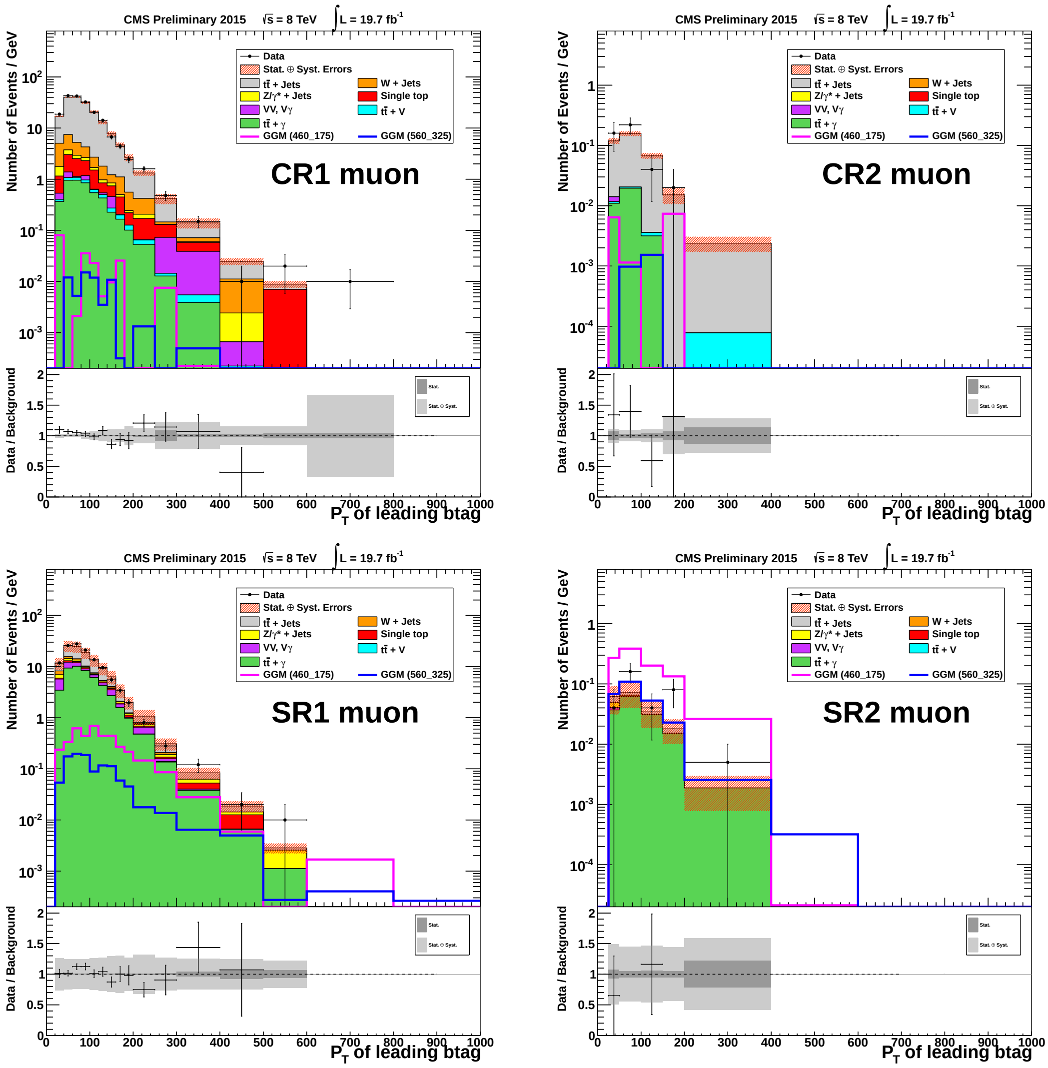

Figure A.6: Comparison of the lead b-jet p_T for the muon channel.

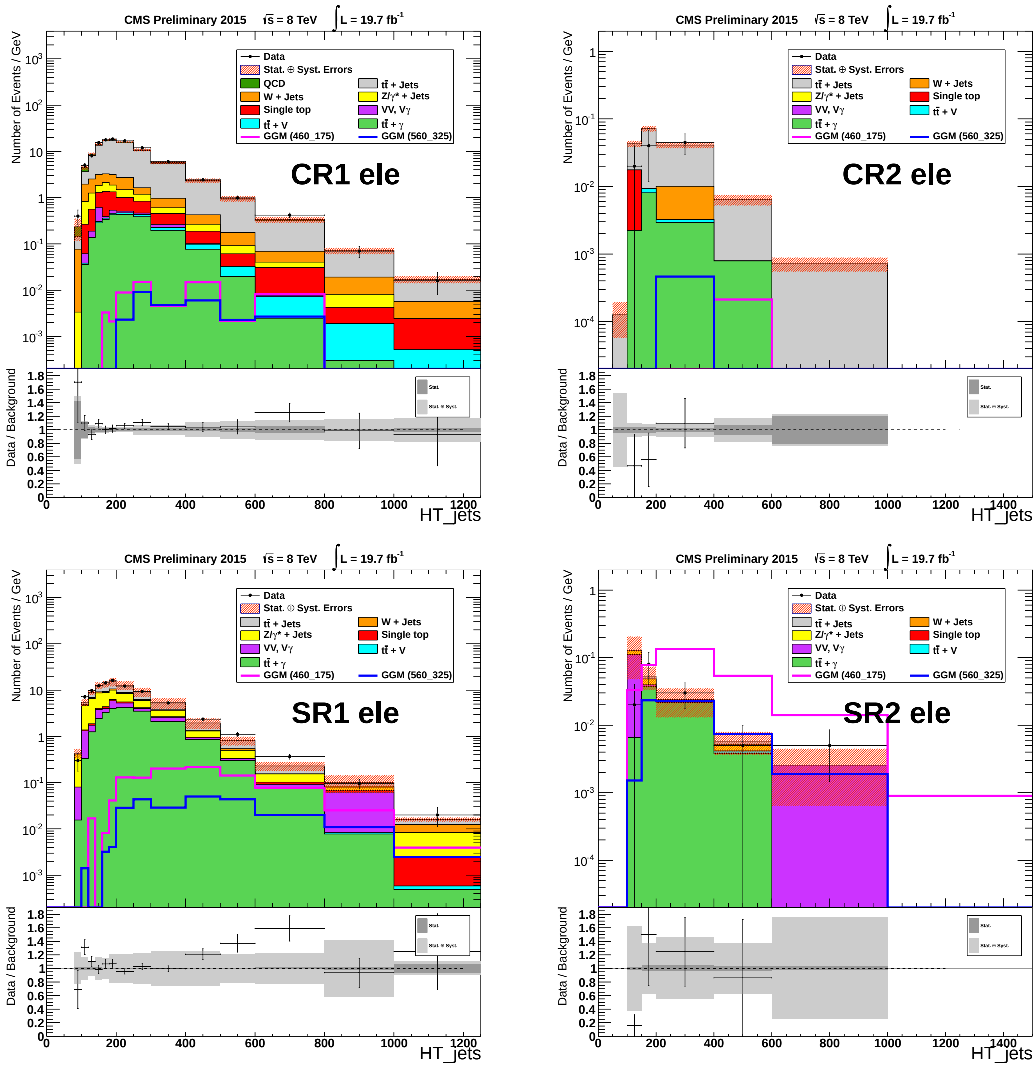

Figure A.7: Comparison of the scalar sum of jet p_{T} known as HT for the electron channel.

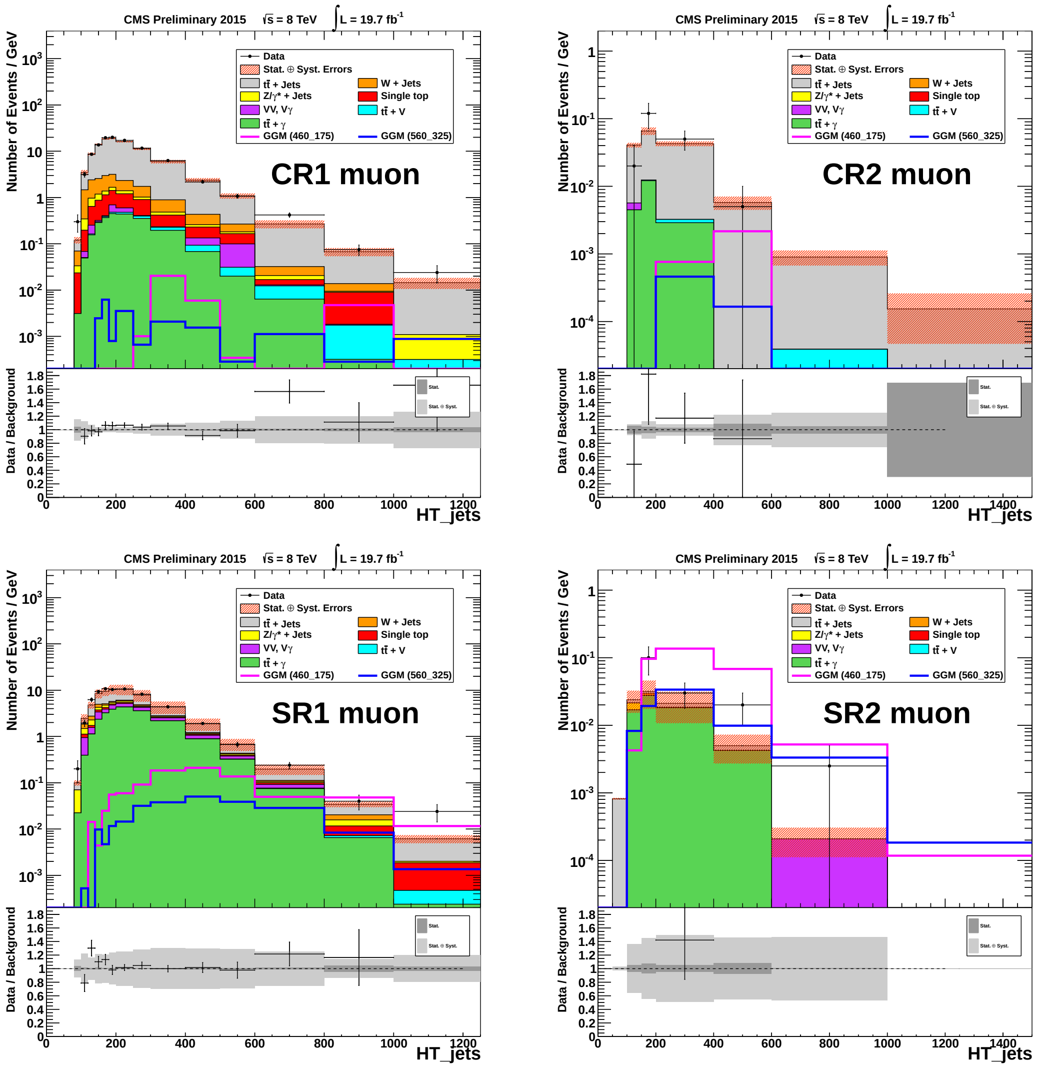

Figure A.8: Comparison of the scalar sum of jet p_{T} known as HT for the muon channel.

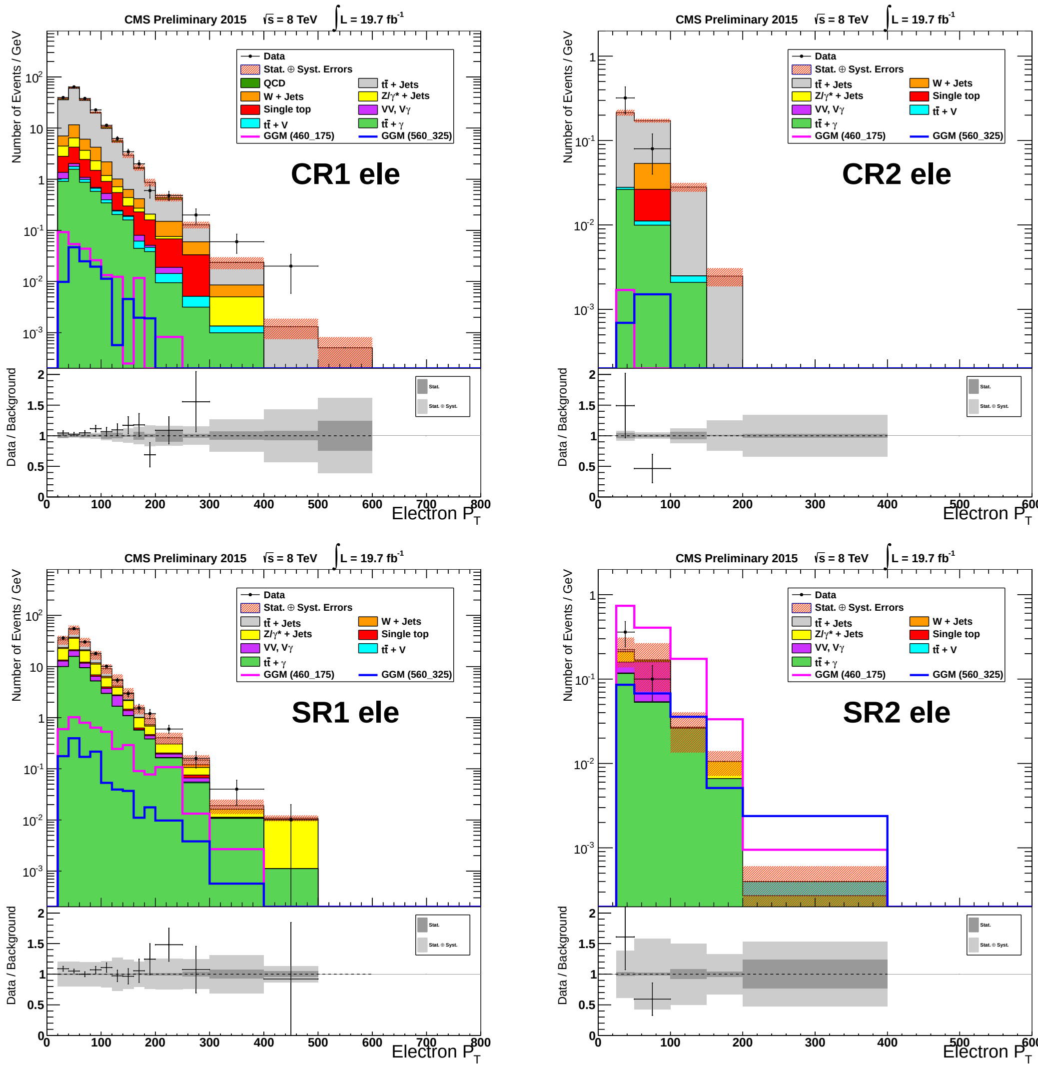

Figure A.9: Comparison of the lepton p_{T} for the electron channel.

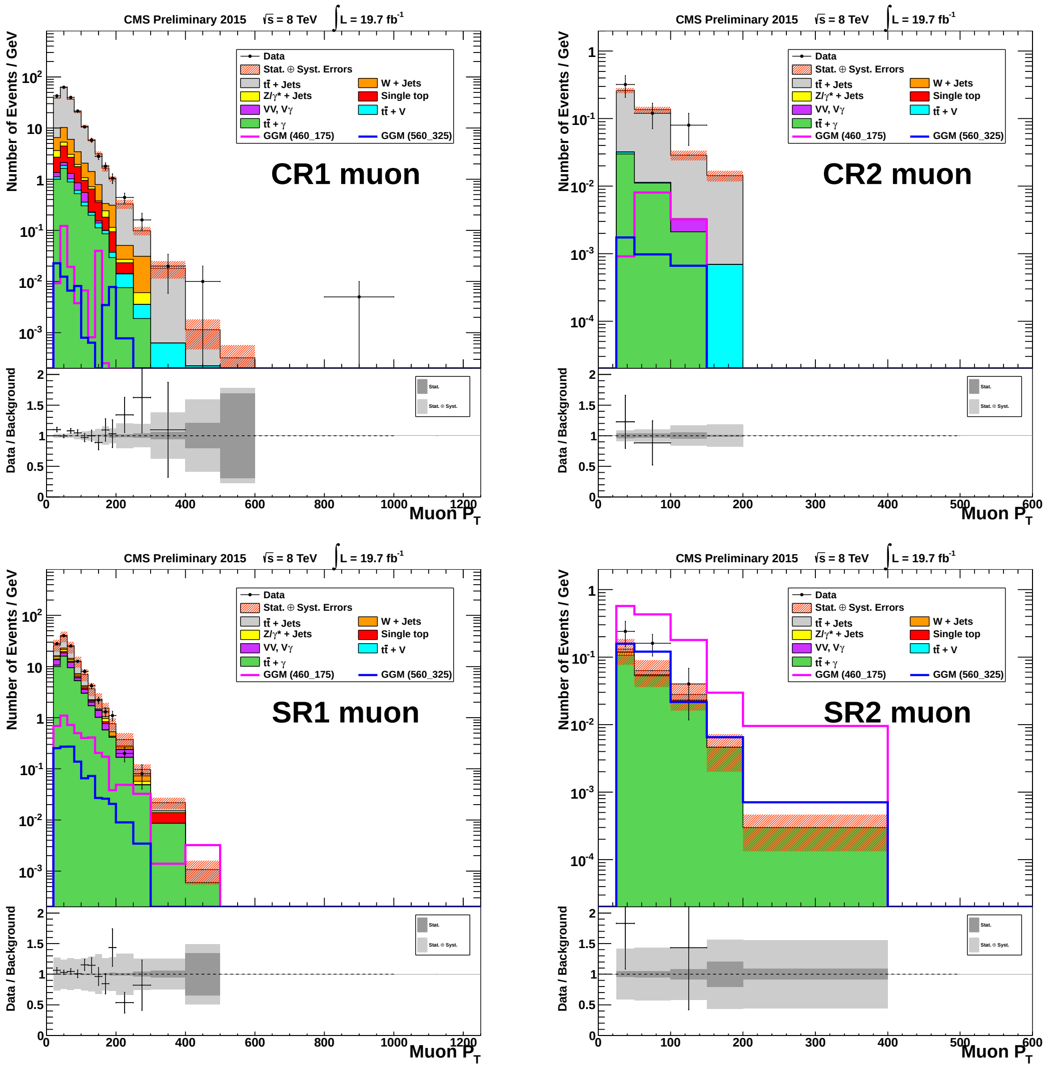

Figure A.10: Comparison of the lepton p_{T} for the muon channel.

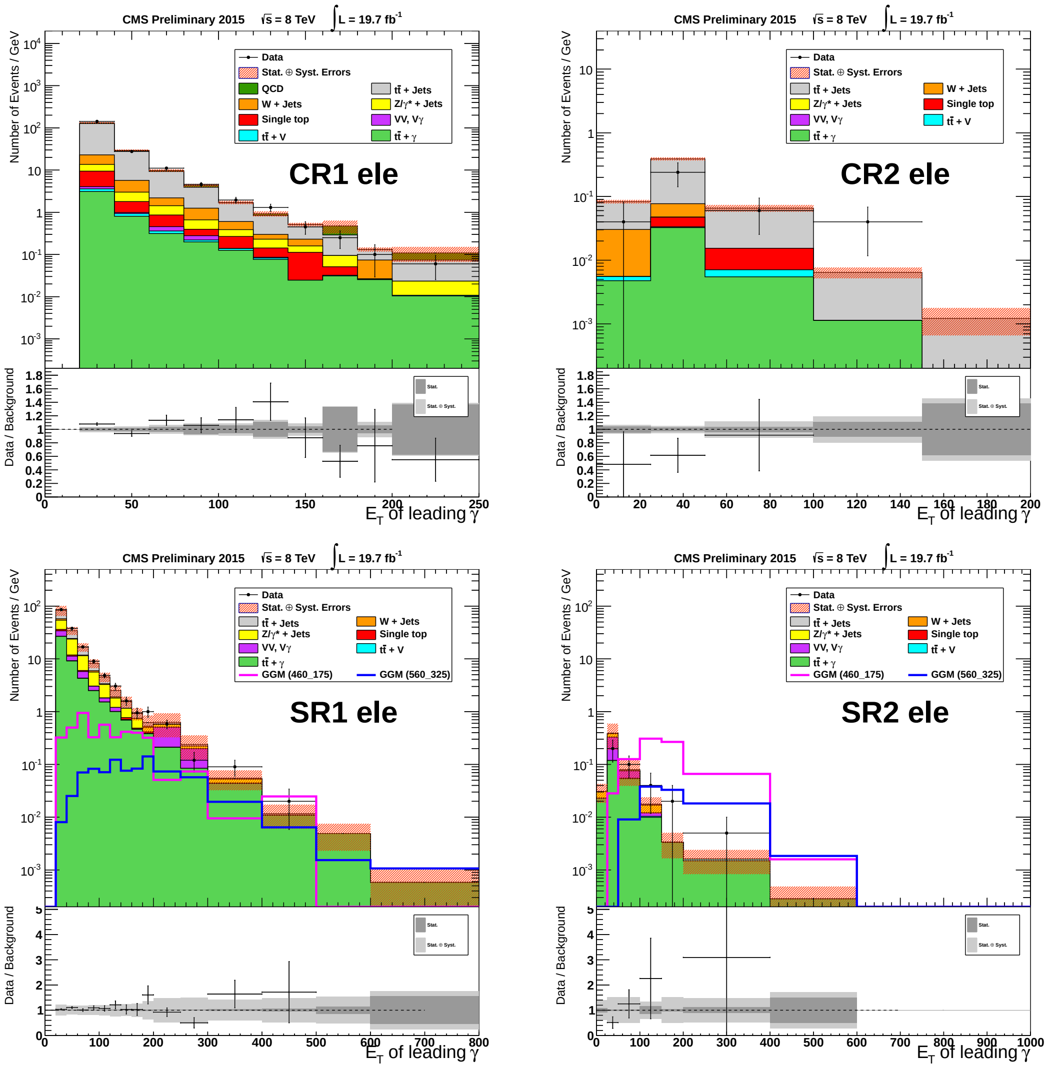

Figure A.11: Comparison of the lead photon E_T for the electron channel.

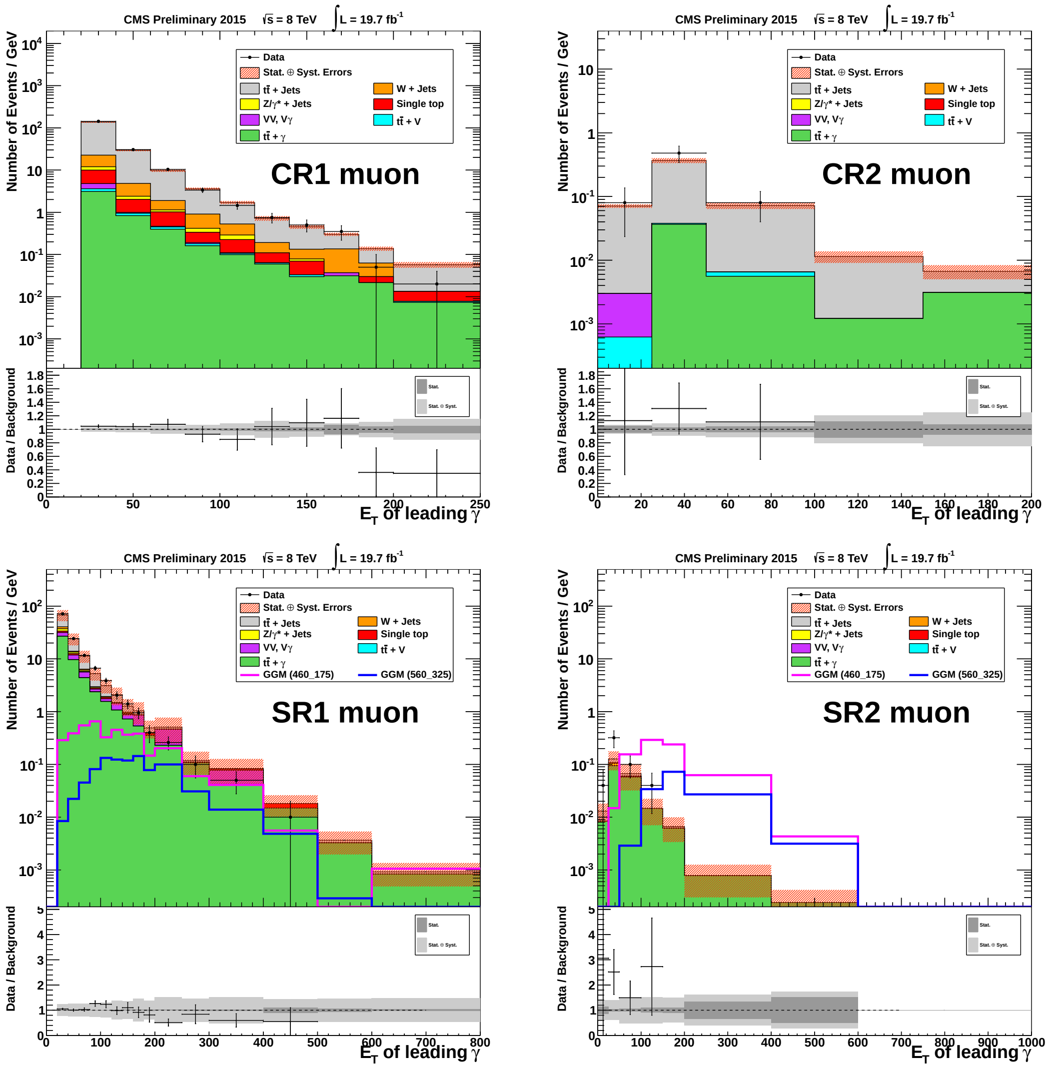

Figure A.12: Comparison of the lead photon E_{T} for the muon channel.

Appendix B

Systematic Shape Comparisons

For brevity of the captions, each figure in this appendix compares shape-based fluctuations of systematic uncertainties of the $\not\!\!E_{\mathrm{T}}$ background estimate. Except where otherwise noted, the electron channels are shown on the left and the muon channels shown on the right, with SR1 shown on the top and SR2 shown on the bottom. In black is the central value, in red is the upwards fluctuation by $+1\sigma$, and in blue is the downwards fluctuation by -1σ. All shapes are normalized to unit area.

B.1 Background Cross Sections

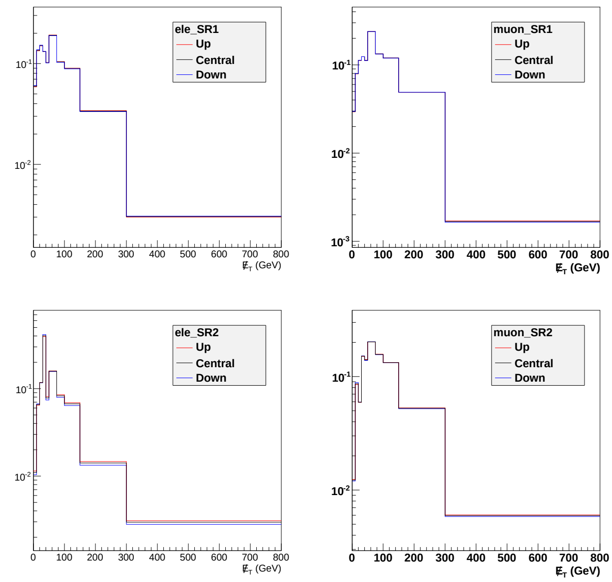

Figure B.1: Comparison of the PDF cross section systematic uncertainty for gg-initiated processes ($t\bar{t}$, $t\bar{t}+Z$, $t\bar{t}+\gamma$).

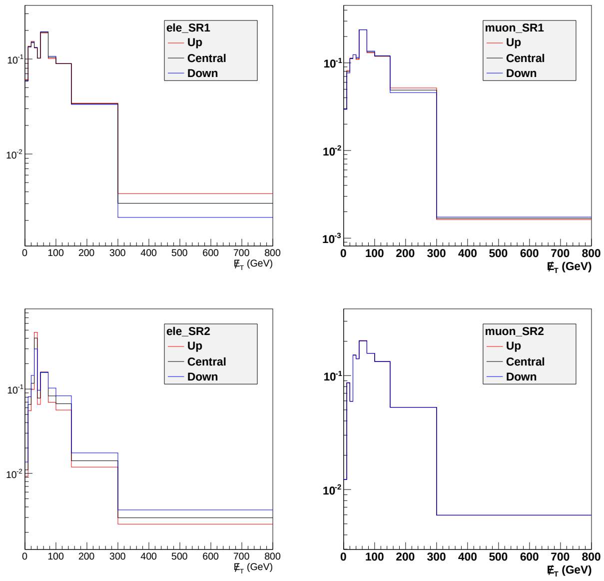

Figure B.2: Comparison of the PDF systematic uncertainty for $q\bar{q}$-initiated processes ($t\bar{t}$ $+W$, W, Z).

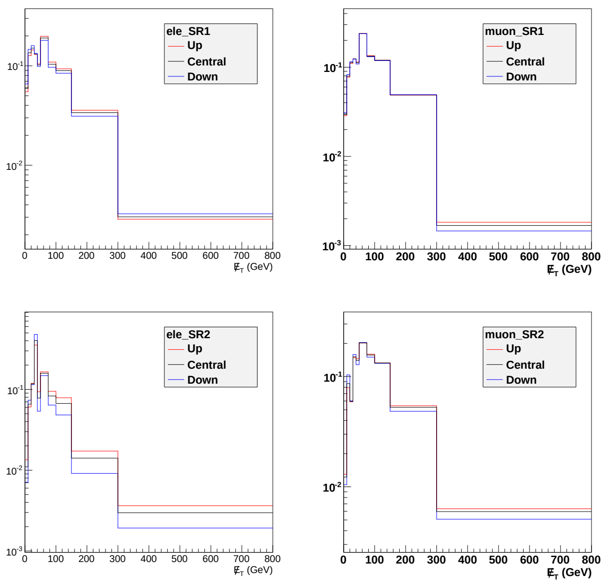

Figure B.3: Comparison of the QCD scale systematic uncertainty for $t\bar{t}$ processes ($t\bar{t}$ $+X$, single top).

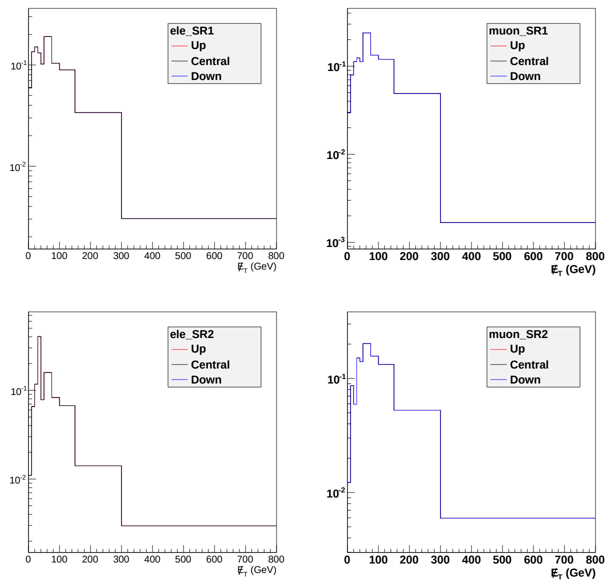

Figure B.4: Comparison of the QCD scale systematic uncertainty for V processes (W and Z).

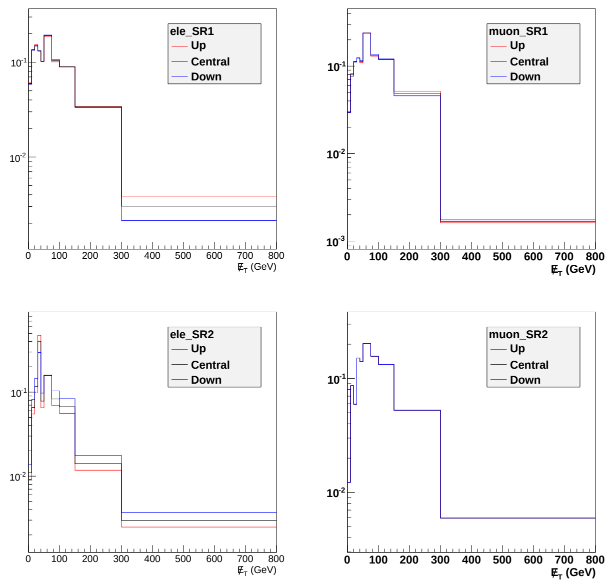

Figure B.5: Comparison of the QCD scale systematic uncertainty for V processes (diboson).

B.2 Jet Energy Scale

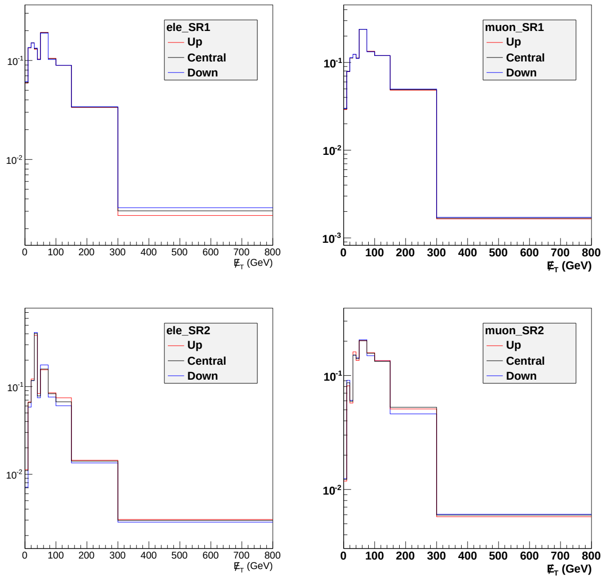

Figure B.6: Comparison of the JES systematic uncertainty.

B.3 b-tag Scale Factors

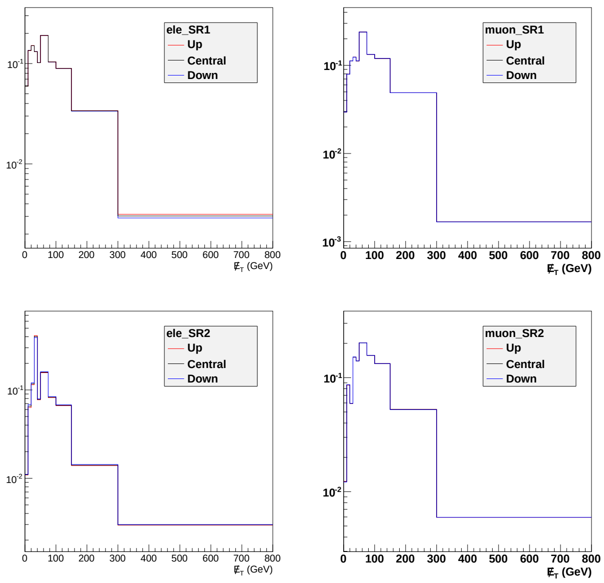

Figure B.7: Comparison of the b-tag scale factor reweighting systematic uncertainty.

B.4 Lepton ID/Trigger Scale Factors

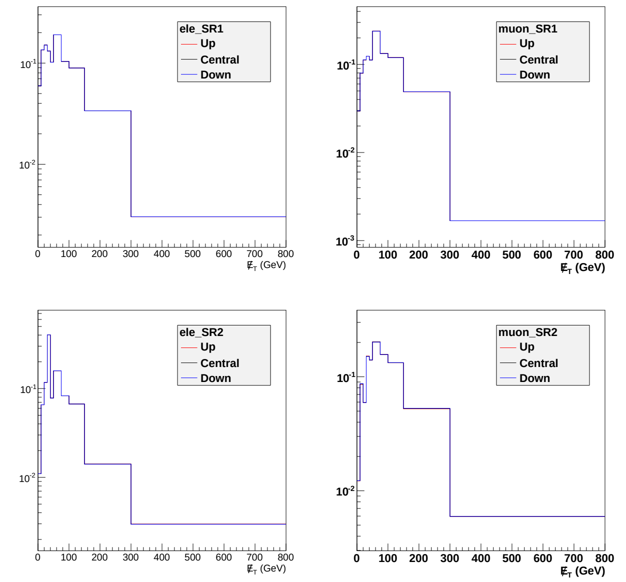

Figure B.8: Comparison of the lepton ID and trigger scale factors systematic uncertainty.

B.5 Photon ID Scale Factors

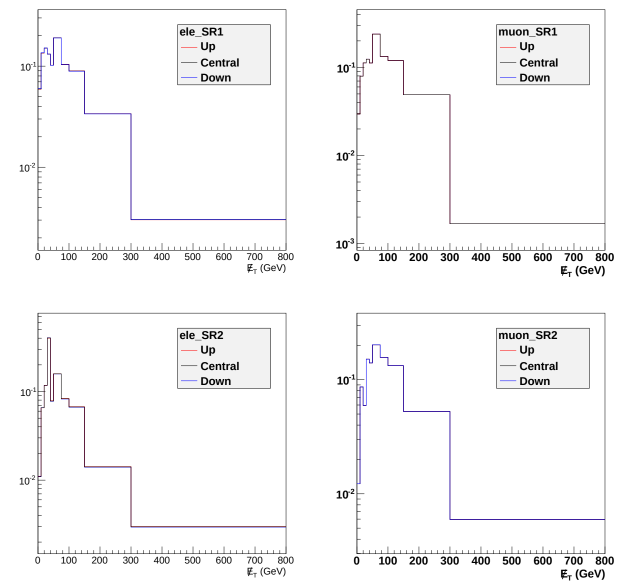

Figure B.9: Comparison of the photon ID scale factor systematic uncertainty.

B.6 Top Quark pT Reweighting

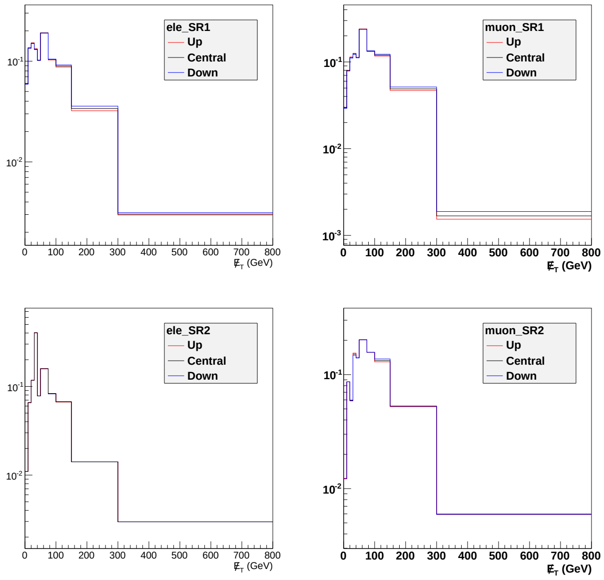

Figure B.10: Comparison of the top quark p_{T} reweighting systematic uncertainty.

B.7 Control Region MET Comparison

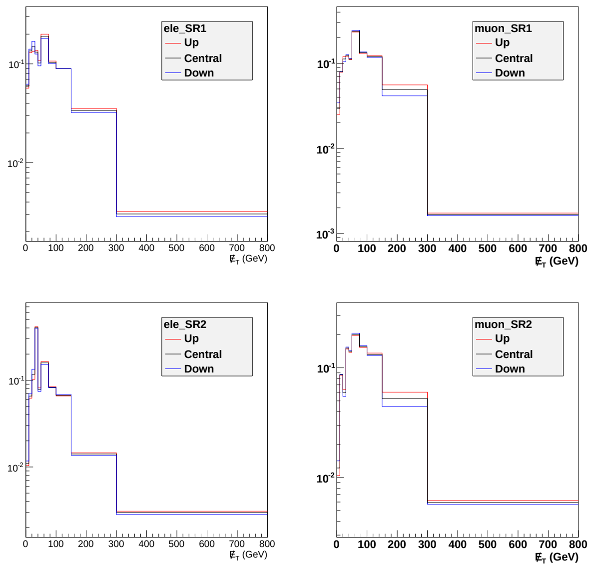

Figure B.11: Comparison of the systematic uncertainty derived from the data-to-MC difference found in CR1, shown in Figure 7.19.

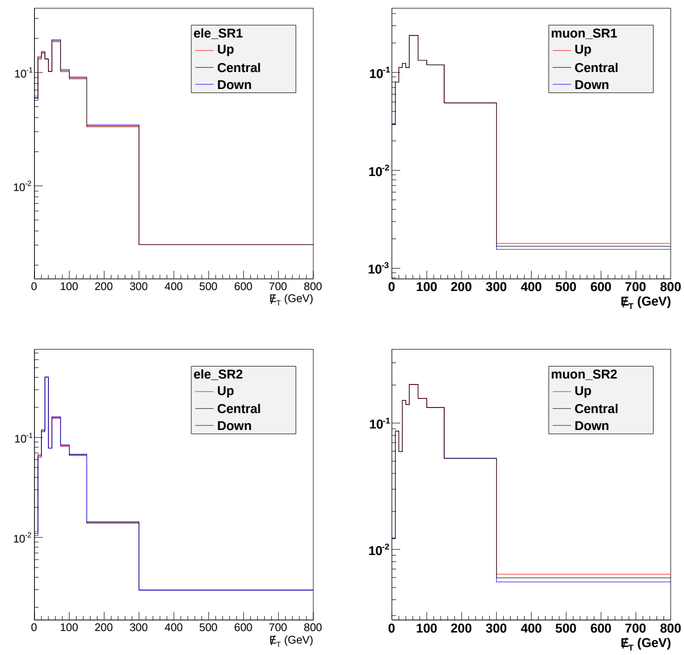

Figure B.12: Comparison of the systematic uncertainty derived from the difference in shape between SR1 and CR1, derived in Equation 7.22.

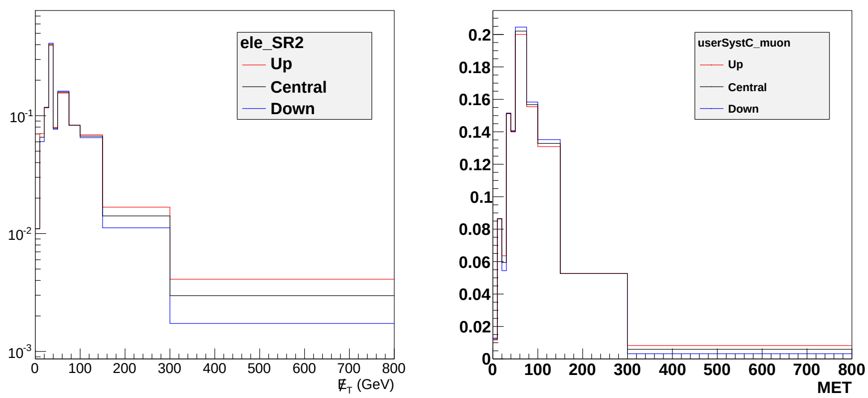

Figure B.13: Comparison of the systematic uncertainty derived from the difference in shape between SR2 and SR1, derived in Equation 7.22. Only SR2 is affected by this uncertainty.

Bibliography

[1] J. Drees, "Review of final LEP results, or, A Tribute to LEP", *Int.J.Mod.Phys.* **A17** (2002) 3259–3283, `doi:10.1142/S0217751X02012727`, `arXiv:hep-ex/0110077`.

[2] S. P. Martin, "A Supersymmetry primer", *Adv.Ser.Direct.High Energy Phys.* **21** (2010) 1–153, `doi:10.1142/9789814307505_0001`, `arXiv:hep-ph/9709356`.

[3] K. G. Begeman, A. H. Broeils, and R. H. Sanders, "Extended rotation curves of spiral galaxies - Dark haloes and modified dynamics", *MNRAS* **249** (April, 1991) 523–537.

[4] J. T. Ruderman and D. Shih, "General Neutralino NLSPs at the Early LHC", *JHEP* **08** (2012) 159, `doi:10.1007/JHEP08(2012)159`, `arXiv:1103.6083`.

[5] URL `https://twiki.cern.ch/twiki/pub/CMSPublic/SUSYSMSSummaryPlots8TeV/barplot_ICHEP2014.pdf`.

[6] URL `https://atlas.web.cern.ch/Atlas/GROUPS/PHYSICS/CombinedSummaryPlots/SUSY/ATLAS_SUSY_Summary/ATLAS_SUSY_Summary.pdf`.

[7] URL `https://atlas.web.cern.ch/Atlas/GROUPS/PHYSICS/CombinedSummaryPlots/SUSY/ATLAS_SUSY_MSUGRA/ATLAS_SUSY_MSUGRA.png`.

[8] URL `https://twiki.cern.ch/twiki/pub/CMSPublic/SUSYSMSSummaryPlots8TeV/T2tt_ICHEP2014_All.pdf`.

[9] CMS Collaboration, "Search for new physics in events with photons, jets, and missing transverse energy in pp collisions at $\sqrt{s} = 7$ TeV", *JHEP* **1303** (2013) 111, `doi:10.1007/JHEP03(2013)111`, `arXiv:1211.4784`.

[10] CMS Collaboration, "Search for supersymmetry in events with photons and missing energy", Technical Report CMS-PAS-SUS-12-018, CERN, Geneva, 2012.

[11] URL `http://cds.cern.ch/record/1295244`.

[12] L. Evans and P. Bryant, “LHC Machine”, *Journal of Instrumentation* **3** (2008), no. 08, S08001.

[13] “Public CMS Luminosity Information”.
URL https://twiki.cern.ch/twiki/bin/view/CMSPublic/LumiPublicResults.

[14] J.-L. Caron, “The LHC injection complex.. L’ensemble d’injection du LHC.”, (May, 1993). AC Collection. Legacy of AC. Pictures from 1992 to 2002.

[15] J.-L. Caron, “LHC quadrupole cross section.”, (May, 1998). AC Collection. Legacy of AC. Pictures from 1992 to 2002.

[16] “Image, CERN LHC, Magnetic Cell Layout”.
URL http://www.lhc-closer.es/img/subidas/4_6_3_4.png.

[17] J.-L. Caron, “Superconducting cavity with its cryostat. Cavité supraconductrice dans son cryostat.”, (May, 1994). AC Collection. Legacy of AC. Pictures from 1992 to 2002.

[18] C. Collaboration, “Detector Drawings”, (Mar, 2012). CMS Collection.

[19] “Image, CMS, Static Slice with tracks”. URL https://cms-docdb.cern.ch/cgi-bin/PublicDocDB/RetrieveFile?docid=4172&version=2&filename=CMS_Slice.gif.

[20] CMS Collaboration, “The CMS experiment at the CERN LHC”, *Journal of Instrumentation* **3** (2008), no. 08, S08004.

[21] “Image, CMS, ECAL crystal shower evolution simulation”.
URL http://www.lepp.cornell.edu/rsrc/Home/Research/CMS/EventReconstruction/fe24elwhite_small.gif.

[22] “Image, CMS, Muon chamber RPCs, exploded view”.
URL http://cms.web.cern.ch/sites/cms.web.cern.ch/files/styles/small/public/field/image/RPClayers.jpg?itok=qtLqtQ89.

[23] “CMS Muon Results”.
URL https://twiki.cern.ch/twiki/bin/view/CMSPublic/PhysicsResultsMUO.

[24] “Image, CMS, Electron Partlicle-Flow Commissioning”. URL https://twiki.cern.ch/twiki/bin/view/CMSPublic/EGMElectronsMoriond2010.

[25] CMS Collaboration Collaboration, “Electromagnetic calorimeter calibration with 7 TeV data”, Technical Report CMS-PAS-EGM-10-003, CERN, Geneva, 2010.

[26] M. Cacciari, G. P. Salam, and G. Soyez, “The Anti-k(t) jet clustering algorithm”, *JHEP* **0804** (2008) 063, doi:10.1088/1126-6708/2008/04/063, arXiv:0802.1189.

[27] “Image, b-Tagging”. URL http://www-d0.fnal.gov/Run2Physics/top/singletop_observation/b_tagging_graphic.png.

[28] CMS Collaboration, “Observation of a new boson at a mass of 125 GeV with the CMS experiment at the LHC”, *Phys.Lett.B* (2012) arXiv:1207.7235.

[29] ATLAS Collaboration, “Observation of a new particle in the search for the Standard Model Higgs boson with the ATLAS detector at the LHC”, *Phys.Lett.B* (2012) arXiv:1207.7214.

[30] CMS Collaboration, “Precise determination of the mass of the Higgs boson and tests of compatibility of its couplings with the standard model predictions using proton collisions at 7 and 8 TeV”, arXiv:1412.8662.

[31] S. Weinberg, “The Making of the standard model”, *Eur.Phys.J.* **C34** (2004) 5–13, doi:10.1140/epjc/s2004-01761-1, arXiv:hep-ph/0401010.

[32] M. Gell-Mann, “A schematic model of baryons and mesons”, *Physics Letters* **8** (1964), no. 3, 214 – 215, doi:10.1016/S0031-9163(64)92001-3.

[33] G. Zweig, “An SU_3 model for strong interaction symmetry and its breaking”, in *Developments in the Quark Theory of Hadrons*, D. B. Lichtenberg and S. P. Rosen, eds., pp. 22–101. Hadronic Press, Nonantum, MA, 1980. Preprint: http://cds.cern.ch/record/570209.

[34] C. Yang and R. Mills, “Conservation of Isotopic Spin and Isotopic Gauge Invariance”, *Phys. Rev.* **96** (Oct, 1954) 191–195, doi:10.1103/PhysRev.96.191.

[35] J. Goldstone, “Field theories with Superconductor solutions”, *Il Nuovo Cimento* **19** (1961), no. 1, 154–164, doi:10.1007/BF02812722.

[36] J. Goldstone, A. Salam, and S. Weinberg, “Broken Symmetries”, *Phys. Rev.* **127** (Aug, 1962) 965–970, doi:10.1103/PhysRev.127.965.

[37] S. L. Glashow, “Partial-symmetries of weak interactions”, *Nuclear Physics* **22** (1961), no. 4, 579 – 588, doi:10.1016/0029-5582(61)90469-2.

[38] A. Salam and J. Ward, “Electromagnetic and weak interactions”, *Physics Letters* **13** (1964), no. 2, 168 – 171, doi:10.1016/0031-9163(64)90711-5.

[39] S. Glashow, J. Iliopoulos, and L. Maiani, "Weak Interactions with Lepton-Hadron Symmetry", *Phys. Rev. D* **2** (Oct, 1970) 1285–1292, `doi:10.1103/PhysRevD.2.1285`.

[40] N. Cabibbo, "Unitary Symmetry and Leptonic Decays", *Phys. Rev. Lett.* **10** (Jun, 1963) 531–533, `doi:10.1103/PhysRevLett.10.531`.

[41] M. Kobayashi and T. Maskawa, "CP-Violation in the Renormalizable Theory of Weak Interaction", *Progress of Theoretical Physics* **49** (1973), no. 2, 652–657, `doi:10.1143/PTP.49.652`, `arXiv:http://ptp.oxfordjournals.org/content/49/2/652.full.pdf+html`.

[42] F. Englert and R. Brout, "Broken Symmetry and the Mass of Gauge Vector Mesons", *Phys. Rev. Lett.* **13** (Aug, 1964) 321–323, `doi:10.1103/PhysRevLett.13.321`.

[43] P. Higgs, "Broken Symmetries and the Masses of Gauge Bosons", *Phys. Rev. Lett.* **13** (Oct, 1964) 508–509, `doi:10.1103/PhysRevLett.13.508`.

[44] G. Guralnik, C. Hagen, and T. Kibble, "Global Conservation Laws and Massless Particles", *Phys. Rev. Lett.* **13** (Nov, 1964) 585–587, `doi:10.1103/PhysRevLett.13.585`.

[45] S. Weinberg, "A Model of Leptons", *Phys. Rev. Lett.* **19** (Nov, 1967) 1264–1266, `doi:10.1103/PhysRevLett.19.1264`.

[46] A. Salam, "Weak and Electromagnetic Interactions", in *Elementary Particle Physics*, N. Svartholm, ed., pp. 367–377. Almqvist & Wiskell, Stockholm, Nobel Symposium No. 8 edition, 1968.

[47] G. Altarelli and M. W. Grunewald, "Precision electroweak tests of the standard model", *Phys.Rept.* **403-404** (2004) 189–201, `doi:10.1016/j.physrep.2004.08.013`, `arXiv:hep-ph/0404165`.

[48] T.-P. Cheng and L.-F. Li, "Gauge Theory of Elementary Particle Physics". Oxford University Press, 1984.

[49] W. N. Cottingham and D. A. Greenwood, "An Introduction to the Standard Model of Particle Physics". Cambridge University Press, second edition, 2007. `http://dx.doi.org/10.1017/CBO9780511791406`.

[50] M. E. Peskin and D. V. Schroeder, "An Introduction to Quantum Field Theory". Westview Press, 1995.

[51] G. Arnison et al., “Experimental observation of isolated large transverse energy electrons with associated missing energy at s=540 GeV”, *Physics Letters B* **122** (1983), no. 1, 103 – 116, doi:http://dx.doi.org/10.1016/0370-2693(83)91177-2.

[52] G. Arnison et al., “Experimental observation of lepton pairs of invariant mass around 95 GeV/c2 at the {CERN} {SPS} collider”, *Physics Letters B* **126** (1983), no. 5, 398 – 410, doi:http://dx.doi.org/10.1016/0370-2693(83)90188-0.

[53] J. F. Gunion, H. E. Haber, G. L. Kane, and S. Dawson, “The Higgs Hunter’s Guide”, *Front.Phys.* **80** (2000) 1–448.

[54] J. L. Feng, “Naturalness and the Status of Supersymmetry”, *Ann.Rev.Nucl.Part.Sci.* **63** (2013) 351–382, doi:10.1146/annurev-nucl-102010-130447, arXiv:1302.6587.

[55] L. Bergstrom, “Nonbaryonic dark matter: Observational evidence and detection methods”, *Rept.Prog.Phys.* **63** (2000) 793, doi:10.1088/0034-4885/63/5/2r3, arXiv:hep-ph/0002126.

[56] G. Bertone, D. Hooper, and J. Silk, “Particle dark matter: Evidence, candidates and constraints”, *Phys.Rept.* **405** (2005) 279–390, doi:10.1016/j.physrep.2004.08.031, arXiv:hep-ph/0404175.

[57] I. Aitchison, “Supersymmetry in Particle Physics. An Elementary Introduction”. Cambridge University Press, 2007.

[58] M. Dine and W. Fischler, “A phenomenological model of particle physics based on supersymmetry”, *Physics Letters B* **110** (1982), no. 34, 227 – 231, doi:http://dx.doi.org/10.1016/0370-2693(82)91241-2.

[59] C. R. Nappi and B. A. Ovrut, “Supersymmetric extension of the SU(3)SU(2)U(1) model”, *Physics Letters B* **113** (1982), no. 2, 175 – 179, doi:http://dx.doi.org/10.1016/0370-2693(82)90418-X.

[60] L. Alvarez-Gaumé, M. Claudson, and M. B. Wise, “Low-energy supersymmetry”, *Nuclear Physics B* **207** (1982), no. 1, 96 – 110, doi:http://dx.doi.org/10.1016/0550-3213(82)90138-9.

[61] M. Dine and A. E. Nelson, “Dynamical supersymmetry breaking at low energies”, *Phys. Rev. D* **48** (Aug, 1993) 1277–1287, doi:10.1103/PhysRevD.48.1277.

[62] M. Dine, A. E. Nelson, and Y. Shirman, “Low energy dynamical supersymmetry breaking simplified”, *Phys. Rev. D* **51** (Feb, 1995) 1362–1370, doi:10.1103/PhysRevD.51.1362.

[63] M. Dine, A. E. Nelson, Y. Nir, and Y. Shirman, “New tools for low energy dynamical supersymmetry breaking”, *Phys. Rev. D* **53** (Mar, 1996) 2658–2669, `doi:10.1103/PhysRevD.53.2658`.

[64] A. H. Chamseddine, R. Arnowitt, and P. Nath, “Locally Supersymmetric Grand Unification”, *Phys. Rev. Lett.* **49** (Oct, 1982) 970–974, `doi:10.1103/PhysRevLett.49.970`.

[65] R. Barbieri, S. Ferrara, and C. Savoy, “Gauge models with spontaneously broken local supersymmetry”, *Physics Letters B* **119** (1982), no. 46, 343 – 347, `doi:http://dx.doi.org/10.1016/0370-2693(82)90685-2`.

[66] L. Ibez, “Locally supersymmetric SU(5) grand unification”, *Physics Letters B* **118** (1982), no. 13, 73 – 78, `doi:http://dx.doi.org/10.1016/0370-2693(82)90604-9`.

[67] L. Hall, J. Lykken, and S. Weinberg, “Supergravity as the messenger of supersymmetry breaking”, *Phys. Rev. D* **27** (May, 1983) 2359–2378, `doi:10.1103/PhysRevD.27.2359`.

[68] N. Ohta, “Grand Unified Theories Based on Local Supersymmetry”, *Progress of Theoretical Physics* **70** (1983), no. 2, 542–549, `doi:10.1143/PTP.70.542`, `arXiv:http://ptp.oxfordjournals.org/content/70/2/542.full.pdf+html`.

[69] J. Ellis, D. Nanopoulos, and K. Tamvakis, “Grand unification in simple supergravity”, *Physics Letters B* **121** (1983), no. 23, 123 – 129, `doi:http://dx.doi.org/10.1016/0370-2693(83)90900-0`.

[70] L. Alvarez-Gaumé, J. Polchinski, and M. B. Wise, “Minimal low-energy supergravity”, *Nuclear Physics B* **221** (1983), no. 2, 495 – 523, `doi:http://dx.doi.org/10.1016/0550-3213(83)90591-6`.

[71] E. Fernandez et al., “Search for Single Photons from Supersymmetric Particle Production”, *Phys. Rev. Lett.* **54** (Mar, 1985) 1118–1121, `doi:10.1103/PhysRevLett.54.1118`.

[72] E. W. Fernandez et al., “Search for single electrons from supersymmetric-particle production”, *Phys. Rev. D* **35** (Jan, 1987) 374–377, `doi:10.1103/PhysRevD.35.374`.

[73] D. Decamp et al., “Search for neutral Higgs bosons from supersymmetry in Z decays”, *Physics Letters B* **237** (1990), no. 2, 291 – 302, `doi:http://dx.doi.org/10.1016/0370-2693(90)91447-J`.

[74] CDF Collaboration Collaboration, “Search for Squarks and Gluinos via Radiative Decays of Neutralinos in Proton-Antiproton Collisions at $\sqrt{s} = 1.8$TeV”, *Phys. Rev. Lett.* **75** (Jul, 1995) 613–617, doi:10.1103/PhysRevLett.75.613.

[75] D0 Collaboration Collaboration, “Search for Squarks and Gluinos in $p\overline{p}$ Collisions at $\sqrt{s} = 1.8$TeV”, *Phys. Rev. Lett.* **75** (Jul, 1995) 618–623, doi:10.1103/PhysRevLett.75.618.

[76] G. Alexander et al., “Topological search for the production of neutralinos and scalar particles”, *Physics Letters B* **377** (1996), no. 4, 273 – 288, doi:http://dx.doi.org/10.1016/0370-2693(96)00502-3.

[77] S. Aid et al., “A search for squarks of Rp-violating SUSY at HERA”, *Zeitschrift für Physik C Particles and Fields* **71** (1996), no. 1, 211–226, doi:10.1007/BF02906978.

[78] S. Aid et al., “A search for selectrons and squarks at {HERA}”, *Physics Letters B* **380** (1996), no. 34, 461 – 470, doi:http://dx.doi.org/10.1016/0370-2693(96)00640-5.

[79] BABAR Collaboration Collaboration, “Search for Lepton Flavor Violation in the Decay $\tau^{\pm} \to \mu^{\pm}\gamma$”, *Phys. Rev. Lett.* **95** (Jul, 2005) 041802, doi:10.1103/PhysRevLett.95.041802.

[80] “CMS Supersymmetry Physics Results”. URL https://twiki.cern.ch/twiki/bin/view/CMSPublic/PhysicsResultsSUS.

[81] “ATLAS Supersymmetry (SUSY) searches”. URL https://twiki.cern.ch/twiki/bin/view/AtlasPublic/SupersymmetryPublicResults.

[82] ATLAS Collaboration, “Search for scalar top quark pair production in natural gauge mediated supersymmetry models with the ATLAS detector in pp collisions at $\sqrt{s} = 7$ TeV”, *Phys. Lett.* **B715** (2012) 44–60, doi:10.1016/j.physletb.2012.07.010, arXiv:1204.6736.

[83] ATLAS Collaboration, “Search for direct top squark pair production in events with a Z boson, b-jets and missing transverse momentum in sqrt(s)=8 TeV pp collisions with the ATLAS detector”, *Eur. Phys. J.* **C74** (2014), no. 6, 2883, doi:10.1140/epjc/s10052-014-2883-6, arXiv:1403.5222.

[84] (CMS Collaboration) Collaboration, “Search for Top Squark and Higgsino Production Using Diphoton Higgs Boson Decays”, *Phys. Rev. Lett.* **112** (Apr, 2014) 161802, doi:10.1103/PhysRevLett.112.161802.

[85] A. Albaid and K. S. Babu, “Higgs boson of mass 125 GeV in GMSB models with messenger-matter mixing”, *Phys. Rev.* **D88** (2013) 055007, `doi:10.1103/PhysRevD.88.055007`, `arXiv:1207.1014`.

[86] J. A. Evans and D. Shih, “Surveying Extended GMSB Models with m_h=125 GeV”, *JHEP* **1308** (2013) 093, `doi:10.1007/JHEP08(2013)093`, `arXiv:1303.0228`.

[87] J. L. Feng, Z. Surujon, and H.-B. Yu, “Confluence of Constraints in Gauge Mediation: The 125 GeV Higgs Boson and Goldilocks Cosmology”, *Phys. Rev.* **D86** (2012) 035003, `doi:10.1103/PhysRevD.86.035003`, `arXiv:1205.6480`.

[88] N. Okada, “SuperWIMP dark matter and 125 GeV Higgs boson in the minimal GMSB”, `arXiv:1205.5826`.

[89] Z. Kang et al., “A Heavy SM-like Higgs and a Light Stop from Yukawa-Deflected Gauge Mediation”, *Phys. Rev.* **D86** (2012) 095020, `doi:10.1103/PhysRevD.86.095020`, `arXiv:1203.2336`.

[90] P. Byakti and T. S. Ray, “Burgeoning the Higgs mass to 125 GeV through messenger-matter interactions in GMSB models”, *JHEP* **1305** (2013) 055, `doi:10.1007/JHEP05(2013)055`, `arXiv:1301.7605`.

[91] R. Ding, T. Li, L. Wang, and B. Zhu, “Towards the Natural Gauge Mediation”, `arXiv:1506.00359`.

[92] A. Bharucha, A. Goudelis, and M. McGarrie, “En-gauging Naturalness”, *Eur.Phys.J.* **C74** (2014) 2858, `doi:10.1140/epjc/s10052-014-2858-7`, `arXiv:1310.4500`.

[93] H. Pagels and J. R. Primack, “Supersymmetry, Cosmology, and New Physics at Teraelectronvolt Energies”, *Phys. Rev. Lett.* **48** (Jan, 1982) 223–226, `doi:10.1103/PhysRevLett.48.223`.

[94] D. Gorbunov, A. Khmelnitsky, and V. Rubakov, “Is gravitino still a warm dark matter candidate?”, *JHEP* **12** (2008) 055, `doi:10.1088/1126-6708/2008/12/055`, `arXiv:0805.2836`.

[95] S. Borgani, A. Masiero, and M. Yamaguchi, “Light gravitinos as mixed dark matter”, *Phys. Lett.* **B386** (1996) 189–197, `doi:10.1016/0370-2693(96)00956-2`, `arXiv:hep-ph/9605222`.

[96] I. Dalianis, “Gravitino dark matter production at finite temperature”, *JHEP* **1311** (2013) 162, `doi:10.1007/JHEP11(2013)162`, `arXiv:1304.7673`.

[97] A. Boyarsky, J. Lesgourgues, O. Ruchayskiy, and M. Viel, “Lyman- constraints on warm and on warm-plus-cold dark matter models”, *Journal of Cosmology and Astroparticle Physics* **2009** (2009), no. 05, 012.

[98] F. Staub, J. Niemeyer, and W. Porod, “Strong dark matter constraints on GMSB models”, *Journal of High Energy Physics* **2010** (2010), no. 1, `doi:10.1007/JHEP01(2010)058`.

[99] E. Komatsu et al., “Five-Year Wilkinson Microwave Anisotropy Probe Observations: Cosmological Interpretation”, *The Astrophysical Journal Supplement Series* **180** (2009), no. 2, 330.

[100] C.-H. Chen and J. F. Gunion, “Probing gauge-mediated supersymmetry breaking models at the Fermilab Tevatron via delayed decays of the lightest neutralino”, *Phys. Rev. D* **58** (Sep, 1998) 075005, `doi:10.1103/PhysRevD.58.075005`.

[101] “LHC experiments are back in business at a new record energy”. URL `http://press.web.cern.ch/press-releases/2015/06/lhc-experiments-are-back-business-new-record-energy`.

[102] O. S. Brüning et al., “LHC Design Report”. CERN, Geneva, 2004.

[103] M. Lamont, “Status of the LHC”, *Journal of Physics: Conference Series* **455** (2013), no. 1, 012001.

[104] M. Benedikt et al., “LHC Design Report”. CERN, Geneva, 2004.

[105] C. E. Hill et al., “Tests of the CERN proton linac performance for LHC - type beams”, *eConf* **C000821** (2000) TUD17, `arXiv:physics/0008102`. [,590(2000)].

[106] CMS Collaboration Collaboration, “Particle-Flow Event Reconstruction in CMS and Performance for Jets, Taus, and MET”, Technical Report CMS-PAS-PFT-09-001, CERN, 2009. Geneva, Apr, 2009.

[107] T. C. Collaboration, “Description and performance of track and primary-vertex reconstruction with the CMS tracker”, *Journal of Instrumentation* **9** (2014), no. 10, P10009.

[108] R. Frühwirth, “Application of Kalman filtering to track and vertex fitting”, *Nuclear Instruments and Methods in Physics Research Section A: Accelerators, Spectrometers, Detectors and Associated Equipment* **262** (1987), no. 23, 444 – 450, `doi:http://dx.doi.org/10.1016/0168-9002(87)90887-4`.

[109] W. Adam, R. Frühwirth, A. Strandlie, and T. Todor, "Reconstruction of Electrons with the Gaussian-Sum Filter in the CMS Tracker at the LHC",.

[110] CMS Collaboration Collaboration, "Commissioning of the Particle-Flow reconstruction in Minimum-Bias and Jet Events from pp Collisions at 7 TeV", Technical Report CMS-PAS-PFT-10-002, CERN, Geneva, 2010.

[111] CMS Collaboration, "Performance of the CMS missing transverse momentum reconstruction in pp data at $\sqrt{s} = 8$ TeV", *JINST* **10** (2015), no. 02, P02006, `doi:10.1088/1748-0221/10/02/P02006`, `arXiv:1411.0511`.

[112] J. Alwall et al., "MadGraph 5 : Going Beyond", *JHEP* **1106** (2011) 128, `doi:10.1007/JHEP06(2011)128`, `arXiv:1106.0522`.

[113] T. Sjostrand, S. Mrenna, and P. Z. Skands, "PYTHIA 6.4 Physics and Manual", *JHEP* **0605** (2006) 026, `doi:10.1088/1126-6708/2006/05/026`, `arXiv:hep-ph/0603175`.

[114] G. Corcella et al., "HERWIG 6.5 release note", `arXiv:hep-ph/0210213`.

[115] Z. Was, "TAUOLA the library for tau lepton decay, and KKMC / KORALB / KORALZ /... status report", *Nucl.Phys.Proc.Suppl.* **98** (2001) 96–102, `doi:10.1016/S0920-5632(01)01200-2`, `arXiv:hep-ph/0011305`.

[116] R. Field, "Min-Bias and the Underlying Event at the LHC", *Acta Phys.Polon.* **B42** (2011) 2631–2656, `doi:10.5506/APhysPolB.42.2631`, `arXiv:1110.5530`.

[117] M. Aliev et al., "HATHOR: HAdronic Top and Heavy quarks crOss section calculatoR", *Comput.Phys.Commun.* **182** (2011) 1034–1046, `doi:10.1016/j.cpc.2010.12.040`, `arXiv:1007.1327`.

[118] P. Kant et al., "HatHor for single top-quark production: Updated predictions and uncertainty estimates for single top-quark production in hadronic collisions", *Comput.Phys.Commun.* **191** (2015) 74–89, `doi:10.1016/j.cpc.2015.02.001`, `arXiv:1406.4403`.

[119] M. Czakon and A. Mitov, "Top++: A Program for the Calculation of the Top-Pair Cross-Section at Hadron Colliders", *Comput.Phys.Commun.* **185** (2014) 2930, `doi:10.1016/j.cpc.2014.06.021`, `arXiv:1112.5675`.

[120] R. Rahmat, R. Kroeger, and A. Giammanco, "The Fast Simulation of The CMS Experiment", *Journal of Physics: Conference Series* **396** (2012), no. 6, 062016.

[121] W. Beenakker et al., "NLL-fast", technical report, 2013.

[122] W. Beenakker, R. Hopker, and M. Spira, “PROSPINO: A Program for the production of supersymmetric particles in next-to-leading order QCD”, `arXiv:hep-ph/9611232`.

[123] M. Botje et al., “The PDF4LHC Working Group Interim Recommendations”, `arXiv:1101.0538`.

[124] CMS Collaboration, “Measurement of the differential top-quark pair production cross section in the lepton+jets channel in pp collisions at $\sqrt{7} = 8$ TeV.”, CMS Physics Analysis Summary TOP-12-027, 2012.

[125] CMS Collaboration, “Measurement of the differential top-quark pair production cross section in the dilepton channel in pp collisions at $\sqrt{7} = 8$ TeV.”, CMS Physics Analysis Summary TOP-12-028, 2012.

[126] “pt(top-quark) based reweighting of ttbar MC”. `https://twiki.cern.ch/twiki/bin/viewauth/CMS/TopPtReweighting`.

[127] “MET Optional Filters”. `https://twiki.cern.ch/twiki/bin/view/CMS/MissingETOptionalFilters`.

[128] T. C. collaboration, “Determination of jet energy calibration and transverse momentum resolution in CMS”, *Journal of Instrumentation* **6** (2011), no. 11, P11002.

[129] CMS Collaboration Collaboration, “8 TeV Jet Energy Corrections and Uncertainties based on 19.8 fb^{-1} of data in CMS”,.

[130] C. Weiser, “A Combined Secondary Vertex Based B-Tagging Algorithm in CMS”, Technical Report CMS-NOTE-2006-014, CERN, Geneva, Jan, 2006.

[131] “Operating Points for *b*-Tag Algorithms”. `https://twiki.cern.ch/twiki/bin/viewauth/CMS/BTagPerformanceOP`.

[132] “Simple Cut Based Photon ID 2012”. `https://twiki.cern.ch/twiki/bin/viewauth/CMS/CutBasedPhotonID2012`.

[133] “EGamma PF Based Isolation”. `https://twiki.cern.ch/twiki/bin/view/CMS/EgammaPFBasedIsolation`.

[134] “Shower Shape Variables”. `https://twiki.cern.ch/twiki/bin/view/CMSPublic/SWGuideEgammaShowerShape`.

[135] CMS Collaboration, “Search for Gauge Mediated Supersymmetry Breaking Using Two Photons and Missing Transverse Energy”, CMS AN AN-11-515, 2012.

[136] CMS Collaboration, “Dilepton trigger and lepton identification efficiencies for the top quark pair production cross section measurement at 8 TeV in the dilepton decay channel.”, CMS AN AN-12-389, 2012.

[137] CMS Collaboration, “Search for Higgs Produced in Association with a Top Quark Pair and Decaying to Bottom Quarks or Tau Leptons”, CMS AN AN-13-145, 2012.

[138] “Muon POG Tag and Probe”. `https://twiki.cern.ch/twiki/bin/viewauth/CMS/MuonTagAndProbe`.

[139] “RooFit Users Manual v2.91”. `ftp://root.cern.ch/root/doc/RooFit_Users_Manual_2.91-33.pdf`.

[140] “Minuit User’s Guide”. `http://seal.web.cern.ch/seal/documents/minuit/mnusersguide.pdf`.

[141] CMS Collaboration, “Measurement of the inclusive top pair production cross section in the semi-leptonic muon and electron channels with the complete dataset from the 2011 data taking period”, CMS AN AN-11-443, 2012.

[142] CMS Collaboration, “Measurement of the $t\bar{t}$ production cross section in the dilepton channel in pp collisions at $\sqrt{s} = 8$ TeV”, *JHEP* **1402** (2014) 024, `doi:10.1007/JHEP02(2014)024,10.1007/JHEP02(2014)102`, `arXiv:1312.7582`.

[143] CMS Collaboration, “Measurement of the top-quark + photon production cross section in the muon + jets channel in pp collisions at 8 TeV.”, CMS AN AN-13-195, 2013.

[144] “SUSY Cross Sections 8 TeV Stop Sbottom”. `https://twiki.cern.ch/twiki/bin/view/LHCPhysics/SUSYCrossSections8TeVstopsbottom`.

[145] “Jet Energy Resolution and Corrections (JERC) Subgroup”. `https://twiki.cern.ch/twiki/bin/viewauth/CMS/JetEnergyScale`.

[146] “b Tag & Vertexing Physics Object Group”. `https://twiki.cern.ch/twiki/bin/viewauth/CMS/BtagPOG`.

[147] R. Barlow and C. Beeston, “Fitting using finite Monte Carlo samples”, *Computer Physics Communications* **77** (1993) 219–228.

[148] J. S. Conway, “Incorporating Nuisance Parameters in Likelihoods for Multisource Spectra”, (2011). `arXiv:1103.0354`.

[149] CMS Collaboration, “Combination of ATLAS and CMS top-quark pair cross section measurements using proton-proton collisions at sqrt(s) = 7 TeV”, CMS Physics Analysis Summary CMS-PAS-TOP-12-003, 2012.

[150] CMS Collaboration, “Measurement of the inclusive top-quark pair + photon production cross section in the muon + jets channel in pp collisions at 8 TeV”, CMS Physics Analysis Summary CMS-PAS-TOP-13-011, 2013.

[151] CMS Collaboration, “Identification of b-quark jets with the CMS experiment”, *JINST* **8** (2013) P04013, `doi:10.1088/1748-0221/8/04/P04013`, `arXiv:1211.4462`.

[152] CERN, “Proceedings of the First Workshop on Confidence Limits”. CERN, Geneva, (2000).

[153] G. Cowan, K. Cranmer, E. Gross, and O. Vitells, “Asymptotic formulae for likelihood-based tests of new physics”, *The European Physical Journal C* **71** (2011), no. 2, `doi:10.1140/epjc/s10052-011-1554-0`.

[154] The ATLAS Collaboration, The CMS Collaboration, The LHC Higgs Combination Group Collaboration, “Procedure for the LHC Higgs boson search combination in Summer 2011”, Technical Report CMS-NOTE-2011-005. ATL-PHYS-PUB-2011-11, CERN, Geneva, Aug, 2011.

[155] J. Conway, “Incorporating Nuisance Parameters in Likelihoods for Multisource Spectra”, `arXiv:1103.0354`.

[156] V. Barger, M. Ishida, and W.-Y. Keung, “Flavor-tuned 125 GeV supersymmetric Higgs boson at the LHC: Test of minimal and natural supersymmetric models”, *Phys. Rev.* **D87** (2013), no. 1, 015003, `doi:10.1103/PhysRevD.87.015003`, `arXiv:1207.0779`.

[157] J. Barnard, B. Farmer, T. Gherghetta, and M. White, “Natural gauge mediation with a bino NLSP at the LHC”, *Phys. Rev. Lett.* **109** (2012) 241801, `doi:10.1103/PhysRevLett.109.241801`, `arXiv:1208.6062`.